Helium effects on irradiation assisted stress corrosion cracking susceptibility of 316L austenitic stainless steel

THÈSE N° 8268 (2018)

PRÉSENTÉE LE 12 JANVIER 2018
À LA FACULTÉ DES SCIENCES DE BASE
LABORATOIRE DE PHYSIQUE DES RÉACTEURS ET DE COMPORTEMENT DES SYSTÈMES
PROGRAMME DOCTORAL EN SCIENCE ET GÉNIE DES MATÉRIAUX

ÉCOLE POLYTECHNIQUE FÉDÉRALE DE LAUSANNE

POUR L'OBTENTION DU GRADE DE DOCTEUR ÈS SCIENCES

PAR

Ignasi VILLACAMPA ROSES

acceptée sur proposition du jury:

Prof. P. Bowen, président du jury
Dr Ph. Spätig, Dr J.-C. Chen, directeurs de thèse
Dr M.-F. Barthe, rapporteuse
Dr M. M. Hernandez Mayoral, rapporteuse
Dr R. Schäublin, rapporteur

EPFL
ÉCOLE POLYTECHNIQUE
FÉDÉRALE DE LAUSANNE

Suisse
2018

Acknowledgements

always there, withstanding my bad mood in difficult days and making me feel important and loved. This PhD thesis would not exist without her support.

Villigen, December 6th, 2017

Abstract

The formation and growth of cracks by irradiation-assisted stress corrosion cracking (IASCC) in light water reactor internals is a critical issue for a safe long-term operation of nuclear power plants. The IASCC susceptibility at relatively low dose is dominated by conventional mechanisms such as radiation-induced segregation and radiation hardening. However, the ageing of the nuclear fleet combined with the increase of their life-span reveals other mechanisms that could play an important role on IASCC susceptibility. Recent studies show that a huge amount of helium (He) can be accumulated in reactor internal components of pressurized water reactors (PWR) after long-term operation. This occurrence could significantly increase the IASCC susceptibility at high doses.

The main objective was to investigate the He effects on IASCC susceptibility of the solution-annealed (SA) and 20% cold-worked (CW) austenitic steel 316L. SA and CW miniaturized tensile samples and a SA plate were homogeneously implanted up to 1000 appm He. He was implanted at ~45 MeV and 300°C at the cyclotron in CEMHTI/CNRS (France). Slow strain rate tests (SSRT) in air and in high-temperature water were then carried out on SA, CW, post-implantation annealed (PIA) and as-implanted samples; instrumented nanoindentation tests were performed at room temperature on non-implanted and implanted specimens; and scanning electron microscope and transmission electron microscope were employed for fractography and microstructural characterization.

The results of SSRTs in high-temperature air and in hydrogenated high-temperature water showed that homogenized implanted He up to 1000 appm corresponding to a displacement damage of about 0.16 dpa (displacement per atom) does not produce intergranular cracking and IASCC. However, the deformation microstructure of non-implanted SA/CW is characterized by high dislocation density arranged in cell walls separated by relatively dislocation-free regions, while the as-implanted SA samples (> 0.05 dpa) exhibit a more planar deformation microstructure. Characterization of as-implanted CW and PIA samples did not show any significant implantation effect on the deformation microstructure.

PIA of the He implanted plate was carried out from 650 to 1000°C for 1h to increase the helium grain boundary coverage, and to reproduce the observed microstructure of the replaced reactor internal components that showed IASCC and use the results for the PIA of tensile samples. The transmission electron microscope investigations showed that an increase of the annealing temperature causes an average bubble size increase and density decrease. The average He bubble size and distribution in the grain interior and on the grain boundary were similar in the range of temperatures studied. In both cases, bubbles grew by the Ostwald ripening mechanism. No preferential He build-up took place on the grain boundaries. The increase of yield stress produced by He bubbles was calculated with three distinct dislocation-localized obstacle and compared to the tensile test results. The bubble strength estimated for these models was used to assess their validity and to compare the results to published data.

Finally, nano-indentation tests in SA, CW, as-implanted SA and PIA (650 to 850°C for 1h) samples did not show He effects on grain boundaries strength. However, the average hardness of the grain interior increased with the He implantation and decreased increasing the PIA temperature.

Keywords
Helium, irradiation-assisted stress corrosion cracking, light water reactors, slow strain rate tests, transmission and electron electron microscope, solution-annealed, cold-worked and post-implantation annealing.

Résumé

La formation et croissance de fissures de corrosion sous contrainte assistée par l'irradiation (CSCAI) des composants internes des réacteurs à eux légère est un problème critique concernant la sûreté à long terme des centrales nucléaires. La susceptibilité de CSCAI à relativement faibles doses est dominée par des mécanismes conventionnels tels que la ségrégation et le durcissement résultant de l'irradiation. De plus, le vieillissement du parc nucléaire conjugué à l'extension de sa durée de vie fait apparaître d'autres mécanismes pouvant jouer un rôle important en CSCAI. De récentes études montrent que quantités importantes d'hélium peuvent s'accumuler dans les composant internes de réacteur à eau pressurisée après une durée d'opération de 40 ans. Cette accumulation d'hélium peut potentiellement augmenter la susceptibilité de CSCAI, voire dominer à hautes doses d'irradiation neutronique.

L'objectif principal a été d'évaluer les effets de l'hélium sur la susceptibilité de CSCAI de l'acier austénitique 316L après traitement de recuit en solution (RS) et de déformation à froid à 20% (DF). Des échantillons miniaturisés de traction RS and DF et des coupons RS ont été implantés à 1000 appm He de façon homogène. L'hélium a été implanté à ~45 Mev et 300 °C dans une ligne du cyclotron CEMHTI/CNRS (France). Des essais à petites vitesses de déformation dans l'air et l'eau à haute température sur des échantillons ont été réalisés en RS, DF, traitements de recuit post-implantation et après implantation; des essais de nanoindentation conduits à température ambiante ont été conduits en échantillons non-implantés et implantés; et de la microscopie électronique à balayage et à transmission a été utilisée pour caractériser les surfaces de fracture et les microstructures.

Les essais de traction à faible vitesse à haute température à l'air et dans l'eau à haute température hydrogénée ont montré que l'hélium implanté de façon homogène jusqu'à 1000 appm, correspondant à une dose d'environ 0.16 dpa (déplacement par atome) ne produit pas ni fissuration intergranulaire, ni de CSCAI. Cependant, la microstructure de déformation des échantillons non-implantés en condition RS et DF est caractérisée par une haute densité dislocation organisé en parois cellulaires séparées par des régions à faible densité de dislocations, alors que les échantillons RS implantés (> 0.05 dpa) présentent vers une structure de déformation plus planaire. La caractérisation d'échantillons implantés RS et DF n'a pas montré d'effet significatif sur la déformation microstructurale.

Des traitements de recuit post-implantation des échantillons ont été réalisés de 650 à 1000 °C pendant une heure afin d'augmenter la couverture en hélium des joints de grains, et reproduire la microstructure observée des composants internes de réacteur remplacés qui présentaient de la CSCAI et utiliser les résultats pour des échantillons de traction. Les observations par microscopie électronique à transmission ont montré que l'augmentation de la température de recuit conduit à une augmentation de la taille moyenne des bulles d'hélium et à une diminution de leur densité. La taille moyenne des bulles d'hélium et leur distribution à l'intérieur des grains et aux joints de grains sont similaires dans le domaine de températures étudiées. Dans les deux cas, les bulles croissent par mécanisme de maturation d'Ostwald. Aucune accumulation préférentielle d'hélium n'a eu lieu aux joints de grains. L'augmentation de la limite d'élasticité due aux bulles d'hélium a été calculée avec trois modèles différents d'interaction obstacle-dislocations et comparée aux résultats des essais de traction. La force de résistance des bulles aux dislocations estimés par ces modèles a été utilisée pour évaluer leur validité et pour comparer ces résultats à des données publiées.

Finalement, des essais de nanoindentation sur des échantillons non implantés en RS, DF ainsi qu'après des recuits entre 650 et 850 °C n'ont pas révélés de fragilisation des joints de grains résultant de l'hélium. Néanmoins, la dureté moyenne à l'intérieur des grains augmente en fonction de de la dose d'hélium implanté and décroît avec la température des recuits.

Mots-clés
Hélium, corrosion sous contraine assistée par irradiation, réacteurs à eau légère, essais de traction à faible vitesse, microscopie électronique à transmission et balayage, recuit en solution, déformation à froid, recuit post-implantation

Content

List of Figures

List of Tables

List of abbreviations

AIDE	Absorption–Induced Dislocation Emission
AISI	American Iron and Steel Institute
appm	Atomic Parts Per Million
ASTM	American Standard Test Method
AuSS	Austenitic Stainless Steel
AVG	AVeraGe
BFB	Baffle to Former Bolts
BKS	Bacon Kocks Scattergood
BWR	Boiling Water Reactor
CEMHTI	Conditions Extrêmes et Matériaux: Haute Température et Irradiation
CGR	Crack Growth Rate
CNRS	Centre National de la Recherche Scientifique
CSM	Continuous Stiffness Measurement
CW	Cold-Worked
DBH	Dispersed Barrier Hardening
DBTT	Ductile to Brittle Transition Temperature
DIN	Deutsches Institut für Normung
dpa	Displacements Per Atom
EBSD	Electron BackScattered Diffraction
ECP	Electrochemical Corrosion Potential
EDX	Energy-Dispersive X-ray spectroscopy
EELS	Electron Energy Loss Spectroscopy
FBR	Fast Breeder Reactor
fcc	Face-Centred Cubic
FEPA	Federation of European Producers of Abrasives
FIB	Focused Ion Beam

FKH	Friedel Kroupa and Hirsh
FTT	Flux Thimble Tubes
GB	Grain Boundary
GCR	Gas Cooled Reactor
GI	Grain Interior
H	Hardness or Hydrogen
HASCC	Hydrogen Assisted Stress Corrosion Cracking
HAZ	Heat Affected Zone
HEDE	Hydrogen-Enhanced Decohesion Embrittlement
HELP	Hydrogen-Enhanced Localized Plasticity
HESIV	Hydrogen-Enhanced Strain-Induced Vacancy
HTA	High-Temperature Air
HTW	Hydrogenated high-Temperature Water (2.2 ppm H_2)
HV	Vickers Hardness
HWC	Hydrogen Water Chemistry
IASCC	Irradiation-Assisted Stress Corrosion Cracking
ICP-AES	Inductively Coupled Plasma Atomic Emission Spectroscopy
IG	InterGranular
IGSCC	InterGranular Stress Corrosion Cracking
ISS	Indentation Stress-Strain
K-P	Kinchin-Pease
LWGR	Light Water cooled Graphite moderated Reactor
LWR	Light Water Reactor
LVDT	Linear Variable Differential Transformer
M	Miniaturised sample
MC	Migration and Coalescence
MTR	Material Test Reactor
MVC	MicroVoid Coalescence

NPP	Nuclear Power Plant
NWC	Normal Water Conditions
OLNC	On-Line NobleChem
OR	Ostwald ripening
PHWR	Pressurised Heavy Water Reactor
PIA	Post-Implantation Annealed
ppb	Parts Per Billion
ppm	Parts Per Million
PSI	Paul Scherrer Institute
PWR	Pressurized Water Reactor
RA	Reduction of Area
RIP	Radiation-Induced Precipitation
RIS	Radiation-Induced Segregation
RSS	Root-Sum-Square
RTA	Room Temperature Air
S	Standard sample
SA	Solution-Annealed
SCC	Stress Corrosion Cracking
SEM	Scanning Electron Microscope
SFE	Stacking Fault Energy
SHE	Standard Hydrogen Electrode
SIF	Stress Intensity Factor
SRIM	Stopping and Range of Ion in Matter Code
SS	Stainless Steel
SSRT	Slow Strain Rate Tests
STD	STandard Deviation
TEM	Transmission Electron Microscope

TG   TransGranular

TG-C   TransGranular Cleavage

TG-D   TransGranular Dimple

TGSCC   TransGranular Stress Corrosion Cracking

UC   Uniform Corrosion

US   Uniform Strain

UTS   Ultimate Tensile Stress

YS   Yield Stress

ZLP   Zero Loss Peak

List of symbols

$\Delta \mathbf{f}$	Defocus TEM micrograph
$\Delta \mathbf{m}$	Mass defect
$\rho_\mathbf{A}$	Atomic density
$\mathbf{a}$	Crack length or projected radius of the indent footprint
$\mathbf{A_m}$	Amplitude crack-tip strain rate
$\mathbf{A}$	Cross-sectional area or projected contact area of the indent
$\mathbf{b}$	Burgers vector
$\mathbf{B}$	Combined scaling parameter of the grain size, projected radii and sessile dislocation distance effect
$\mathbf{B(T)}$	First two terms of the adjusted virial expression of the compressibility factor
$\mathbf{c}$	Speed of light
$\mathbf{c^*}$	Concentration around the defect
$\mathbf{C_b}$	Bubble density
$\mathbf{C_{He}}$	Helium concentration in a bubble or implanted helium concentration
$\mathbf{\hat{c}_{He}}$	Helium concentration in solid solution
$\mathbf{d}$	Obstacle diameter
$\mathbf{D'}$	Effective obstacle diameter
$\mathbf{D}$ or $\mathbf{D(T)}$	Diffusion coefficient or combined length scale parameter
$\mathbf{\bar{d}}$	Average diameter
$\mathbf{D_0}$	Temperature-independent diffusion pre-exponential constant
$\mathbf{D_B}$	Pressure dependent self-diffusion coefficient
$\mathbf{D_i}$	Pressure-dependent effective diffusivity of helium in the matrix or volume self-diffusion coefficient
$\mathbf{dl}$	Displacement of the dislocation normal to the dislocation line segment
$\mathbf{\dot{dpa}}$	Displacement per atom rate
$\mathbf{ds}$	Dislocation line segment
$\mathbf{d\theta}$	Half angle circular sector formed by the dislocation segment

E_b	Binding energy
$E_{2He,i}^B$	Binding energy of two-interstitial He atoms
$E_{2He,i}^M$	Migration energy of two-interstitial He atoms
$E_{He,Dis}^M$	Migration energy of He by dissociative mechanism
$E_{He,Ex}^M$	Migration energy by exchange mechanism
$E_{He,i}^f$	Formation energy interstitial He
$E_{He,i}^M$	Migration energy interstitial He
$E_{He,v}^B$	He-vacancy binding energy
$E_{He,v}^M$	Migration energy of He by vacancy mechanism
$E_{He,v}^T$	Energy needed to transfer a substitutional He atom into a neighbouring vacancy
E_{eff}	Effective modulus
E_{ind}	Apparent indentation modulus
E_m	Chemical composition dependent parameter
E_0	Incident electron energy
E_{test}	Apparent tensile modulus
E_v^f	Vacancy formation energy
E_v^M	Vacancy migration energy
E_a	Apparent activation energy
E_d	Displacement energy threshold
E_F	Energy Fermi level
E_i	Indenter tip modulus
E_s	Sample modulus
E_{vac}	Vacuum energy level
F	Relativistic factor
f	Atomic fraction element
F_0	Harmonic load
G	Grain size number ASTM E112 or $M_6Ni_{16}Si_7$ phase

H	Hardness or hydrogen
h	Penetration depth implantation
$\tilde{h}_e$	Elastic penetration recorded by the instrumented indenter
h_e^*	Elastic penetration depth at the actual point of initial contact
h_0	Displacement amplitude
h_{act}	Active penetration
h_{app}	Apparent penetration
h_e	Elastic penetration depth
h_{rms}	Root-mean-squared amplitude penetration
I	Beam intensity
I_c	Low-temperature implantation
I_h	High-temperature implantation
I_0	Integral of the ZLP in the EELS spectrum
I_R	Irradiation/Implantation rate
I_t	Integral of the unfiltered EELS spectrum
K	Indent geometry constant, stress intensity factor or hardening constant
k	Boltzmann constant
k_1	Scaling parameter of the projected radii
k_2	Scaling parameter of the grain size
k_3	Scaling parameter of the sessile dislocations distance
k_4	Scaling parameter of the helium bubble distance
K_p	Plastic strain constant
K_f	Load frame stiffness
k_{hp}	Hall-Petch constant
K_{HP}	Averaged/combined Hall-Petch constant
K_I	Stress intensity factor mode-I
K_{Ic}	Fracture toughness mode-I

K_{ISCC} Stress corrosion cracking threshold of the stress intensity factor

K_s Support spring stiffness

l Average obstacle spacing (centre to centre)

l_b Average obstacle spacing (centre to centre) for helium bubbles

l_s Average obstacle spacing (centre to centre) for sessile dislocations

L Average bubble spacing (without obstacle radii)

m Indenter mass

M Taylor factor

m^* Exponent contact stiffness correction

N_i Volume or areal obstacle density of defect type i

n Strain hardening exponent, exponent value for diffusion mechanism or neutron

n^* Exponent crack-tip strain rate

n_p Plastic strain hardening exponent or helium particle density in a bubble

P Indentation load or bubble internal pressure

p Proton

$\widetilde{P}$ Load recorded by the instrumented indenter

P^* Load at the actual point of initial contact

P_{act} Active load

P_{app} Apparent load

P_{rms} Root-mean-squared amplitude load

q_{alpha} Helium ion charge

Q Activation energy

R Grain size radius or ideal gas constant

r Obstacle radius (bubbles, precipitates, etc.)

$\bar{r}_b$ Average bubble radius

r_0 Temperature-independent radius pre-exponential constant

r_c Dislocation core radius

R_h High-temperature irradiation

$\mathbf{Rp_{0.2\%}}$	Tensile yield stress at 0.2% strain
$\mathbf{Rp_{ind\ 0.2\%}}$	Indentation yield stress at 0.2% strain
$\mathbf{s}$	Grain size (diameter)
$\mathbf{S_{act}}$	Active contact stiffness
$\mathbf{S_{act}}$	Apparent contact stiffness
$\mathbf{S_c}$	Contact stiffness
$\mathbf{t}$	Time
$\mathbf{T}$	Temperature or annealing temperature
$\mathbf{t_a}$	Annealing time
$\mathbf{T_m}$	Melting temperature
$\mathbf{T_{threshold}}$	Threshold temperature
$\mathbf{T_{tr}}$	Transition temperature
$\mathbf{\nu_i}$	Poisson's ratio tip
$\mathbf{\nu_l}$	Fluid volume upon freezing
$\mathbf{\nu_s}$	Poisson's ratio sample
$\mathbf{w}$	Sample width
$\mathbf{x}$	Sample thickness
$\mathbf{x_c}$	Critical sample thickness
$\mathbf{Z}$	Atomic number
$\mathbf{z}$	Compressibility factor
$\mathbf{z_l}$	Compressibility factor on freezing
$\mathbf{Z_{eff}}$	Effective atomic number
$\mathbf{\alpha}$	Hardening coefficient, GB coverage or alpha particle
$\mathbf{\beta}$	Constant dependent of tip geometry or collection semi-angle
$\mathbf{\Gamma}$	Line tension dislocation
$\mathbf{\gamma}$	Surface free energy
$\mathbf{\gamma(x)}$	Atom displacement per unit length

δ	Conversion factor from $Rp_{ind\ 0.2\%}$ to $Rp_{0.2\%}$.
ε	Strain
ε_{eng}	Tensile engineering strain
ε_{ind}	Indentation (true) strain
$\varepsilon_{ind,p}$	Indentation (true) plastic strain
ε_p	Tensile true plastic strain
ε_t	Tensile true strain
λ	Electron mean free path or gamma rays
μ	Shear modulus
ξ	Exponential contact for superposition hardening law
σ	Stress or square root of variance
$\sigma_{0,ind}$	Fundamental friction stress under indentation
σ_{eng}	Tensile engineering stress
σ_i	Resistance experienced by a dislocation moving through the crystal
σ_{ind}	Indentation (true) stress
σ_t	Tensile true stress
σ_y	Yield stress or yield stress at 0.2% strain
τ	Uniform shear stress
φ	Phase shift
$\dot{\Phi}$	Ion flux rate
ω	Frequency

Chapter 1   Introduction

Light water reactor (LWR) internals are critical components for safety (safe shut-down, core coolability, reactivity/criticality control) and plant lifetime because replacement of some reactor internals is very challenging or extremely costly. The possibility of repair welding of highly irradiated material is limited or even impossible. Under certain combinations of mechanical stress and environment, cracks can be formed and grow in reactor internal components by stress corrosion cracking (SCC), potentially resulting in an unexpected failure. Irradiation produces changes in the microstructure of the materials affecting grain and grain boundaries (GB), in the environment and in the stress/strain state, which in turn can produce an increase of the SCC susceptibility (Figure 1.1) [1].
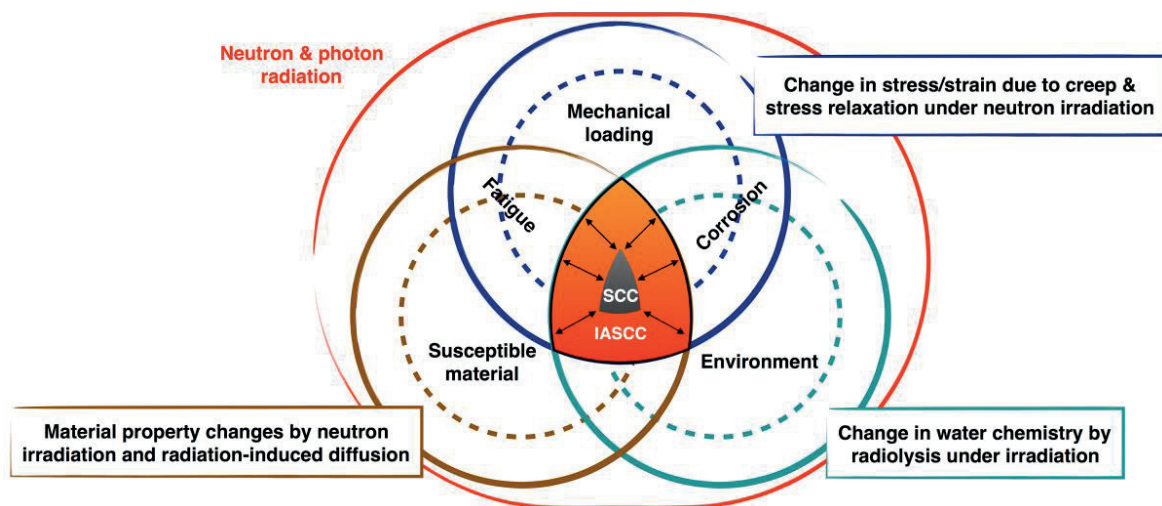
Figure 1.1. Irradiation-assisted SCC and SCC intersection zones.

The reactor internals are mainly made of austenitic stainless steels (AuSS), a material which possesses a good combination of corrosion and irradiation resistance and high toughness. During normal operation conditions, these components are subjected to different irradiation-induced or -assisted degradation mechanisms such as irradiation-assisted stress corrosion cracking (IASCC), irradiation hardening and embrittlement (increase of strength, reduction of ductility and fracture toughness) [1, 2, 3, 4, 5].

The IASCC cracking mode is intergranular (IG) and it can be seen as intergranular stress corrosion cracking (IGSCC) that is enhanced by irradiation. At relatively low dose, IASCC susceptibility is dominated by conventional mechanisms like radiation-induced segregation (RIS) and radiation hardening. However, the ageing of the nuclear fleet combined with the increase of their life-span reveals other mechanisms that could play an important role on IASCC susceptibility.

Recent studies show that a huge amount of helium (He, up to 1000 appm) can be accumulated in some reactor internal components of pressurised water reactors (PWR) after long-term operation (above 40 years). He accumulation could significantly increase (or even dominate) the IASCC susceptibility at

high doses in addition to conventional mechanisms [6, 7]. This thesis focuses on the potential He effects on IASCC susceptibility.

1.1 Statement of the problem

He produced in the reactor internals has a low solubility in metals and a strong tendency to be trapped, to cluster or to form bubbles as it accumulates. In addition, a thermal transient (e.g. weld repairs) permits migration of He and the formation of bubbles along the GB, thus weakening the material [8, 9].

He stabilizes void embryos, resulting in a shortening of the nucleation stage of voids. This reduces the incubation dose to reach steady state (breakaway) swelling. Swelling can impact IASCC indirectly by causing heterogeneous strains, resulting in stresses in welded or bolted components, especially when swelling occurs at different rates (e.g. in baffle to former bolts (BFB) and plates).

Recent laboratory studies tried to reveal the minimum He concentration to produce IG fracture [8, 10, 11]. Miura et al. [10] found IG brittle cracks in 316L single GBs using micro-tensile specimens when the He concentration and the bubble average spacing in the GB was more than 2 at. % and less than 5 nm, respectively. Schroeder and Liu [8] and Ullmaier and Chen [11] showed that a He concentration above 1 at. % can change the fracture mechanism in miniaturized specimens tested in vacuum, from transgranular (TG) ductile with micro-voids coalescence to TG cleavage fracture. Those He concentrations were significantly above the expected He accumulation at end of life in reactor internal components. Radiation damage up to 48 displacements per atom (dpa) alone is insufficient to produce significant TG cleavage (below 2%) or IG fracture in simulated PWR environment as was shown by Chen et al. in [12]. However, a 304L sample irradiated by 800 MeV protons at <250°C showed partial cleavage at 3.3 dpa (~500 appm He) and partial IG brittle fracture mode at 8 dpa (~1200 appm-He) after tensile test at room temperature [13]. Therefore at low dpa (< 3-4 dpa), He is postulated to be the main contributor to TG cleavage and at higher dpa ($\sim$ 8 dpa), it is contributing to the IG fracture. The synergistic interaction between He and dpa reduces the dpa threshold to produce embrittlement in AuSS.

The potential role of He on IASCC is unclear and it is unknown if He alone can induce IASCC or only in combination/synergy with other irradiation effects (e.g., He + hardening/localization of plastic deformation). Moreover, the synergistic interaction between He-LWR water chemistry and He-displacement damage-LWR water chemistry has not been clarified yet.

1.2 Objective of the thesis and selected approach

The main objective of the PhD project was to investigate the possible impact of He on IASCC up to 1000 appm in the 316L at displacement damage smaller than 0.2 dpa. To do so, slow strain rate tests (SSRT) were performed with as-implanted solution-annealed (SA), as-implanted cold-worked (CW) and post-implantation annealed (PIA) samples in hydrogenated neutral high-purity water (HTW) with 2.2 ppm H_2 at 290 °C, which simulates a PWR environment. As-irradiated SA and CW samples were used to simulate normal operating conditions in components with normal cooling (290 °C, SA-baffle plates and CW-BFB, respectively), whereas PIA samples were used to simulate conditions where gamma and/or neutron irradiation increases the temperature (380 ºC, CW-BFB).

The second objective was to reproduce the observed bubble/void microstructure of the replaced reactor internal components that showed IASCC and use the results for the PIA of tensile samples. To

do so, PIA was performed to He implanted plates with 1000 appm at temperatures ranging from 650 to 1000°C for 1 hour. The bubble size distribution, density, location and hardening were assessed and compared to literature data.

Another important part of the PhD work consisted on the validation of the sample designed for the He implantation (from now on: "miniaturized sample"). The miniaturized sample validation was performed at room temperature in air (RTA, ~25°C), high-temperature in air (HTA, ~290°C), HTW and normal water conditions (NWC) using SSRT. The tensile test and the post-test analysis are compared to the results obtained with a standard sample. The same testing conditions and sample geometry were applied to the irradiated samples.

The post-test analysis, using scanning electron microscope (SEM) and transmission electron microscope (TEM), was made to determine the fracture morphology, the He bubbles location, their size and density, as well as to gain insight into the deformation structures/mechanisms.

1.3   Thesis structure

The present thesis is divided into five chapters: Introduction, Literature Review, Experimental, Results & Discussion and Conclusion & Perspectives. The introduction chapter introduces the reader to the thesis subject, the statement of the problem, the thesis objectives and the selected approach for achieving these objectives. The literature review chapter covers from the most basic understanding of nuclear physics, nuclear reactors and AuSS to the current understanding of IASCC and He effects in AuSS. The experimental chapter describes the material properties of the AuSS 316L used in this project, the apparatus designed during this PhD, the tensile machines used, the electron microscopy devices and techniques, the instrumented nanoindenter and techniques and the He implantation time and damage calculations. The results & discussion chapter is divided into six different topics, which are discussed independently: the miniaturised sample validation, the He evolution after annealing, the effect of He implantation on GB segregation, the He effects on IASCC, the He hardening and the He effects on nanoindentation on GB and matrix. In the last chapter, conclusions and perspectives, the main conclusions and future work are provided.

Chapter 2   Literature review

The literature review is divided into three subchapters. The first, the nuclear energy subchapter explains the nuclear fission and the types of nuclear power plants and operating modes putting emphasis on the most popular technologies. The second, the AuSS subchapter justifies their use in LWR, presents their physical and mechanical properties and the corrosion and radiation effects. The last, the SCC subchapter presents the basic understanding of SCC, summarizes the effect of different parameters on SCC, deals with the generation of He, the coarsening of He bubbles, its effect on IASCC and mechanical properties, the production dependence on neutron fluence and the observations made in materials replaced from LWR.

2.1   General overview of nuclear energy

2.1.1   Nuclear fission

Nuclear fission was discovered on December 17th, 1938 by Otto Hahn and his assistant Fritz Strassmann, while intending to produce heavier elements bombarding uranium with neutrons. The fission process was explained theoretically in January 1939 by Lise Meitner and her nephew Otto Robert Frisch.

In a nuclear reactor, a neutron (projectile) collides with a heavy element (target) and if the neutron energy and the target are the right ones, the neutron can be captured by the heavy element nucleus. The unstable nucleus usually splits into two lighter elements of different mass, neutrons and photons (Figure 2.1). Sometimes, a fission reaction can produce more than two lighter elements, but this is rarely observed.
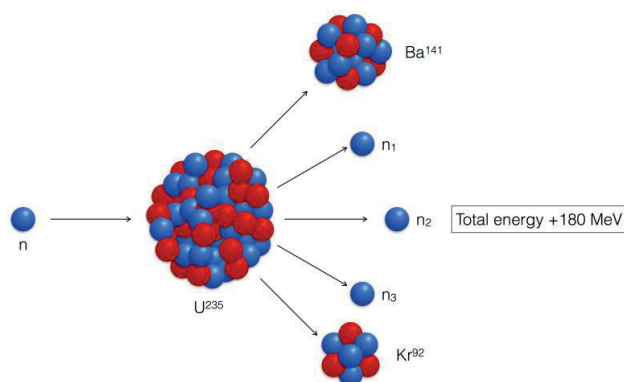
Figure 2.1. Representation of the fission reaction example with Uranium-235.

The nuclear fission probability depends on the neutron energy and the element. Some natural elements like uranium-235 and uranium-233 can undergo fission with all neutron energies, but the probability increases with decreasing neutron energy, i.e. with low energy neutrons (also called thermal neutrons), these are fissile elements; while others like uranium-238 and thorium-232 are only fissionable with high energy neutrons (also called fast neutrons).

The fission reaction is a form of transmutation because the resulting elements are different from the original ones. The energy released in a fission reaction depends on the binding energy of the element. The binding energy is calculated using the mass defect of the elements, which is the difference between the mass of the nucleus and the sum of the masses of the nucleons. Using Einstein equation the binding energy can be determined:

$$E_b = \Delta m \, c^2$$
<div style="text-align: right;">Eq. 2.1</div>

Where E_b is the binding energy in J, Δm is the mass defect in kg and c is the speed of light in m/s^2. Figure 2.2 shows the binding energy per nucleon for different elements. Heavier elements release energy with a fission reaction and lighter elements release energy with fusion reaction.
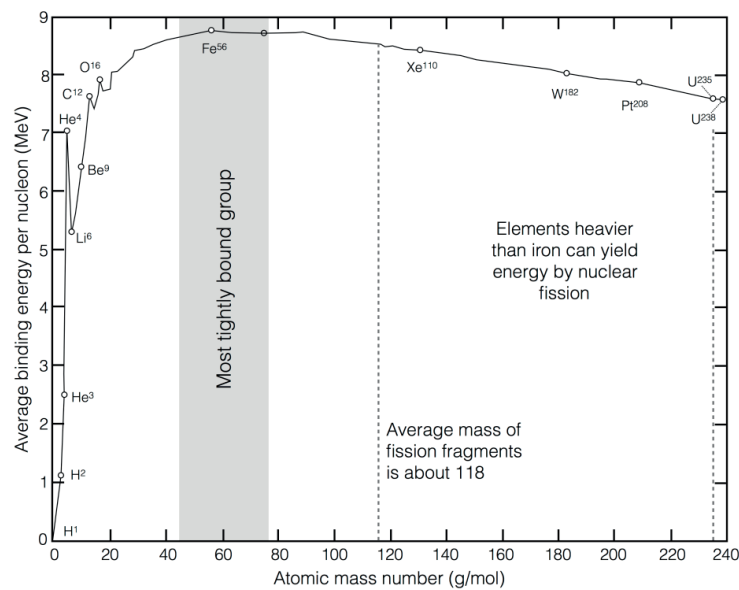
Figure 2.2. Average binding energy per nucleon for different elements. Adapted from ref. [14].

2.1.2 Nuclear power plant fleet

The fission reaction can occur with thermal or fast neutrons, therefore the nuclear power plants (NPP) have to be fuelled accordingly. For this reason, two types of reactors can be distinguished in function of the neutron energy: fast reactors and thermal reactors. For each type of reactor different technologies have evolved, but the fission reaction is basically the same. Table 2.1 shows the types of reactors worldwide, the moderator, and the number of operating NPP. All the reactors that use a moderator are thermal reactors since these reactors need to thermalize (decrease) the neutron energy for increasing the probability of the fission reaction.

Reactor type	Coolant	Moderator	Number	%
Pressurized water reactor (PWR)	Light water	Light water	278	63
Boiling water reactor (BWR)	Light water	Light water	80	18
Pressurized heavy water reactor (PHWR)	Heavy water	Heavy water	49	11
Gas-cooled reactor (GCR)	Carbon dioxide or He	Graphite	15	3.4
Light water cooled graphite moderated reactor (LWGR)	Light water	Graphite	15	3.4
Fast breeder reactor (FBR)	Sodium	-	2	<1

Table 2.1. Worldwide reactor types and quantity.

The majority of nuclear power plants are BWR and PWR. Both systems are thermal reactors and represent more than 80% of the NPP fleet. 50% of these reactors have been operating for more than 30 years and 75% more than 20 years [15].

2.1.2.1 Light water reactors operation and chemistry

BWR and PWR reactors are LWR since these reactors use light water to cool and moderate the reactor. However, these reactors have different operating conditions.

PWR reactors are closed systems that operate at high pressure (~16 MPa) and high temperatures (~300°C) in the primary coolant circuit with liquid phase only. The heat from the reactor core is removed by water flowing through the primary cooling loop. In the steam generator, the heat from the primary loop is transferred to a secondary loop, which operates at lower pressure (~7 MPa) allowing production of superheated steam that drives a steam turbine to produce electricity. BWR reactors are open, direct cycle systems that operate at about 7 MPa and 288°C, where the steam is directly generated in the reactor core. Thus, the primary loop of the BWR reactors contains water in the liquid (feedwater, reactor water) and gaseous phase (steam).

The reactivity control, i.e. the neutron thermalization and absorption, is controlled by different mechanisms in both types of reactors as well. Roughly speaking, the control rods and the feedwater flow rate control the reactivity and the outlet power in BWR reactors. In PWR reactors, the boric acid (H_3BO_3) dissolved in the feedwater compensates the decrease of reactivity due to the fuel burnup, and the neutron poisoners in the fuel pellet made of gadolinium oxide (Gd_2O_3) absorb the excess of reactivity at the beginning of the cycle. The neutron thermalization is less effective in BWRs since the water density is lower (steam and liquid). For this reason, the BWR core is bigger, but the neutron flux is an order of magnitude lower than in PWR [16].

The operation of both reactors is quite different and also the water chemistry in which they operate. Table 2.2 summarizes the reactor water chemistry of both reactor types [17, 18].

Reactor type	Op. temperature	Op. pressure	Water conditions	ECP of AuSS	pH$_{290°C}$	Important chemical species
PWR	290-325	150 bar	Primary water	-800 to -700 mV_{SHE}	6.9-7.4	10-4000 ppm B 0.5-3.5 ppm Li 2-3 ppm H$_2$ <10 ppb O$_2$ & H$_2$O$_2$ <10 ppb Cl$^-$, SO$_4$
BWR	274-290	70 bar	Hydrogen water chemistry (HWC)	-500 to -200 mV_{SHE}[1]	5.65	0.1-0.3 ppm H$_2$ <10 ppb O$_2$ <1 ppb Cl$^-$, SO$_4$
			Normal water chemistry (NWC)	100 to 250 mV_{SHE}	5.65	200-800 ppb O$_2$ & H$_2$O$_2$ 5-40 ppb H$_2$ <1 ppb Cl$^-$, SO$_4$

[1] In the upper core region, the ECP is 150- 200 **mV_{SHE}** due to the boiling and strong hydrogen partitioning to the steam phase.

Table 2.2. PWR and BWR reactor water chemistry for stationary power operation.

All the PWRs operate with slightly alkaline, borated, lithiated and hydrogenated water in the primary coolant circuit. The inlet and outlet core temperatures are about 290 and 320 °C, respectively. H_3BO_3 is added to control the reactivity and LiOH to keep the pH$_{290°C}$ at ~ 7, which minimizes the corrosion

product release, activation and crud formation on the fuel elements. A large amount of hydrogen is added to suppress the radiolysis in the reactor core and to achieve lower electrochemical corrosion potential (ECP) of the structural materials, from -800 to -700 mV_{SHE} (standard hydrogen electrode, SHE).

BWRs are operated with neutral ($pH_{290°C} \sim 5.7$) high-purity water. The inlet and outlet core temperatures are about 274 and 288 °C, respectively. High-purity water is needed to avoid excessive crud formation on the fuel elements due to boiling and to reduce the enrichment of aggressive anions in cracks/crevices at high ECP or, in case of boiling, to mitigate SCC. In NWC, no hydrogen is added to the system. The radiolysis of the cooling water in the reactor core produces stoichiometric amounts of reducing (H_2) and oxidizing (O_2, H_2O_2) species. Due to the non-volatility of H_2O_2 and strong partitioning of H_2 into the steam phase, there is an excess of oxidizing species in the reactor water that results in high ECPs of reactor internals, from 100 to 250 mV_{SHE}. In hydrogen water chemistry (HWC), H_2 is injected into the feedwater, which recombines with O_2 and H_2O_2, forms H_2O and reduces the ECP. Due to the strong H_2 partitioning to the steam phase, this technique is less efficient in BWRs than in the PWRs, the ECPs are thus higher and in the range from -500 to -200 mV_{SHE}. Above the upper core level and in the upper plenum, the environment remains highly oxidizing in BWR/HWC. To increase the efficiency and to reduce some negative side effects of HWC (increased [16]N dose rates), the on-line noblechem (OLNC) technique was developed, where platinum (Pt) complex solutions are injected into the feedwater during reactor operation, and they finally deposit as nano-sized Pt particles on the water-wetted surfaces [19]. Pt particles electrocatalysis the recombination of H_2 with O_2 and H_2O_2 to produce H_2O. The majority of BWRs are now operating with HWC or HWC/OLNC. The main differences between BWR/NWC, BWR/HWC/OLNC and PWR with regard to corrosion are the different ECP, pH, H_2 contents and temperatures. Due to the high ECP, NWC environment is more aggressive than HWC and PWR environments, so IGSCC and IASCC of reactor internals are a bigger issue. The main difference, with regard to IGSCC and IASCC between BWR/HWC and PWR, is the higher temperature and H_2 contents of the later, whereas pH (in the plant relevant range) has little effect on SCC in deoxygenated water. On the other hand, the crack-tips are always deoxygenated and at low ECP in all three environments, and the environmental conditions under which cracks grow are thus quite similar.

2.1.2.2 Light water reactor internals and radiation damage

In LWR reactors, AuSSs are extensively used as structural materials in reactor pressure vessels internals because of their relatively good strength, ductility, fracture toughness and corrosion resistance. The fracture of these ductile steels occurs well above the yield stress (YS) and requires high plastic deformation. However, the microstructure changes under neutron irradiation and degrades the fracture properties (see subchapter 2.2.3).

AuSSs are employed for the main piping system, reactor vessel and pressurizer cladding, pumps, valves and core internals (core barrel, core baffles, threaded structural fasteners, etc.) [18, 20]. The most commonly used AuSS in reactor internals are the 304, the low carbon grades 304L and 316L and the stabilized grades 321 and 347 as can be seen from ref. [20]. These materials are mostly used in SA and sometimes in CW conditions.

As mentioned earlier, the neutron flux is different in PWR and BWR reactors, therefore results in different neutron dose rate in reactor internals. Furthermore, the distance of the reactor internals from the core and the water access for cooling the components are important parameters for radiation damage. In PWR reactors, the structural components like the flux thimble tubes (FTT, CW 316L), the

baffle plate (SA, 304/347), the BFB (CW 316L/316) and the core barrel (SA 304/347/304L) receive an average dose rate of 3, 2, 1 and 0.2 dpa per year, respectively. On the other hand, the BWR structural components like the shroud (SA 304) and the core support (SA 304), receive an average dose rate of 0.1 and 0.03 dpa per year. The dose rate and the accumulated dose in BWRs are thus significantly lower than in PWRs.

The BFBs in PWRs with limited cooling can reach local temperatures close to 380°C (instead of 300°C) due to gamma eating and the average dose per year is relatively high.

2.2   Austenitic stainless steels

The AuSS are used for applications where good corrosion resistance, non-magnetic, relatively low YS, high ductility and low ductile to brittle transition temperature (DBTT) are required. This part is fundamentally based on AuSSs putting emphasis on 316L, since this material has shown and still shows IASCC failures, especially in BFBs.

2.2.1   Physical metallurgy

<u>Chemical composition</u>

The AuSSs are essentially iron-based alloys of Fe-Cr-Ni, which owe their name to their room temperature austenitic structure. This structure is achievable thanks to austenitic stabilizers in the alloy (e.g. nickel and manganese). The equilibrium phases depend on the proportion of the three main elements. Figure 2.3 shows the ternary diagram for Fe-Cr-Ni at 600°C obtained with experimental data and calculations with FactSage [21], where the austenite region is marked in red. The AuSSs have a chromium content from 16% to 30% and a nickel content from 8 to 35% (weight %). The other alloying elements are introduced to improve mechanical properties, corrosion resistance or/and radiation resistance.
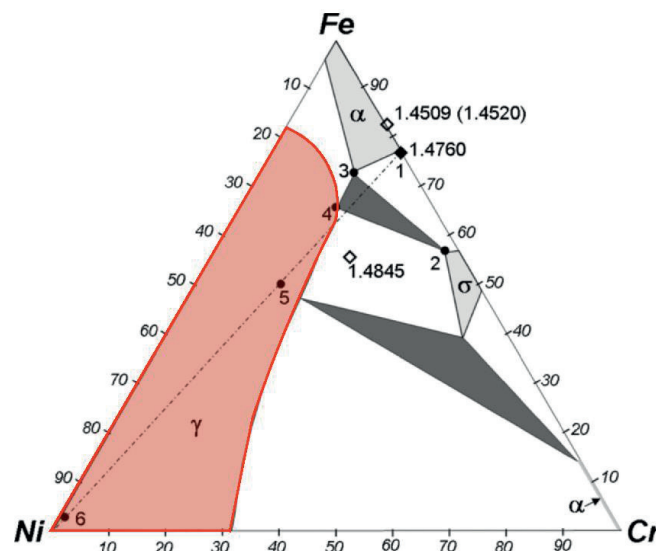
Figure 2.3. Isothermal section ternary Fe-Cr-Ni diagram (concentrations in at. %) at 600°C. In red the austenite region [21].

2.2.1.1   Influence of alloying elements

Each alloying element has a specific effect on the steel properties. It is the combined effect of all the alloying elements and, to some extent, the impurities that determine the property profile of a certain steel grade. The main purposes of the alloying elements in AuSS are to: stabilize the austenitic phase at room temperature, enhance mechanical properties, stabilize carbon, increase corrosion resistance, etc. The most important alloying elements of the AuSS 316L are given below along with their effect on the steel [22, 23, 24, 25].

- Carbon (C) increases the strength by solid solution strengthening. However, it causes sensitization in the steel at relatively high temperatures.
- Chromium (Cr) is added to steel to increase resistance to oxidation. The surface chromium oxide blocks the diffusion of oxygen ions preventing the steel from further oxidation.
- Nickel (Ni) greatly improves resistance to oxidation and corrosion, especially in sulphuric acid environments and it strengthens the steel by solid solution strengthening. It also increases toughness (impact strength) at both, high and low temperatures.
- Manganese (Mn) is added to steel to improve hot working properties and increase strength, toughness and hardenability. Moreover, it is a strong oxide and sulphide former (MnO and MnS). It is usually added to improve deoxidation and with the purpose of minimizing the formation of FeS which is much more unstable than MnS at high temperatures. Manganese is also used to increase the solubility of nitrogen in austenite.
- Molybdenum (Mo) decreases the required oxidizing effect to form a passive layer and the tendency for already formed passive films to break down. It improves resistance to pitting and crevice corrosion especially in chlorides and sulphur containing environments, and improves the creep properties by solid solution hardening. However, it is a ferrite stabilizer, facilitates carbides precipitation and promotes σ Laves phase formation on long-term ageing.
- Cobalt (Co) provides resistance to cavitation erosion. However, it becomes highly radioactive when exposed to the intense radiation in nuclear reactors, and, as a result, any stainless steel (SS) that is in nuclear service will have a Co restriction, usually 0.2% maximum.
- Silicon (Si) promotes ferritic structure and is used as a deoxidizing (killing) agent in the melting of steel (prevents carburizing at high temperatures) and, as a result, most steels contain a small percentage of Silicon. RIS produces an enrichment of Si on the GBs up to high levels and it has been shown to correlate with IASCC [3].

The alloying elements are divided in ferrite and austenite stabilizers, where Cr is a ferrite stabilizer and Ni is an austenite stabilizer. One tool commonly used to predict the structure at room temperature from the chemical composition is the Schaeffler-DeLong diagram (Figure 2.4). By studying the diagram it is seen that high Ni-equivalents are required to maintain an austenitic structure at room temperature.
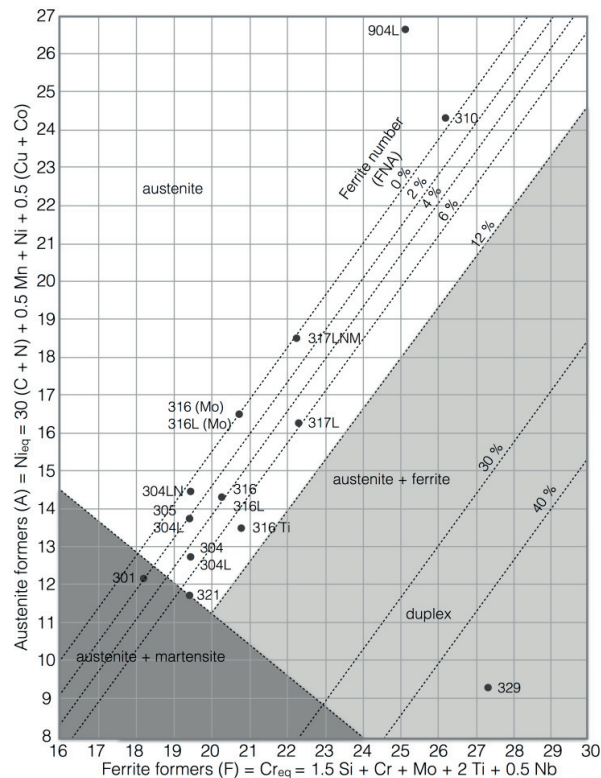
Figure 2.4. Schaeffer-DeLong diagram with nickel and Chromium equivalent equations for determining the structure of the steel at room temperature. Adapted from ref. [26].

Austenitic steels close to the "austenite + martensite" region in the Schaeffer-DeLong diagram (lower left corner) are called metastable AuSS. They are susceptible to deformation-induced martensitic transformation (e.g. 304 and 316) and hence hardening due to phase transformation. Austenitic steels with higher content of Ni_{eq} are more stable and will not transform to martensite during plastic deformation.

2.2.1.2 Crystal structure

AuSS are a class of alloys with a face-centred-cubic (fcc) lattice structure of austenite over the whole temperature range from room temperature (and below) to the melting point. The austenite crystal structure is shown in Figure 2.5.
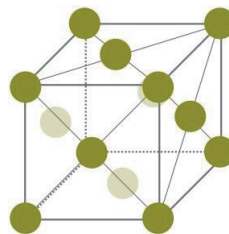
Figure 2.5. Crystal structure of AuSS.

2.2.1.3 Microstructure and second phases

The microstructure of AuSS can be quite complex. They are usually quenched from annealing temperatures (1000-1100 ºC depending upon the particular grade) to avoid precipitation of unwanted

phases. After the high-temperature annealing, the microstructure will be equiaxed austenite. The word "equiaxed" means that the dimensions of an individual austenite grain will be essentially the same regardless of orientation or direction. The SA AuSS is a single-phase material with only some non-metallic inclusions inherent to steel making, which are visible within the microstructure. This will generate a pure austenitic structure with a low dislocation density. Stacking faults are likely to form due to the low stacking fault energy (SFE) of AuSS. However, the structure is not always this simple, several carbide and intermetallic phases might be present and the austenite might have partially transformed to martensite [27].

AuSS may undergo microstructural changes during short or long-term exposure to high temperature and/or stress. In the case of longer ageing times, other precipitates such as intermetallic phases are formed and they are usually accompanied by dissolution of carbides. Intermetallic precipitations are of great interest not only because they exert influence on the mechanical properties, but also because of their strong effect on the corrosive properties. The most common secondary phases in the AuSS 316L with their composition and properties are summarized in Table 2.3.

Phase, crystal lattice	Elemental comp. (%)	Properties
σ-phase, tetrag.	50Fe-33Cr-5Ni-10Mo-1Si	Formed between 600°C and 1000°C. Detrimental effect on creep properties when precipitated on GBs [28].
Laves, hexag.	37Fe-11Cr-5Ni-22Mo-5Si	It requires long ageing times but it is a minor constituent. It precipitates in the grain interior. It could be detrimental to creep properties.
χ-phase, bcc	52Fe-24Cr-5Ni-20Mo-1Si	Formed above 750°C. After prolonged ageing, it transforms to sigma phase. It forms on GBs, incoherent twin boundaries or in the grain interior on dislocations. This phase degrades the impact toughness [29].
M_6C, fcc	11Fe-30Cr-23Ni-25Mo	Formed after long ageing times and enhanced by radiation. This phase is brittle, hard to deform and easy to crack in the interphases [30].
$M_{23}C_6$, fcc	14Fe-72Cr-3Ni-10Mo	Formed from 500 and 750°C. Precipitates on GBs causing sensitization of the steel (Chromium depletion). Hence increase the susceptibility to IG corrosion [31].
Cr_2N, hexag.	89Cr-11N	Formed from 650°C to 950°C. Usually, IG precipitation producing a decay of hardness (H) in the grain interior, loss of toughness and ultimate tensile strength (UTS) [32].
Martensite, hcp or bcc	-	Formed with deformation induced martensite or fast quenching. This phase is harder, stronger and brittle. Formed in 316L at temperatures well below 0°C [33].

Table 2.3. The most common second phases encountered in AuSS 316L, their composition and properties.

2.2.1.4 Physical properties

AuSS generally have low thermal conductivity, high thermal expansion and high electrical resistivity. The alloying elements have a clear effect on these properties. For instance, Ni, Cu and Cr will decrease the thermal conductivity significantly and Ni and Cu can decrease the thermal expansion. Table 2.4 summarizes some general physical properties of AuSS 316L.

Density	Young modulus	Thermal expansion	Thermal conductivity	Heat capacity	Resistivity	Ferromagnetism
8 g/cm^3	193 GPa	16 μm/mK	16.2 W/mK	500 J/kgK	74 μΩ cm	No

Table 2.4. Physical properties of AuSS 316L at room temperature [34].

2.2.1.5   Mechanical properties

AuSS have a relatively low YS and high strain hardening capacity. The mechanical properties are mainly affected by the CW, microstructure and alloying elements.

Cold work effect

When the 316L is deformed plastically at room temperature, in the so called "cold working" process, dislocations form and glide along a favourable plane producing permanent plastic deformation. This process sets a large dislocation density in the material, which hinders the formation and glide of new dislocations. As a result, the YS at 0.2% strain ($Rp_{0.2\%}$), the UTS and the hardness (H) increase, but the elongation and the reduction of area (RA) decrease (Figure 2.6).
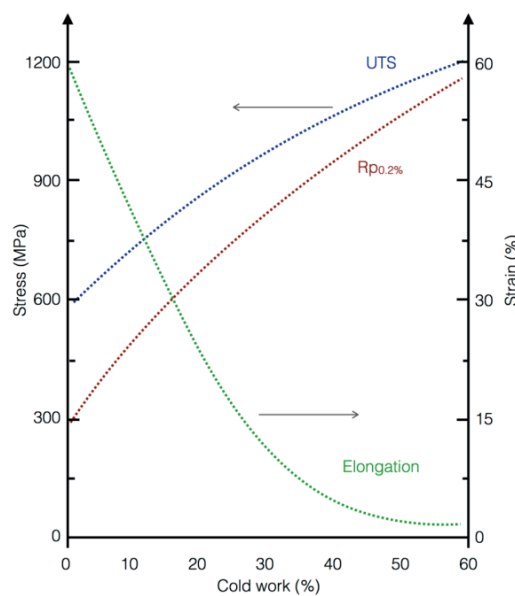
Figure 2.6. Effect of CW on 316L tensile properties. Adapted from the American standard test method, ASTM-1980.

Grain size effect

GBs act as obstacles, hindering the dislocation glide along the slip planes. A change in grain size affects the onset of plasticity and therefore the YS value. Accurate modelling is difficult, but it is found that the tensile YS is related to the grain size by the Hall-Petch equation [35, 36]:

$$\sigma_y = \sigma_i + \frac{k_{hp}}{\sqrt{s}}$$

Eq. 2.2

Where σ_y is the YS, σ_i is the resistance experienced by a dislocation moving through the crystal, k_{hp} is the strengthening coefficient (unique to each material) and s is the average grain diameter. Following Eq. 2.2, grain refinement increases yield strength.

2.2.2   Corrosion resistance

Corrosion is an electrochemical process that requires the presence of an electrolyte in the form of a liquid or a moisture film. The following sections contain various forms of aqueous corrosion that may occur in a nuclear reactor.

2.2.2.1 Uniform corrosion

Uniform corrosion (UC) occurs and proceeds at the same rate over the whole surface of the steel exposed to the environment. In AuSS, UC normally only occurs in acids and hot caustic solutions, but corrosion resistance usually increases with increasing levels of chromium, nickel and molybdenum (environment dependent). The aggressivity of an environment normally increases with increasing temperature, while the effect of the acid concentration is variable. It is important to note that impurities can have a marked effect on the aggressivity of the environment [37].

316L usually reacts with oxygen and form a thin passive layer of chromium oxide on the surface preventing further oxidation to occur. The passive layer has the ability to self-heal, which means that if the surface is scratched a new chromium oxide will form in the scratch, and protect the steel from further corrosion.

2.2.2.2 Pitting and crevice corrosion

The protective passive film is never completely perfect and always contains microscopic defects, which usually do not affect the corrosion resistance. However, if there are chlorides or sulphates present in the water, those can break down the passive film locally and prevent the reformation of a new film. This leads to localized corrosion, i.e. pitting or crevice corrosion. Both types of corrosion usually occur in chloride or sulphate-containing aqueous solutions in the LWRs, which are present as impurities in the water environment coming from adhesives, gaskets, lubricants, etc.

Pitting is characterized by more or less local points of attack with considerable depth and normally occurs on free surfaces. Crevice corrosion occurs in narrow, solution-containing crevices in which the passive film is more readily weakened and destroyed. This may be under washers, flanges, deposits or fouling on the steel surface. Both forms of corrosion occur in neutral environments although, the risk for attack increases in acidic solutions [38].

2.2.2.3 Intergranular corrosion

The precipitation of chromium carbides on the GBs causes depletion of chromium next to the GBs. In those regions, the material is sensitized and hence susceptible to IG corrosion (see subchapter 2.2.1.3 for chromium carbides formation). Earlier this type of corrosion caused large problems in welded AuSS parts. Currently, the use of low carbon steels (e.g. 316L) and/or stabilized SSs (e.g. 321) have significantly reduced the susceptibility to IG corrosion.

2.2.2.4 Galvanic corrosion

Galvanic corrosion can occur if two dissimilar metals are electrically connected together and exposed to a corrosive environment. The corrosion attack increases on the less noble metal and is reduced or prevented on the more noble metal, in comparison to the situation in which the materials are exposed to the same environment without galvanic coupling.

The difference in "nobility", the ratio of the area of the noble metal to the area of the less noble metal in the galvanic couple and the electrical conductivity of the corrosive environment are the factors that have the largest influence on the risk for galvanic corrosion. An increase in any of these factors increases corrosion rates.

The larger the difference between the corrosion potentials, the greater the risk for an attack to the less noble component; small differences in corrosion potential have a negligible effect. However, galvanic

corrosion is rarely seen on alloys that are resistant to the service environment because the corrosion can be avoided/minimized at low ECP in the water.

2.2.3 Radiation effects

The fission products (see subchapter 2.1.1) produced in the nuclear reactor have a kinetic energy that is lost by electronic and/or nuclear interactions [39]. The electronic stopping power is the energy lost by the interaction of the electronic cloud of the atoms in the material and the projectile nucleus (fission product) and vice versa, which produces excitation/ionization of the electrons/atoms in either of both. The nuclear stopping power is the energy lost when a projectile knockout an atom from its lattice position. The knockout atoms can displace more than one atom from their lattice position after the primary collision if their energy is above the displacement energy (energy threshold to displace an atom from its lattice position). Thus, the damage produced in the material is quantified with displacement per atom (dpa), which is a value that stands for how many times an atom has been knockout from its lattice position. Hence, mainly the nuclear stopping power contributes to the damage in the material and the resulting damage increases with increasing dpa. Besides of displacement damage, an energetic particle can also be absorbed by the nucleus of an atom producing its transmutation, i.e. formation of new element/s.

Charged particles (heavy elements, alpha particles, protons, etc.) are rapidly stopped in the material due to their large electronic cloud (high electronic stopping power), so they mainly produce damage in the fuel. However, neutrons can readily escape from the fuel and produce damage and, to a lesser extent, heating in the structural materials. The neutron irradiation changes the microstructure and/or microchemistry of the AuSSs both in the grain and on the GB.

In this part, the conventional radiation effects are described: RIS, radiation-induced precipitation (RIP), radiation hardening, swelling, creep and transmutation.

2.2.3.1 Radiation-induced segregation

Radiation enhances the diffusion of the elements by the creation of vacancies and interstitials. This produces an enrichment of some elements on GBs and other defect sinks (e.g. near surfaces, dislocations, voids, etc.), and a depletion of other elements. This segregation occurs faster and at lower temperatures than the thermal segregation.

Enrichment or depletion of the elements is principally influenced/driven by the binding (formation) and the migration energy of the elements, the flow of vacancies/interstitials, the interstitial binding of the undersized solutes, the solute size, temperature and dose [39]. The slowest diffusing element (Ni) becomes enriched at sinks, while the faster diffusers (Cr and Fe) are depleted by the flow of vacancies to the GB. Undersized minor elements and impurities such as silicon and phosphorus bind with interstitials and migrate preferentially to sinks (Figure 2.7) [40]. The chromium depletion together with the enrichment of Si and P in the GB produce sensitization and weakening of the GB (see subchapter 2.2.2) which might assist the occurrence IASCC. RIS is characterized by its narrowness, often confined within 5-10 nm, whereas the thermal-induced segregation affects about 100 nm [41].

Segregation of elements towards the GB does not reach the saturation below 50 dpa, neither in LWR nor FBR, but the change rate slows down after 5-10 dpa (Figure 2.8) [42]. However, segregation is more severe in LWR than in FBR, whereby it might be more detrimental for the IASCC susceptibility.
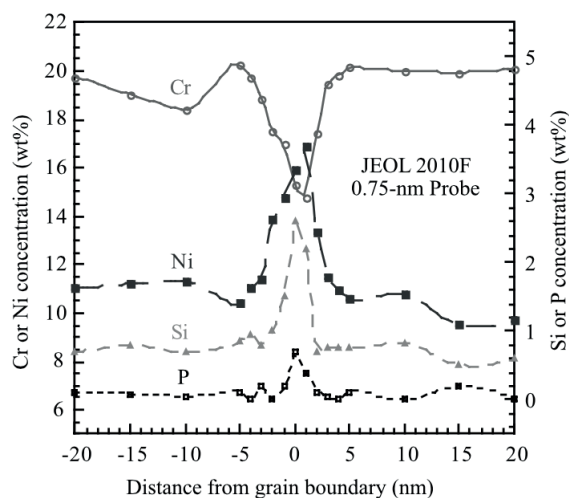
Figure 2.7. Analytical TEM measurement of composition profiles across a GB in a neutron-irradiated 300-series SSs [43].
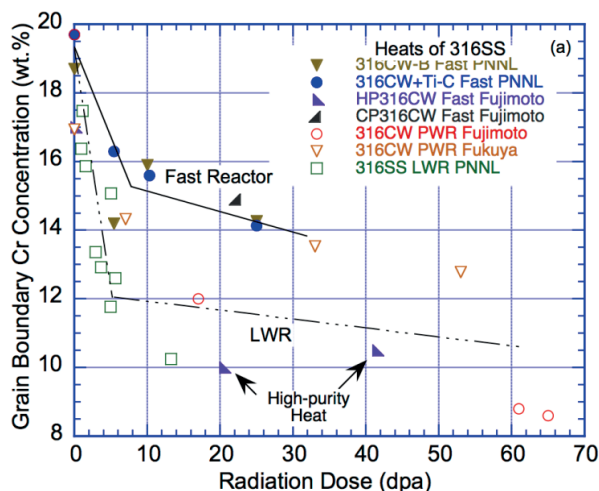
Figure 2.8. Comparison of RIS of Cr in LWR and in BOR-60 fast reactor irradiated 316 [42].

2.2.3.2 Radiation-induced precipitation

Radiation can either enhance or delay the formation of some phases and modify the composition of M_6C and Laves phases. Radiation-induced phases include γ' silicide (Ni_3Si), phosphides (M_2P and M_3P), and G phase ($M_6Ni_{16}Si_7$).

The most direct way in which irradiation can alter phase stability is by causing local enrichment or depletion of solute such that the solubility limit is exceeded. But irradiation can also dissolve phases by recoil dissolution, cause disordering by creating anti-site defects, and lead to nucleation and growth of distinct phases. Hence, it can create phases with different mechanical properties, different corrosion resistance, etc. However, most of these observations are based on fast reactor irradiations at temperatures above 350°C, and data obtained on materials irradiated under LWR irradiation conditions at 320-350°C are limited. However, it is believed that RIP in LWR conditions (i.e. below 350°C) might not be of relevance [44].

2.2.3.3 Radiation hardening

Under irradiation, the microstructure of AuSS changes rapidly at LWR service temperatures. At very low dose, defect clusters (referred as "black dots" in TEM micrographs) begin to form, dislocation loops and network dislocation densities evolve with dose over several dpa, and the possibility exists for the formation and growth of He bubbles, voids and precipitates in core components in locations exposed to higher dose and temperature. Small clusters and faulted loops are the main defects below 300°C whereas, near 300°C, the microstructure is dominated by larger faulted loops plus perfect dislocation network from loop unfaulting and cavities at higher doses [39, 43, 45]. All above-mentioned defects impede the motion of dislocations, leading to the material hardening.

The dislocation loop population grows in size and number density with increasing dpa until the adsorption of interstitials and vacancies equalize, at which point the population is saturated. The loop density roughly saturates at 1 dpa, but the loop size increases until 4-5 dpa (Figure 2.9). These changes, together with the contribution of black dots, cavities and precipitates, which also evolve with irradiation, increase the YS up to a maximum stress of about 800 MPa (in SA AuSS) as shown in Figure 2.10.

16
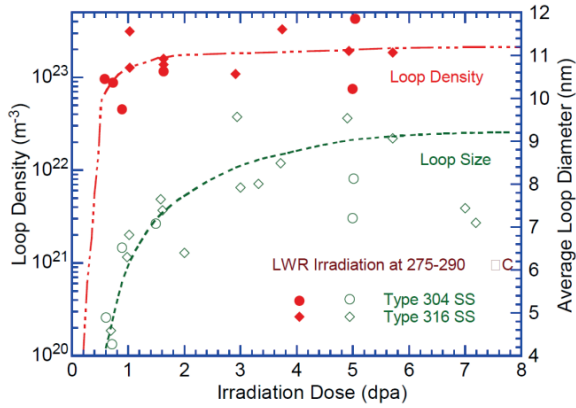
Figure 2.9. Change in density and size of interstitial loops versus irradiation dose (dpa) during LWR irradiation at 275-290°C [46].
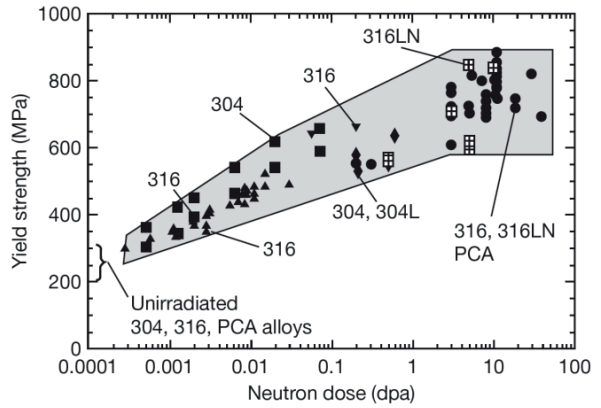
Figure 2.10. YS of various annealed 300 series SSs versus dpa in various water-cooled reactors at 280–330°C [47].

A dislocation line starts to propagate through the material when the applied stress is above the YS. In the simple case where uniform shear stress is applied (τ), the line tension of the dislocation (Γ) produces an inward radial force that maintains the dislocation curvature, which is pinned by two defects (Figure 2.11). The equilibrium of forces is giben by:

$$2\tau bRd\theta = 2\Gamma d\theta \rightarrow \tau = \frac{\Gamma}{bR}$$

Eq. 2.3
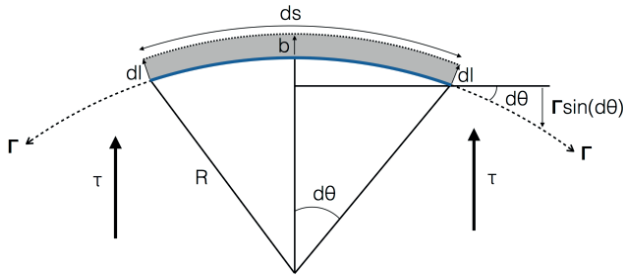
Figure 2.11. Dislocation line segment ds sweeping out an area ds·dl in direction of the Burgers vector and the inward restraining force due to the applied shear stress. Adapted from [39].
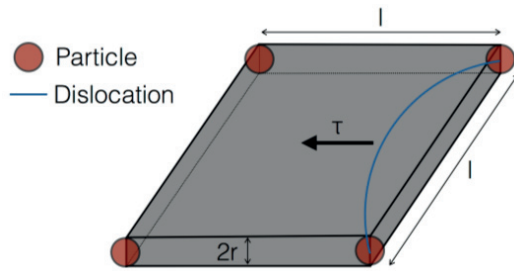
Figure 2.12. Schematic showing a distribution of spherical obstacles in the slip plane.

Where b is the Burgers vector, R is the grain size radius, ds is the dislocation line segment, dl is the displacement of the dislocation line segment normal to ds, and $d\theta$ is the half angle of the circular sector formed by the dislocation segment. The dislocation bows out between two pinning obstacles separated a distance l that lay in its slip plane (Figure 2.12). A dislocation can climb the obstacle, cut it through or produce an Orowan loop around it [39]. The type of interaction depends on the obstacle nature and on the temperature. For instance, the climb of the obstacles is favoured above 500°C in AuSS. From Figure 2.12, one can relate the average obstacle spacing (l) to the obstacle density (N) and diameter (d) as:

$$l = (Nd)^{-\frac{1}{2}}$$

Eq. 2.4

The line tension of an edge dislocation with a dislocation core radius r_c is [39]:

$$\Gamma \approx \frac{\mu b^2}{4\pi} ln\left(\frac{R}{r_c}\right)$$

<div align="right">Eq. 2.5</div>

Where µ is the shear modulus. By substituting Eq. 2.5 in Eq. 2.3 and given that 2R≈l, it follows:

$$\tau = \frac{1}{l}\frac{\mu b}{2\pi} ln\left(\frac{l}{2r_c}\right)$$

<div align="right">Eq. 2.6</div>

Substituting l from Eq. 2.4, introducing the hardening coefficient, α, and the Taylor factor, M, to transform the relation to YS:

$$\sigma_y = \alpha M\mu b\sqrt{Nd}$$

<div align="right">Eq. 2.7</div>

Where $\alpha = \frac{1}{2\pi}\ln\left(\frac{l}{2r_c}\right)$ and it represents the strength of the barrier obstacle. For an obstacle that cannot be cut through, an Orowan loop is formed and the value of the hardening coefficient is maximum (α=1). For weaker obstacles, the α value is smaller than one. Eq. 2.7 is usually represented by $\Delta\sigma_y$, it was first formulated by Seeger in [48] and is currently called dispersed barrier hardening (DBH) model:

$$\Delta\sigma_y = \alpha_i M\mu b\sqrt{N_i d_i}$$

<div align="right">Eq. 2.8</div>

Where i the type of defect (voids, bubbles, dislocation loop, etc.), M ~3, µ is ~76 GPa, b is ~0.255 nm for fcc, N_i is the particle density of type i defects and d_i is the diameter of type i defects. Fukuya et al. [49] correlated the $\Delta\sigma_y$ increase from hardness measurements ($\Delta\sigma_y \approx 3.6\Delta H$) with the $\Delta\sigma_y$ contribution from different defects using the DBH model and assuming constant α values of 0.45, 0.2 and 0.4 for dislocation loops, black dots/cavities and γ' precipitates, respectively. That study found that dislocation loops were the main contributor to the increase of hardness below ~450°C, but cavities had a remarkable contribution at higher annealing temperatures.

Simulations of the hardening produced by voids/bubbles showed that the hardening coefficient depended on the cavity size [50] and on the helium/vacancy ratio [51] using the DBH model. On the other hand, the α value did not change with the dislocation core size.

2.2.3.4   Creep and swelling

Reactor internal components exposed to neutron irradiation might undergo swelling. Swelling occurs when the material increases its volume and decreases its density due to the production of cavities. It is considered that irradiation swelling does not occur at temperatures below 365°C, and therefore PWR internal structures should not be affected. The resulting swelling in LWRs remains very limited and it seems not to represent a significant risk for 40 years of operation (0.24% for 60 dpa BFB), but it remains a potential issue in case of long-term operation and thermal transients [52].

Swelling is also a potential issue in mechanical connections between different materials. After long-term operation in LWRs, the differential swelling between component connections could lead to exceeding the stress limits to produce IASCC. For instance, this is the case for the BFBs (CW 316L) and the former and the baffle plates (SA 304L). The AuSS 304L is more sensitive to irradiation and it might increase the bolt load at high doses due to the differential swelling [53].

Thermal creep is relevant at temperatures above half of the melting temperature (T_m, in K) so at LWR temperatures, radiation creep is orders of magnitude higher than the former, which is rather small

[39, 54]. Radiation creep results from diffusion of the radiation-produced vacancies and interstitial atoms to dislocations; enhancing the climb-to-glide process that controls time-dependent deformation. Radiation creep can be both, beneficial and detrimental. Relaxation of weld residual stresses reduces IASCC susceptibility, but relaxation of constant load stresses stimulates high radiation creep rates that may help to initiate and sustain SCC [55]. This deformation can be highly localized and concentrate stresses in the GBs.
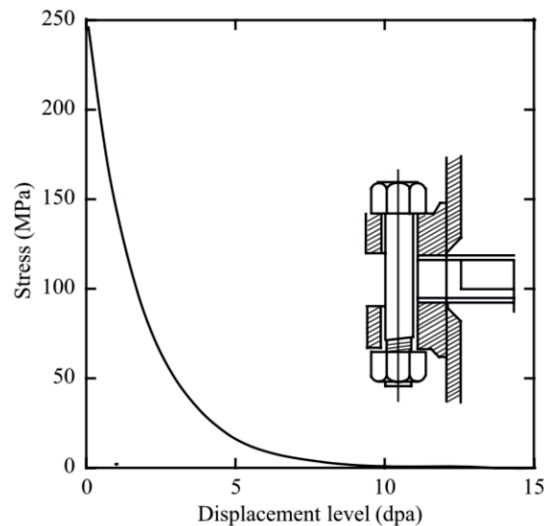
Figure 2.13. Irradiation-induced creep causing stress relief in a bolt that was originally torqued at 250 MPa and then exposed to neutron flux [39].

2.2.3.5 Transmutation

Some elements in 316L can capture a neutron and become radioactive isotopes. The unstable isotopes lose energy by emitting radiation which is majorly in a form of photons, electrons, protons (hydrogen ions) and/or alpha particles (He ions). Thus, a significant amount of hydrogen and He can be produced in AuSS [6].

Hydrogen can be produced in SSs by transmutation of $^{58}Ni(n,p)^{58}Co$ which is mainly caused by fast neutrons (> 1 MeV). Even though hydrogen diffuses rapidly in the material, the effects on the mechanical properties are important and many embrittlement mechanisms have been developed (see subchapter 2.3.4.2).
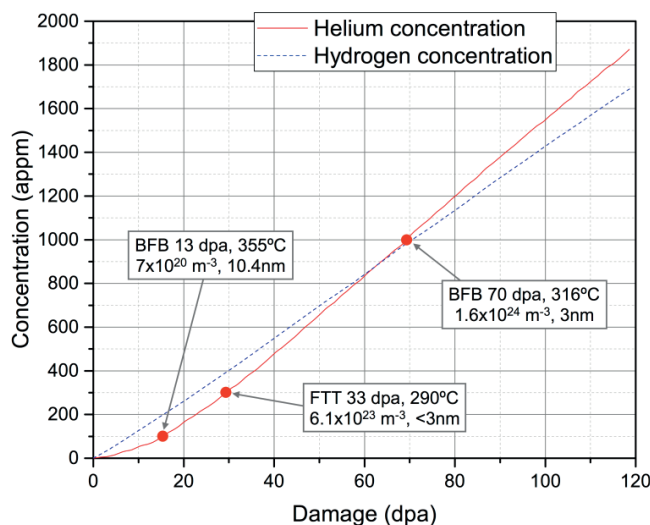
Figure 2.14. Calculated He and hydrogen production for a mid-core BFB position in a PWR versus radiation damage. The dots at 15, 31 and 70 dpa represent the He concentrations at which this study is focused. Adapted from ref. [56].

There are two main sources of He in the AuSS components of LWRs with thermal neutrons. ^{10}B, which strongly segregates to GBs and it is consumed within a few dpa, $^{10}B(n, \alpha)^{7}Li$. ^{10}B only represents 20% of the natural boron, and its He contribution is below 50 appm since only some traces are present in AuSS. ^{59}Ni is created by transmutation of ^{58}Ni and is not found in natural nickel. In the latter case, He is produced in two steps, the build-up of ^{59}Ni and then its consumption, $^{58}Ni(n, \gamma)^{59}Ni(n, \alpha)^{56}Fe$. Since the ^{59}Ni must be produced first, the production of He from this reaction starts to be significant around 5-10 dpa. The He generation from ^{58}Ni continuously accelerates in rates with dose reaching saturation at thermal neutron fluences $> 10^{23} \frac{neutrons}{cm^2}$, which are well above of those achieved in LWRs lifetime [6]. He atoms are produced in a surprisingly large amount (above 10 appm/dpa) in the late stage of PWR operation of the internal parts in nickel-containing steels and alloys (Figure 2.14) [4, 6, 7, 57]. Moreover, Ni-enrichment at GB by RIS can further increase the local He content at GB where it is known to lead to more embrittlement [1, 2].

2.3   Stress corrosion cracking of AuSS

The corrosion resistance of AuSS in LWR is based on a thin 0.5 to 2 μm service-grown protecting oxide film that typically has a double layer structure. The inner protection layer is formed at the metal/oxide interface, whereas the outer layer is formed either by precipitation from the aqueous phase [58] or from growing oxide particles (Figure 2.15) [59]. The slow mass transport of metal cations or oxygen anions through the inner oxide film governs the slow UC rate. Similar oxide films are formed on the external surfaces and crack flanks. Although providing an excellent UC resistance, local corrosion phenomena like pitting, SCC or IG corrosion may occur due to localized (mechanical or chemical) oxide film damage. Among these local corrosion phenomena, SCC is the most critical one in LWRs.
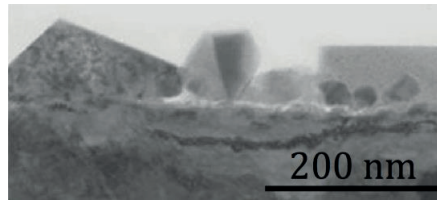
Figure 2.15. STEM micrograph of the oxide layer formed on 316L after exposure to 288°C pure water with 2 ppm O_2 for 10 h. Adapted from [59].

SCC is the formation (at $\sigma <$ UTS, often $<$ YS) and sub-critical growth (at $K_I < K_{IC}$ which are the stress intensity factor (SIF) and fracture toughness mode-I, respectively) of cracks in a material (usually in a susceptible condition) under simultaneous and synergistic interaction of an approximately constant (applied or residual) mechanical tensile stress and a corrosive environment. It is usually alloy-environment specific and only occurs for a critical combination of environmental, material and loading parameters. SCC is extremely slow, and involves complex damage evolution process, and is affected by a large number of synergistic and interrelated environmental, loading and material parameters. Very long incubation periods are quite common. The cracks can be TG or IG and often show very small crack openings and micro- or macro-branching as well as very rough fracture surface. SCC has resulted in many catastrophic failures since the detection of such fine cracks can be very difficult and the damage cannot be easily predicted. Hence, a failure may occur unexpectedly, with minimal overall material loss and negligible plastic deformation.

2.3.1   SCC crack initiation and growth

The crack initiation and growth is understood as a continuum that depends on material, environment and loading parameters. The process is generally divided into five stages (Figure 2.16). The first stage corresponds to the (1) manufacturing process of the material (e.g. surface finish), which is determinant to the subsequent crack initiation. During the SCC initiation period, the material is exposed to load/environment, and three stages can be distinguished. The (2) precursor stage is defined by the time associated to develop the necessary conditions for incubation, when changes in the material are produced and the material becomes susceptible to SCC. Microscopic penetration on the material surface occurs during the (3) incubation stage. This subsequently leads to the (4) slow growth phase, which can take up to a penetration depth of 10 μm. Finally, a rapid crack growth is observed in the (5) propagation period. The last period can consist of up to three sub-regions, as indicated in Figure 2.17. The improved resolution of the crack growth rate (CGR) detection has changed the SCC threshold since previously hidden crack growths are now detectable.
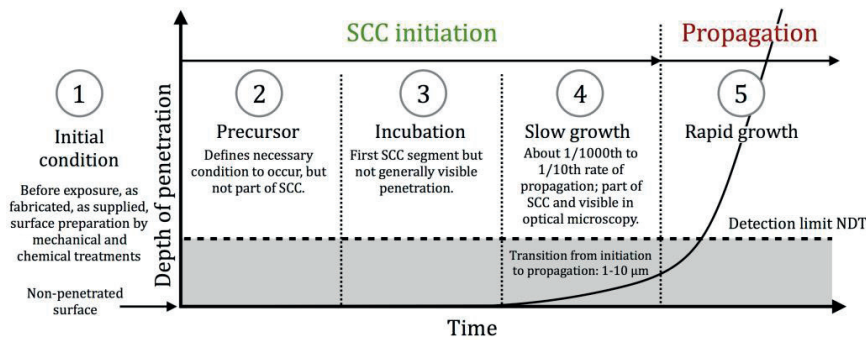
Figure 2.16. Schematic of SCC crack initiation and propagation versus time. Adapted from [60].
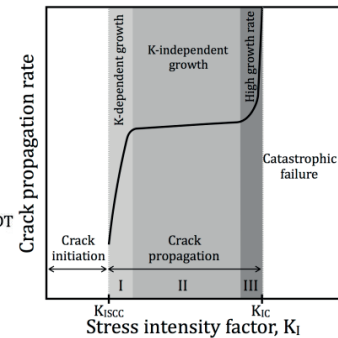
Figure 2.17. Schematic of the SCC propagation stages.

2.3.2 SCC fracture type and root cause

The SCC fracture can be TG, IG or mixed. Figure 2.18 shows optical micrographs of crack propagation and SEM micrographs of fracture morphology for pure IG (Figure 2.18 A, B) and TG (Figure 2.18 C, D) fractures. Both types of fracture can show crack bifurcation or branching.

Transgranular stress corrosion cracking (TGSCC) is mainly caused by chlorides in the water [61]. It is a recurrent but not a critical problem in LWRs. The number of events is not increasing with time, hence TGSCC does not pose a problem of plant ageing [62, 63]. On the other hand, IGSCC can be enhanced by many different parameters (water chemistry, corrosion potential, temperature, SIF, material impurities, GB chromium depletion, GB silicon enrichment, CW level, weld residual stresses and neutron irradiation) which, at the same time, can influence each other [64, 65].
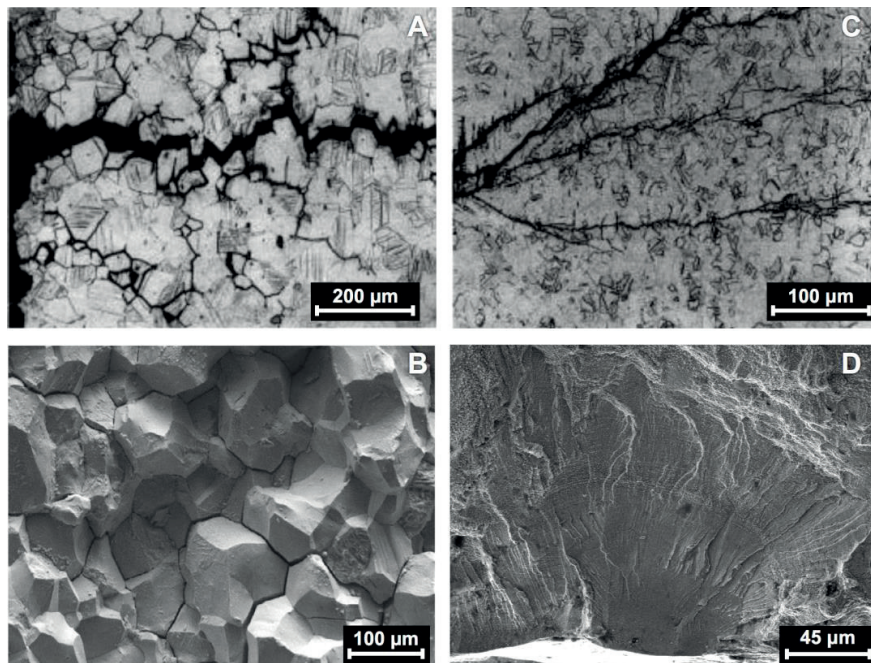
Figure 2.18. Optical micrographs of the SCCs propagation (A and C [66]) and SEM micrographs of the fracture surface morphology (B [67] and D): A) IG crack propagation in AuSS (Deutsches Institute för Normung, DIN 1.4571) exposed to an alkaline environment at 80°C, B) Typical IG fracture surface, C) TG crack propagation in AuSS (DIN 1.4541) exposed to a chloride-containing environment at 100°C and D) Typical TG fracture surface.

2.3.3 Intergranular stress corrosion cracking

2.3.3.1 Service experience

IGSCC occurs in unirradiated BWR and PWR reactor components. In BWRs, it is frequently found in sensitized heat affected zones (HAZ) of welds and in CW AuSS. In PWRs, IGSCC is less frequent and it is observed in occluded, creviced and high hardness/CW steels with high concentration of oxidants [68, 69]. Figure 2.19 shows the typical IGSCC cracks encountered in BWR pipings made of AuSS.
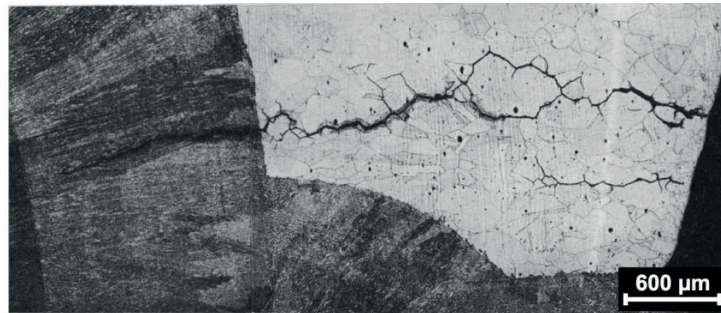
Figure 2.19. IGSCC found in shut-down cooling system line of TVO I plant showing a crack in the fusion line and two cracks in the HAZ. Adapted from [70].

2.3.3.2 Main factors of influence to IGSCC

The key parameters involved in IGSCC are discussed and divided into two main topics: environment, material and loading effect.

Environment effect

The CGR in constant load tests changes dramatically with changes in corrosion potential, temperature, chloride/sulphate content in the water and material condition. The increase of dissolved hydrogen in PWR primary water environment did not reveal an impact on the IGSCC CGR, but the increase of corrosion potential in high-temperature water affected significantly the CGR (Figure 2.20). Below -500mV$_{SHE}$, the SCC CGR is minimised but, above -200mV$_{SHE}$, the CGR increases up to 3 and 1 orders of magnitude for sensitised and unsensitized CW316, respectively.

The sulphate and chloride contents increase the CGR with rather low concentrations. Their effect is more pronounced in NWC than in HWC (Figure 2.21). In sensitized AuSS there is a strong increase in SCC rates with increasing sulphate from 0 to 50 ppb. Above 50 ppb, the sulphate effect saturates. In HWC, the sulphate concentration is less detrimental and a concentration of 100 ppb only increases the CGR by one order of magnitude. Chloride concentration generally has similar effect to sulphate (in molar concentration). In NWR, only 30 ppb is enough to double the CGR but, higher concentrations have little impact on the CGR. Like in the sulphate case, chloride concentration has little impact on CGR in HWC conditions. Nevertheless, chloride promotes and accelerates all forms of corrosion: TGSCC of annealed steel [71, 72], IGSCC [71], pitting [73] and crevice corrosion [74]. A reduction of oxygen and chloride/sulphate in high-temperature water is the key to reduce SCC (Figure 2.22).
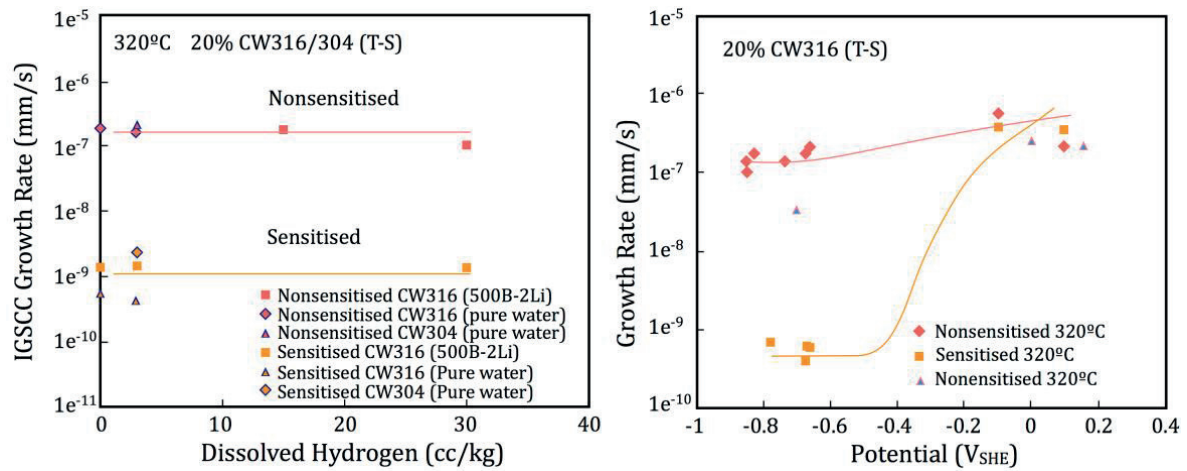
Figure 2.20. CGR versus dissolved hydrogen on nonsensitized and sensitised 20% CW316 (T-S) in a PWR primary environment (left), and CGR versus corrosion potential of nonsensitized and sensitised CW316 (T-S) in high-temperature water (right). Adapted from [75].
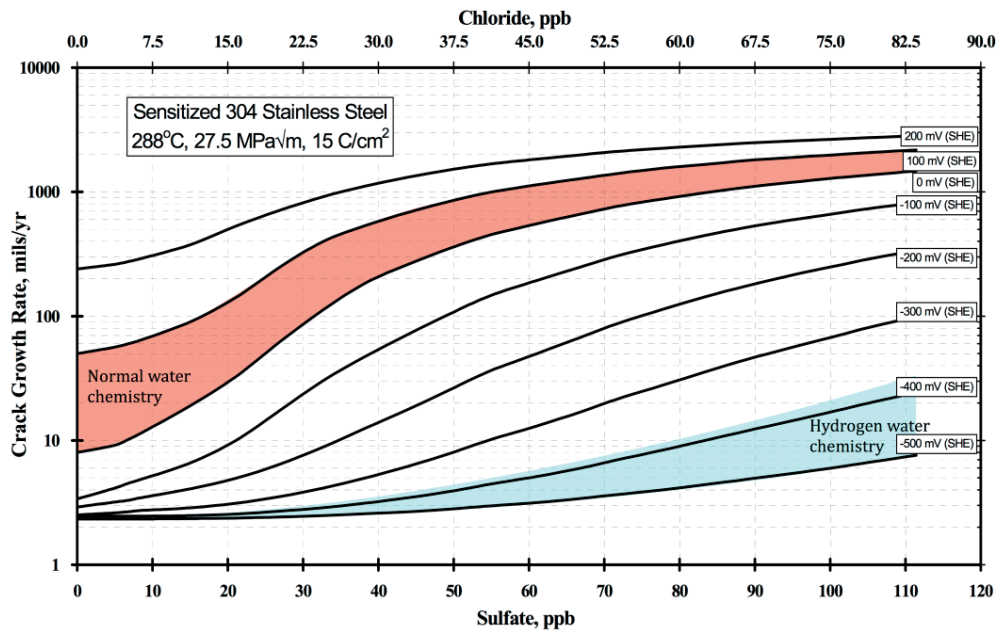
Figure 2.21. Predicted (with PLEDGE model from General Electric) sulphate and chloride effect on CGR in sensitized 304 AuSS with different corrosion potentials. Adapted from [76].

It is widely accepted that SCC CGR is a thermally activated process [65]. The increase of temperature can produce a monotonic increase of CGR, a maximum CGR at a certain temperature ($T_{Threshold}$) where the CGR starts to decrease with temperature, or a temperature where the CGR shows less dependence on temperature [77, 78, 79, 80]. For instance, the SCC CGR increases with temperature under oxidising conditions from 200 to 325 °C, but a SCC CGR peak is observed at 250°C in deaerated water (Figure 2.23).
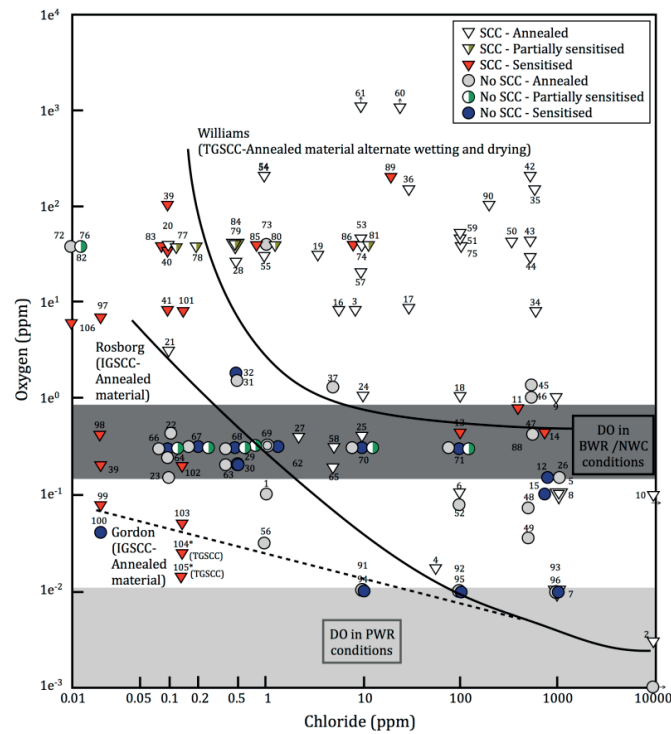
Figure 2.22. Test map of chloride and oxygen effect on SCC initiation in AuSS in high-temperature water. Adapted from [71].

The combined effect of CW level and an increase of temperature in simulated PWR conditions can be observed in Figure 2.24. The CGR increases with temperature, but the activation energy increases with decreasing the level of CW, which means that the effect of temperature is more pronounced at low levels of CW.
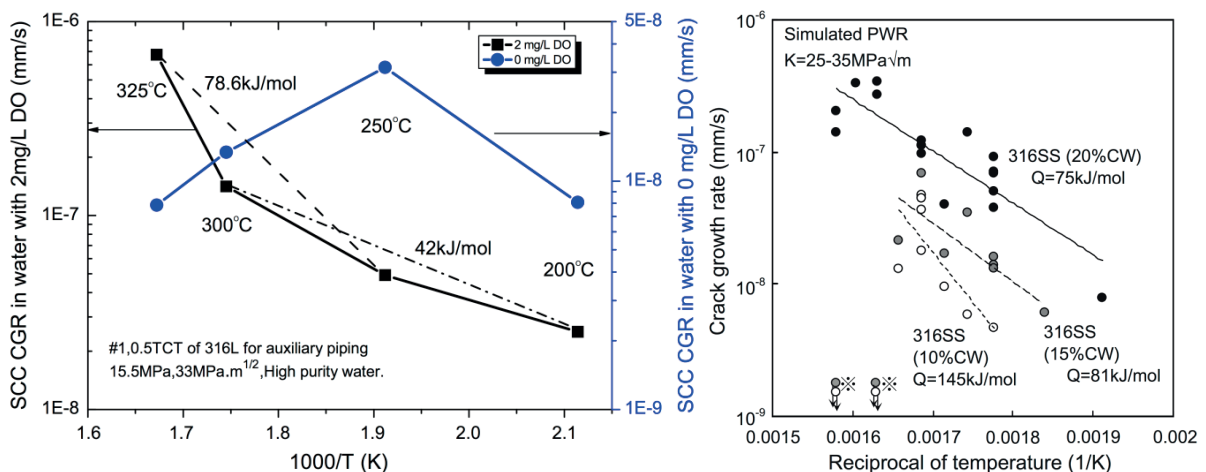
Figure 2.23. Temperature dependence on SCC CGR in 0 and 2 mg/L dissolved oxygen condition for CW 316L in high purity water [67].
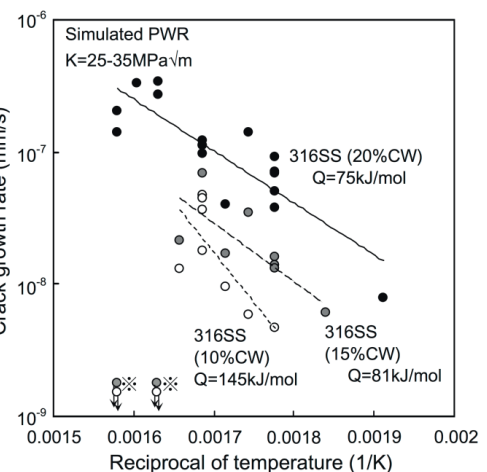
Figure 2.24. Temperature dependence on CGR of CW 316SS under simulated PWR primary water conditions [79].

Material effect

As mentioned earlier, carbides formed in sensitised AuSSs have a beneficial effect at low corrosion potential and the CGR can be up to two orders of magnitude smaller than in nonsensitized AuSSs

(Figure 2.20). However, at high corrosion potential, this effect is suppressed and sensitised GBs are more susceptible to IGSCC. Moreover, sulphate and/or chloride contamination accelerates SCC CGR at low and high corrosion potentials in sensitised and SA AuSSs [81, 82, 83, 84]. On the other hand, it was observed that GB carbides impede SCC at high corrosion potential if chromium depletion is healed [85].

The level of CW has also an important influence on the CGR. The SCC CGR has been reported to increase with increasing CW degree in both BWRs and PWRs water chemistry (Figure 2.25) [79, 77]. The CW effect is more relevant in hydrogenated water than in oxygenated water, but in general, an increase of CGR is observed with increasing CW level. Higher YS results in a small plastic zone and steeper strain gradient at the crack-tip, which in turn, results in a high crack-tip strain rate and thus high SCC CGR.
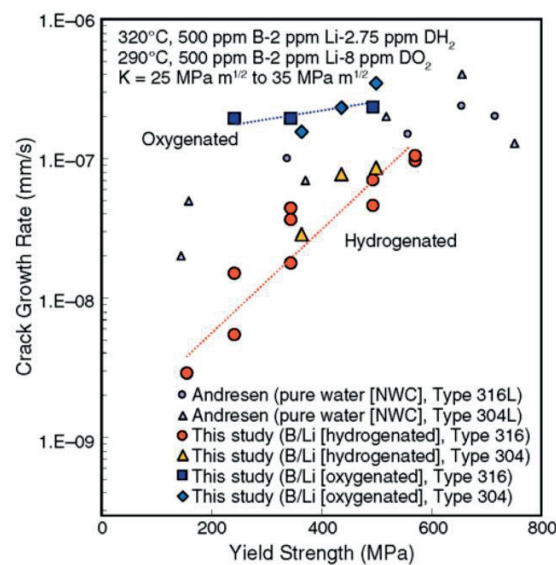
Figure 2.25. CGR versus yield strength for specimens exposed to hydrogenated and oxygenated water environments [77].

<u>Mechanical loading effect</u>

A sharp crack in a material under applied stress reduces the cross-section and hence, increases the stress in its plane. More importantly, this applied stress is amplified at the crack tip and can locally produce plastic deformation. The SIF is a measure of stress concentration at the crack tip under small-scale yielding conditions, which depends on the crack tip geometry and the load level [86]. The material will fail if a critical SIF (K_I) is exceeded, the fracture toughness (K_{IC}). In a corrosive environment, cracks in AuSS propagate below the K_{IC}, when the SIF is above a SCC SIF threshold (K_{ISCC}), which can be much below the K_{IC}. The effect of mechanical loading can be studied under constant SIF, under constant load or varying (positively or negatively) dK/da (a stands for crack length).

As it is expected, the CGR is higher when the SIF increases in both, hydrogenated (Figure 2.26) and oxygenated (Figure 2.27) high-temperature water. For a given SIF, the CGR is higher in oxygenated water. The SIF effect is more pronounced for a lower level of CW than for a higher level up to a certain threshold where the CGR seems to equalize. An exponential relationship is generally observed between CGR and K_I with an exponent coefficient between 2 and 3.
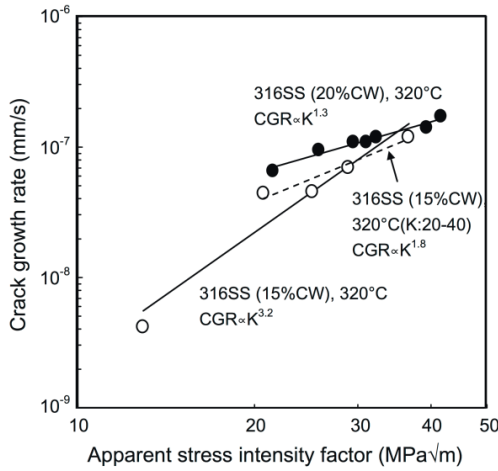
Figure 2.26. Effect of SIF on the CGRs of 316SS with 20%CW and 15%CW at 320°C in simulated PWR primary water [79].
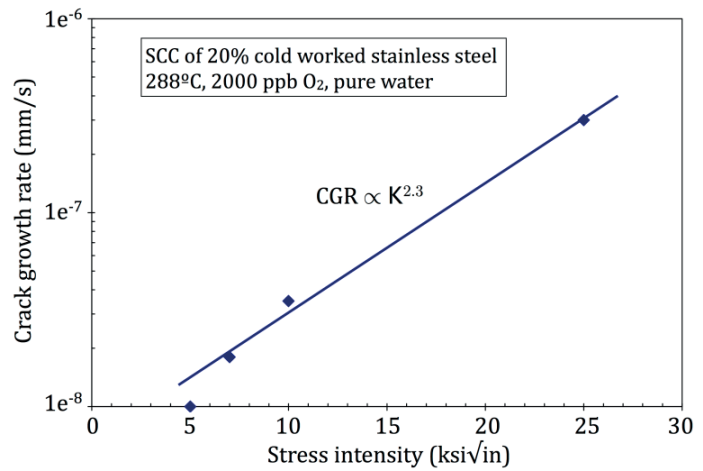
Figure 2.27. Effect of SIF on the CGRs of 316SS with 20%CW at 288°C in oxygenated water [64].

Generally, gentle cycle loading of the components increases slightly the CGR, but materials with high CW level show very high CGR during re-loading (Figure 2.28). Similarly, high CGR are observed in materials with high CW level under high SIF or under positive dK/da. Under these circumstances, the corrosion potential effect only has a little effect on CGR [64].

All these published results show the complexity of SCC and the difficulty to find thresholds that ensure the integrity of the structural materials.
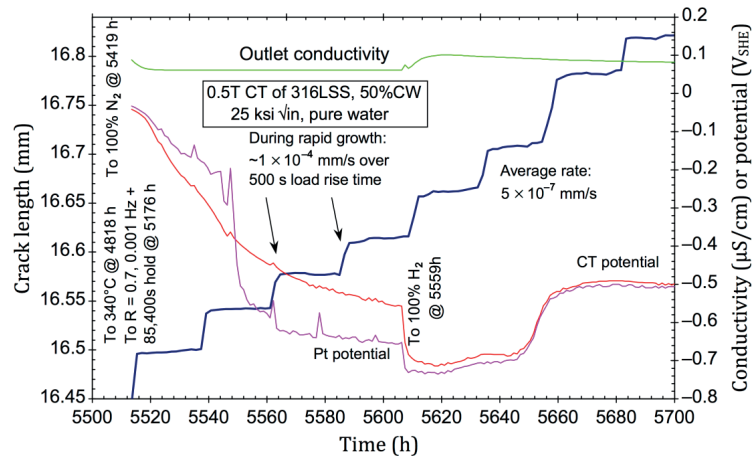
Figure 2.28. Crack length versus time of an unsensitized 316L 50%CW showing the effect of gentle unloading cycles.

2.3.4 SCC mechanisms

The most popular models for SCC in AuSS are based on anodic dissolution (slip dissolution or film rupture anodic dissolution mechanism) or hydrogen-embrittlement phenomena and hydrogen-plasticity interactions (hydrogen-assisted SCC mechanisms, HASCC). Both basic mechanisms may be simultaneously active and even be controlled by the same rate-limiting steps (film rupture frequency, repassivation kinetics, etc.), which makes their differentiation difficult. Usually, at lower temperatures

with high strength steels (e.g. CW or irradiated steels), the hydrogen-related mechanisms dominate, whereas at higher temperatures with lower strength steels dissolution seems to dominate.

The limited hydrogen availability, low trapping efficiency, fast diffusion/permeation and release rates under LWR conditions at 274 to 320 °C impede the necessary significant hydrogen accumulation for hydrogen embrittlement and HASCC in AuSS. Furthermore, many fundamental observations are hardly consistent with most of the hydrogen embrittlement mechanisms. For instance, an increase in hydrogen content and a decrease in ECP or catalytic surfaces (noble metal chemical addition [87] or OLNC) usually result in a significant decrease in SCC CGRs in SA AuSS. The cracking can be TG and IG for both mechanisms. For IG cracking, the GB nature, deformation, segregation and strength are evidently important material factors for SCC.

In the following, the basic elements of these two fundamental mechanisms and of the crack crevice chemistry are briefly described.

2.3.4.1 Film rupture anodic dissolution mechanism

As mentioned earlier, AuSSs form a protective oxide layer that protects the material from further oxidation in high-temperature water. Under applied load, the stress concentration at an existing crack-tip induces plastic straining, which can result in the mechanical rupture of the oxide film by plastic steps ("activation"). Then, the crack grows by anodic dissolution on the bare metal matrix, whereas a passive film protects the cracks flanks. The nucleation and formation of a new oxide film ("repassivation") slows down and stops the anodic dissolution and hence, the crack-tip advance. Further activation-repassivation cycles will depend on the strain rate at the crack-tip [88]. The basic steps of this mechanism are shown in Figure 2.29 and Figure 2.30.
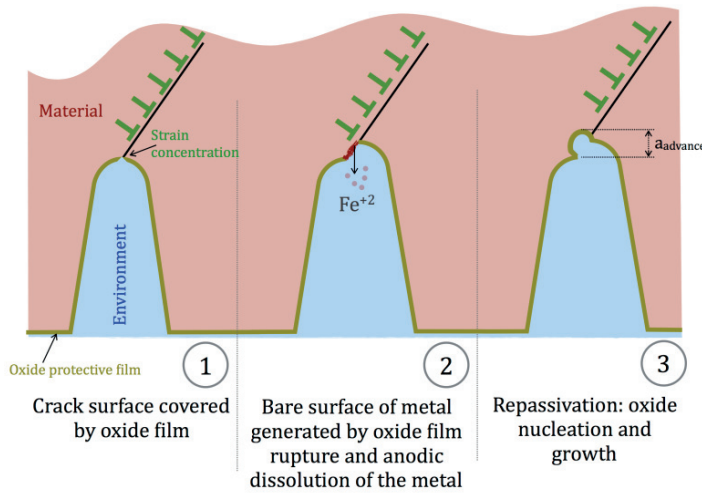
Figure 2.29. Schematic of the basic steps of film rupture anodic dissolution mechanism.
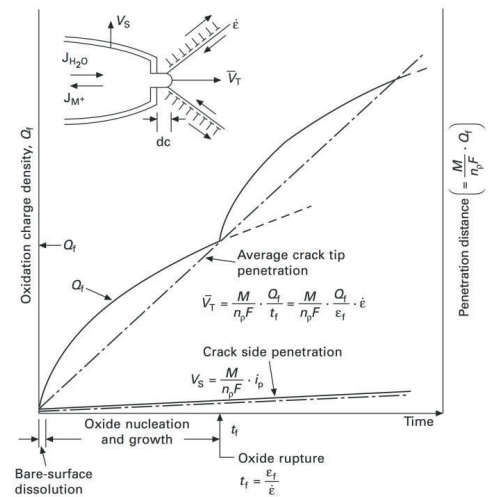
Figure 2.30. Schematic of the crack tip system, including film "rupture" and repassivation processes [64].

For a given material and environment conditions, the change in oxidation charge density with time and the frequency of oxide film rupture at the strained crack-tip control the crack propagation rate. The local crack-tip chemistry of the electrolyte and the material govern the anodic dissolution and repassivation kinetics, which in turn control the change in oxidation charge density with time. The oxide film and the crack-tip strain rate determine the oxide film rupture frequency.

Based on this mechanism, a power law relationship between SCC CGR (da/dt) and crack-tip strain rate (dε/dt) is predicted, $da/dt = A_m(d\varepsilon/dt)^{n^*}$, with the amplitude (A_m) and exponent (n^*) being strongly dependent on crack crevice environment and local material [88, 89].

Sulphur species (sulphate or sulphites), pH of the environment and chromium content in the material strongly influence the dissolution and the repassivation kinetics. Low pH or high concentrations of sulphur-anions was reported to delay repassivation and therefore, the crack advance is increased by anodic dissolution in those environments [90, 91, 92]. Chromium GB depletion by thermal sensitization or RIS also significantly retard repassivation under occluded crevice conditions. Chloride may strongly interact with the oxide films and alter their protecting properties locally (e.g. reduce local thickness and film rupture strain).

Loading of the components, thermal/radiation creep and crack advance itself are sources of dynamic crack-tip straining [91]. Moreover, strain localisation by dynamic strain ageing or dislocation channelling at high irradiation doses and corrosion-deformation interactions (hydrogen-assisted mechanisms, vacancy fluxes, etc.) might also contribute to local plastic straining. Strain localisation facilitates local film rupture by plastic slip and micro-crack formation processes. CW or high YS materials develop higher stress concentration in the crack-tip which, results in steeper strain gradient and higher crack-tip strain rate. The SCC CGR in macroscopic positive stress gradients may result in a strong K_I increase and a positive dK/dt. Due to the relation between CGR and crack-tip strain rate, this can result in a positive dK/da feedback and strong acceleration of SCC crack growth.

For IG cracking, the GB nature, deformation, segregation, precipitation and strength are evidently important material factors for SCC. Production of He by transmutation and/or hydrogen diffusion into the metal can be accumulated on GB, where they decrease the GB cohesion. The formation of GB carbides has a positive effect on GB strength and increase the resistance to GB sliding. However, Cr depletion and Si enrichment increase the electrochemical activity on GB. The GB deformation behaviour depends on grain size, plastic deformation in the grain, grain to grain orientation and grain orientation with respect to the loading.

Many of the influencing parameters are interrelated and may be synergistic or competitive. Depending on the exact value of the different corrosion system parameters, an individual factor can have a pronounced or only a minor influence on SCC initiation and crack growth.

2.3.4.2 Hydrogen-assisted SCC mechanisms

<u>Hydrogen-uptake in AuSS</u>

Hydrogen can be accumulated in AuSS during manufacturing [93], surface treatment [93, 94] and/or welding [95]. However, currently those hydrogen sources are controlled and minimized and the initial hydrogen content is very low. In LWRs, hydrogen added to suppress radiolysis (PWR and BWR/HWC) can diffuse rapidly from the environment into the material at LWR temperatures [96]. Moreover, environmental processes from corrosion reactions and radiation-induced radiolysis can also increase hydrogen pick up locally. Hydrogen production by radiolysis is possible in BWR/NWC environment but, the hydrogen content on its reactor internal component surfaces is still much lower than in PWRs. Although the hydrogen content in BWR water is significantly lower than in PWR primary water, the absorbed hydrogen is similar in both type of reactors and eventually higher in BWR crevices, where the crevice chemistry might be very aggressive. In general, an increase of corrosion rate or dissolved hydrogen in the environment raises the hydrogen uptake.

Radiation-induced transmutation (see subchapter 2.2.3.5) and recoil injection of protons after neutron-water collisions also contribute to the hydrogen pickup but, these are believed to be less important than the corrosion and the environmental processes. However, radiation increases the hydrogen trapping capability of the material by increasing the number of defects (vacancies, voids and dislocations) which adds up to existing traps in the material (precipitates, GB, etc.) [97].

The stationary UC rate is from one to three orders of magnitude lower than the exchange current density of the hydrogen redox reaction in high-temperature water on AuSS. Therefore, AuSS corrosion potential is similar to the equilibrium electrode potential of the hydrogen redox redaction. Moreover, hydrogen supersaturation from local corrosion reactions and cathodic over-potentials are limited by the poor conductivity of the LWR coolant [98]. Since oxide films are not a barrier for hydrogen diffusion, and permeation and release rates are high in AuSS, the diffusible lattice hydrogen content in the steel (so the enrichment of hydrogen in the material) close to the surface is usually controlled by dissolved hydrogen content from the water as for the Sievert's law [99].

Generally, the quantity of hydrogen contained in non-irradiated AuSS in high-temperature water is too low to produce any hydrogen embrittlement in the bulk. However, under stress, AuSS might undergo local hydrogen pick-up in plastically deformed crack-tips. The combination of aggressive occluded crack crevice chemistry and local corrosion processes at the plastically strained crack-tip might enhance hydrogen pick-up, which might produce local crack-tip embrittlement.

Hydrogen tends to segregate and to accumulate in regions with high positive hydrostatic stress and dilatation strain fields like crack-tips and sharp notches and, at material defects like precipitates, GBs, cavities and dislocations. Also, He generation in irradiated steels has been reported to increase hydrogen retention in the material [100]. Thus, the concentration of hydrogen trapped in AuSS depends on the nature and concentration of those traps, the local stresses and the local plastic strains. Given that radiation-induced defects increase significantly the numbers of traps in the material, the total bulk hydrogen concentration (diffusible + trapped) can be significantly higher than the bulk lattice hydrogen. It is worth to mention that, strongly trapped hydrogen is not available for hydrogen-dislocation interactions and hence, it is not harmful to any of the HASCC mechanisms.

<u>Characteristics of hydrogen in AuSS</u>

Hydrogen atoms are usually located interstitially and molecular H_2 can form in micro-cracks or/and voids. Atomic hydrogen has low solubility in steels but its interstitial diffusion is relatively fast (especially at LWR relevant temperatures), $D = (6.2 \times 10^{-7} \exp(-53630/RT))$ [96]. Where D is the diffusion coefficient in m^2s^{-1}, T is the temperature in K and R is the gas constant in $JK^{-1}mol^{-1}$. Hydrogen has a large molar partial volume that makes it sensitive to hydrostatic stress and dilatation strain fields. The electronic environment of the metals atoms and their cohesive strength are modified by the atomic hydrogen. As a result, dislocation mobility is enhanced and the metal atoms cohesive strength decreased [101]. The hydrogen atmosphere reduces the interaction forces between obstacles and dislocations producing a shielding mechanism, thus enhancing plasticity and easing dislocation glide [102, 103].

The trap-hydrogen binding energy can be weak/reversible like impurities and elastic interactions with dislocations or strong/irreversible like GBs, dislocation cores and inclusions. However, the trapping efficiency decreases with increasing temperature and it egresses more readily to the surface so, hydrogen embrittlement is more relevant at low temperatures (< 100°C) [104]. Hydrogen at

dislocation cores might be dragged faster by mobile dislocations than by lattice diffusion. This hydrogen transport might be important for accumulating hydrogen in GB and promoting IG cracking.

The minimum concentration of hydrogen to produce embrittlement in AuSS depends on the SFE of the material. Higher SFE requires higher hydrogen concentration to produce embrittlement [105]. However, cracking (TG or IG) will occur once a critical hydrogen concentration over a critical volume is reached.

<u>Hydrogen embrittlement and HASCC mechanisms</u>

The hydrogen effect is governed by three factors: (1) the availability, source and nature of hydrogen, (2) its easiness in entering the material and the transport velocity to susceptible locations, and (3) the nature and concentration of traps in the susceptible location. Enhancing at least one of these factors will raise the embrittlement effect of hydrogen.

Many different hydrogen embrittlement mechanisms have been proposed, although experimental evidence of most of them is still very weak: phase change mechanism (or hydride formation and fracture) [106], hydrogen-enhanced localized plasticity mechanism (HELP) [107, 108], internal hydrogen pressure mechanism [109, 110], hydrogen-enhanced strain-induced vacancy mechanism (HESIV) [111], absorption–induced dislocation emission (AIDE) [112, 113] and hydrogen-enhanced decohesion embrittlement (HEDE) [114, 115].

Brittle hydride formation on the crack tip is unlikely in AuSSs [104, 116] and hydrogen availability in LWRs is too small for internal hydrogen pressure mechanism. Thus, the four main hydrogen embrittlement mechanisms in LWR conditions are briefly described:

Hydrogen-enhanced decohesion embrittlement. HEDE postulates that hydrogen decreases the lattice strength by charge transfer between atomic hydrogen and iron atoms, which locally reduces the cohesive bonding energy in strained regions. It follows that the stress necessary for crack initiation and propagation is lower and cleavage (or quasi-cleavage) occurs in preference to slip. Hence, hydrogen can reduce the cohesive energy of the metal matrix, GBs or matrix/inclusions interface (Figure 2.31-a). This mechanism requires high local hydrogen concentrations.

Adsorption-induced dislocation emission. AIDE claims that hydrogen facilitates nucleation of dislocations at sinks (surfaces, crack tips, voids) and their emission into the plastic zone (Figure 2.31-b).

Hydrogen-enhanced localized plasticity. HELP postulates that hydrogen reduces the elastic interactions forces between dislocations and dislocation-obstacles (shielding effect), with local softening and concomitant plastic strain localization. The SFE is also reduced, which restricts dislocation cross slip, increasing dislocation density and favouring shear localization [116]. Shielding effects for dislocation-dislocation interactions are only relevant at high dislocation densities when the average distances between interacting dislocations are small. Hence, the resistance to dislocation motion is reduced by the "shielding effect" of dislocations and other elastic singularities in regions with high concentration of solute hydrogen and dislocation density, such as a precipitate or a crack. The fracture surface is majorly TG and sometimes in the GB vicinity, where hydrogen is accumulated (Figure 2.31-c).

Hydrogen-enhanced strain induced vacancies. HESIV claims that the formation of vacancies and nanovoids is facilitated under strain in the presence of hydrogen, and leads to ductile crack growth by slip localization [117]. Microvoid coalescence (MVC) is enhanced in highly strained regions with very high vacancy and hydrogen concentrations by enhancing the climbing of edge dislocations, vacancy clusters and nanovoids as dislocation obstacles.

Often, the failure of structural materials can be produced by a combination of two or more mechanisms in AuSS under LWR conditions [104]. The relative contribution of each mechanism will depend on strain rate, microstructure, temperature and hydrogen concentration. HELP, HESIV and AIDE can produce both, MVC and brittle cleavage (or quasi-cleavage) fractures. Ductile MVC and brittle crack growth occur at lower stresses in the presence of hydrogen than in air or hydrogenated free conditions and synergies or competition with other mechanisms might also occur.
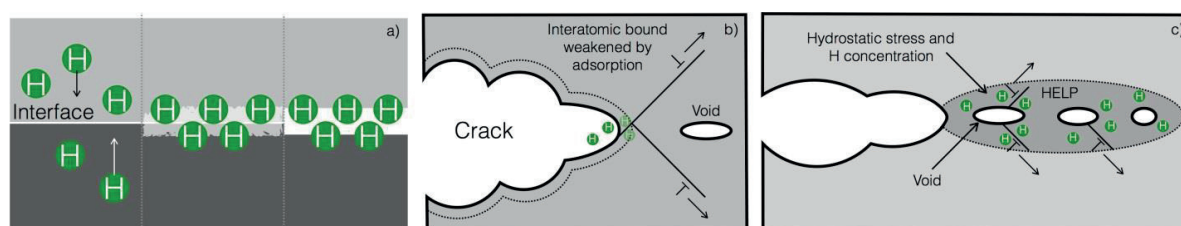
Figure 2.31. Schematic representations of hydrogen embrittlement mechanisms: a) HEDE, b) AIDE and c) HELP. Adapted from [104].

2.3.4.3   Crack-tip environment conditions and occluded crevice electrochemistry

Fundamental concepts of crack electrochemistry in AuSS under LWR conditions

SCC is significantly affected by the evolution of occluded water chemistry in cracks with restricted mass transport. Its effects are described hereafter.

Mass transport in crack crevice: The bulk concentration of specific species outside the crack crevice, their production/depletion rate and their transport into/out the crevice govern the concentration of species in the crack-tip. The mass transport mechanisms in the crack crevice can be by diffusion (concentration gradient-induced), migration (potential gradient-induced) and/or convection (flow- or cyclic stress-induced). If convection is present, it usually dominates over diffusion and migration, but in those cases, homogeneous potential and concentration exist in the crack crevice. Increasing the frequency of cyclic stresses and decreasing stress ratio enhance convection in crack crevice, which is believed to flush out or dilute the aggressive crack-tip environment and to slow down SCC CGR in high-purity water. On the other hand, under low-frequency cyclic stress or constant load, diffusion dominates the mass transport in reducing conditions (PWR and BWR/HWC), whereas the mass transport in oxidizing conditions (BWR/NWR) is controlled by diffusion and migration.

Occluded crevice electrochemistry: The electrochemical processes and mass transport occurring in a crack crevice in AuSS are shown in Figure 2.32. In NWC, a differential aeration cell (3 & 4 in Figure 2.32) is formed in the crack-mouth. Oxide film rupture in the crack-tip due to dynamic straining results in the formation of a dissolution cell (1 & 2 in Figure 2.32). Restricted mass transport at the crack-tip only requires certain crevice geometry and given the limited conductivity in LWR conditions and the oxygen depletion in the crack-tip, a high potential drop is created between the crack-tip and the crack-mouth.
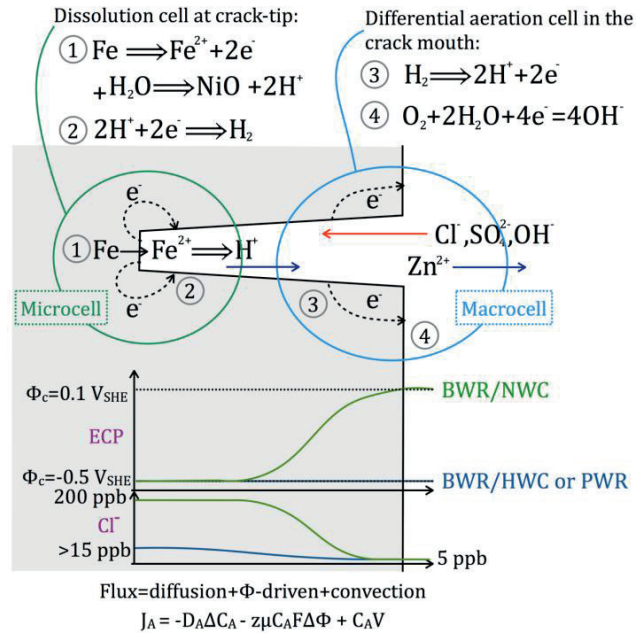
Figure 2.32. Schematic of crack electro and water chemistry showing the differential aeration cell at the crack-mouth (reaction 3 and 4) that establishes the crack-tip chemistry and the local microcell (reaction 1 and 2) associated with metal dissolution and crack advance. Because of the high ohmic resistance of the electrolyte, there is no direct coupling of electronic currents between these two cells. The potential gradient between the aerated crack-mouth (+0.1 V_{SHE}) and the de-aerated crack-tip (-0.5 V_{SHE}) results in an additional flux of anions/cations into/out of the crack enclave and an enrichment of anions and pH-shifts in the crack-tip environment in the case of non-OH--anions in the bulk environment. Adapted from [1, 118].

Differential aeration cell at the crack-mouth: Oxygen mass transport by diffusion into the cracks is slower than its reduction and consumption on oxide films. Crack crevices with restricted mass transport (high depth to width ratio) readily consume all the oxygen over a short distance from the crack-mouth. This effect produces a potential drop between the de-aerated crap-tip (~-0.5 V_{SHE}) and the aerated crack-mouth (~+0.1V_{SHE}) and also, migration of anions and cations towards the crack-tip and crack-mouth, respectively. Thus, the crack-tip enriches with ionic impurities that can produce acidic pH shift in case of Cl^-, SO_4^{2-} migration. Hydrolysis of metal cations produced during anodic dissolution and dissolution of MnS-inclusions (from the AuSS) might also contribute to shifting the pH. The pH shifts increase exponentially with the potential gradient (crack-tip versus -mouth). In a de-aerated crack-tip, the potential is always low and close to the equilibrium potential of the H_2/H_2O reaction. In BWR/HWR or PWR conditions, the H_2/H_2O reaction controls the ECP in both, the crack-tip and crack-mouth. For this reason, there is a small potential gradient between the crack-tip and crack-mouth and the mass transport is only controlled by diffusion. The hydrogen concentration at the crack-tip is similar as in the bulk environment since there is almost no consumption of hydrogen in the crack crevice and some hydrogen is produced by corrosion reactions.

Dissolution cell at the crack-tip: The rupture of the oxide film at the crack-tip results in crack advance by anodic dissolution until the formation of a new protective oxide film is formed. Given the lack of oxygen in the crack-tip region (microcell in Figure 2.32), the anodic dissolution current on the fresh bare metal at the crack-tip is balanced in the immediate vicinity by reduction of hydrogen or water. Corrosion processes and hydrolysis of metal cations keep high hydrogen availability in the microcell.

The high ohmic potential drop due to the poor conductivity of the water in LWRs strongly limits the spatial extension of the galvanic elements, so the electronic coupling between the crack-tip and crack-mouth is avoided. In any case, SCC is not directly affected by conductivity. SCC crack growth in AuSS is mainly governed by the concentration of specific anionic impurities as sulphate/sulphides or chloride and the pH in the crack-tip, which significantly influence the oxide film stability or the dissolution/repassivation kinetics.

The repassivation kinetics limits the dissolution cell current, whereas the cathodic reactions and the ohmic polarisation do not appear to be limiting factors. Due to sufficient high availability of hydrogen and the very high ratio of cathodic to anodic area at the crack-tip, the balancing cathodic reaction does not limit the dissolution. Many experimental investigations confirmed this hypothesis by tests with microsampling technique and by repassivation measurements in simulated crack-tip conditions [90, 119, 118, 120, 121]. Those results also confirmed that the crack-tip dissolution was enhanced by the aggressive chemistry in the crack rather than the potential gradient per se.

<u>Typical crack-tip electro- and water chemistry in AuSS under LWR conditions</u>

Crack-tip potential and potential gradients: As mentioned earlier, the ECP in both, BWR/NWC and PWR or BWR/HWC conditions, at the de-aerated crack-tip is always low ($\sim$-0.5 V_{SHE}) and governed by the H_2/H_2O-line regardless of the bulk dissolved oxygen content and radiation levels (ECP shift due to radiolysis in hydrogenated or oxygenated water is small) [122, 123]. In BWR/NWC, the pH at the crack-tip is more acidic (up to two units) and the ECP more positive (0.1-0.25 V_{SHE}) than in PWR (or BWR/HWC) due to lack of hydrogen overpressure and H_3BO_3/LiOH [124].

In BWR/NWC, the O_2/H_2O-line governs the ECP at the crack-mouth. Typical values of ECP in the crack-mouth range from 0.05 to 0.25 V_{SHE}. Increasing the bulk oxygen dissolved increases the potential gradient between the oxygenated crack-mouth and the de-aerated crack-tip which usually amounts 0.5-0.75 V_{SHE} [118]. On the other hand, in PWR (or BWR/HWC) conditions, the crack-tip and the crack-mouth have similar ECP, so negligible potential gradient is induced.

Crack-tip pH and crack-tip sulphur-anion concentration: Under BWR/NWC conditions, acidification at the crack-tip (up to two pH units) is caused by hydrolysis of metal cations, dissolution of MnS-inclusions (more important in carbon and low alloy steels) and migration and enrichment of specific anionic bulk impurities [118]. Because of the absence of a potential gradient, a higher pH (one or two units) in PWR (or BWR/HWC) compared to BWR/NWC environment is observed.

The anion activity at the crack-tip is 20 to 30 times and 2 to 3 times higher than the bulk anion activity in BWR/NWC and PWR (or BWR/HWC) conditions, respectively (see Cl⁻ activity in Figure 2.32).

Crack tip conductivity: Most of the corrosion products and ionic species have low solubility in neutral high-temperature water and the small pH changes have little impact on their solubility. Generally, the maximum increase of conductivity at the crack-tip is about 100 to 1000 times higher than in the bulk. Regardless of this large increase, the conductivity values are still very low.

2.3.5 Irradiation-assisted stress corrosion cracking in AuSS

As mentioned earlier, in high-temperature water, IGSCC in AuSS is observed in unirradiated-SA and -CW conditions at very high ECP and at low ECP, respectively. Irradiation usually results in higher CGRs and shorter initiation times than in unirradiated conditions. IASCC can be understood as IGSCC since the fracture is IG, but with increased susceptibility due to the irradiation effect (Figure 1.1) [125, 126]. IASCC occurs at different thresholds in BWR and PWR. In BWR (oxygenated water), IASCC appears at a minimum dose of about 0.5 dpa [1], whereas in PWR (deoxygenated water) is at about 3 dpa [5, 127].

IASCC and IGSCC show similar dependencies and influencing factors and there is thus a continuous spectrum between IGSCC and IASCC. IASCC is caused by a synergy of different phenomena affecting the material microchemistry and microstructure (transmutation products, RIS and hardening, radiation-enhanced diffusion, radiation-induced creep/relaxation and swelling), stress state (relaxation of residual stress, built-up of stress due to differential swelling, etc.) and the environment (radiolysis), which have been studied thoroughly for the last decades [43, 128, 129, 130].

Many of the large number of interrelated environmental, loading and material parameters that influence IGSCC may be synergistic or competitive and be aggravated or mitigated by irradiation. Some of these parameters may be time-dependent (fluence, hardening, chromium GB depletion, residual stress relaxation, etc.) and/or crack-depth dependent (through wall thickness residual stress distribution, surface CW, fluence, etc.). This finally results in a rather complex overall IASCC behaviour. There is no established single mechanism that controls IASCC, although the long service experience, because of its complexity.

2.3.5.1 Service experience in PWR internals

Published studies on components replaced from PWR internals with IASCC in service are summarized in Table 2.5. Both, the BFB and the FTT have shown IASCC from 6 to 70 dpa, with different cavity concentrations and estimated operating temperatures between 290 and 400 °C. The dpa level and the operating temperature had a significant impact on the microstructure of the component and so to the mechanical response of the material.

The BFB represents fairly well all the radiation and temperature variations in the reactor even though they are placed in the core surroundings (Figure 2.33). The bolt head (Figure 2.33-Region 1) is the closest part to the reactor and where there is the highest irradiation and cooling. In this region, cavities are below the resolution limit of the TEM (< 2 nm) and the microstructure is characterized by black dots. The bolt shank (Figure 2.33-Region 2) receives slightly less dose than the head, but the cooling is worse, so it enhances the coarsening of cavities and the formation of dislocation loops. In the bolt threat (Figure 2.33-Region 3), both, dose and temperature are lower than in the shank so smaller cavities are observed. IASCC cracks/failures were found between the BFB head and shank.

The FTTs receive higher dose rate than the BFB, but the cooling is similar to the bolt head. Hence, even though the accumulated dose in the FTT increases faster than in the bolt head, the expected microstructure for a given dose should be similar. Therefore, the BFB observations can be extrapolated to any other component with similar neutron spectra and dose.

Element & Material	Dose (dpa)	Temperature (°C)	Service time (years)	Cavities/bubbles		Hardness	Ref.
				Avg. diameter (nm)	Density (m⁻³)		
BFB head CW316 (12%)	9	312	29	3	2×10^{21}	3.92 GPa (HV0.1)	[131]
BFB shank CW316 (12%)	7	325	29	6	9.8×10^{21}	3.33 GPa (HV0.1)	[131]
BFB CW316 (15%)	13	345-365	20	10.4	0.7×10^{21}	N/A	[132]
BFB head CW316 (20%)	17	320	20	<2	$<10^{20}$	3.71 GPa[b]	[133, 134]
BFB shank CW316 (20%)	10	343	20	8.6	6.1×10^{21}	3.48 GPa[b]	[133, 134]
BFB shank CW316 (20%)	6	333	20	7.7	10×10^{21}	3.59 GPa[b]	[133, 134]
FTT CW316 (15%)	33	290	23	<3	610×10^{21}	N/A	[135]
FTT CW316 (15%)	70	315	23	<3	1600×10^{21}	N/A	[135]
BFB head 316 (CW[a])	~9[a]	376	15	2	5.8×10^{21}	3.9 GPa (HV0.1)	[136]
BFB shank 321Ti (CW[a])	~8[a]	398	15	3.5	4.6×10^{21}	3.72 GPa (HV0.1)	[136]
BFB shank 321Ti (CW[a])	~7[a]	398	15	6.9	2.3×10^{21}	3.65 GPa (HV0.1)	[136]
FTT CW316 (15%)	25	324	-	0.96	600×10^{21}	3.69 GPa (HV0.5)	[49]
FTT CW316 (20%)	35	305-315	11 EFPY	1	600×10^{21}	N/A	[137]

[a] Unknown level of CW.

[b] Calculated using a linear regression between the top and the bot of the bolt. It is 30mm bolt going from 11.4 to 7 dpa.

Table 2.5. Results of the TEM observations of the BFB and FTT replaced from PWR reactors. In parenthesis in the "Element & Material" description the CW level is shown.
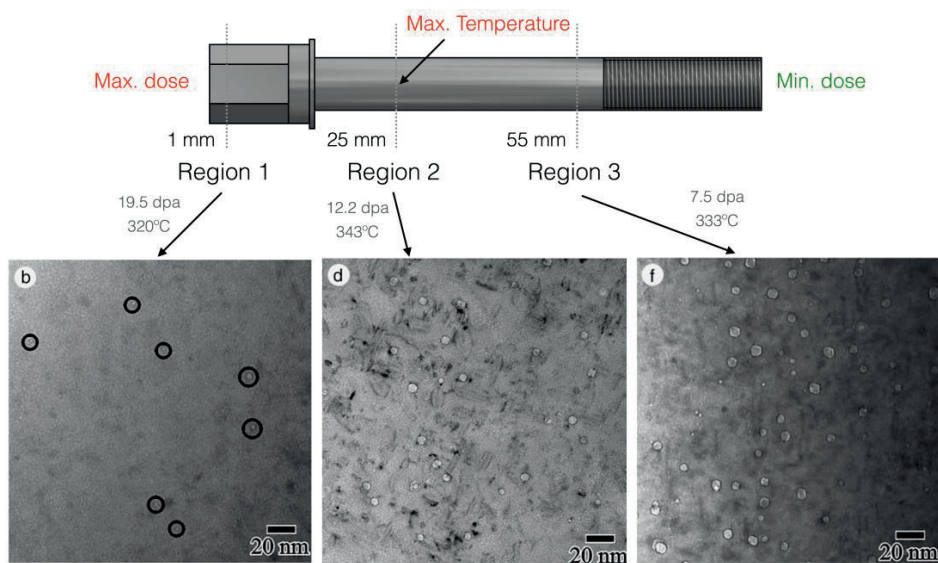
Figure 2.33. Observed TEM microstructure of a BFB extracted from a PWR. The bolt head has almost invisible cavities, but in the shank region where the temperature is higher, the cavities are bigger. Adapted from ref. [134].

2.3.5.2   Radiation effects on the main factors of influence to IGSCC

The level and extent of the neutron damage depend on its energy. RIS, radiation hardening and radiolysis of the water are mainly produced by fast neutrons. On the other hand, transmutation and out of core heating are mainly produced by thermal neutrons. During the fission process, γ rays are also emitted. γ-irradiation plays an important role for γ-heating (swelling), radiolysis and enhanced recombination of H_2 with oxidants (e.g. downcomer of the annulus of a BWR). The linear energy transfer (or energy deposition rate) for fast neutrons is three orders of magnitude greater than for γ-irradiation, so radiolysis is principally caused by fast neutrons [138]. Moreover, the neutron flux is also higher than the gamma flux.

Some of the radiation effects are cumulative and persistent with dose (e.g. hardening), others only occur in-situ during radiation (radiolysis). For many reactor internals, the (weld) residual stress is the main mechanical driving force for IASCC crack growth.

Effects of radiation in LWR environment

In hydrogenated or oxygenated high-temperature water, radiolysis does not produce a significant shift in ECP. Below 500 ppb H_2 (BWR reactors in NWR and HWC upper core), the formation of radicals and peroxides by radiolysis is not effectively suppressed, so it produces an increase of the bulk ECP. Due to the strong H_2 partitioning to the steam phase in BWR/HWC, about three-quarters of the core have a bulk H_2 concentration below 500 ppb [1]. The bulk ECP increase was shown to be fairly correlated to the content of H_2O_2 [1]. However, Andresen et al. [139] showed that radiation did not significantly increase the ECP in crack crevices (<+0.05 V). Thus, in BWR (NWR and HWC in upper core) conditions, the increase of bulk ECP results in a small increase of the potential gradient between the crack-mouth and the crack-tip and therefore, in a little increase of the CGR (Figure 2.34). On the other hand, in PWR and in BWR/HWC in the lower core region, radiolysis has a negligible impact on the CGR.
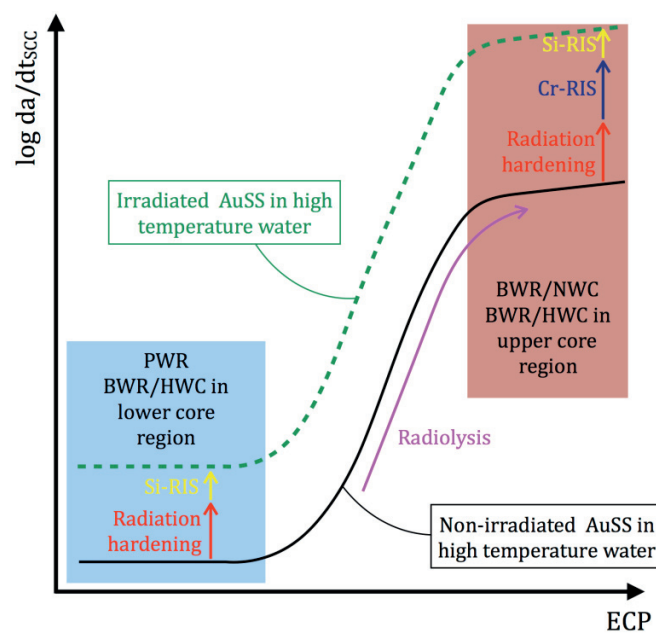
Figure 2.34. Schematic representation of the irradiation effects on CRG versus ECP in AuSS in high-temperature water.

Effect of radiation in the material

Both, RIS and radiation hardening, simultaneously evolve and increase with dose up to 5 - 10 dpa (see subchapter 2.2.3). Above 10 dpa, radiation hardening is saturated and RIS evolution rate slows down significantly. However, both are fairly well correlated to IASCC susceptibility (Figure 2.35 and Figure 2.36).
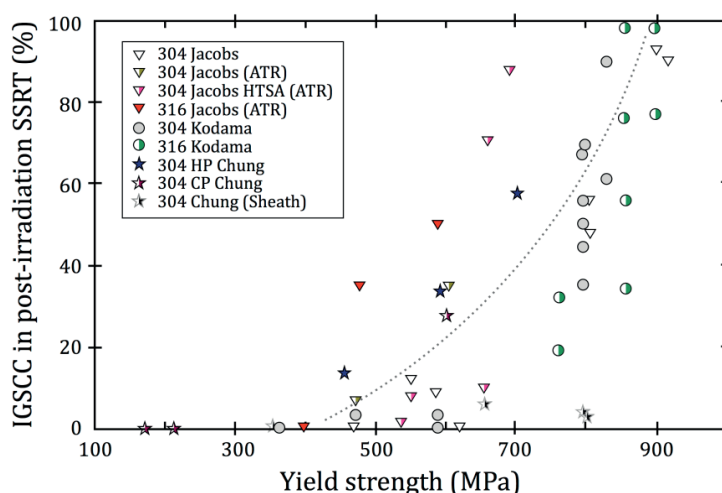
Figure 2.35. Correlation of measured tensile YS and IGSCC susceptibility in oxygenated high-temperature water for neutron-irradiated AuSS. Adapted from [40, 140].
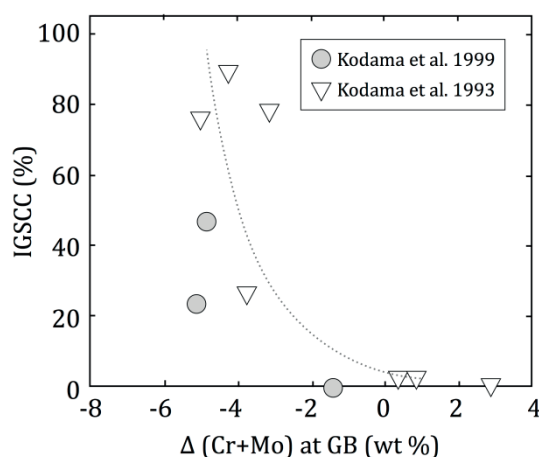
Figure 2.36. Correlation between Cr+Mo depletion on GB and IGSCC in irradiated AuSS 304 and 316L. Adapted from [141]. References: Kodama et al. 1999 [141] and Kodama et al. 1993 [142].

The failure mechanism at low dose in BWR conditions (NWC or HWC in upper core region) is widely attributed to sensitization of the GBs by RIS, radiation hardening and radiolysis of the water. In PWR conditions (or BWR/HWC in lower core region), the failure mechanism cannot be attributed to the GB sensitization since the corrosion potential is much lower. For this reason, the observed IASCC initiation with dose is higher for PWR (2-3 dpa) than for BWR/NWC (~0.5 dpa).

Thus, in high purity water, chromium depletion is only detrimental under oxidizing water chemistry conditions, where the bulk material is at high corrosion potential and the crack-tip in deaerated water with aggressive occluded crevice chemistry and acidic pH. SCC depends on the minimum level of GB chromium and not on its width. The formation of chromium carbides in the GB can further deplete the

chromium near the GB and increase the IGSCC susceptibility. Besides the chromium depletion, RIS also produces, among other elements, silicon enrichment in GB where it can eventually oxidize (SiO_2) at all relevant potentials. The dissolution of this oxide in high-temperature water can weaken the GB strength. Silicon is considered to be one of the potential contributors to IASCC at high dose [65].

<u>Effect of radiation on the stress state</u>

Radiation can produce differential swelling in mechanical connections and stress relaxation. For instance, the differential swelling between the baffle former plates (SA 304) and the BFB (CW 316L) can produce reloading of components, which might exceed the stress to initiate IASCC (Figure 2.37) [1]. Stress relaxation of weld residual stress, bolt or spring load causes a decrease of stress, which might be beneficial to suppress IASCC initiation and growth (Figure 2.38). However, under constant load, irradiation creep can promote localised plastic deformation at the crack-tip, which might help to initiate and sustain SCC [2].
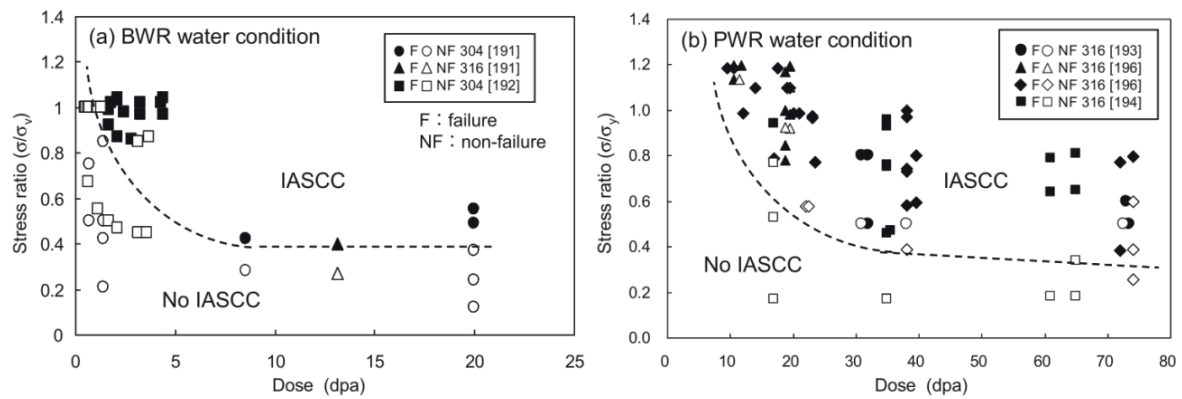
Figure 2.37. Constant load SCC test data as a function of the stress ratio to YS (σ/σ_y) versus dose in (a) BWR (288°C, 32 ppm O_2) and (b) PWR water conditions (320-340°C, 2.7 ppm dissolved hydrogen) [2].
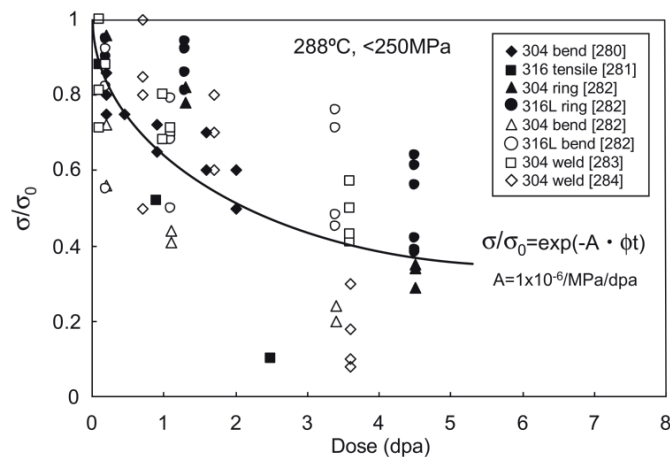
Figure 2.38. Stress relaxation in type 304 and 316L AuSSs under material test reactor irradiation at 288°C [2].

2.3.5.3 Low versus high dose

It is believed that IASCC might be a combination of different irradiation-induced defects. Radiation-induced environmental changes can alter the severity of cracking, but the main concern is produced by the radiation-induced microstructural and microchemistry changes. The microstructural and microchemistry evolve simultaneously with dose, hindering the understanding of IASCC. Moreover, at

low (<5-10 dpa) and high doses (>20 dpa), the IASCC susceptibility might be controlled by different parameters.

At low dose, the simultaneous increase of hardening, RIS and dislocation loop microstructure (conventional mechanisms) with dose is fairly well correlated to the IASCC susceptibility (Figure 2.39). However, above 5 dpa, these mechanisms saturate or slow down [42, 46, 55]. Because the conventional mechanisms reached saturation, other mechanisms might be responsible for increasing the IASCC susceptibility at doses above 10 dpa. The stress level needed to initiate IASCC decreases with increasing dose and seems to saturate at high doses at about 40%YS (Figure 2.37). In BWR/NWC conditions, the stress level to initiate IASCC dropped to 40%YS within less than 10 dpa, whereas in PWR conditions this level was shifted to above 30 dpa. The fast relaxation of weld residual stress with a very few dpa is the main reason of the lower IASCC susceptibility.
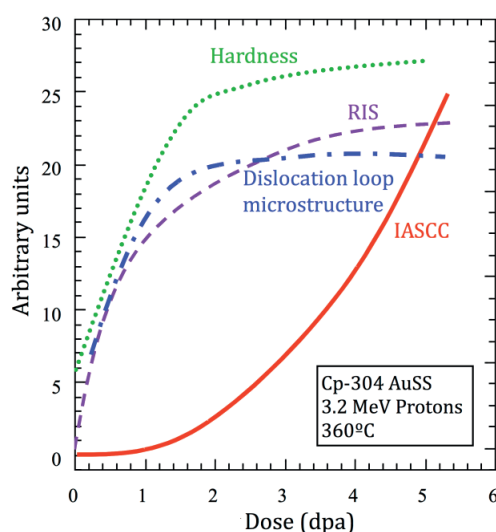
Figure 2.39. Schematic representation of the dose dependence of IASCC and other principal irradiation-induced changes [143].

At high doses, the knowledge of IASCC susceptibility has been mainly acquired by irradiation in fast neutrons material test reactors (MTR) with much lower He production rates (0.2 appm/dpa) than in a PWR at late operation lifetime (10 appm/dpa). The IASCC susceptibility of AuSS irradiated in a FBR showed significantly lower susceptibility in SSRT in simulated PWR environment than in irradiated PWR at the same high dose level, in spite of similar microstructures, hardening/YS levels and GB segregation [144]. The results showed a clear correlation between the He concentration and the IASCC susceptibility (Figure 2.40). Cavity formation was observed not only inside the grains but also on the GB of the highly irradiated AuSS in a PWR. Therefore, it is suggested that the He could play an important role in IASCC of PWR core internals in addition to the conventional mechanisms and that, the mechanism at low dose and high dose might be different. The neutron spectrum and the He concentration could also play a role, especially in long-term operation (> 50 years) [4, 57].
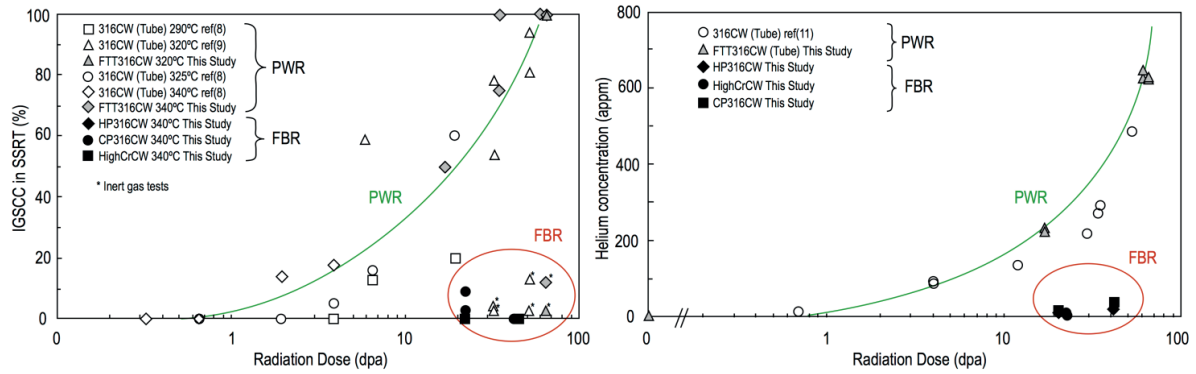
Figure 2.40. Ratio of IG fracture surface by SSRT test (left) and He concentration (right) as a function of radiation dose in PWR and FBR [144].

2.3.5.4 Post-irradiation annealing effect

Identifying the main parameter/s responsible for IASCC is a challenging task. Currently, there are no studies that demonstrate the failure of a component due to a specific single irradiation-induced defect. Many authors performed PIA treatments in irradiated AuSS in order to separate microstructural and microchemical effects (Figure 2.41) [49, 145, 146, 147]. The results suggested that the change in IASCC susceptibility with PIA could not be primarily attributed to chromium depletion due to RIS in either PWR or BWR conditions, but rather to a combination of hardening and chromium depletion. During PIA, the IASCC susceptibility drops rapidly to zero far before the GB segregation is recovered. Fukuya et al. [49] claimed that IASCC could be attributed to the change of microstructures and hardening, whereas Busby et al. [145] believed that the dislocation microstructure and the hardening were not enough to increase the IASCC susceptibility, but rather the dense population of small clusters (black dots). These black dots are the main reason to impede dislocation motion, which is consistent with the decrease of localized deformation observed after annealing by Jiao et al. [148].
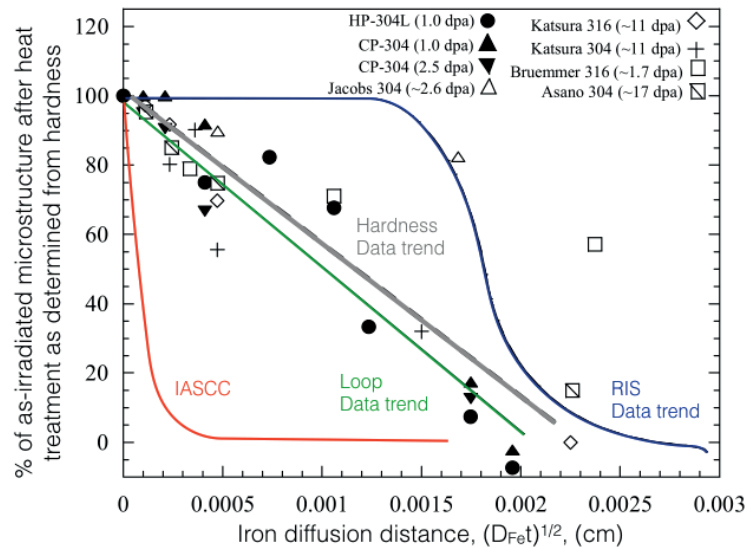
Figure 2.41. As-irradiated feature remaining after heat treatment measured by $(D_{Fe}t)^{0.5}$ for iron, to account from annealing at different times and temperatures [145].

2.3.5.5 Localized deformation

The irradiation hardening, the SFE and the precipitates/particles have an impact on localized deformation. The defects formed during irradiation act as obstacles for the gliding of dislocations, so the stress to produce plastic deformation increases with dpa up to ~10 dpa, where this effect saturates (Figure 2.10). The dislocations are pinned by these obstacles and eventually, under certain stress, a dislocation is able to glide overcoming and partially sweeping out the encountered defects. A channel with lower density of defects is formed along the dislocation path. The following dislocations (close to this channel) will see this region partially free of defects and preferentially glide on it, and thus forming a dislocation channel. The dislocation channelling results in highly localized deformation, in which the plastic deformation can reach up to 200% [149]. Dislocation channelling in irradiated AuSS can already appear above 0.1 dpa [150, 151]. Byun et al. [152] reported that deformation by channelling was dominant above 0.1 dpa and true stress above 600 MPa. This is consistent with other published results where localized deformation increased with increasing dose [153, 154, 155] and that increased the susceptibility to IASCC.

The SFE is alloy- but not irradiation-dependent, unless second phases are formed during irradiation. The SFE decreases with lower concentration of nickel and/or higher concentrations of silicon in AuSS. It was shown that low SFE in AuSS was correlated to planar deformation (2D deformation) and to SCC [156, 157]. Recent studies performed in high-temperature water have shown that non-irradiated and, even more, irradiated AuSSs with low SFE are more susceptible to IGSCC/IASCC than with medium/high SFE [153, 154, 158, 159].

Fournier et al. [160] showed that the presence of channels without precipitates before performing SSRT in simulated PWR conditions increased the susceptibility to IGSCC, whereas samples that did not have channels without precipitates did not practically show SCC susceptibility. Those channels free of precipitates acted similarly than the dislocation channels formed in irradiated material, so localized plasticity was enhanced in those regions.

Under stress/strain, GBs, precipitates/inclusions and previously formed channels can be sources of dislocations [161, 162]. Dislocation channels usually initiate on GBs and cross the grains interacting with the other GBs. Depending on the orientation of the neighbouring grain and the loading direction four different processes can occur: a) slip transfer to the neighbouring grain, b) cross-slip within the same grain, c) GB sliding and d) dislocations pile-up in the GB.

In LWR conditions, localized deformation occurring in grains close to the surface might contribute to the rupture of the oxide film protecting the material. This could initiate and sustain the crack in the GB thanks to the localized stress produced by the dislocation channels. Jiao and Was [154] have shown that IASCC susceptibility is more correlated to the degree of localized deformation than other parameters like SFE, radiation hardening or RIS. However, the main contribution to localized deformation was not clarified. In any case, localized deformation accelerates the GB sliding and contributes to the GB void formation and growth. Thus, the build-up of He in GBs can assist the GB crack growth by the link-up of voids [39].

2.3.5.6 Helium effects

Several investigations demonstrated that He has a significant influence on swelling, creep, fatigue and strength [39, 163]. He has a detrimental impact on the mechanical properties of the material and induces brittle fracture in the GBs. However, this is mainly based on creep tests [164], welding of irradiated materials [165] or highly irradiated materials [144] where relatively high stress and

temperature were also present during the tests and/or during the helium accumulation/bubble formation and coarsening.

The He effects on IASCC are difficult to reveal due to the synergistic interaction of He, dpa and environment. Radiation damage up to 48 dpa alone (irradiation in fast reactor) is insufficient to produce significant TG cleavage (< 2%) or IG fracture in SSRT in simulated PWR environment, whereas in BWR conditions (8 ppm O_2) one out of five samples showed partial IG fracture as was shown by Chen et al. in [12]. On the other hand, irradiation on a mixed spectrum (damage + He production) consistently produces partial IG fracture in BWR conditions (8 ppm O_2) above 1.4 dpa. Hence, irradiation in fast reactors is less detrimental than in a mixed spectrum, which might be due to the He production. Fujimoto et al. [144] carried out SSRT in simulated PWR conditions in reactor internals extracted from PWR and FBR. The results showed an evident correlation between IASCC and He content of the samples (Figure 2.40), which is consistent with the laboratory results from Chen et al. in [12].

So far, the effect of He alone, i.e. with negligible or low radiation damage, has been studied by many authors in SSRT in air and in vacuum at ~25°C and at ~300°C [8, 10, 11]. Schroeder and Liu in [8] showed that He implanted at 25°C up to 1000 appm and tested at 200°C had higher hardening impact than implanted hydrogen (Figure 2.42), but the fracture surface remained TG dimple fracture with MVC. Ullmaier and Chen [11] showed that only a He concentration above 1% can change the fracture mechanism in miniaturized specimens tested in vacuum (at both, 25°C and 300°C) from TG ductile with MVC to TG cleavage fracture. Miura et al. [10] found IG brittle cracks in 316L in single GBs using micro-tensile specimens, when the He concentration and the bubble average spacing in the GB was more than 2% and less than 5 nm, respectively. Those He concentrations were significantly above the expected He accumulation at end of life in reactor internal components. However, a 304L sample irradiated by 800 MeV protons at <250°C showed partial cleavage at 3.3 dpa (~500 appm He) and partial IG brittle fracture mode at 8 dpa (~1200 appm-He) after tensile test in RT air [13]. Therefore at low dpa (< 3-4 dpa), He is postulated to be the main contributor to TG cleavage and at higher dpa (~ 8 dpa), it is contributing to the IG fracture.

Summing up, there is a clear synergistic interaction between He and dpa which reduces the dpa threshold to produce embrittlement in AuSS. However, studies with high He concentrations and negligible dpa (< 0.1 dpa) in LWRs environment are missing.
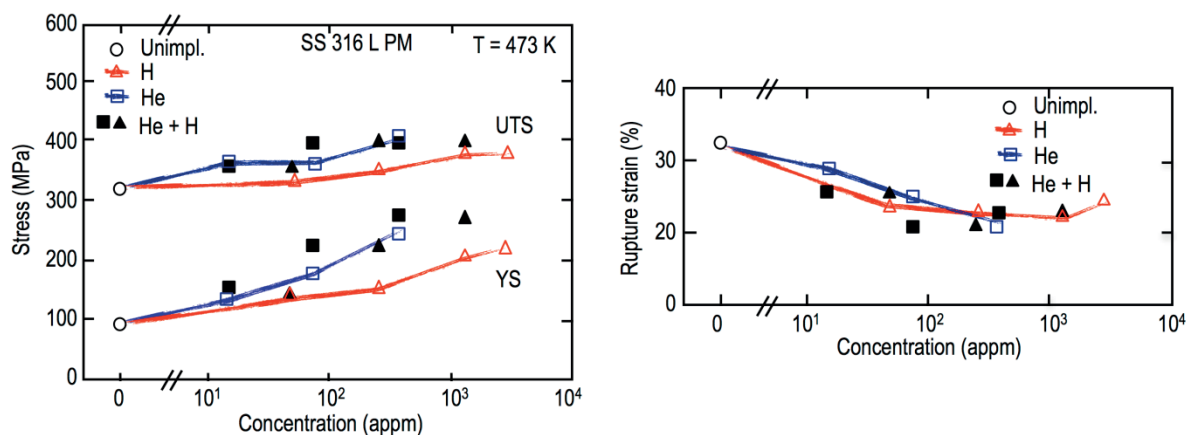
Figure 2.42. Tensile properties of hydrogen and/or He implanted 316L at 473K versus implanted gas concentration: on the left YS and UTS; on the right rupture strain. Adapted from [8].

Helium diffusion mechanisms in AuSS

The different He diffusion mechanisms are described in Figure 2.43. Without irradiation, the interstitial migration mechanism ("1" in Figure 2.43) is generally fast and dominant at temperatures below $0.5 \cdot T_m$, until He is trapped by another defect (e.g. vacancy). Above $0.5 \cdot T_m$, the diffusion of He by interstitial migration is limited due to trapping of He in thermally formed vacancies. At that temperature, the He migration occurs by vacancy migration mechanism ("3" in Figure 2.43) or by He-vacancy dissociation mechanism. The latter mechanism involves the thermal dissociation of He from its vacancy, its interstitial migration and re-trapping in another vacancy. The schematic representation of the energy thresholds, the relevant migration and the binding energies are given in Figure 2.44 and in Table 2.6, respectively. As it is shown in Table 2.6, the He-vacancy dissociation mechanism is more favourable than the He-vacancy dissociation mechanism in AuSSs since the required energy is lower.
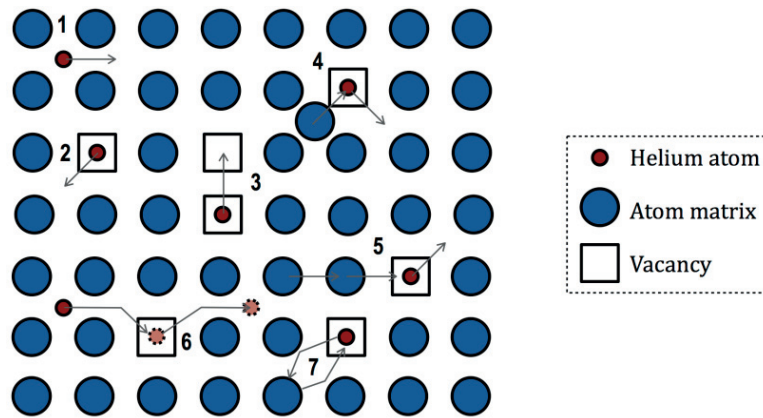
Figure 2.43. Schematic illustration of defect configurations and jump processes relevant for He diffusion without and with irradiation: (1) Interstitial diffusion, (2) transformation of substitutional He atom to interstitial by thermally activation dissociation from its vacancy, (3) vacancy migration mechanism, (4) transformation of a substitutional to an interstitial due to its replacement by a self-interstitial atom, (5) collisional displacement of a He atom, (6) impeded interstitial mechanism or dissociative mechanism, and (7) He migration by exchange mechanism. Adapted from [166].
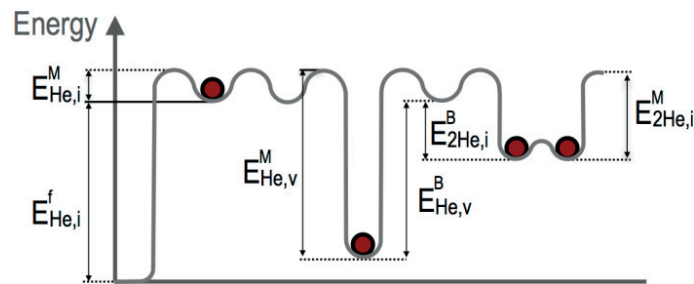
Figure 2.44. Schematic representation of the He diffusion energy in metals: $E_{He,i}^M$, migration energy of interstitial He; $E_{He,i}^f$, formation energy of interstitial He; $E_{He,v}^M$, migration energy of He by vacancy mechanism; $E_{He,v}^B$, He-vacancy binding energy; $E_{2He,i}^B$, binding energy of two-interstitial He's; and $E_{2He,i}^M$, migration energy of two-interstitial He's. Adapted from [167].

Vacancy formation energy	E_v^f	1.84
Vacancy migration energy	E_v^M	1.04
Formation energy interstitial He	$E_{He,i}^f$	4.02-4.5
He-vacancy binding energy	$E_{He,v}^B$	~2.63
Migration energy interstitial He	$E_{He,i}^M$	~0.66
Migration energy of He by vacancy mechanism	$E_{He,v}^M = E_v^f + E_v^M + E_{He,v}^T$	2.88
Migration energy of He by dissociative mechanism	$E_{He,Dis}^M = E_{He,v}^B + E_{He,i}^M - E_v^f$	1.45
Migration by exchange mechanism	$E_{He,Ex}^M$	3.1

Table 2.6. Formation, migration and binding energies in eV of vacancies and He in a typical fcc metal (nickel) [168, 167, 169, 170]. $E_{He,v}^T$ is the energy needed to transfer a substitutional He atom into a neighbouring vacancy, which is typically very small and $E_{He,Dis}^M$ is similar to the self-diffusion energy of the metal [169].

Helium bubble nucleation

He produced in the reactor internals has an extremely low solubility in metals and a strong tendency to be trapped and clustered and to form bubbles as it accumulates. The temperature, the He to dpa rate and the He concentration are the most important parameters controlling the evolution of the He bubble size and density [166]. However, in high He to dpa ratios the He bubble nucleation is dominated by the He diffusion. Figure 2.45 shows a schematic representation of the helium evolution during implantation/irradiation and its coarsening during PIA.

Under implantation/irradiation, the nucleation rate of He bubbles increases with the He concentration until the production and absorption rates of He equalize at time "t". At this point, the He density is very high and it is more likely that a He atom finds an existing bubble than to form a new one. For this reason, the He concentration and the He bubble nucleation rate decrease with time and the bubble density is saturated above "t". Thus, the bubble size increases to the detriment of the He concentration and nucleation.
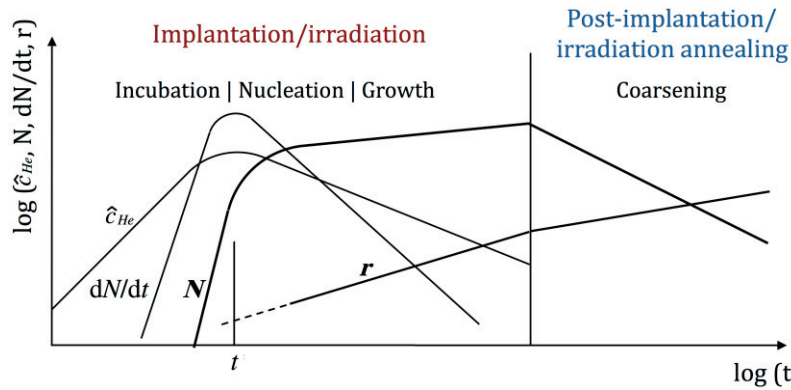
Figure 2.45. Schematic representation of the time-dependence of the main quantities characterising bubble nucleation during He production and bubble coarsening during annealing: $\hat{c}_{He}$, He concentration in solid solution; dN/dt, He bubble nucleation rate; N, He bubble density; and r, He bubble average radius [166].

Heterogeneous versus homogeneous nucleation

Defects in the material like GB, precipitates and dislocations are strong traps for He. At low temperatures, the thermal dissociation of He atoms from its trap is negligible. Homogenous nucleation will be dominant if the sink strength of the bubble nuclei is larger than the sink strength of pre-existing traps. High He production rates and low-temperature implantation/production will enhance homogenous nucleation.

At high temperatures, the concentration of He atoms at the edge of the He bubble and their state are important. Assuming that internal pressure (P) of the bubbles is in equilibrium with the surface energy (γ), P=2γ/r, then the pressure depends on the radius of curvature of the bubble (r). Bigger curvature radius produces lower internal pressure and thus lower He concentration around the defect (c*). Increasing the number of interfaces involved in the bubble nucleation facilitates bubble nucleation (Figure 2.46). Therefore, heterogeneous nucleation would occur at lower He concentration than for homogeneous concentration in the presence of defects.
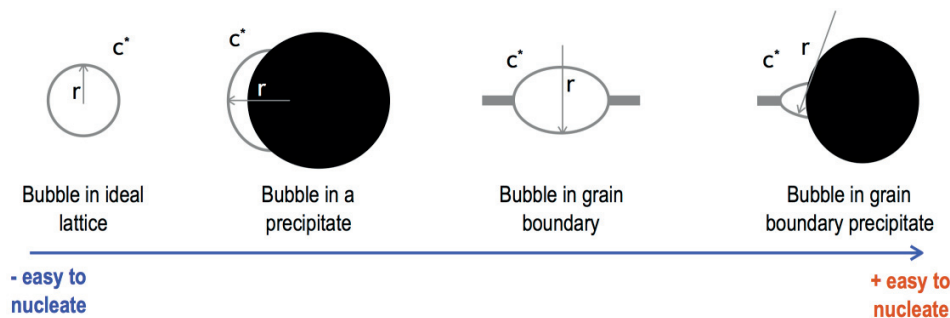
Figure 2.46. Schematic examples of bubble sites with decreasing nucleation barrier: in an ideal lattice, at a precipitate within the grain, on a GB and at a GB precipitate. Adapted from [167].

Helium bubble coarsening

PIA at high temperatures (> 500°C) after the He implantation results in an increase of the average bubble size and a decrease of its density (Figure 2.45). The bubble coarsening mechanism depends on the irradiation/implantation temperature, the annealing temperature, the annealing time and the He concentration [171, 172, 173, 174]. Generally, the He bubble coarsening shows two different mechanisms: one with low apparent activation energy at low annealing temperature, called migration and coalescence (MC, [175]); and the other with high apparent activation energy at high annealing temperature, called Ostwald ripening (OR, [176, 177, 178, 179]).

The MC mechanism is based on the migration of bubbles by diffusion of matrix atoms (Figure 2.47). The atoms diffusion can be by surface diffusion, vacancy diffusion or by vapour transport [175]. However, the surface diffusion has been reported to be the most likely mechanism [166]. The bubbles migrate towards each other with a velocity inversely proportional to its size until they coalesce. This mechanism can explain the He bubbles migration towards sinks, dislocations or precipitates.

The OR mechanism is caused by the thermally activated dissociation of He atoms from small bubbles and re-absorption into large bubbles (Figure 2.47). The equilibrium concentration of He around the bubble drives the He flux from the small bubble (higher pressure and higher He concentration at the bubble edge) to the large bubble (lower pressure and lower He concentration at the bubble edge). The OR mechanism has the same energy than the dissociation mechanism of the He diffusion, which is significantly higher than the MC mechanism.
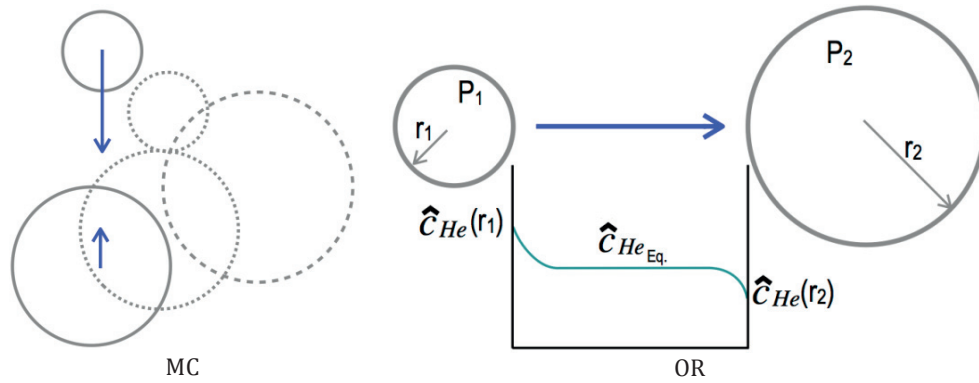
Figure 2.47. Schematic representation of the two main coarsening mechanisms, MC (left) and OR (right).

Generally, low and high-temperature implantations in nickel and in AuSS have shown well defined high and low-temperature regimes (Figure 2.48). The temperature at which the bubble coarsening changes the mechanism is called transition temperature (T_{tr}). Some general trends have been observed:

- OR is enhanced in case of high availability of vacancies (e.g. near the surface), whereas MC is prevalent in case of low availability of vacancies (e.g. in the bulk) [171].
- T_{tr} shifts to lower temperature with increasing annealing time, increasing He implantation rate and increasing He concentration (Figure 2.48). However, the higher the bubble density the higher the T_{tr} [172].
- Low-temperature implantation (I_c) followed by PIA results in higher T_{tr} than in high-temperature implantation (I_h) followed by high-temperature irradiation (R_h), in $I_c + R_h$ or in R_h.
- The bubble density increases with the He implantation rate and the He concentration.
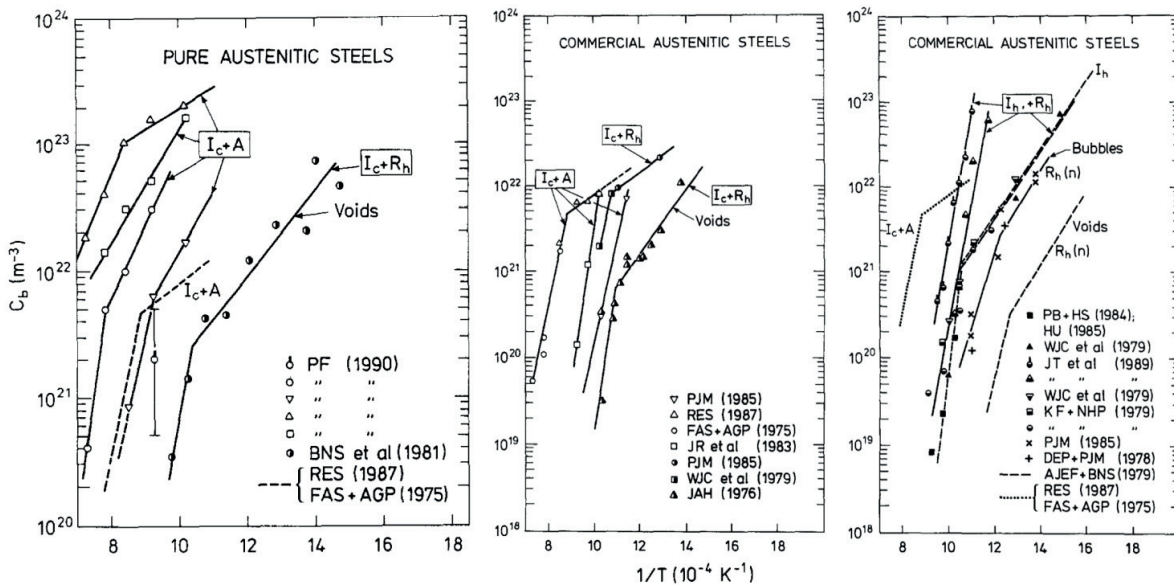
Figure 2.48. Temperature dependence of the observed bubble density (C_b) in pure (left) and commercial (centre and right) AuSS [172].

Chapter 3   Experimental Procedures

The following chapter presents the studied material, the samples, the tensile testing machines and the water loop designed for performing SSRT in LWR environments. The characterization techniques employed (TEM, SEM and instrumented indenter) as well as the He implantation facility, and He content and dose calculations (implantation time and dpa) are also described hereafter.

3.1 Material

The studied material is the AuSS 316L and it is taken from a 30 mm thick plate produced by rolling. A basic characterization has been performed (i.e. chemical analysis, metallography and hardness tests) to determine the state of the material before implantation and tensile tests. Prior to anything, the material was always SA at 1050°C for 30 minutes and quenched in water.

3.1.1 Chemical analysis

Shavings from a 316L block were extracted in three different positions. The carbon, sulphur and nitrogen contents are identified using a combustion method (with Leco equipment). The other elements are characterized using inductively coupled plasma atomic emission spectroscopy (ICP-AES). The averaged results obtained from the shavings are shown in Table 3.1. The elemental composition of the block is consistent with the composition of the AISI (American iron and steel institute) 316L, which has very low carbon, high manganese and high molybdenum contents.

Fe	Ni	Cr	Mo	Mn	Si	Cu	Co	N
65	12.32	17.61	2.379	1.768	0.466	0.198	0.164	0.067

V	C	P	W	Al	Ti	Sn	Nb	S
0.036	0.028	0.024	0.023	0.018	0.007	0.006	0.003	0.0029

Table 3.1. Composition of the 316L AuSS block (wt.%).

3.1.2 Metallography

In order to check the texture of the 316L block, three samples were cut from the original block and the surfaces from different orientations were polished with a final particle size of 1 μm (see subchapter 3.7.1). The three orientations of the block were studied by optical microscope: sample 1, L-T section; sample 2, S-T section; and sample 3, L-S section following the orientation description given in the ASTM E399. The samples were etched with etchant 87 from ASTM E407-99 (50 mL HCl, 10 mL HNO$_3$ and 30 mL glycerol) and the grain size was calculated using a semi-automatic method assisted by computer. The average results of each sample are shown in Table 3.2.

Sample	1 (L-T)	2 (S-T)	3 (L-S)
G (ASTM E112)	6.0	5.6	5.3
$\bar{d}$ (ASTM E112 in μm)	45	52	58

Table 3.2. Grain size number (G) in the three orientations of the block.

Although the data has some scatter between the three orientations, a fairly good homogeneous distribution of equiaxed austenite grains can be observed. No texture was observed in any of the orientations (Figure 3.1). As a result, the average standard grain size for all the orientations is 5.6 G which corresponds to an average diameter ($\bar{d}$) of about 52 μm.
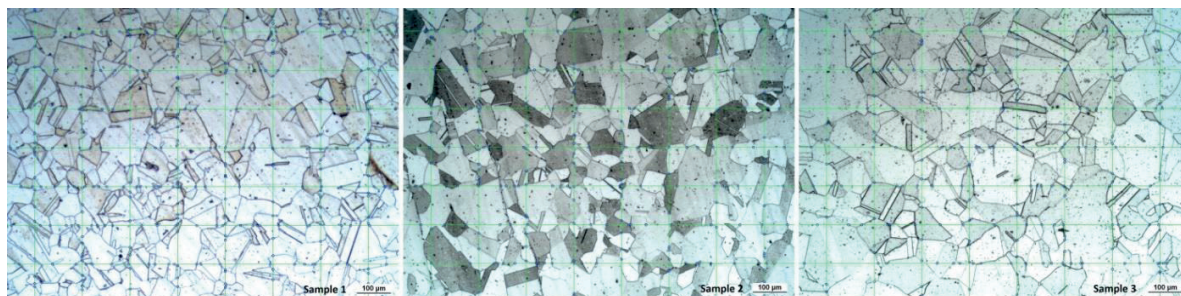
Figure 3.1. Optical microscope observations with the automatic grain size measurement mesh (from left to right): L-T, S-T and L-S orientations.

3.1.3   Hardness measurement

The gauge length of tensile samples was oriented in the S direction (Figure 3.2 left). A manual indentor from Leitz was used to measure the hardness in the T-L plane, which is the cross-section of the samples. Two samples were cut from each corner of the block (Figure 3.2 left) and polished with a final particle size of 0.05 μm (see subchapter 3.7.1). The hardness characterization was performed in the T-L plane along the T direction with a Vickers tip and 500 g (HV0.5). The hardness profiles in the T-L plane are shown in Figure 3.2 right. The average hardness is about 157 HV0.5 and no difference is found on the T-L plane and along T and S directions. The diameter of the projected Vickers indent was about 77 μm and the depth 11 μm, therefore some of the scatter in Figure 3.2 might be produced by the grain size (Hall-Petch) effect.
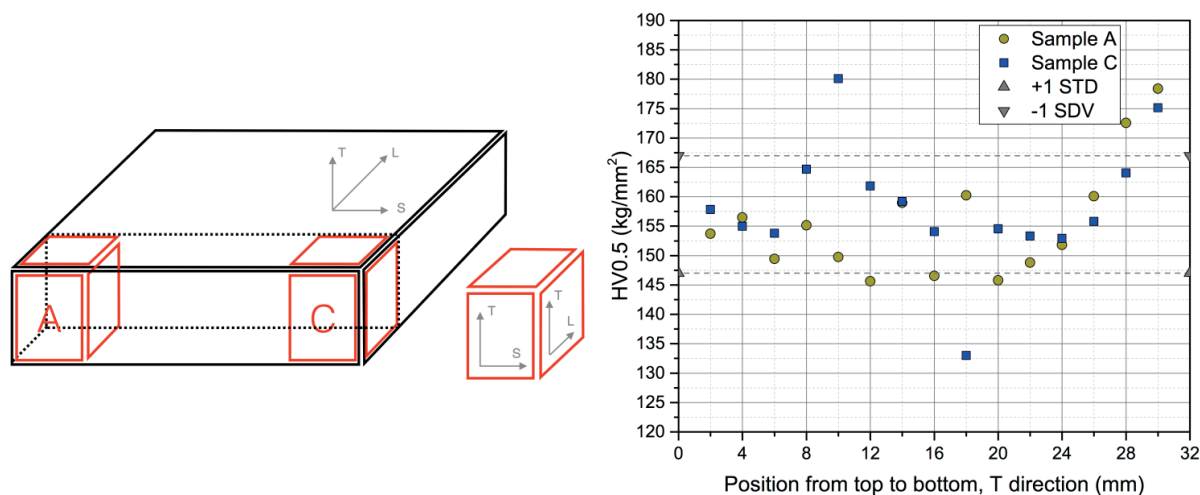
Figure 3.2. Samples position from the original block (left) and hardness profile in the T-L plane (right) along T and S direction using HV0.5.

3.2   He implantation

The irradiation/implantation facility was built in the late 1970's at the Institute for solid state research in the research centre Jülich. Because of the dismantling of the Jülich cyclotron, the device was acquired by Paul Scherrer Institute (PSI) and installed on one of the beamlines of the "Conditions

Extrêmes et Matériaux: Haute Température et Irradiation/ Centre National de la Recherche Scientifique" (CEMHTI/CNRS) cyclotron (Aug-2009). The facility was designed for performing in-situ stress effects on swelling [180], irradiation-creep experiments [181], helium-embrittlement [182] and fatigue [183]. Metallic and ceramic specimens can be homogeneously irradiated/implanted with light ions (e.g. helium) thanks to a magnet scanning system and a degrader wheel. The load on the sample can be monitored with a linear variable differential transformer (LVDT) connected to a spring [184]. The sample temperature is controlled by ten helium jets, five jets symmetrically distributed to each side of the sample. The temperature and elongation are measured by infrared pyrometers [185] and by two linear variable differential transformers (one in each side of the specimen [184]), respectively.

The He concentration and the Frenkel pair production were calculated with the stopping and range of ion in matter code (SRIM) [186]. SRIM calculations were performed with Fe-12.32Ni-17.61Cr-2.379Mo-1.768Mn alloy, the main elements given in Table 3.1, with 45 MeV He ions and a displacement threshold energy of $E_d = 40$ eV. The calculations were carried out using the Kinchin-Pease approach (K-P) as suggested in ref. [187]. These calculations provided the data needed to define the implantation conditions in CEMHTI/CNRS cyclotron and were used for the tensile test results analysis.
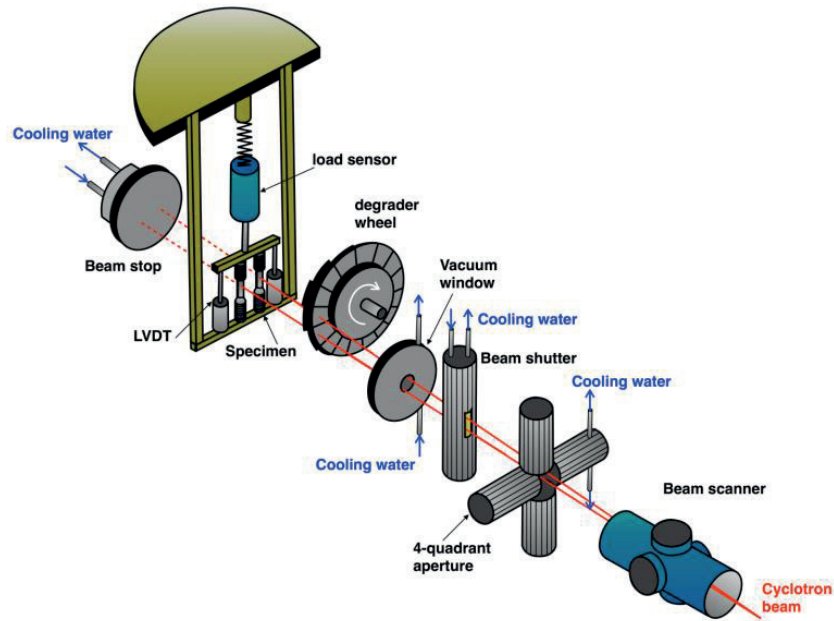
Figure 3.3. Schematic of the He implantation facility.

3.2.1 Implantation time

Within the frame of this project, homogenised He concentrations of 100, 300 and 1000 appm were selected to assess the He effects on SCC. To do so, an aluminium degrader was used to slow down the alpha particles and control their deposition along the sample thickness. The aluminium degrader had 24 different thicknesses from 94 μm to 700 μm to modify the penetration depth of the ions. The maximum range of the alpha particles in AuSS 316L with the thinnest aluminium foil is about 250 μm, so implanting from both sides of the samples give a total implantation thickness of 500 μm (first one side and then the other). The He implantation rate (I_R, $\frac{appm}{h}$) depends on the ion flux ($\dot{\Phi}$, $\frac{ions}{s*cm^2}$), the sample thickness (x, cm) and the atomic density of the target (ρ_A, $\frac{atoms}{cm^3}$):

$$I_R = \frac{\Phi}{x} \cdot \frac{1}{\rho_A} \cdot \frac{3600 \, s}{1 \, h} \cdot 10^6 \qquad \qquad \text{Eq. 3.1}$$

The ion flux ($\dot{\Phi}$) is proportional to the beam intensity (I, 4.5×10^{-6} A) of the CEMHTI/CNRS cyclotron but inversely proportional to the implantation area (A, 70 mm²) and to the helium ion charge (q_{alpha}, $1.6 \times 10^{-19} \times 2$ C):

$$\dot{\Phi} = \frac{I}{A \cdot q_{alpha}} \qquad \qquad \text{Eq. 3.2}$$

Thus, for this particular case, the ion flux was 2.01×10^{13} ions/(s * cm²) and the He implantation rate was 34.23 appm/h. Hence, a He concentration of 100, 300 and 1000 appm required about 3, 9 and 30 implantation hours, respectively. Since the implantation had to be performed from both sides, the real implantation time was 6, 18 and 60 hours.

3.2.2   Damage calculation

The average damage rate produced by the He implantation was calculated using Eq. 3.3 [188].

$$\dot{dpa} = \frac{1}{x} \int_0^x \frac{\gamma(x) \, \dot{\Phi}}{\rho_A} dx \qquad \qquad \text{Eq. 3.3}$$

Where $\dot{dpa}$ is the dpa rate in atoms/s and $\gamma(x)$ is the atom displacements produced per ion and sample thickness in atoms/(s · cm). The $\gamma(x)$ is equivalent to the Frenkel pair production per ion and sample thickness, which is calculated with SRIM using the K-P approach. Figure 3.4 shows the Frenkel pair production per ion and sample thickness after the α passed through each of the 24 aluminium layers using the K-P approach. The total Frenkel pairs production created per ion were obtained integrating the average Frenkel pair production per ion and depth along the sample thickness. In the present case, the average damage was 157 vacancies/ion. Thus, the damage rate calculated with Eq. 3.3 gave 0.0054 dpa/h. Using the implantation time found in the subchapter 3.2.2, the He implantation damage for 100, 300 and 1000 appm were 0.0162, 0.0485 and 0.162 dpa, respectively.
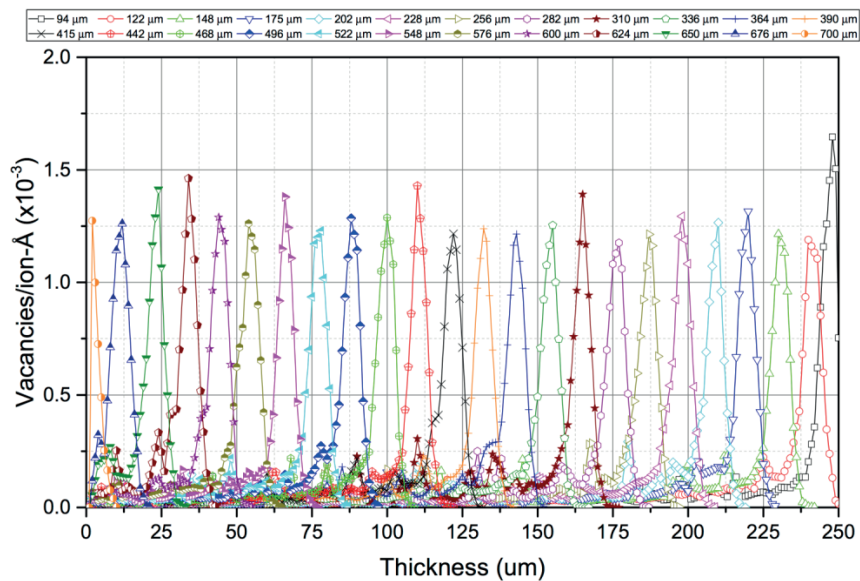
Figure 3.4. Number of Frenkel pair production per ion on half sample thickness obtained from SRIM output using the K-P approach and different aluminium foils.

The dpa profile along half of the sample thickness was calculated from the results showed in Figure 3.4. On the other hand, the He concentration profile along half of the sample thickness was calculated from the range of alpha particles in the material obtained with SRIM. Figure 3.5 shows the average He and dpa profile along half of the sample thickness for a He implantation with 1000 appm. It is noticeable that both, He and vacancy concentration, have similar profiles along the sample thickness, which will ensure a homogeneous effect of He and dpa. The results with 300 and 100 appm are 3 and 10 smaller than 1000 appm in Figure 3.5, respectively.
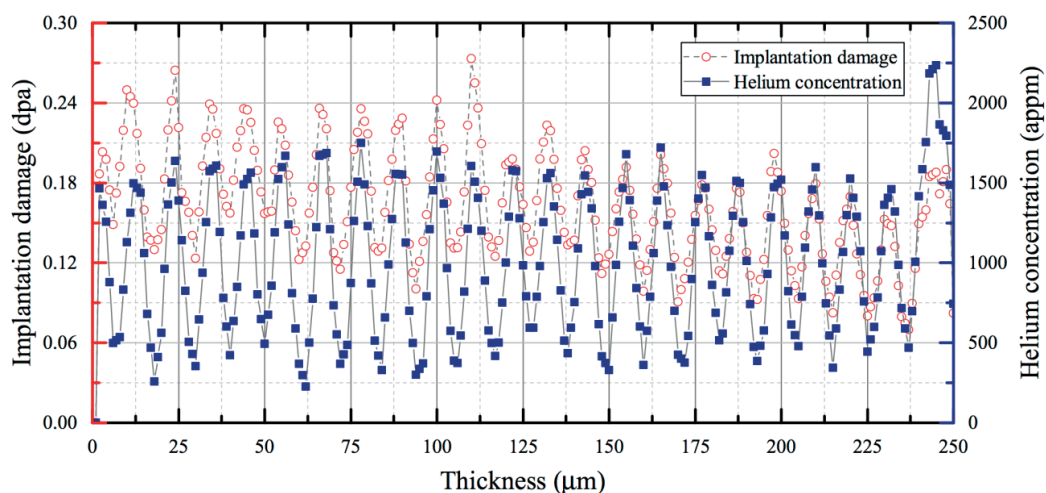
Figure 3.5. He and vacancy concentration profiles (along half sample thickness) for 1000appm He, calculated in Fe-12.32Ni-17.61Cr-2.379Mo-1.768Mn alloy with 45 MeV He ions to a fluence of 2.17×10^{18} He cm^{-2} using SRIM code in K-P approach with a displacement threshold energy of 40 eV.

3.3 Samples

Two types of samples were used: tensile samples and a helium-implanted plate (called He-plate afterwards). The He-plate was used to find the conditions to reproduce the bubble distribution observed in reactor internals containing He, to study the He evolution after annealing at different temperatures and to assess the He bubbles effect on hardening. The main purpose of the tensile samples was to study the He effect on IASCC susceptibility by performing SSRT in HTW.

3.3.1 "He-plate"

A 316L plate was cut from the original block with 8×13 mm^2 area and 1 mm thickness and implanted up to 1000 appm He. Then, the "He-plate" was cut into squared specimens with a size of 1.1×1.1 mm^2. The specimens were PIA in vacuum ($<10^{-4}$ Pa) at temperatures ranging from 650°C to 1000°C for 1 h. They were inserted into and pulled out from the furnace at temperature under vacuum. The typical time for heating and cooling down the specimens was about 5 minutes. The schematic of the process is shown in Figure 3.6.
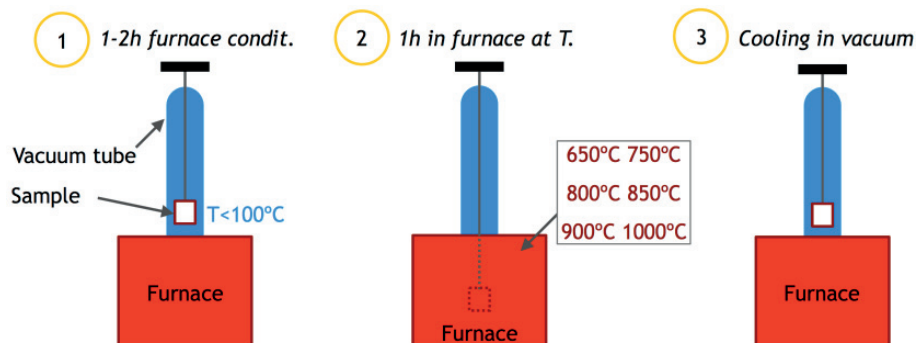
Figure 3.6. Schematic of the annealing treatment performed in the He-plates.

3.3.1.1 TEM samples

In order to avoid surface effects, the TEM samples were prepared after annealing far from the surface and the non-implanted material as indicated in Figure 3.7. The material was polished away with a final particle size of 2.5 μm (see subchapter 3.7.2). Then, small disks with a diameter of 1 mm were carefully punched and embedded in 3 mm disks with an inner hole of 1 mm. The embedding glue (G1 from "Gatan") was removed by mechanical polishing with a particle size of 2.5 μm. Finally, those disks were electro-polished to perforation with a Tenupol-5 at -20 °C and 25 V with a solution of 5% perchloric acid and 95% methanol.
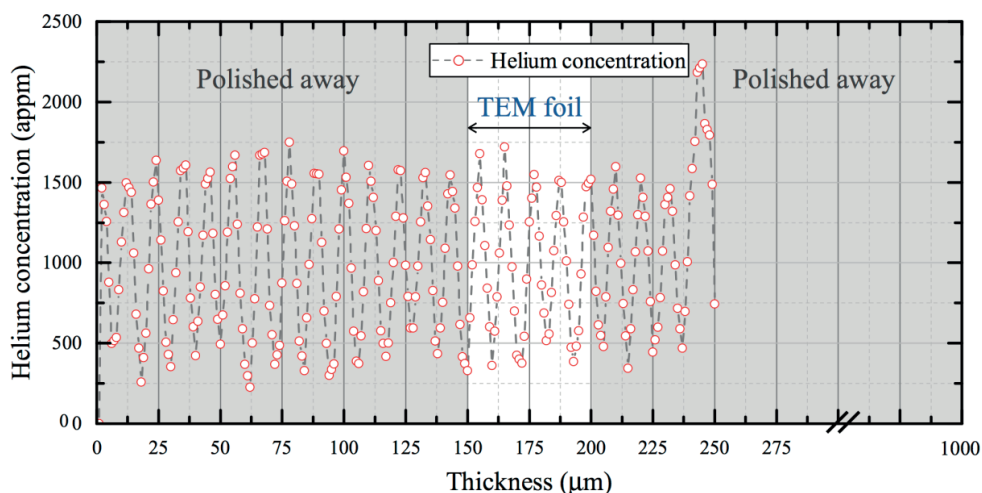
Figure 3.7. Helium concentration profile along the sample thickness. The TEM sample was prepared from the white region.

3.3.1.2 Indenter samples

After annealing, the surface of the He-plates was polished away with a final particle size of 2.5 μm (see subchapter 3.7.2) as indicated in Figure 3.8. At this point, the samples were not active so they were embedded with KonductoMet (graphite and mineral fillet, from "Buehler") at 150°C and 290 bar. A posteriori, the sample was polished away with a final particle size of 50 nm (see subchapter 3.7.1).
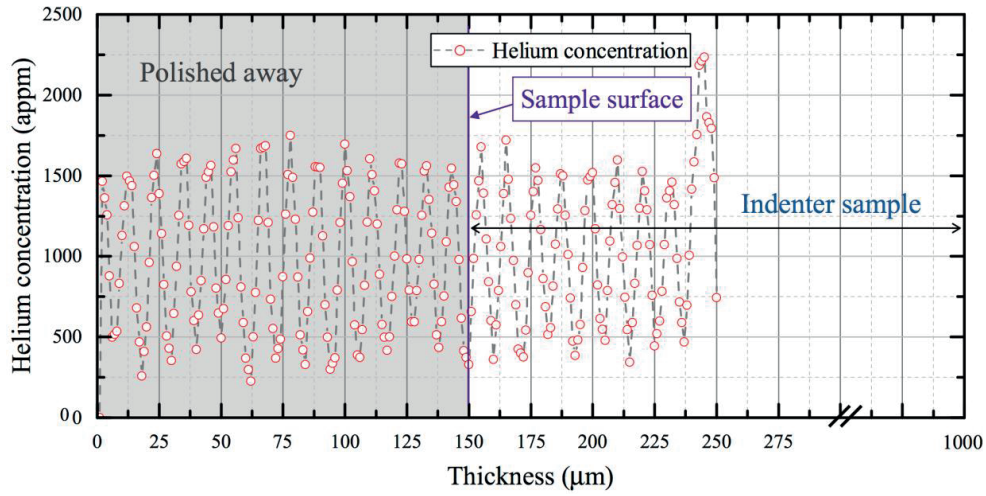
Figure 3.8. Helium concentration profile along the sample thickness. The indenter sample was prepared from the white region.

3.3.2 Tensile samples

Two geometries of tensile samples were manufactured: miniaturized (M) flat samples, for the helium implantation; and cylindrical standard (S) samples, to validate the tensile properties measured with miniaturized samples (Figure 3.9). Both samples were electro-polished after machining in order to remove any possible remaining surface hardening. However, some hydrogen uptake could occur on the sample surface during this process and that could impact the tensile properties [94].

The design of the miniaturized samples follows two important criteria: i) maximum penetration depth of the α particles and ii) similar measured tensile properties to those of standard samples. Eq. 3.4 is used to calculate the minimum thickness for which the YS represents that of the bulk material and, Eq. 3.5 is used to calculate the minimum width required to measure the bulk UTS and uniform strain (US) [189]:

$$\frac{x_c}{s} \geq 7 \qquad \text{Eq. 3.4}$$

$$\frac{x}{w} \geq 0.2 \qquad \text{Eq. 3.5}$$

where x_c is the critical sample thickness, s the grain size and w the sample width. The other dimensions are determined using relations of proportionality of standard samples according to "ASTM E8" or "DIN 50125-2004".

The critical sample thickness is imposed by the penetration depth of the helium implantation at 45 MeV (~0.25 mm) which is described above. The implantation was carried out from both sides of the sample, so the maximum sample thickness is 0.5 mm. Given that the average grain size is 52 μm, this thickness widely fulfils Eq. 3.4. As described by Eq. 3.5, the width of the sample has to be below 2.5 mm. In order to have some safety margin, a width of 2 mm was taken (Figure 3.9).
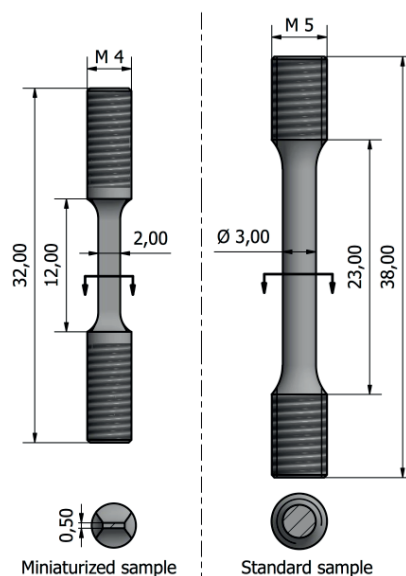
Figure 3.9. Sketches of miniaturized (left) and standard samples (right). All the dimensions are in mm.

3.4 Tensile testing machines and high-temperature water loop

3.4.1 Testing machines

Three tensile machines were used: one installed in a high-temperature water loop designed and built at PSI, which simulates LWR environment conditions for testing standard and miniaturized specimens; a second one designed and built at PSI, for testing miniaturized specimens in air; and a third one operating in air from "Roell + Korthaus", for testing standard specimens. Each machine can operate in the temperature range 25-300 °C. The detailed description of the water loop can be found hereafter (see subchapter 3.4.2).

The elongation of the samples in the tensile test machine installed in the water loop was measured with a displacement sensor connected to the pull rod above the autoclave. In the tensile machine designed at PSI, the elongation of the samples was measured with two displacement sensors (each one connected to one sample holder). In the "Roell + Korthaus" tensile machine, the elongation was measured with an extensometer placed on the sample holders. The gauge length considered for the miniaturized and standard samples was 8.1 mm and 18 mm respectively.

SSRTs were performed at a strain rate of 10^{-6} s^{-1} with the exception of one test that was performed at 10^{-7} s^{-1} in order to increase the exposure time to the environment. The strain rate of 10^{-6} s^{-1} was mainly selected as a reasonable compromise between susceptibility and number of possible tests due to time constraints. A lower strain rate usually further increases the susceptibility but then restricts the number of investigated parameters and samples.

3.4.2 High-temperature water loop

The water loop has a high pressure and high-temperature side with an autoclave containing an integrated electro-mechanical tensile machine, and a low pressure and low-temperature side for conditioning the autoclave water chemistry (Figure 3.10). Tensile tests were carried out at 90 bar ($\pm$ 1 bar) and ~290 °C ($\pm$ 5 °C).

In the high-pressure side, the system records: load, sample displacement, temperature, pressure, water flow and ECP. In the low-pressure side, the system records: pressure, temperature and water conductivity. The gases dissolved are controlled by bubbling hydrogen, nitrogen or oxygen gas through the tank. The dissolved gases content were calculated by Henry's law.

The pressure in the high-pressure side was controlled by a manual back pressure regulator located after the cooling. The high-pressure pump fed the autoclave with high purity water with the desired dissolved N_2, H_2 or O_2.

In the low-pressure side, the water was continuously purified with a set of filters, so the conductivity was always kept below 0.06 µS/cm at room temperature. The gas insertion took place on the storage tank and it was regulated by manual valves.

Three high-purity high-temperature water (~290°C) chemistries were used: NWC with 500 ppb dissolved O_2, NWC with 8 ppm dissolved O_2 and HTW with 2.2 ppm dissolved H_2.
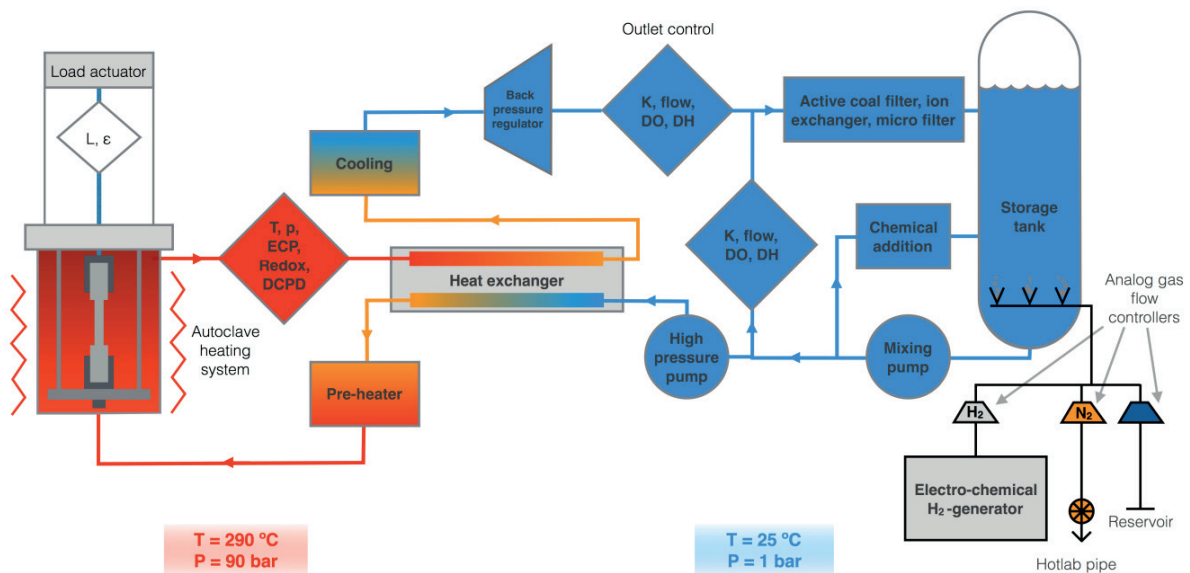
Figure 3.10. Water loop scheme. In red the high-pressure and high-temperature side and in blue the low pressure and low-temperature side.

3.4.3   Apparatus design

The tensile load frames of the water loop and of the tensile machine operating in air were designed, manufactured and built during this project. The design approaches and the calculation are described in this section.

3.4.3.1   Water loop load frame

The tensile load frame installed in the water loop has to operate in NWC or HTW. 316L AuSS has a proven performance in high-temperature water so all the structure was designed and built with this material. The only two existing parts of the tensile machine were the autoclave and the pull rod. Therefore, the design was imposed by the existing configuration and by the YS of the structural material. The complete designed assembly is shown in Figure 3.11. In the water loop, irradiated miniaturized and standard samples were tested.

Three structural rods connect the autoclave to the bottom plate. These four components are fixed. Due to the limitations of this autoclave head (dimensions and shape), two out of three structural rods were used for water recirculation. Those two rods were designed with an inner hole for water recirculation, in one rod the hole finished at the top and in the other at the bottom. The main purpose of this configuration was to improve water recirculation. Thus, the three structural rods had a different design.

In the centre of the bottom plate, there is a hole where the bottom holder sits freely. The bottom holder is fixed with a nut (made of CW 316L) without fasten in order to have up to 2 mm of free vertical move and free rotation. The bottom holder is connected to the sample holder through a pin which allows 60° rotation (±30°) around the pin axis. The other sample holder is connected to the upper holder with a pin that again allows 60° rotation (±30°) when the bottom part is not attached. The sample holders were designed to be electrically isolated from the autoclave by means of a high temperature and stress resistance ceramic (ZrO_2-stabilized with MnO). This ceramic was fixed inside the pin hole of the sample holder. Finally, the upper holder is screwed to the pull rod.

These connections allow correcting for possible misalignments produced by the manufacturing and/or construction process of the components. A standard praxis was to keep the sample free of load during the conditioning time (~5 days) at temperature, and then slowly load the sample to 50 MPa before starting the test. This procedure helped to minimize the misalignment with the pull rod.
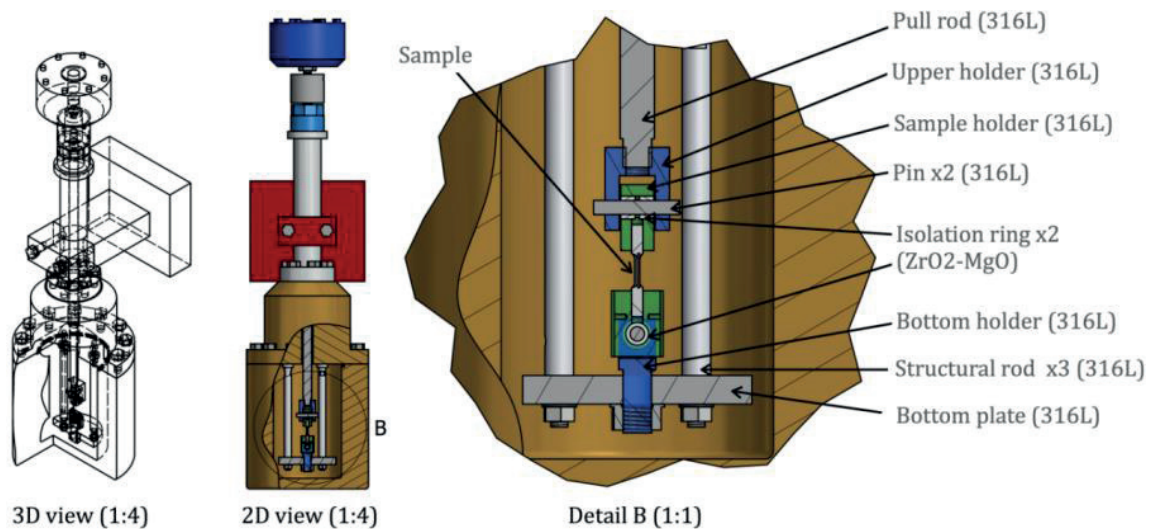
Figure 3.11. From left to right, 3D view, 2D view and detail of the tensile structure designed with Autodesk Inventor. The components designed are marked in the detail B.

3.4.3.2 Tensile testing load frame for the miniaturized specimens in air

The top plate and the pull rod were the only two existing parts of the tensile machine (Figure 3.12). The top plate has six holes: three for structural rods, two for displacement sensors and one in the centre for the pull rod. Hence, the existing configuration limited the design.

Three thick rods connect the head of the tensile structure to the top plate. The structural rods pass through the passing through holes in the upper holder, and then they are screwed to the top plate. The pull rod is screwed in the centre of the upper holder, which has a range of about 15 mm.

In the middle of the structural rods, there is a region of 10 mm where the diameter is bigger in order to block the upper and bottom holders mechanically. The bottom holder also has three passing through holes for the structural rods and it is fixed by the change of the diameter of the structural rod and two nuts at each structural rod end. Hence, this component is completely fixed during the tests. The miniaturised samples are screwed to the sample holders, which allow an easy insertion to the upper and bottom holders.
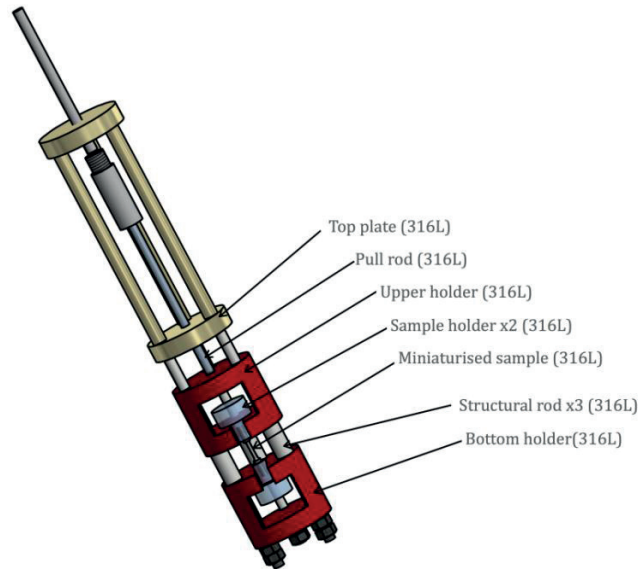
Figure 3.12. Assembly of the components designed for the SSRT machine with Autodesk Inventor.

3.5   Instrumented nanoindentation

Instrumented indenters are used to determine some mechanical properties of ion-implanted materials because they allow sampling nano-metric volumes below the surface that correspond to the implantation depth [190, 191, 192]. In this project, a fully instrumented nano-indenter, Nano Indenter MTS G200, was used from which the load versus indenter penetration depth curve is recorded. The main purpose was to correlate the hardness curves to the tensile ones and to assess the GB cohesion/strength in the He implanted samples.

The angle between the GB and the indenter geometry appears to be an issue for Berkovich and Vickers indent tips as it is shown in Figure 3.13. The plastic response of the material under indentation is not symmetrical around the indent footprint, so the GB effect cannot be properly assessed. Thereby, a spherical tip of 10 µm was used in order to avoid this problem. The tests were carried out with the continuous stiffness measurement (CSM) with harmonic displacement target of 2 nm (45Hz) and normalized load rate of 0.05 s^{-1}; defined as $(dP/dt)/P$, which is the same as $(dh/dt)/h$, where P and h are the load and the penetration depth, respectively. An indentation stress-strain (ISS) method was used to evaluate the mechanical properties of the material.
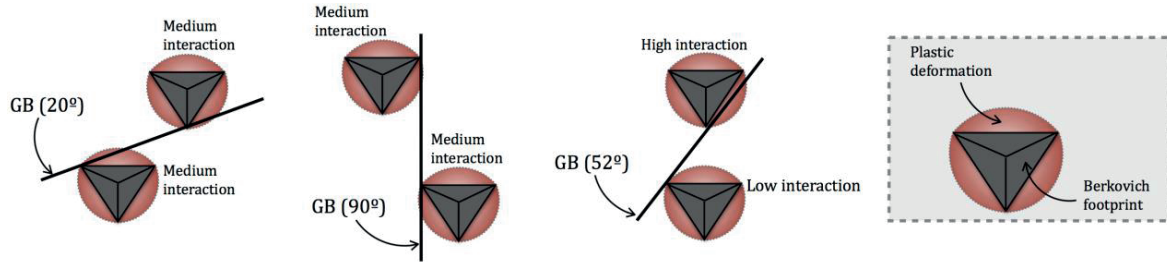
Figure 3.13. Effect of GB-indent miss-orientation for (from left to right) 20, 90 and 52° using Berkovich tip shape.

3.5.1 Continuous stiffness measurement

The instrumented indenter used is equipped with a CSM, so it allows calculating the modulus during the loading in the load-displacement curve with precision (Figure 3.14). A small harmonic load (F_0) is imposed to the increasing nominal load with a frequency, ω. The response of the harmonic displacement (h_0) and the harmonic load are recorded, and the phase shift (φ) between them experimentally found. The contact stiffness (S_c) is then determined using Eq. 3.6 [193].
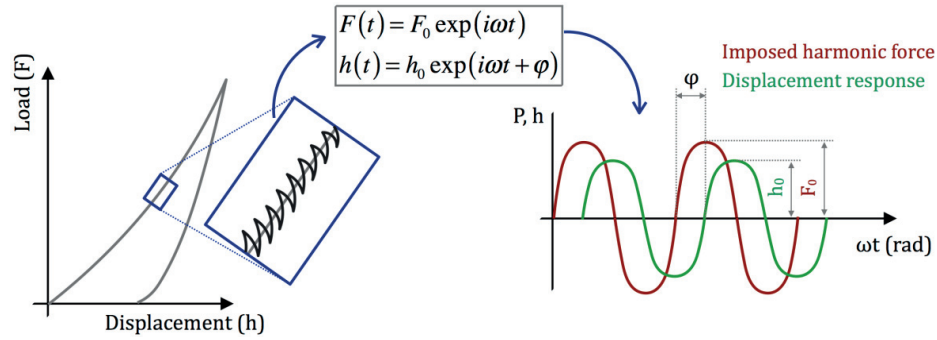
Figure 3.14. Schematic explanation of the CSM approach.

$$S_c = \left[\frac{1}{\frac{F_0}{h_0} \cos\varphi - (K_s - m\omega^2)} - \frac{1}{K_f} \right]^{-1} \qquad \text{Eq. 3.6}$$

where K_s is the support spring stiffness, K_f is the load frame stiffness and m is the mass of the indenter. The user does not need to provide the input parameters since K_s, K_f and m are known manufacturing parameters. Then, the modulus of the sample can be determined using the Hertz theory:

$$S_c = \beta \frac{2}{\sqrt{\pi}} E_{eff} \sqrt{A} \qquad \text{Eq. 3.7}$$

where β is a constant that depends on the tip geometry ($\beta = 1$ for spherical tip), E_{eff} is the effective modulus that depends on the modulus and Poisson's ratio of the tip and the sample (Eq. 3.8), and A is the projected contact area of the indent. The projected contact area depends on the penetration or contact depth (depends on the approach used), and it can be calculated during the tip calibration procedure provided by the machine supplier.

$$\frac{1}{E_{eff}} = \frac{1 - v_s^2}{E_s} + \frac{1 - v_i^2}{E_i} \qquad \text{Eq. 3.8}$$

Where E is the modulus, υ the Poisson's ratio and the subscripts s and i stands for the sample and the indenter tip, respectively ($E_{eff} \approx 183$ GPa).

3.5.2   Stress-strain approach

Instrumented indenters are typically used to evaluate the materials hardness. At shallow indents, the hardness significantly depends on the penetration depth (micro- and nanoindentation) therefore it cannot be considered a constant [194, 195]. Given that macro-indentation cannot be carried out because the average grain size is 52 μm and the remaining implantation depth is about 100 μm, the hardness can only be used to compare the results obtained at the same depth. However, the load-displacement curve obtained with the spherical tip can be used to calculate the ISS curves [196]. This should allow a comparison between the data and any other set of data regardless the penetration depth (> 30 nm). The indentation stress (σ_{ind}) and strain (ε_{ind}) are calculated as:

$$\sigma_{ind} = \frac{P}{\pi a^2} \qquad \text{Eq. 3.9}$$

$$\varepsilon_{ind} = \frac{4}{3\pi}\frac{h}{a} \qquad \text{Eq. 3.10}$$

Where P is the load, a is the projected radius of the indent footprint and h is the penetration depth. The load and the displacement are recorded by the instrumented indenter (Figure 3.15) and the projected radius is calculated with Eq. 3.7 given that $A = a^2\pi$. Thus, the ISS can be obtained for each data point. Figure 3.15 shows the stress-strain curve calculated with a spike in the elastic region of the curve. The contact point, zero-load and zero-displacement, is determined using the default "MTS Test Works software", which takes the first data point when S_c is equal or above 200 N/m. This approach typically yields an error of up to 30 nm in the contact point detection and produces the spike observed in Figure 3.15 [197]. Pharr et al. [198] reported three more sources of error with the CSM measurement system active: first, although the material experiences the maximum values, the MTS G200 records the average values during the oscillating cycle instead of the peak load and displacement values; second, the contact stiffness is calculated as the ratio of the peak-to-peak amplitudes of the load and displacement signals, although this relationship is not completely linear, and hence the contact stiffness is underestimated; and third, at small depths, the peak-to-peak load amplitude might be larger than the total force on the contact and produce tapping. The recorded and calculated errors can be corrected using the following equations:

$$P_{act} = P_{app} + \sqrt{2}\Delta P_{rms} \qquad \text{Eq. 3.11}$$

$$h_{act} = h_{app} + \sqrt{2}\Delta h_{rms} \qquad \text{Eq. 3.12}$$

$$S_{act} = \frac{1}{\sqrt{2}\pi}\frac{P_{act}}{\Delta h_{rms}}\left(\frac{1}{K}\right)^{\frac{1}{m^*}}\left[1 - \left(1 - \frac{2\sqrt{2}\Delta h_{rms}S_{app}}{P_{act}}\right)^{\frac{1}{m^*}}\right] \qquad \text{Eq. 3.13}$$

Where K is a constant that depends on the indent geometry (K=0.6524 for spherical tip), m* is 3/2 for spherical nanoindentation and the subscripts act, app and rms stands for active (maximum), apparent (raw) and root-mean-squared amplitude. Figure 3.16 shows the comparison between the apparent

and the active load and displacement, but also the load amplitude ($2\sqrt{2}\Delta h_{rms}S_{app}$). The full contact starts at a point where the actual load is higher than the load amplitude, but the precise point is difficult to determine experimentally due to the scatter of the data.
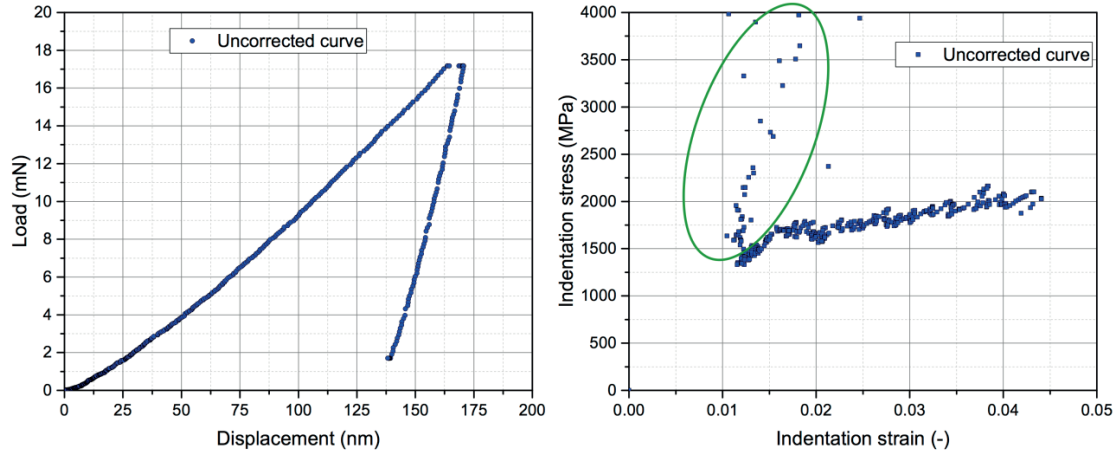
Figure 3.15. Instrumented indenter load-displacement curve (left) and its corresponding stress-strain curve (right).

The corrections proposed by Pharr et al. [198] seem to be more significant in materials with high modulus to hardness ratio (e.g. fused silica) and when using high displacement amplitudes ($h_{rms} > 2$) [198, 199]. However, Vachhani et al. [199] found that the effect of these corrections was especially important for low indenter radius (e.g. 1 μm) and showed that, the corrections applied to tests with 45 Hz and 2 nm harmonic displacements had little or no remarkable effect on load, displacement and stiffness. Moreover, while correcting for the stiffness signal, Eq. 3.13 when $P_{act} < 2\sqrt{2}\Delta h_{rms}S_{app}$, resulted in imaginary values, hence most of the initial elastic segment was lost. Vachhani et al. [199] concluded that the corrections could be skipped altogether when using 45 Hz and 2 nm harmonic displacements and relatively large indent tips.
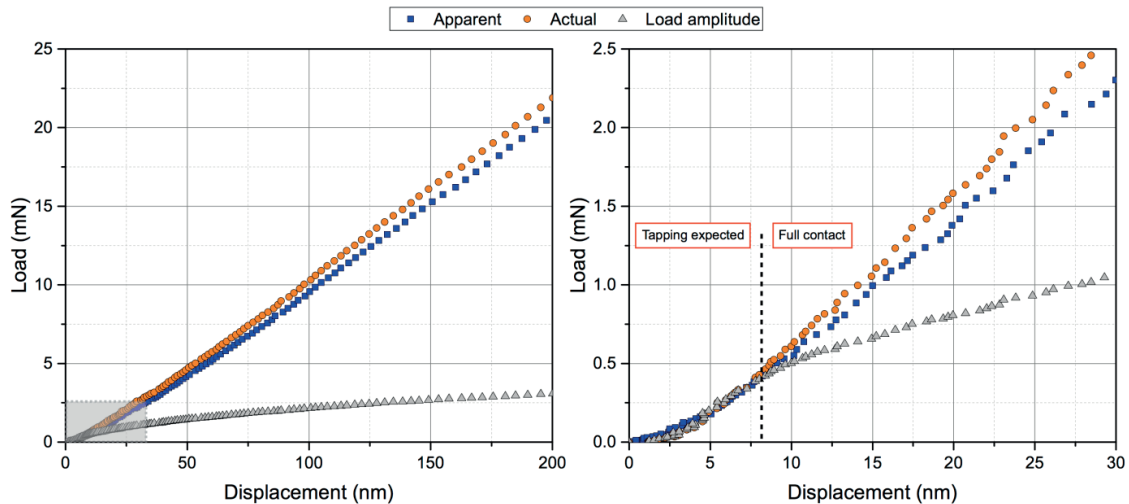
Figure 3.16. Corrected and uncorrected load-displacement curves with the calculated load amplitude (left) and magnification of the shadowed region (right) showing the experimental transition from tapping to full contact.

Here, when applying the corrections given in Eq. 3.11-Eq. 3.13, most of the elastic segment was unnecessarily lost (~10 to 25 nm) hindering the determination of the indentation modulus (E_{ind}) and the $Rp_{ind\ 0.2\%}$. For this reason, the corrections proposed by Pharr et al. [198] were not adopted. However, the effective contact point issue was addressed in order to correct for the stress-strain spikes. Kalidindi and Pathak [196] suggested looking for an effective initial contact point which minimizes the artefacts produced by the surface detection. According to Hertz theory in the elastic loading segment:

$$S_c = \frac{3P}{2h_e} = \frac{3(\tilde{P} - P^*)}{2(\tilde{h}_e - h_e^*)}$$
Eq. 3.14

where $\tilde{P}$, $\tilde{h}_e$ and S_c are the load, the elastic penetration depth and the contact stiffness recorded by the instrumented indentor and P^* and h_e^* are the values of load and elastic penetration depth at the actual point of initial contact.

Rearranging Eq. 3.14 one can obtain a linear relationship between the recorded data and the contact stiffness, which slope is $-h_e^* \frac{2}{3}$ and intercept with the y axis P^*:

$$\tilde{P} - S_c \tilde{h}_e \frac{2}{3} = P^* - S_c h_e^* \frac{2}{3}$$
Eq. 3.15

The linear relationship is represented in Figure 3.17. The regression of the curve has to be determined in the elastic region of the load-displacement curve, but avoiding the initial artefacts produced by the surface conditions. The problem arises in the selection of the pure elastic segment when the tapping information is not used (Figure 3.16). To solve this issue and to deal with each particular solution, an iterative process was performed in order to find the elastic segment that provided the lowest independent value of the regression of the elastic ISS curve. An elastic segment length of 6 μm was imposed, and for each indent; 198 elastic segments were used to find the stress-strain curves, the first starting at a penetration depth of 0.5 nm (ending at 6.5 nm), and the last at 20 nm (ending at 26 nm). Each elastic segment was used to calculate the effective contact point as shown in Figure 3.17.
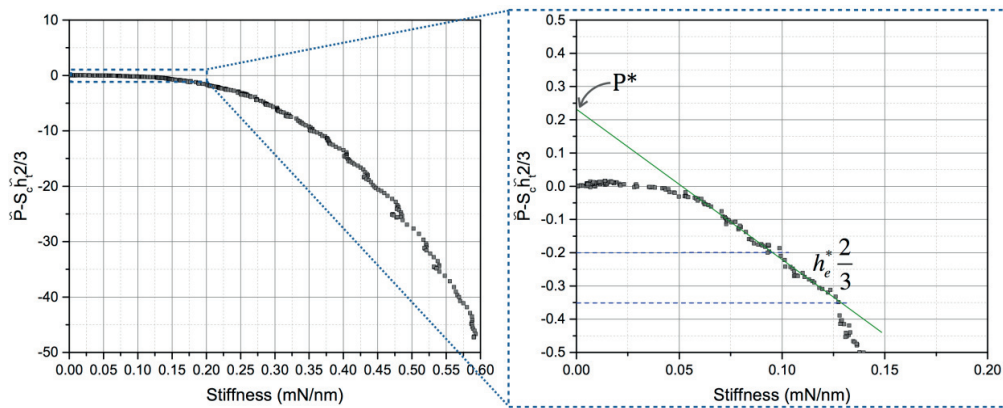
Figure 3.17. Representation of Eq. 3.15 (left) and elastic correction detail (right) for determination of the effective load-displacement initial point.

The correction calculated for each elastic segment, as shown in Figure 3.17, was applied to the corresponding raw load-displacement curve. Three examples of the resulting ISS curves are shown in Figure 3.18. The elastic regression was calculated from 100 to 500 MPa in SA and PIA samples and

from 100 to 1000 MPa in the As-implanted and CW samples. A stress-spike or a high scatter at low strain was observed when the selected elastic segment started at too shallow depths (case a Figure 3.18), indicating that the correction was insufficient to remove the contact artefacts (tapping and/or surface conditions). On the other hand, when the elastic segment started at too deep depths (case c Figure 3.18), part of the plastic deformation was used for the calculation of the indentation modulus ($E_{ind.}$), thus reducing its value significantly. In both cases, either the independent value of the regression in the elastic part was too far from the origin or the modulus was too small. The optimal solution (case b Figure 3.18) was selected to be the one that passed closest to the origin, among the 198 solutions, and with a modulus within 150 and 240 GPa.
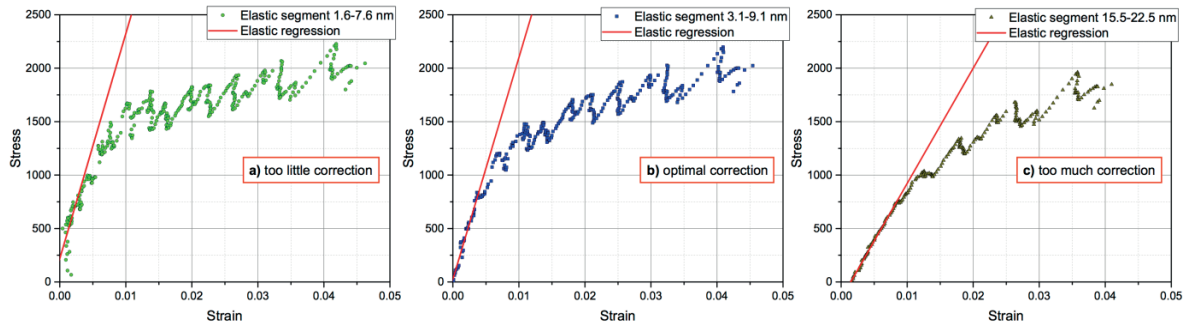
Figure 3.18. Stress-strain curves obtained for three different elastic segments showing (a) too little correction, (b) optimal correction and (c) too much correction.

According to Vachhani et al. [199], and the results of the method presented here, the correction to the raw data proposed by Pharr et al. [198] had a lower effect on the ISS curves than in the raw data. It is likely that the correction of the individual signals compensates each other.

3.5.3   Indentation details

The indenter samples (see subchapter 3.3.1.2) were marked using carbon deposition with the "NVision 40 FIB-SEM" as it is shown in Figure 3.19. The marks were separated 100 µm in the vertical direction and 150 µm in the horizontal direction, thus producing window sizes equivalent to the visible image size in the optical microscope installed in the instrumented indenter. Given that the grain size is quite big (~52 µm), seven regions were marked, each one consisting of two windows of 150×100 µm^2.

The carbon marks and the symbols below each region were used to identify the regions during and after the electron backscattered diffraction (EBSD) map (Figure 3.19). The grain orientation was used to identify and to select the appropriate GB for performing the indentation. A matrix of 40-50 indents was carried out for each analysed GB. The nano-indent centres were separated 10 to 12 µm. The indent penetration depth was about 180 nm, this corresponds to an indent footprint below 4 µm in diameter using a spherical tip of 10 µm. This penetration depth allowed having from three to five rows of indents crossing the same GB, so increasing the number of indents close to the GB.
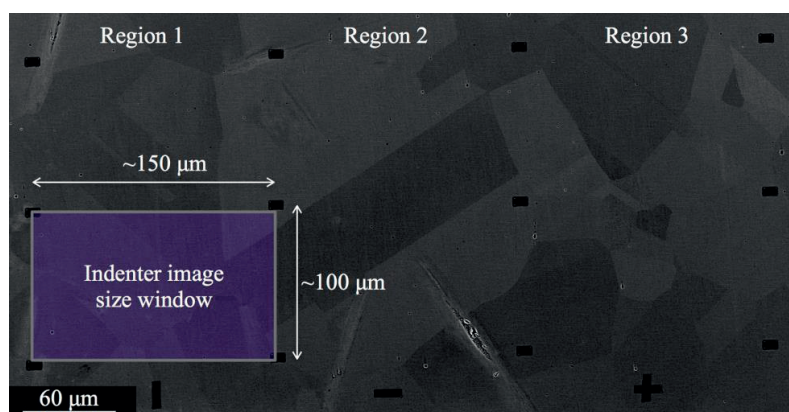
Figure 3.19. SEM image obtained with the QBSD detector at 20 kV showing three regions marked with carbon deposition using FIB. The purple window corresponds to the image size window observed in the instrumented indenter.

3.6 Scanning and transmission electron microscopy

The electron microscope analysis was focused on understanding the fracture morphology, the surface appearance, the deformation microstructure and the He bubble size and location. The fracture morphology and the surface appearance were analysed with SEM, whereas the TEM was used to study the deformation microstructure and the He bubble size, location and density.

3.6.1 Scanning electron microscope

Metallurgical investigations were performed with the "NVision 40 FIB-SEM" at 15kV. The investigation was conducted on the fracture surface in order to determine the fracture morphology/mode (IG or TG) and the RA. Furthermore, a longitudinal cross-section of the non-implanted samples was used to characterize the crack morphology and to obtain information on the initiation and propagation mechanisms. The longitudinal cross-section of the samples was embedded and polished down with a final particle size of 0.5 μm (see subchapter 3.7.1). Some of the samples showing cracks in the sample surface were etched with V2A-Beize in order to characterize the fracture morphology.

3.6.2 Transmission electron microscope

The TEMs used were the JEOL 2200, the JEOL 2010 and the FEI Talos F200X, all operating at 200kV. TEM samples were prepared by mechanical polishing to a thickness of 100 μm with a final particle size of 2.5 μm (see subchapter 3.7.2) followed by JET electro-polishing to perforation at -20°C and 25 V with 5% perchloric acid and 95% methanol using Tenupol-5. The final sample thickness was calculated to be between 10 and 300 nm. All the TEM micrographs had 4096×4096 pixels with 16 bit per pixel.

The TEM samples were prepared from the gauge length of the tested samples or from the specimens cut from the He-plates. The He bubble population (size and density) and location were determined using the through focal series imaging technique (typical bubble resolution of about 1 nm radius) and the deformation microstructure was studied with diffraction contrast mechanisms, 2-beam dynamical or 2-beam kinematical conditions. To calculate the bubble density required the knowledge of the sample thickness, so the electron energy loss spectroscopy (EELS) technique was also used. The GB

segregation was studied using energy dispersive X-ray spectroscopy (EDX). The approaches taken to determine the helium bubble distribution are also described here.

3.6.2.1 Diffraction contrast

The strain field of the defects distorts the atom lattice structure locally. The resulting image characteristics were observed using two techniques:

- 2-beam dynamical conditions. The foil is tilted in order to have the transmitted beam and the first diffraction spot on the diffracted plane of interest (Figure 3.20). The images can be taken in bright or dark field, but the later has generally higher diffraction contrast. This technique is particularly well suited to investigate strain fields of small clusters.

- 2-beam kinematical conditions. The foil is tilted in order to have the non-diffracted beam and the first diffraction spot slightly away from the Bragg condition, so the image loses most of its dynamical features (Figure 3.20). This technique is particularly well suited for imaging accurately the size of the clusters, i.e. with the minimum strain field contrast width created by the clusters.
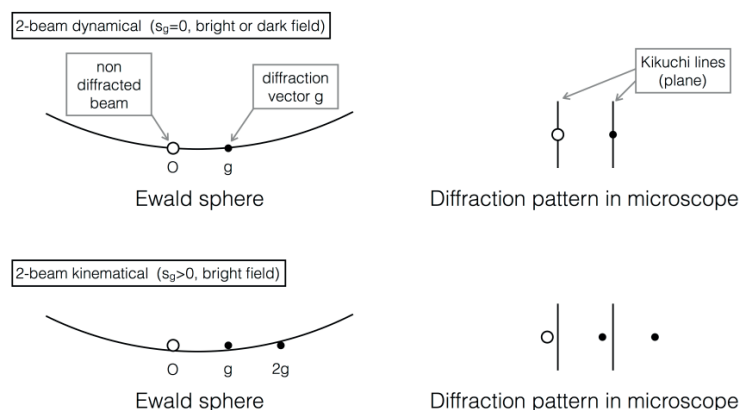
Figure 3.20. Schematic representation of the different diffraction conditions used in diffraction-contrast imaging in this project: 2-beam dynamical conditions (top) and 2-beam kinematical conditions (bottom). In each case, the Ewald sphere is sketched on the left-hand side, and a schematic diffraction pattern showing the position of the relevant Kikuchi lines on the right side. Adapted from ref. [200].

3.6.2.2 Focal series imaging technique

This imaging technique is based on phase contrast. The specimen produces changes in the phase of the electron wave when it passes through. This phase variations produce a phase shift, which induces amplitude variations via the Scherzer phase shift produced by the microscope, over which the operator has control by defocusing [201]. The contrast arises from the change in mean inner potential between the void and the matrix. The phase shift can be manipulated with the degree of under- and over-focus of the objective lenses. The best imaging mechanism is in 2-beam kinematical conditions, where voids appear white surrounded by a dark fringe or dark surrounded by a white fringe in under- or over-focus, respectively.

Bubble observation and size determination

Rühle and Wilkens [202] reported a significant change of the measured bubble diameter in under-focus condition when they measured the inner and outer diameter of the first black fringe in different

bubble sizes. They found that the inner diameter of the first black fringe gave the best diameter estimation in bubbles above 2 nm. However, the effect of defocusing in experimental observations was never explored. Here, the effect of defocus was studied, not changing the bubble diameter but the defocus level. The bubbles can be identified in focus thanks to the mass contrast if the sample thickness is smaller than 20 times its diameter [200]. For this reason, a big bubble (r~13 nm) was used to calculate the effect of defocusing in 100k and in 40k magnifications. The real bubble diameter was measured in focus and used to normalize the measured radius in the different defocus conditions.

The measurements of the radii were performed on the inner and outer black (under-focal) and white (over-focal) bubble fringes (Figure 3.21). The measured radii can change dramatically with over- and under-focus conditions but, it strongly depends on the magnification. At 100kx, small error (< 5%) can be obtained with an under-focus below 1 μm or an over-focus below 0.7 μm. At 40kx, these limits increase to 2 μm and 1.1 μm for under- and over-focus imaging, respectively. Hence, lower magnification is more tolerant to higher phase contrast. Typically, about ~4-5 pixels are needed to clearly distinguish the bubble fringe. At 40kx, the pixel size is about 0.32 nm, whereas at 100kx is about 0.13 nm. The bubble fringe increases with increasing the defocus. The smaller is the pixel size, the easier it is to see the contrast change in the image; thus lower defocus is needed at higher magnifications to achieve a similar level of bubble distinction. However, higher magnification produces higher convergence angle, i.e. the beam is less parallel, and therefore the defocus effect is higher. This could be corrected by increasing the alpha selector, keeping the brightness constant when increasing the magnification or inserting a smaller condenser aperture. In this study, for magnifications above 100kx, a smaller condenser aperture was used. The alpha selector was not used because it is only available in JEOL, so the results can be compared to other instruments.
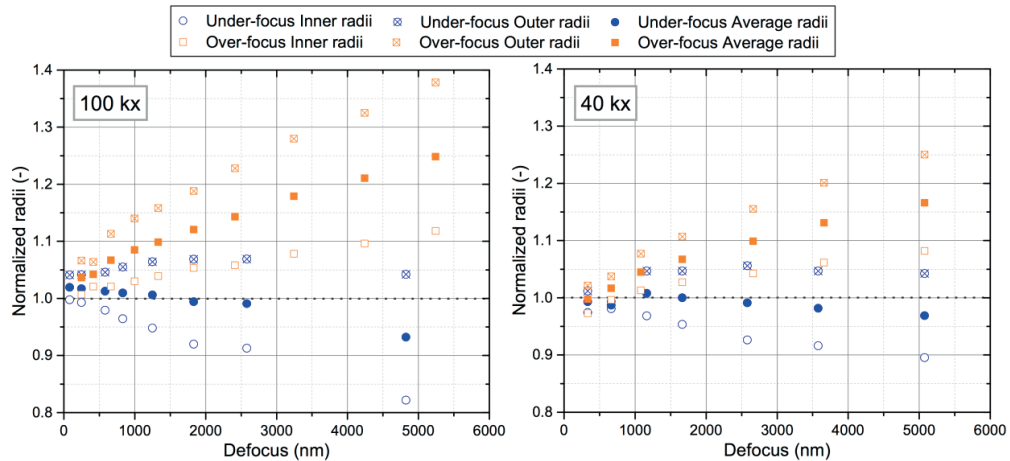
Figure 3.21. Normalized radii measured with different phase contrast conditions at 100 kx (left) and at 40 kx (right).

The best radii estimation is, in both cases, the average radii obtained in under-focal conditions which could be obtained measuring the radii in the centre of the black fringe. Surprisingly, the outer bubble radii in under-focal imaging and the inner radii in over-focal imaging give a reasonable error (< 5%) up to a defocus of 3-5 μm but these results might not be applicable at smaller bubble sizes.

Different defocusing conditions with 100 kx magnification from Figure 3.21 are shown in Figure 3.22. Low defocusing (<0.4 μm) does not allow clear identification of small bubbles (r < 3nm) and high defocusing might undergo significant error of the bubble size as it is shown in Figure 3.21. In this

example, Figure 3.22 shows that the optimum measurement is obtained with an under-focus of about 0.6 μm at 100 kx, which would give an error of about 2.5%. According to Schaublin simulations [203], a decrease of defocus in small bubble sizes improves the spatial resolution of the bubbles, so small bubbles can be significantly overestimated with high defocus.
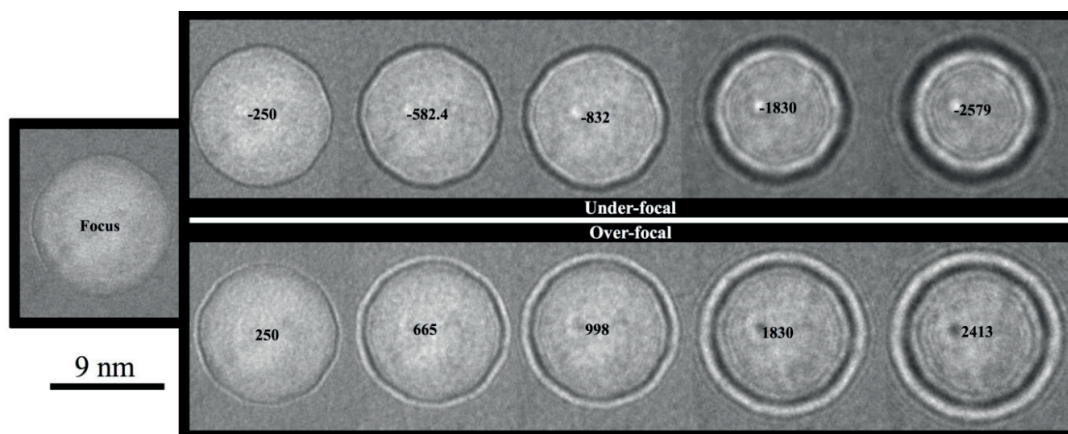
Figure 3.22. Phase contrast effect in nm (indicated inside the bubles) to the bubble fringes in over and under-focal imaging with 100 kx magnification.

The bubbles in the grain interior (GI) and on the GB were imaged in under-focal conditions and carefully brushed away until the inner black ring using ImajeJ software. According to Figure 3.21, the measured error was assumed to be within 5 %. This approach (manual) allowed distinguishing and counting superposed bubbles. The over-focal micrographs were used to cross-check the existence of the bubbles. The statistical analysis of each micrograph was also carried out with ImageJ. The standard deviation of the bubbles distribution was significantly bigger than the standard deviations associated with the measurement of the bubbles and to the defocus so it was not considered. The bubble size after annealing at 650°C was close to the resolution limit of the phase contrast technique (~2 nm) [202, 200, 203]. The bubbles were clearly distinguished in the TEM micrographs (reliable bubble density), but their size was not; for this reason, the biggest bubbles at 650°C were used to estimate the maximum average size and their measurement error was estimated from the pixel size instead of the measurement error; therefore, the resulting average radii at this temperature should be taken with care. Moreover, the oxide formed during electro-polishing might hinder the correct measurement of the bubbles as suggested for other authors [204, 205].
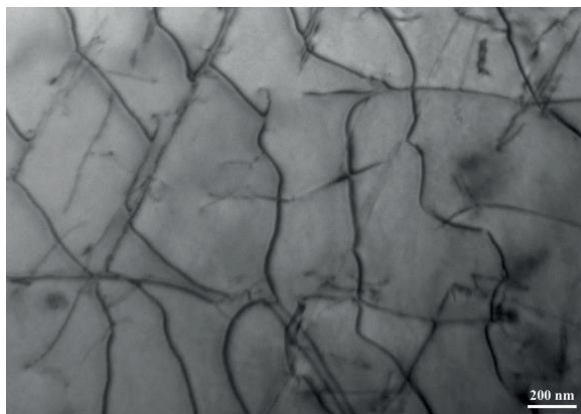
Figure 3.23. Bright field 2-beam dynamical {2$\bar{2}$0} micrograph of a SA sample showing many dislocation
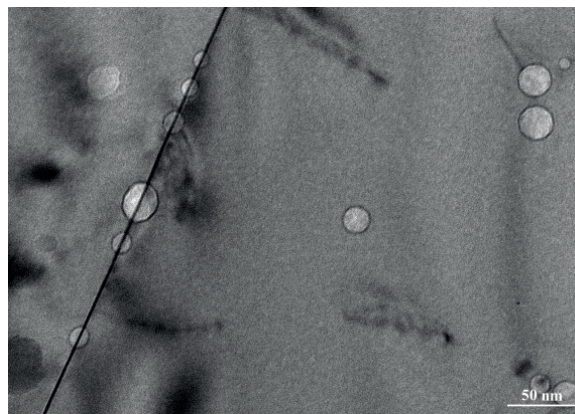
Figure 3.24. Detailed GB and matrix bubbles geometry in a plate implanted with 1000 appm He and annealed

lines in the matrix.   at 900°C for 1h.

In general, for lower and higher magnification, higher ($\Delta f \approx \pm 3$ μm) and lower defocus ($\Delta f \approx \pm 0.5$ nm) were used for the measurements, respectively. The GI on the 316L bulk material contained a lot of dislocation lines and it was not possible to find regions free of dislocations (Figure 3.23). Moreover, for simplification purposes, the bubbles in the GBs are considered to be spherical (Figure 3.24).

3.6.2.3 Electron energy loss spectroscopy

The electron beam generated in the TEM gun interacts with the atoms of the TEM sample when they pass through it. This interaction can produce a loss of energy in the electron or not, what is called inelastic scattering and elastic scattering, respectively (Figure 3.25). Elastic scattering is produced when the electron beam interacts with the positive potential inside the electron cloud [206], the electrons are deflected, but a negligible amount of energy is transferred to the nucleus, i.e. negligible amount of energy is lost by the electron. Most of the electrons undergo elastic scattering with the TEM sample which produces a zero loss peak (ZLP) in the EELS spectra (Figure 3.26). However, a small part of the electron beam is scattered inelastically by the electron cloud of the atom leaving the atom in an excited state. The atom excitation can be produced by the ejection of an inner-shell electron or of an outer-shell electron (Figure 3.25). The former has higher binding energy, so the incident electron loses at least the binding energy of the electron and this inner-shell electron is ejected from its orbital. In the EELS spectra, this energy loss produces the atom core-peak which is characteristic of each element and electron orbital (Figure 3.26). Outer–shell electrons are less bound to the atom so the incident electron losses less energy and produces what is called the plasmon resonance peak (Figure 3.26).
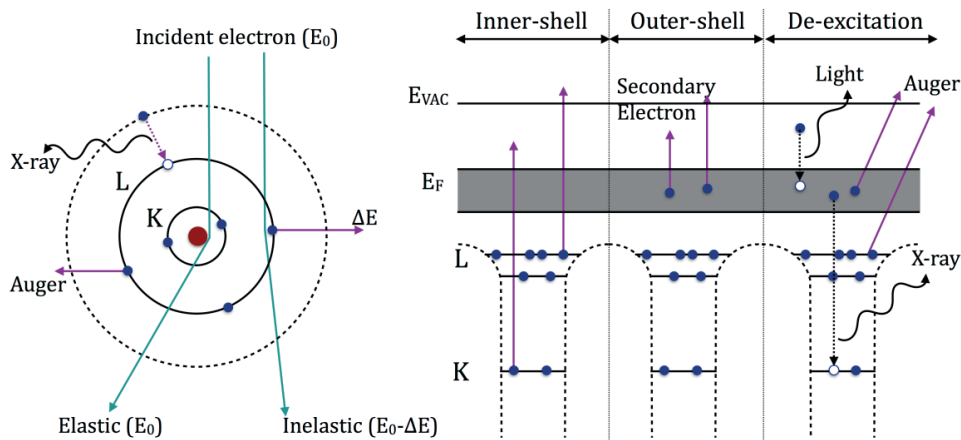
Figure 3.25. Schematic of elastic and inelastic scattering due to the interaction of the electron beam with an atom (left) and the diagram of inelastic excitations, X-ray, photon and Auger emissions with respect to different energy levels (right). E_F is the Fermi level and E_{vac} is the vacuum energy.

The EELS spectrum was not used in this project, but its knowledge is fundamental for the thickness determination and the bubble density calculation.
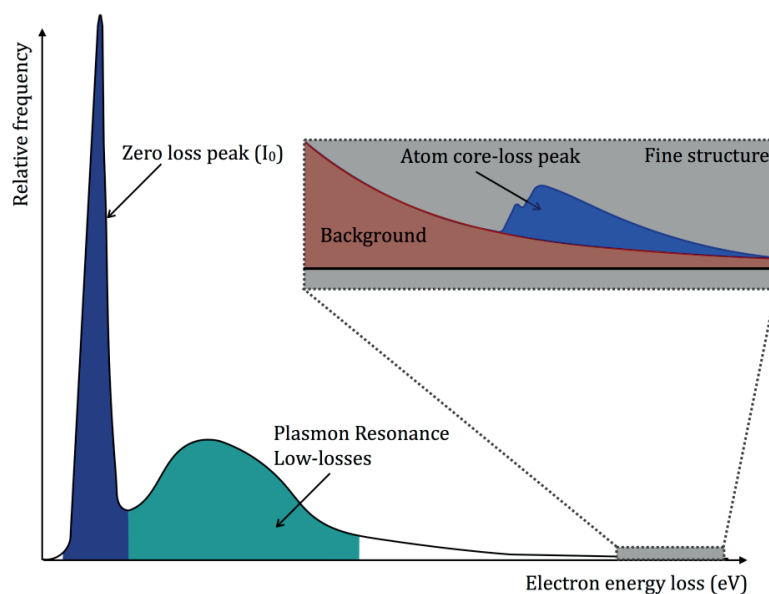
Figure 3.26. Schematic of the EELS spectrum containing the ZLP, the plasmon losses and a detail of an atom core-loss.

3.6.2.4 Energy-dispersive X-ray spectroscopy

The EDX is an analytical technique that analyses the X-rays emitted by the sample when it is bombarded by an electron beam. If the inelastic scattering of the electron beam ejects an inner-shell electron, an electron hole is created where the electron was. Eventually, an electron from an outer higher energy shell fills the hole, and the difference in binding energy is emitted by a characteristic X-ray (Figure 3.25). In some cases, this difference on energy might be coincident with the binding energy of an outer shell electron and then this outer shell electron is emitted (Auger emission in Figure 3.25).

Four types of X-rays can be generated: characteristic X-rays, which have a specific energy peak for each material and electron shell; bremsstrahlung X-rays, which are produced by deaccelerating of the incident electron beam when passing through the sample; spurious X-rays, which are produced by uncollimated electrons outside the region of analysis; system X-rays, which come from other parts of the microscope (e.g. backscattered electrons). The characteristic X-rays have energies within a natural linewidth of 1-5 eV, but due to electronic limitations, the typical linewidth observed is 100-150 eV. Moreover, the bremsstrahlung X-rays produce a continuous non-characteristic background that has to be removed from the energy-dispersive spectroscopy.

EDX is an easy and quick routine suitable for high energies, so it is not good for light elements (< 20 Z) and has low energy resolution (100 eV). On the other hand, EELS is more difficult to interpret, has higher resolution (1 eV) and is suitable for energies below $\sim$3 keV [207].

3.6.2.5 Thickness measurement

Two images of the same region were taken, an unfiltered image and an image with a mechanical slit that allowed forming the image only with the elastic scattered electrons, i.e. the ZLP electrons. Thus, each pixel of the sample had the number of counts (electrons), in one case with all electron energies and in the other only the ZLP electrons. The logarithmic ratio between the area of the whole spectrum (I_t, pixel counts in the normal image) and the ZLP area (I_0, pixel counts in the ZLP image) is

proportional to the ratio between the sample thickness (x) and the effective electron mean free path (λ) [208, 209]:

$$\frac{x}{\lambda} = \ln\left(\frac{I_t}{I_0}\right)$$

Eq. 3.16

Before applying Eq. 3.16, the background should be subtracted from the spectrum, i.e. the dark current spectrum acquired before or after the energy loss spectrum. The effective mean free path depends on the collection semi-angle (β). Reasonable values (10% error) of the effective mean free path can be calculated in function of incident electron energy (E_0), collection semi-angle and a parameter that depends on the chemical composition of the specimen (E_m) [209, 210]:

$$\lambda \approx \frac{106F\left(\frac{E_o}{E_m}\right)}{ln\left(\frac{2\beta E_0}{E_m}\right)}$$

Eq. 3.17

Where λ is in nm, E_0 in keV, β in mrad, E_m in eV and F is a relativistic factor that depends on the incident energy (0.618 for E_o= 200 keV). E_m hinges on the effective atomic number, $E_m \approx 7.6Z_{eff}^{0.36}$, which can be calculated according to the Lenz model:

$$Z_{eff} = \frac{\sum_i f_i Z_i^{1.3}}{\sum_i f_i Z_i^{0.3}}$$

Eq. 3.18

Where f_i is the atomic fraction of each element i of atomic number Z_i. In this case, Z_{eff} was calculated with the elemental composition 65.6Fe-17.7Cr-12.4Ni-2.5Mo-1.8Mn (wt.% main elements in Table 3.1) resulting in an effective atomic number of $\sim$26. The effective mean free path was 110 and 102 nm for 7.6 and 11.4 mrad collection semi-angles, respectively.
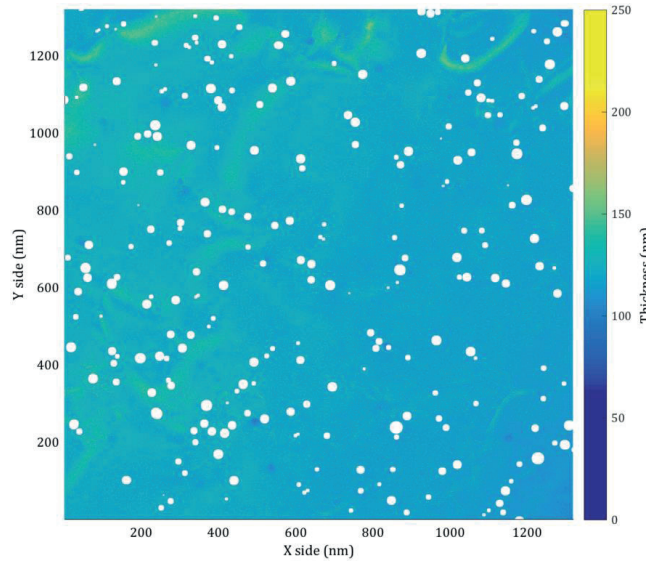
Figure 3.27. Absolute thickness map obtained from a He implanted sample with 1000 appm and annealed at 850°C during 1h. The He bubbles were removed and appear in white.

A typical absolute thickness map is shown in Figure 3.27. It can be seen that the bubbles are removed from the images in order to prevent their effect on the thickness measurement. The presence of He-

bubbles reduces the electron beam interaction on its column so the mean free path is bigger than the value used and the measured thickness would be erroneously thinner. The average thickness is calculated averaging the thickness calculated in each pixel of the image.

3.6.2.6 Bubble density calculation

TEM micrographs were performed in areas with foil thickness between 10 and 300 nm. The intersection of bubbles with the foil surface, the small cluster visibility in thick areas and the quality of the foil can be checked by analysing the surface bubble density versus the foil thickness. The slope of the linear regression, passing through the origin, between the areal densities and their thicknesses for a given temperature is the bubble density [211]. Figure 3.28 shows the correlation found in the implanted plates with 1000 appm He and annealed between 750°C and 1000°C. According to the defocus effect shown in Figure 3.21 and Figure 3.22, and the thickness of the samples studied (Figure 3.28), the bubble size variation with the thickness and defocus at a given magnification is below 0.5%, and therefore negligible.
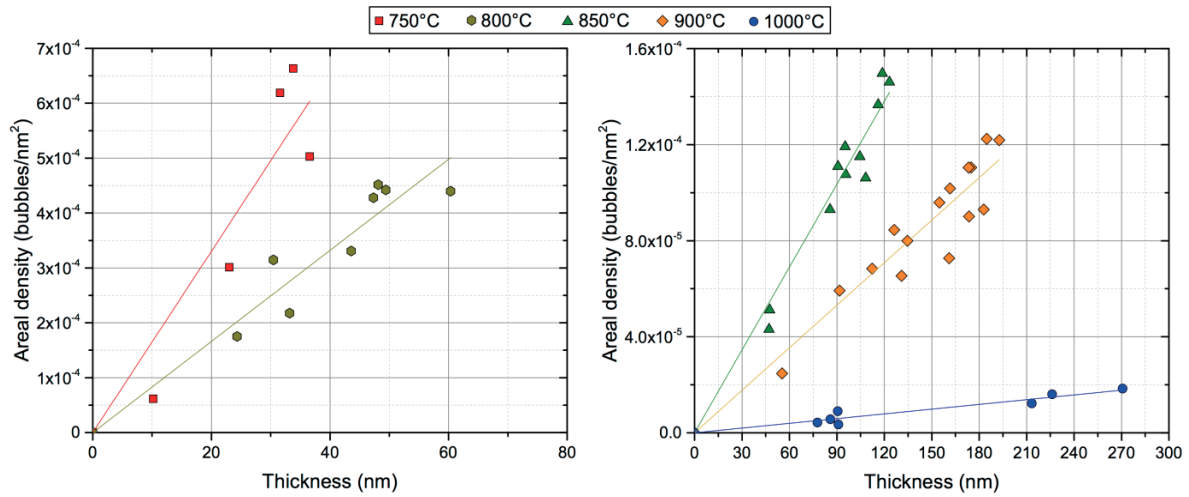
Figure 3.28. Linear correlation between the bubble areal densities versus TEM foil thickness for plates implanted with 1000 appm He. The slope of the regression at each temperature is the bubble density.

3.6.2.7 Bubble average spacing and GB coverage and helium concentration

The bubble average spacing (L) and the GB coverage (α) were calculated by the following equations.

$$L = \sqrt[n]{1/N_i} - 2r \qquad \text{Eq. 3.19}$$

$$\alpha = N_s \pi r^2 \qquad \text{Eq. 3.20}$$

Where r is the bubble radii in nm, N_i is the areal (i = s) or volume (i = v) bubble density in bubbles/nm^n and n is 2 or 3 for the areal and volume density, respectively. The concentration of He atoms contained in an average bubble size at a given temperature was calculated using the equation of state (EOS) described below Eq. 3.21.

$$\frac{P}{kTn_p} = z \qquad \text{Eq. 3.21}$$

Where P is the pressure in Pa, k is the Boltzmann constant (1.38×10^{-23} J/K/atom), n_p is the He density in atoms/bubble/m³ and z is the compressibility factor. Trinkaus in ref. [212] described the calculation of the compressibility factor for He fluid:

$$z = \left(1 - n'_p v_l\right)\left(1 + n'_p v_l - 2\left(n'_p v_l\right)^2\right) + \left(1 - n'_p v_l\right)^2 n'_p B(T) \\ + \left(3 - 2n'_p v_l\right)\left(n'_p v_l\right)^2 z_l - 50\left(1 - n'_p v_l\right)\left(n'_p v_l\right)^2$$

Eq. 3.22

Where n'_p is the He density in atoms/bubble/Å³, v_l is the fluid volume upon freezing in Å³, z_l is the compressibility factor on freezing and B(T) is the first two terms of the adjusted virial expression of the compressibility factor in Å³:

$$v_l = 56 T_m^{-1/4} \exp\left(-0.145 T_m^{1/4}\right)$$

Eq. 3.23

$$z_l = 0.1225 v_l T_m^{0.555}$$

Eq. 3.24

$$B(T) = 170 T^{1/3} - 1750/T$$

Eq. 3.25

Where T_m is the melting temperature of the material in K and T is the annealing temperature in K. If z is equal to 1, the ideal gas EOS is obtained. Figure 3.29 shows that for radii above 100 nm or, what is equivalent for bubbles in equilibrium, pressure below 50 MPa the behaviour can be assumed to be ideal.
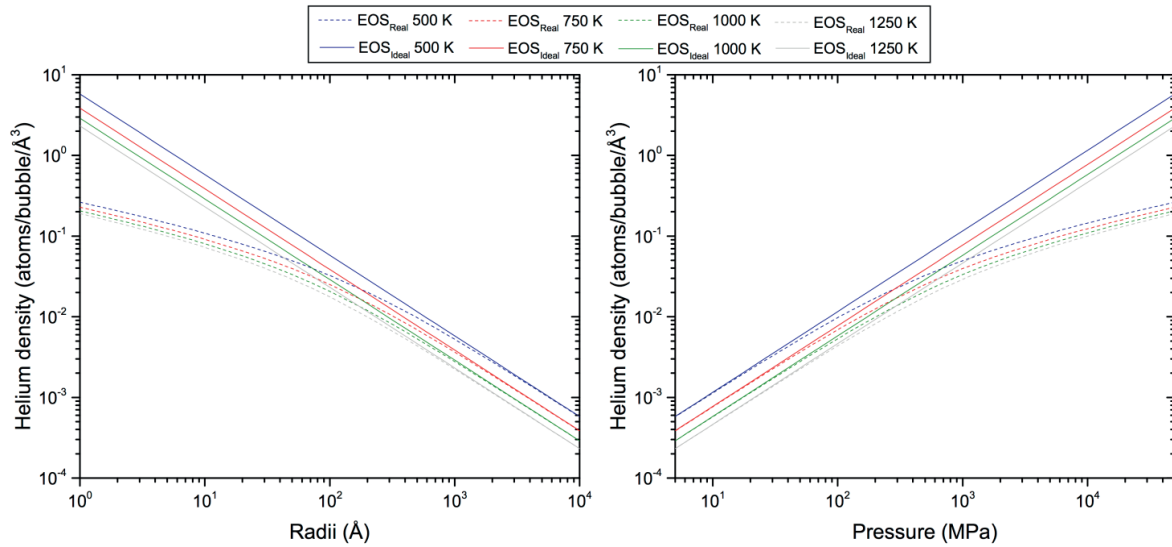
Figure 3.29. Helium density versus radii (left) and pressure (right) for various temperatures with the ideal EOS and the real EOS from Eq. 3.21.

The pressure of the bubbles for each analysed condition is calculated assuming to have the He bubbles in equilibrium with the surface free energy (γ, in N/m). Therefore, if the helium concentration with the average bubble size calculation gives values below the implanted concentration either, the bubbles are over-pressurized or some bubbles are too small to be observed or both.

$$P = \frac{2\gamma}{r}$$

Eq. 3.26

In most of the studies presented earlier [213, 214], the surface free energy is considered to be constant for the whole range of temperatures. However, the effect of the surface energy on the calculated helium density can vary the He density values up to 30% (Figure 3.30), so the surface free energy was assumed to change as reported by Murr et al. in 304L [215]:

$$\gamma \simeq 3.92 - 0.0017T$$ Eq. 3.27

The atom density (n_p) found equalling Eq. 3.21 to Eq. 3.22 is used to obtain the He concentration (C_{He} in Eq. 3.28, appm) in the samples assuming that the entire He is contained in the bubbles.

$$C_{He} = \frac{4r^3 \pi n_p C_b}{3\rho_A} 10^6$$ Eq. 3.28

Where C_b is the bubble density in bubbles/m³ and ρ_A is the 316L atomic density (8.45×10^{28} atoms/m³).
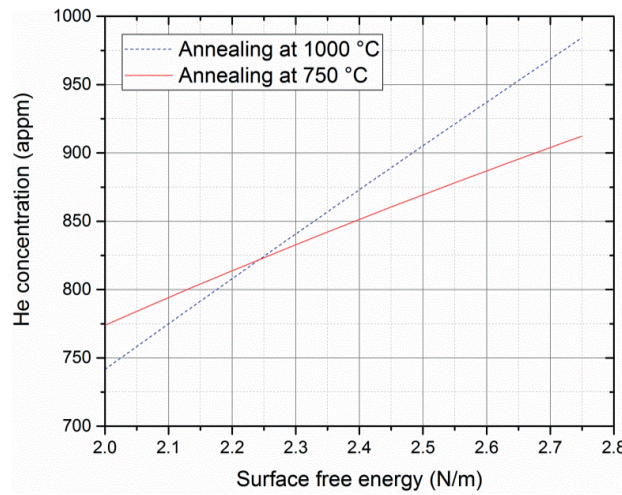
Figure 3.30. Variation of the calculated He concentration versus the surface free energy with PIA at 750 and 1000°C for 1h.

3.7 Sample polishing

The sample preparation for post-test analysis is a key factor to have reproducible and reliable results. Here, the main procedure for the sample polishing is described. Some techniques require part of the polishing and other techniques require the whole procedure. This is always specified in the description of technique with the diamond particle size, that is, the last step reached.

3.7.1 Polishing non-active samples

Each polishing step with abrasive grinding took about 3 minutes. If the surface of the sample was not flat, the polishing started with P320 (particle size, p~46.2 μm) otherwise it started with P500 (p~30.2 μm). The polishing continued with the grid P1200 (p~15.3 μm) and finished with P2500 (p~8.4 μm). These grinding papers were FEPA P-grades.

The sample preparation proceeded with a polishing suspension. The liquids had either 6, 3 or 1 μm particle size. Each particle size had its own polishing tissue and it was carried out for at least 3 minutes from the biggest to the smallest particle size. Once completed the steps above, the sample was placed in the VibroMet with a polishing suspension of particle size 50 nm (MasterPrep-Alumina polishing

suspension). This last step took a minimum of 4h and a maximum of 12h, depending on the final use of the sample.

3.7.2   Polishing active samples

Again, each polishing step with abrasive grinding took about 3 minutes. After the tensile tests, the gauge surface of the miniaturized samples was relatively smooth so the first polishing step was performed with smaller particle size. The polishing already started with P1200 (~15.3µm), continued with P2400 (~6.5µm) and finished with P4000 (~2.5 µm). In this case, the gridding papers were European P-grade.

Chapter 4 Results and discussion

This chapter is divided into seven subchapters presented and discussed separately. The first one deals with the sample miniaturization and its validation against the standard sample. The miniaturized sample was designed for the He implantation and was validated at different temperatures in air and water environments. The second subchapter presents the He evolution after annealing at different temperatures, which provides an understanding of how the bubble size distribution, density and location evolve. The third subchapter studies the GB segregation before and after He implantation. The fourth subchapter analyses the He effects on IASCC in as-implanted SA, CW and PIA samples. The fifth subchapter deals with the He hardening contribution to the total irradiation hardening in function of the bubble size and density. The instrumented nanoindentation results are reported in the sixth subchapter, where the nano-hardness data are compared with the tensile test results. Finally, the last subchapter is devoted to general discussion of the PhD topic.

4.1 Miniaturized sample validation

The validation of the miniaturized tensile sample was performed by comparing the tensile results, the fracture surface and the surface cracks with those of the standard sample (Figure 3.9). The deformation microstructure is also studied here. The study includes the comparison of the results obtained in different environments: RTA, HTA, NWC (0.5 and 8 ppm O_2) and HTW (2.2 ppm H_2). These results constitute the basis for assessing the He effects on IASCC later with miniaturised samples.

4.1.1 Tensile test results

The tensile tests results are presented in Table 4.1 for both sample geometries at different test conditions. The average and standard deviation of the tensile properties for a given testing condition and a representative plot for each condition (samples that approximately represent the average behaviour) are shown in Table 4.2 and Figure 4.1, respectively.
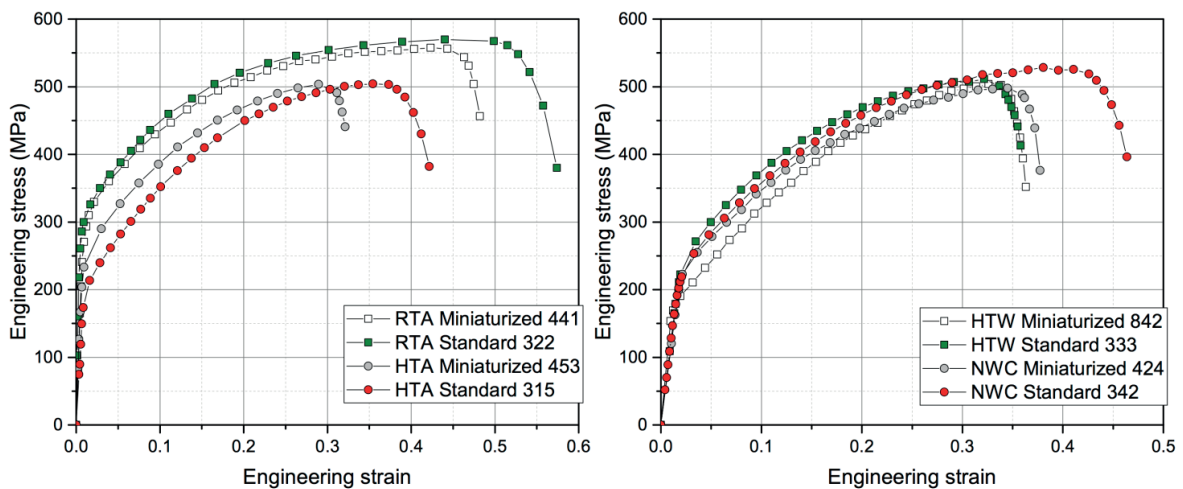
Figure 4.1. Representative stress-strain curves for miniaturized and standard samples in air (left) and water (right).

4.1.1.1 Tests in air

The standard deviation of the samples tested in the same condition was usually well below 10% of the average (Table 4.2). The main difference between the samples was observed in US whereas $Rp_{0.2\%}$, UTS and RA were similar for each condition (Figure 4.2). The US showed systematically lower values in miniaturized samples. Roughly, US was about 11% higher in standard samples in both, RTA and HTA. The tensile tests were carried out in different tensile machines with different stiffness and with different strain measurements, which produced a consistent difference in strain.

The increase of temperature caused a drop in $Rp_{0.2\%}$ of about 55-90 MPa (20-30%), in UTS of 50-70 MPa (10%), in US of 0.12 (30-27%) and in RA of 0.05-0.13 (5-15%) for both samples which is consistent with the results published in ref. [216].

Sample ID	Temp. (°C)	Environment	$Rp_{0.2\%}$ (MPa)	UTS (MPa)	US	RA	Fracture mode
M252	25	RTA	239	550	0.45	0.83	100% TG-D
M431	25	RTA	283	568	0.35	0.81	100% TG-D
M255	25	RTA	284	557	0.42	0.81	100% TG-D
M256	25	RTA	285	549	0.40	0.80	100% TG-D
M215	25	RTA	279	556	0.40	0.85	100% TG-D
M441	25	RTA	277	558	0.41	0.82	100% TG-D
S241	25	RTA	283	566	0.45	0.81	100% TG-D
S322	25	RTA	299	591	0.44	0.83	100% TG-D
S343	25	RTA	282	570	0.44	0.86	100% TG-D
S331	25	RTA	316	586	0.43	0.84	100% TG-D
S334	25	RTA	272	570	0.47	0.82	100% TG-D
M453	288	HTA	209	507	0.29	0.76	100% TG-D
M423	288	HTA	222	492	0.26	0.82	100% TG-D
M425	288	HTA	209	499	0.30	0.78	100% TG-D
M452	288	HTA	212	491	0.30	0.81	100% TG-D
M434	288	HTA	217	523	0.30	0.86	100% TG-D
M433	288	HTA	247	532	0.26	0.72	100% TG-D
M412	288	HTA	221	509	0.27	0.81	100% TG-D
M413	288	HTA	223	482	0.24	0.69	100% TG-D
S321	288	HTA	219	523	0.32	0.67	100% TG-D
S315	288	HTA	193	509	0.32	0.71	100% TG-D
S351	288	HTA	196	497	0.34	0.71	100% TG-D
S324	288	HTA	217	514	0.30	0.66	100% TG-D
S354	288	HTA	192	501	0.35	0.74	100% TG-D
M113	288	HTW (2.2 ppm H_2)	178	492	0.33	0.75	98% TG-D 2% TG-C
M842	288	HTW (2.2 ppm H_2)	172	508	0.33	0.47	86% TG-D 14% TG-C
S333	288	HTW (2.2 ppm H_2)	232	511	0.32	0.49	99% TG-D 1% TG-C
S335	288	HTW (2.2 ppm H_2)	237	490	0.25	0.54	99.4% TG-D 0.6% TG-C
M424	288	NWC (0.5 ppm O_2)	223	498	0.34	0.71	100% TG-D
S342	288	NWC (0.5 ppm O_2)	210	529	0.38	0.68	100% TG-D
M825	288	NWC (8 ppm O_2)	191	498	0.29	0.72	100% TG-D
S345	288	NWC (8 ppm O_2)	203	521	0.39	0.71	100% TG-D
S325	288	NWC (8 ppm O_2)	209	-	-	-	100% TG-D
S355	288	NWC (8 ppm O_2)	194	503	0.38	0.63	100% TG-D

Table 4.1. Engineering tensile test results in RTA, HTA, HTW and NWC for miniaturized (ID with "M") and standard (ID with "S") samples. TG-D stands for transgranular dimples fracture and TG-C for transgranular cleavage.

4.1.1.2 Tests in water

In HTW and in NWC environments, the number of tests was much lower than in air but the results look quite similar to those in HTA. The expected standard deviation should be higher in water than in air tests since many more parameters are involved during the tensile tests that were not present in air,

such as the high-pressure fluctuation and the water flow vibration. Nevertheless, assuming the same standard deviation as in the tests carried out in HTA (indicated in Table 4.2 as SD_{HTA}), the miniaturized sample data fall in the standard sample error band except for the $Rp_{0.2\%}$ in HTW (Table 4.2/Figure 4.2). Note however, that the RA had higher error. This was especially relevant at high temperature regardless of the environment and it will be analysed in the subsection 4.1.2.3 hereafter.

Sample type (# samples)	Temperature (°C)	Environment		$Rp_{0.2\%}$ (MPa)	UTS (MPa)	US	RA
Miniaturized (6)	25	RTA	AVG	275	556	0.40	0.82
			STD	17.5	6.7	0.03	0.03
Standard (5)	25	RTA	AVG	287	577	0.45	0.83
			STD	16.6	11.2	0.01	0.02
Miniaturized (8)	288	HTA	AVG	220	504	0.28	0.78
			STD	12.2	17.1	0.02	0.08
Standard (5)	288	HTA	AVG	200	509	0.33	0.70
			STD	12.8	10.2	0.02	0.03
Miniaturized (1)	288	NWC (500 ppb O_2)	AVG	223	498	0.30	0.71
			STD_{HTA}	12.2	17.1	0.02	0.08
Standard (1)	288	NWC (500 ppb O_2)	AVG	210	529	0.34	0.68
			STD_{HTA}	12.8	10.2	0.02	0.03
Miniaturized (1)	288	NWC (8 ppm O_2)	AVG	191	498	0.25	0.72
			STD_{HTA}	12.2	17.1	0.02	0.08
Standard (2)	288	NWC (8 ppm O_2)	AVG	202	512	0.34	0.67
			STD	7.6	13.1	0.004	0.06
Miniaturized (2)	288	HTW (2.2 ppm H_2)	AVG	175	500	0.29	0.60
			STD	3.9	11.2	0.01	0.14
Standard (3)	288	HTW (2.2 ppm H_2)	AVG	235	501	0.25	0.51
			STD	3.6	15.3	0.05	0.03

Table 4.2. Average (AVG) and standard deviation (STD) engineering tensile test results in RTA, HTA, NWC and HTW for miniaturized and standard samples.
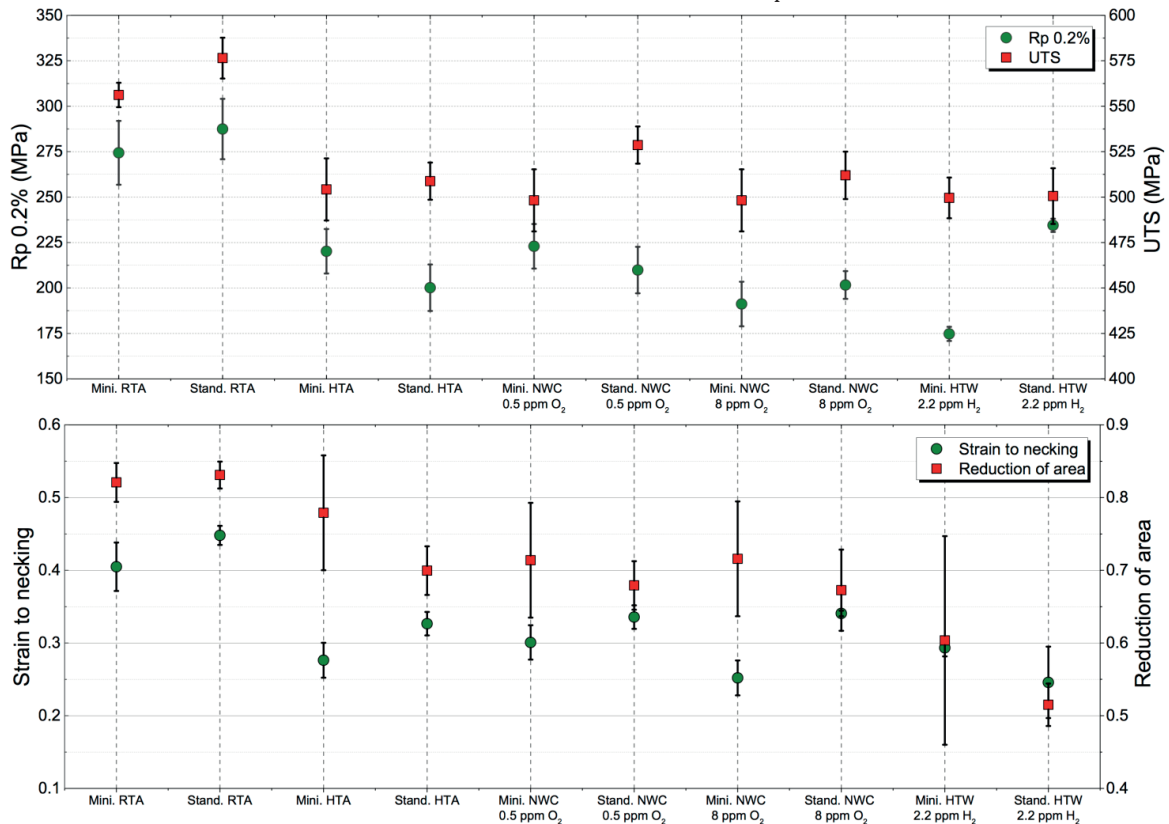
Figure 4.2. Averaged engineering tensile test results, at the top the $Rp_{0.2\%}$ and the UTS and at the bottom the US and RA for both samples at different testing conditions.

<u>Effect of NWC environment</u>

In this study, no remarkable difference was observed between the tests at HTA and NWC in both 0.5 ppm and 8 ppm O_2. This result is expected for the SA low-carbon non-sensitized AuSS. More significant effects might be expected for longer exposure periods, for precracked/notched specimens or sensitised material.

<u>Effect of HTW environment</u>

A remarkable softening with ~15 % decrease of $Rp_{0.2\%}$ was consistently observed in miniaturized samples, whereas the other tensile properties like UTS, US or RA were not affected (Table 4.1/Table 4.2). The softening might be related to hydrogen absorbed from the environment and corrosion reactions and hydrogen-dislocation interactions (e.g., HELP). Interestingly, this effect was not observed in standard specimens. At 288 °C, the hydrogen diffusion distance during the pre-oxidation period (~5 days) is above the size of the used standard specimens (D ≈ 6.29×10^{-12} m^2s^{-1} [96]), thus the hydrogen absorbed from the dissolved hydrogen in the environment cannot explain this difference. The crack depths observed in the gauge length of the samples were about 50-70 μm (see subsection 4.1.2.3 hereafter) which means that the hydrogen was predominantly concentrated within the first μm of the sample. Therefore assuming the same absorption, the effect of hydrogen would be more relevant in a thinner sample because the relative affected area would be greater. Thus, hydrogen has a stronger effect on the overall plastic behaviour of the thin miniaturized sample than in the thick standard sample.

4.1.2   Fracture investigation

The fracture mode was investigated with fractography observations and the crack initiation was analysed along the gauge length (longitudinal cut) of the tested samples. The longitudinal cuts were also used to study the fracture shape (shear or cup and cone fracture). The surface of the samples was also investigated in order to clarify the effect of the environment. These observations provided an indication of the susceptibility to SCC.

4.1.2.1   Fracture morphology

The fracture morphology in different environments for miniaturized and standard samples is shown in Figure 4.3 and Figure 4.4, respectively. The fracture changes from fully transgranular dimple (TG-D) fracture by MVC in RTA, HTA and NWC to a combination of predominantly TG-D fracture with minor contributions (a few %) of transgranular cleavage (TG-C) in HTW (Table 4.1). In the latter, TG-C occurs close to the sample surface, whereas the TG-D fracture still occurs in the centre. Crack-arrest markings can also be observed in the sample surface region as shown in Figure 4.3 and Figure 4.4 for samples M113 and S333 in HTW, respectively. In general, the fracture surface looks very similar for given tensile test conditions for both types of samples indicating no significant effects of specimen geometry or size. As mentioned earlier, TG-C might be caused by hydrogen-assisted SCC and hydrogen embrittlement mechanism (AIDE, HEDE, HELP or/and HESIV) as suggested by other authors [217, 218].
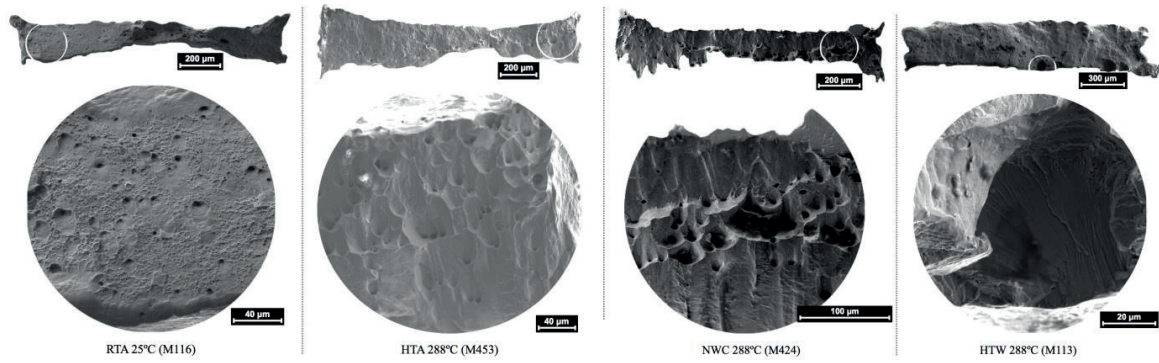
Figure 4.3. Fracture surface of the miniaturized samples tested at different conditions: RTA, HTA, NWC (500 ppb O_2) and HTW. Fracture surface in NWC with 8 ppm O_2 is omitted since it is similar to 500 ppb. All the images are obtained with the secondary electron detector.
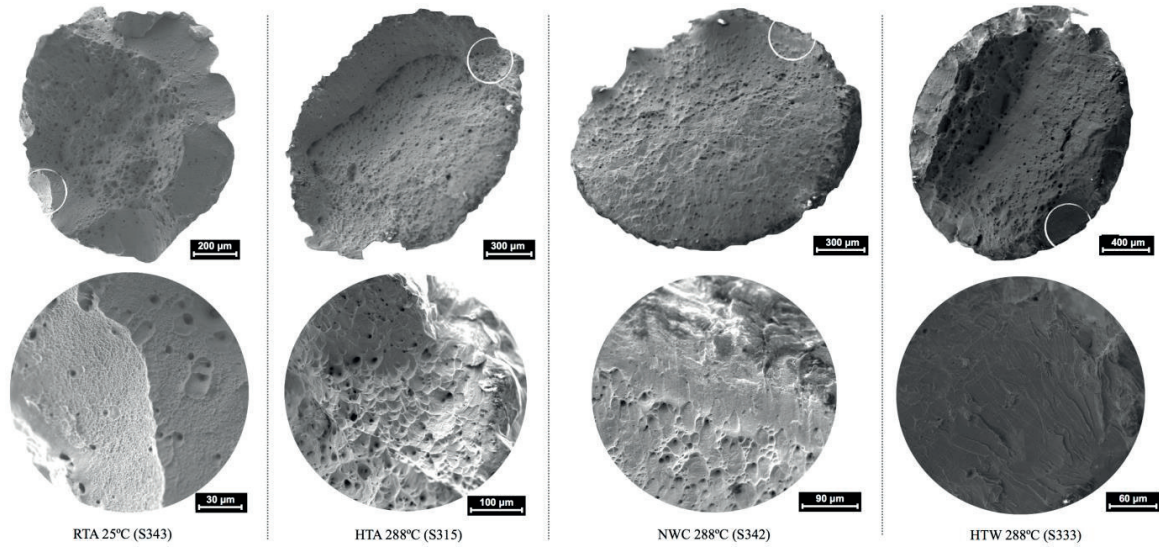
Figure 4.4. Fracture surface of the standard samples tested at different conditions: RTA, HTA, NWC (500 ppb O_2) and HTW. Fracture surface in NWC with 8 ppm O_2 is omitted since it is similar to 500 ppb. All the images are obtained with the secondary electron detector.

4.1.2.2   Sample surface

The sample surface showed many deformation bands in all the tested environments. Surface micro-cracks always formed in HTW at the surface in contact with water along deformation bands (Figure 4.5), but not in NWC with up to 8 ppm O_2, HTA and RTA (see subsection 4.1.2.3 for further details). They were observed along the whole gauge section and even in the specimen shoulders suggesting that they already initiated before the onset of necking (Figure 4.6 and Figure 4.7). These surface cracks contained some striation-like features that seemed to be crack arrest markings from intermittent crack growth or slip steps (Figure 4.8), as also described by Herms et al. [219]. These cracks are thus environment-induced TG-C cracks (as in the fracture surface), probably due to hydrogen-assisted SCC and/or embrittlement mechanism (HELP or HESIV) [218]. There was no evidence of IG cracks in the fracture surface or in the sample surface since those cracks did not propagate smoothly.
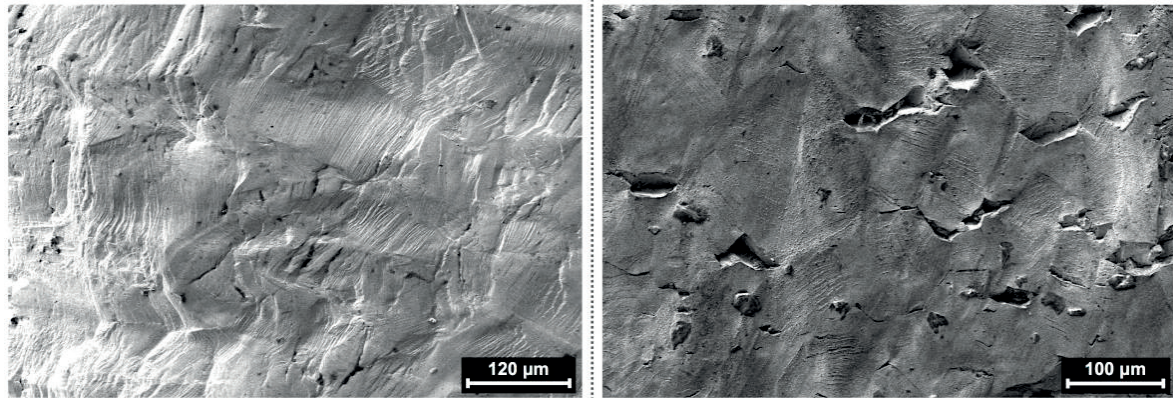
Figure 4.5. Sample surface of the samples tested in HTA (left) and HTW (right).
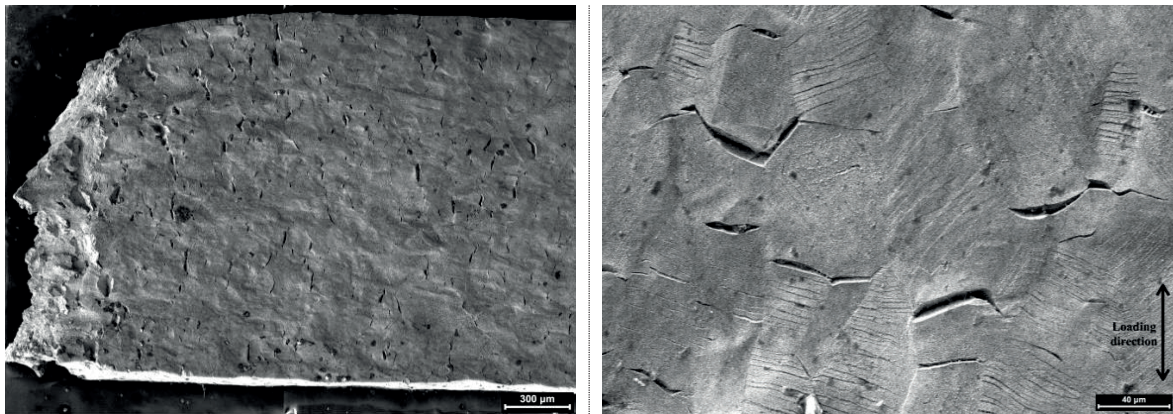
Figure 4.6. TG cracks formed along the gauge length (left) and a close look to those cracks (image rotated 90°) far from the necking region (right) in a non-implanted SA sample tested in HTW.
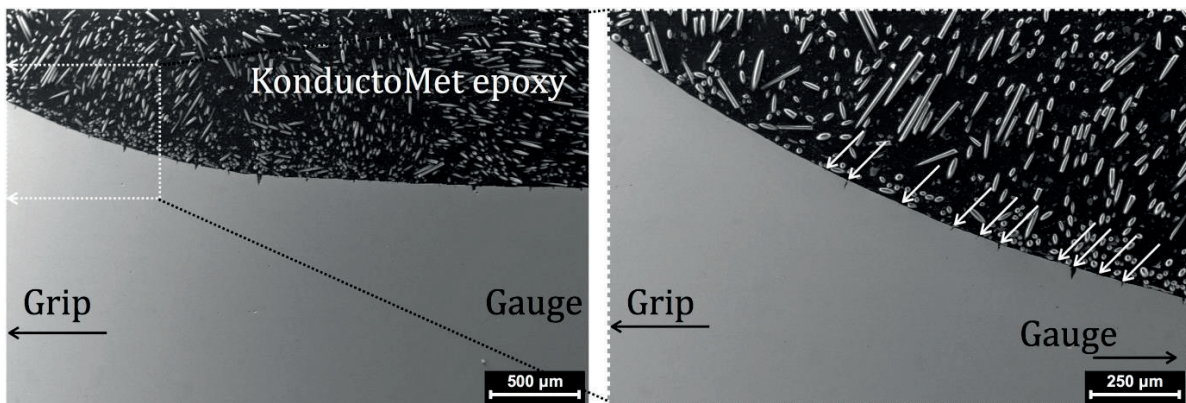
Figure 4.7. Detail of the cracks formed in the gauge section and in the grip-to-gauge section (left) and a magnified image in the grip-to-gauge section showing the formation of cracks in this region (right).
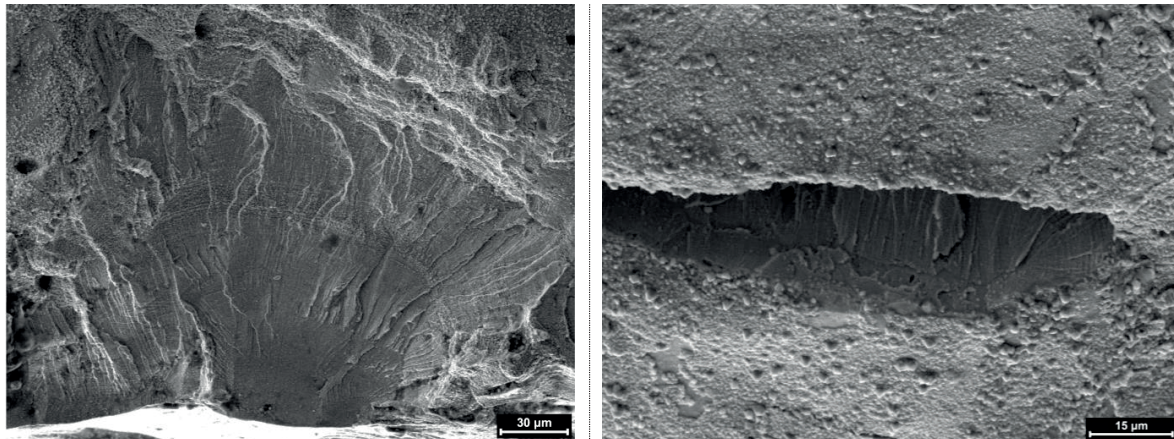
Figure 4.8. Typical TG-C crack formed in the fracture surface (left) and on the sample surface (right).

4.1.2.3 Longitudinal cuts

Longitudinal cuts of the miniaturized and standard samples are shown in Figure 4.9 and Figure 4.10, respectively. HTA, NWC and HTW showed shear dominated fracture inclined 20-45° from the loading axis, but RTA tests did not show shear fracture. This effect was reported when hydrogen was present in the samples, both at low and high temperature for different types of steels [96, 98]. Some residual hydrogen content is expected on the surface of the sample and in the bulk due to the electropolishing and manufacturing of 316L, respectively [93, 94]. The SA treatment might reduce the hydrogen content from manufacturing slightly, but the initial concentration of hydrogen should be similar in all the samples. The low concentration and the diffusion of hydrogen at 25°C (D ≈ 2.47×10^{-16} m^{2}s^{-1} [96]) might be not enough to have detrimental effects on the tensile properties and fracture surface. On the other hand, the diffusion of hydrogen at 288°C (D ≈ 6.29×10^{-12} m^{2}s^{-1} [96]) was found to have an impact on the fracture surface and the available dissociated hydrogen in the sample surface from the HTW was found to have an impact on the tensile properties and the formation of TG-C cracks.

The tensile properties reported above showed an increase of the RA standard deviation at high temperature. The measurements of the RA should be taken with care since they were measured perpendicular to the loading direction and the resulting RA depends on the shear angle. Thus, a large scatter is expected due to the shear fracture and the sample geometry.

Significant necking with ductile MVC in RTA and no other crack formation mechanism were observed. With the increase of temperature, the necking was visually smaller and crack formation and growth occurred by ductile MVC in HTA and NWC with no other crack formation in the gauge length. However, in HTW, the necking is moderately reduced and cracks initiating from the specimen surface in contact with water appear along the whole gauge length and even between the gauge and the grip section (Figure 4.6). These cracks were also identified as TG-C in the longitudinal cuts shown in Figure 4.11-A and Figure 4.12-D for the standard and miniaturized samples, respectively.

The reduction of the necking in HTW could be caused by the formation of the TG surface cracks. In ref. [93], it is suggested that hydrogen enhances localization of shear deformation and that would explain the RA by increasing temperature and increasing hydrogen content. This effect was observed in this study after the longitudinal cut in the tests carried out at high temperature for both samples (Figure 4.9 and Figure 4.10).
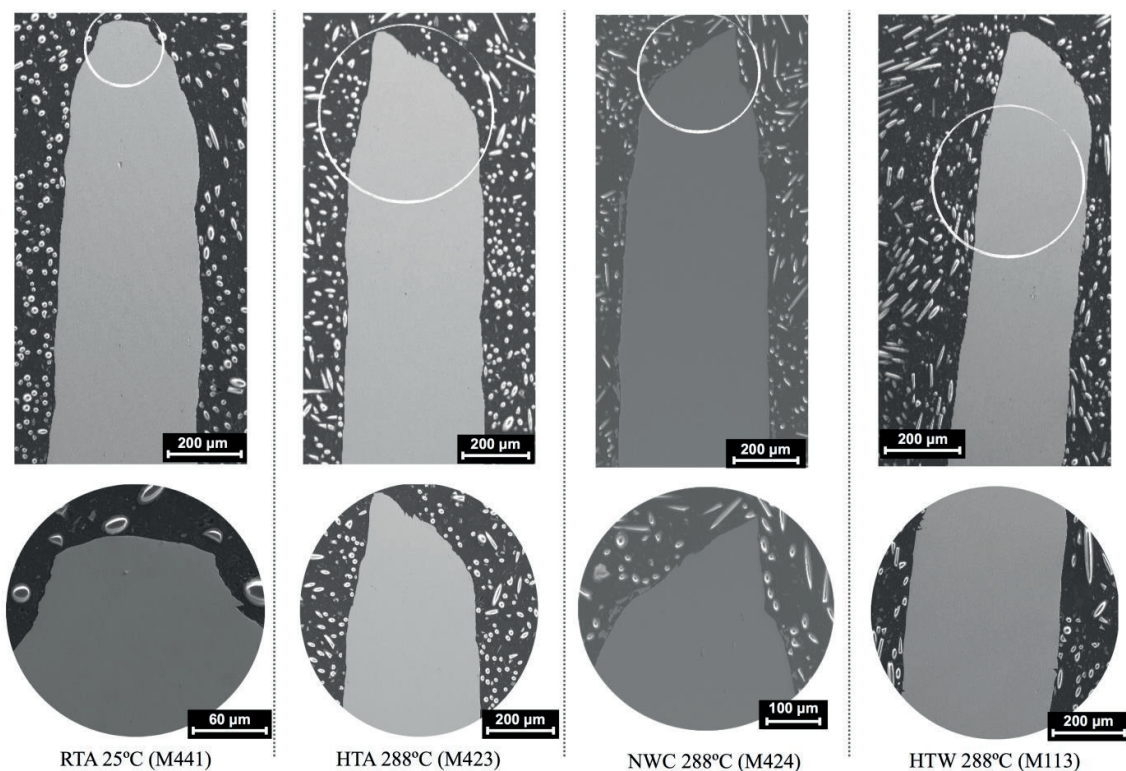
Figure 4.9. Longitudinal cross-section of miniaturized samples tested at RTA, HTA, NWC (500 ppb O_2) and HTW. Fracture in NWC with 8 ppm O_2 is omitted since it is similar to 500 ppb O_2. All the images are obtained with the secondary electron detector.
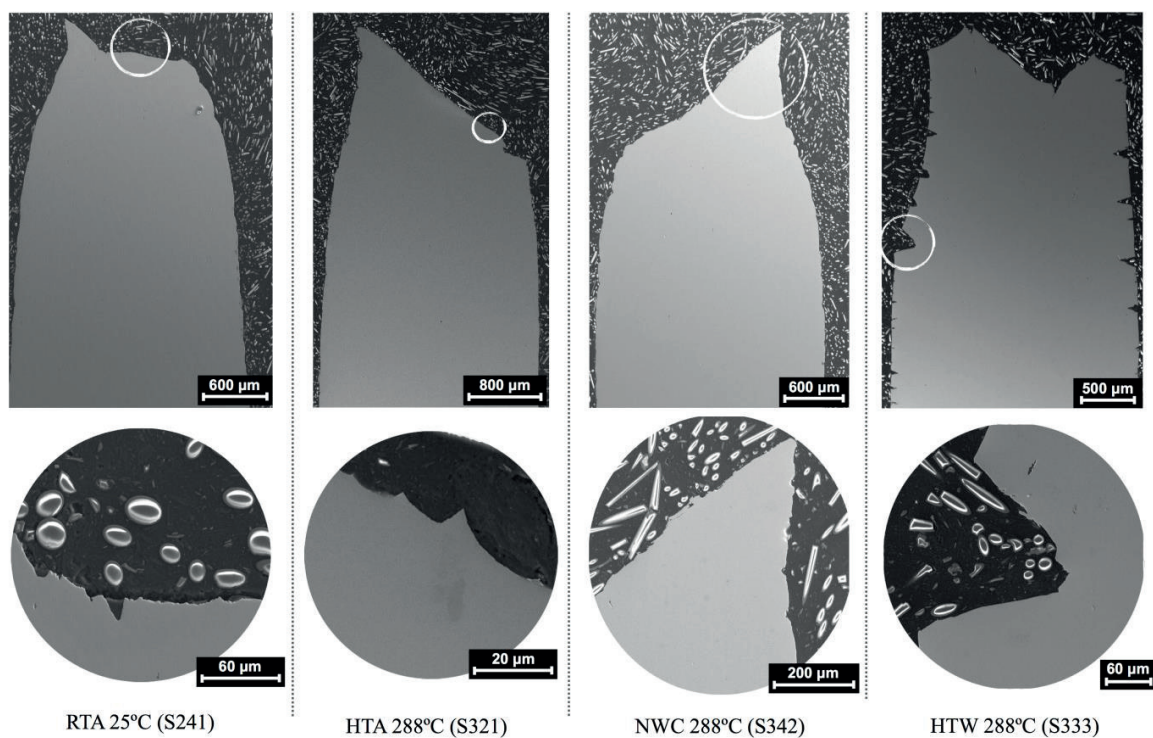
Figure 4.10. Longitudinal cross-section of standard samples tested at RTA, HTA, NWC (500 ppb O_2) and HTW. Fracture in NWC with 8 ppm O_2 is omitted since it is similar to 500 ppb O_2. All the images are obtained with the secondary electron detector.

Different crack sizes were observed in the gauge length and in the necking region of the samples tested in HTW. Standard samples showed crack openings of 1 to 240 μm and crack depths of 1 to 240 μm in the necking region, whereas in the gauge length, the cracks showed openings of 1 to 45 μm and depths of 1 to 70 μm (Figure 4.11-B). Miniaturized samples showed crack openings of 1 to 65 μm and crack depths of 1 to 65 μm in the necking region, but in the gauge length, the cracks showed openings of 1 to 50 μm and depths of 1 to 30 μm (Figure 4.12-D and 9-E). These results confirm that the samples keep high ductility since cracks had an aspect ratio close to unity (particularly in the necking region). In general, those cracks were wider and deeper in the necking region. This (and the following observation) strongly suggests the presence of a ductile hydrogen embrittlement mechanism like HELP or HESIV in HTW. In hydrogen-free NWC, there is just a minor hydrogen uptake from the slow corrosion reactions and the residual hydrogen content might not be sufficient contributor. For this reason, HTA and NWC test have similar results in the conditions tested.
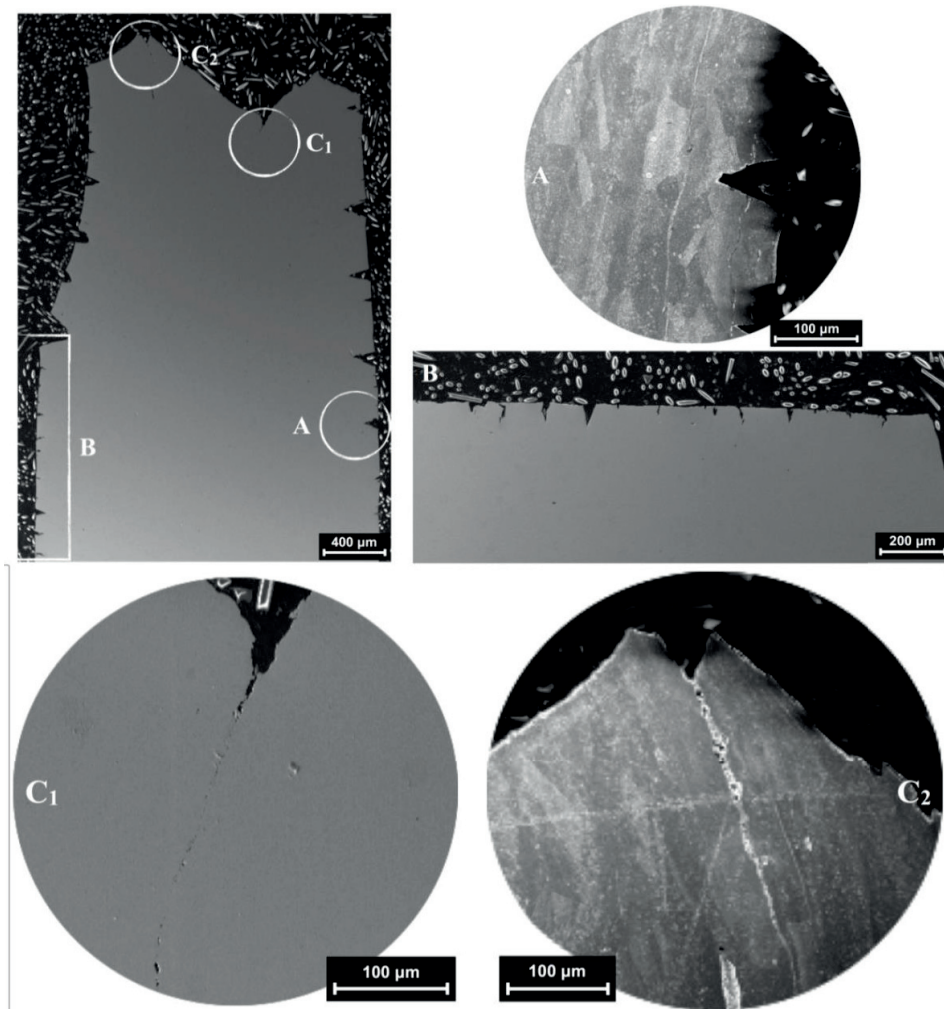
Figure 4.11. Details of the cracks observed in the longitudinal cross-section of the standard sample S333 in HTW. A, etched detail of the crack in the gauge section (etched with "V2A-Beize"); B, gauge section cracks; C_1, fracture surface dimple detail with aligned voids towards the gauge section; C_2, etched fracture surface dimple showing TG voids alignment towards the gauge section (etched with "V2A-Beize"). A and C_2 images are obtained with the in-lens detector whereas the other images are obtained with the secondary electron detector.

A TG alignment of the micro-voids formed close to the fracture surface was observed below some dimples of the fracture surface as shown in Figure 4.11-C_1 and -C_2 in HTW. These micro-voids are usually aligned and elongated parallel to the loading axis in the necking region, but randomly distributed and almost equiaxed in the gauge region for all the tensile tests presented here (Figure 4.13). The micro-voids alignment and the micro-voids might be formed from pre-existing inclusions/defects during the manufacturing of the material (usually rolled CW and SA).
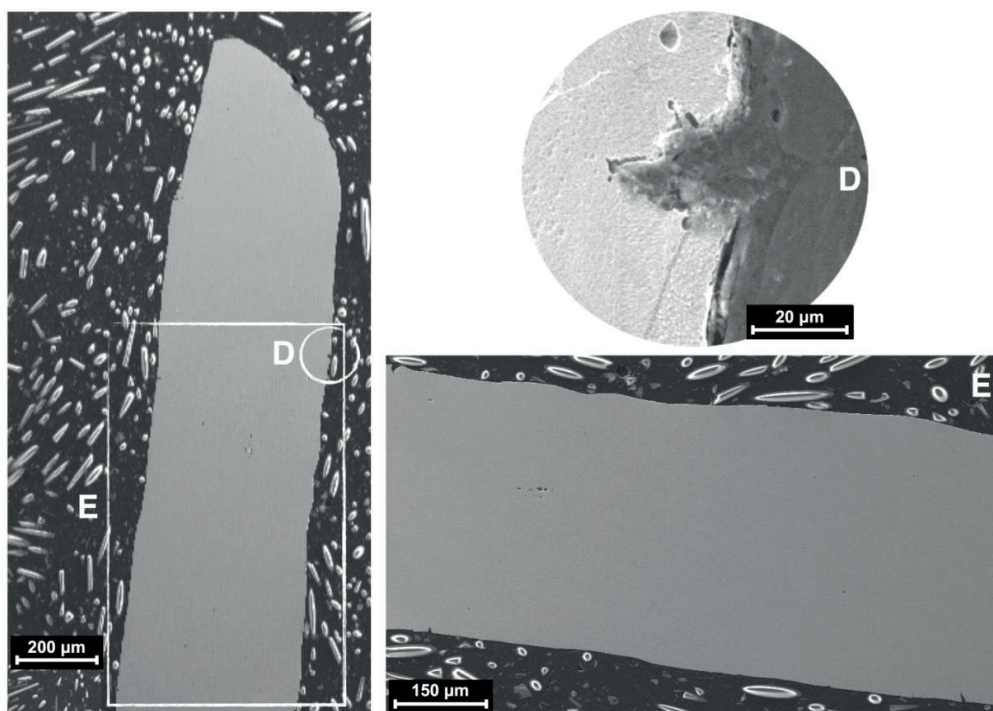
Figure 4.12. Details of the cracks observed in the longitudinal cross-section of the miniaturized sample M133 in HTW. D, etched detail of the crack in the gauge section (etched with "V2A-Beize; E, gauge section cracks. All the images are obtained with the secondary electron detector.
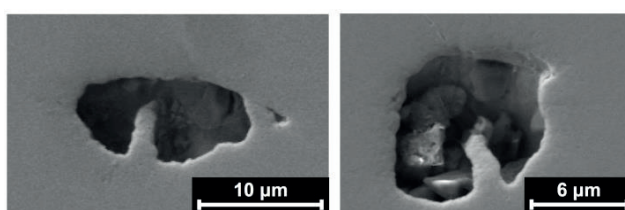
Figure 4.13. Voids formed in the gauge length of the sample S321 presumably during the HTA tensile test in the necking region (left) and far from the necking region (right).

4.1.3 Deformation microstructure

The deformation microstructure was investigated for both samples and all testing conditions. TEM samples were taken from the gauge length far from the necking region and were thus plastically strained up to the US (e.g. ~25-40 %). Hydrogen and temperature affected the tensile properties and the fracture mode. However, the TEM investigation did not show a clear difference in the microstructure between the tested conditions. Figure 4.14 shows the deformation microstructures observed in miniaturized samples tested in RTA (A and B), HTA (C and D) and HTW (E and F).

The samples showed high dislocation density arranged in cell walls separated by relatively low dislocation-density regions (Figure 4.14-A, C and E). Deformation bands, both twins and slip bands were also observed but their presence was rare (Figure 4.14-B, D and F). According to ref. [220], a requirement for cell formation, i.e. dislocation tangles, is that dislocations have enough mobility out of their slip plane (cross slip). Swann in [156] showed that Ni concentration above 8% (wt.) in AuSS with 18% Cr prevents the formation of stacking faults and it is harder to find slip planes in the material microstructure. Thus, dislocation cross slip is easier and the susceptibility to TG or IG fracture is reduced. These results are consistent with the TEM observations presented in Figure 4.14.
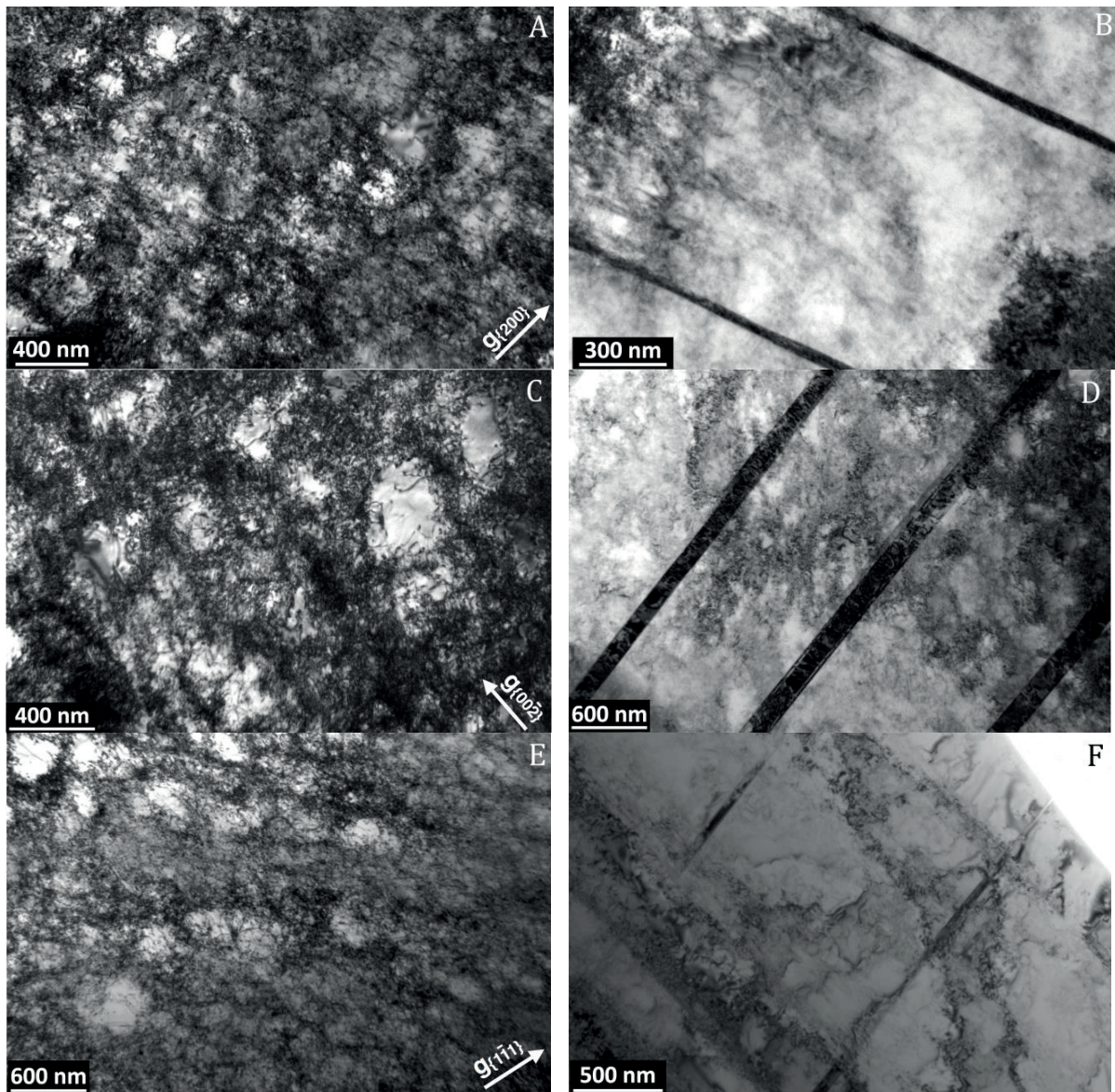
Figure 4.14. A, C and E are bright field 2-beam dynamical micrographs of the TEM samples prepared from samples tested in RTA, HTA and HTW, respectively. B, D and F are bright field micrographs in kinematical conditions of the TEM samples prepared from samples tested in RTA, HTA and HTW, respectively.

4.2   He evolution after annealing

This subchapter has a double purpose: to find the conditions to reproduce the bubble microstructure observed in replaced reactor internal components and to use the results for understanding the tensile results of the PIA samples. To do so, the He-plate was cut in different pieces and then annealed from 650 °C to 1000 °C. The relationship between annealing temperature and He coarsening mechanism is studied along with the bubbles location and size distribution, average spacing, GB coverage and He density in the bubbles. The summary of the results is given at the end of this subchapter in Table 4.3.

4.2.1   Bubbles location and size distribution

The He bubbles could not be found in the as-implanted specimens, but many black dots and dislocation lines were observed (Figure 4.15-A). The PIA above 650 °C resulted in an increase of the bubbles size and annealed most of the black dots (implantation damage, Figure 4.15-C). At first glance, the bubbles in the GI and in the GB grew with increasing annealing temperature (Figure 4.15). The bubbles in the GI were primarily located on dislocation lines, observation consistent with that of Chen et al. in 304L [173], Chernikov et al. in nickel [171] and Singh et al. in Aluminium [221]. Dislocation lines reaching the GBs gave the perception of not having depletion area since helium bubbles are sitting on dislocations with a distance of about 20 nm to the GB. There is no evidence of preferential bubble accumulation on the GBs (Figure 4.15 - D, F, H, J). The GB micrographs did not show bigger GB bubbles than GI bubbles.
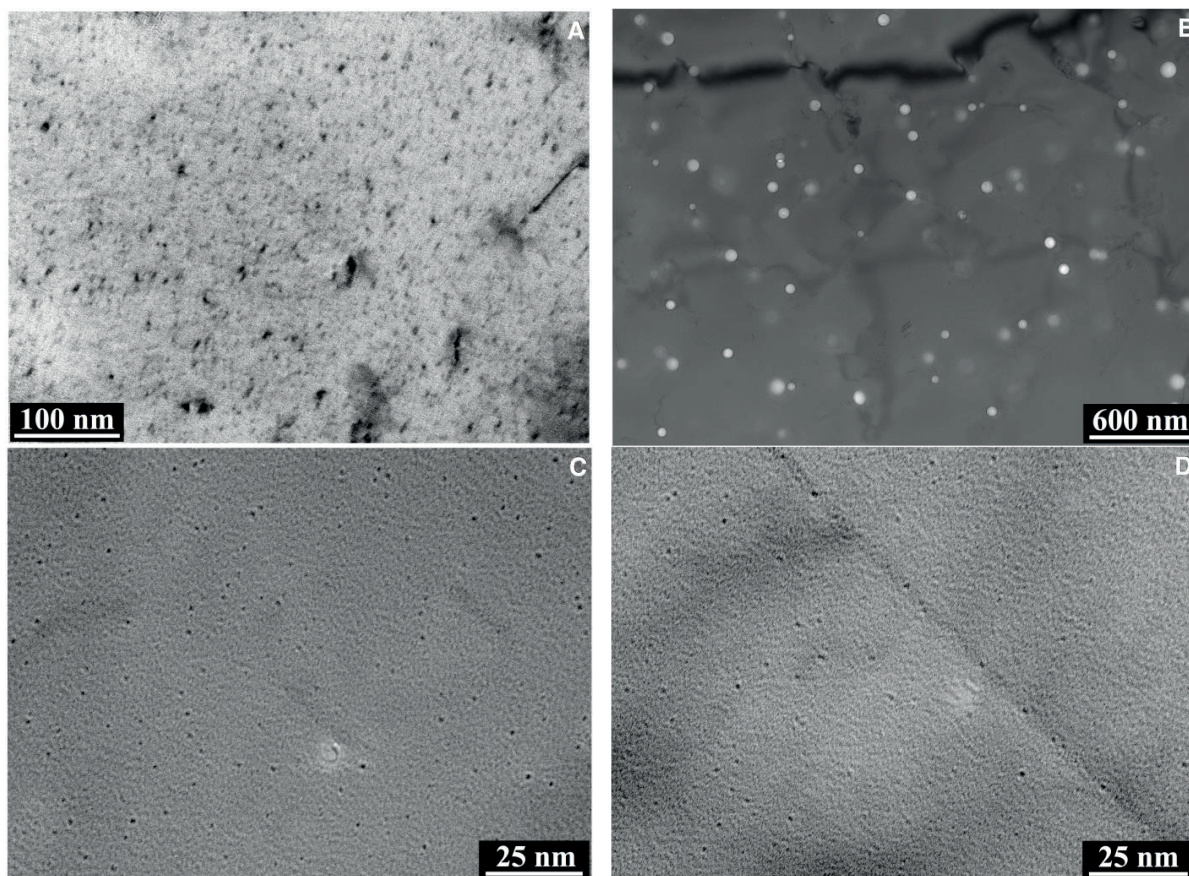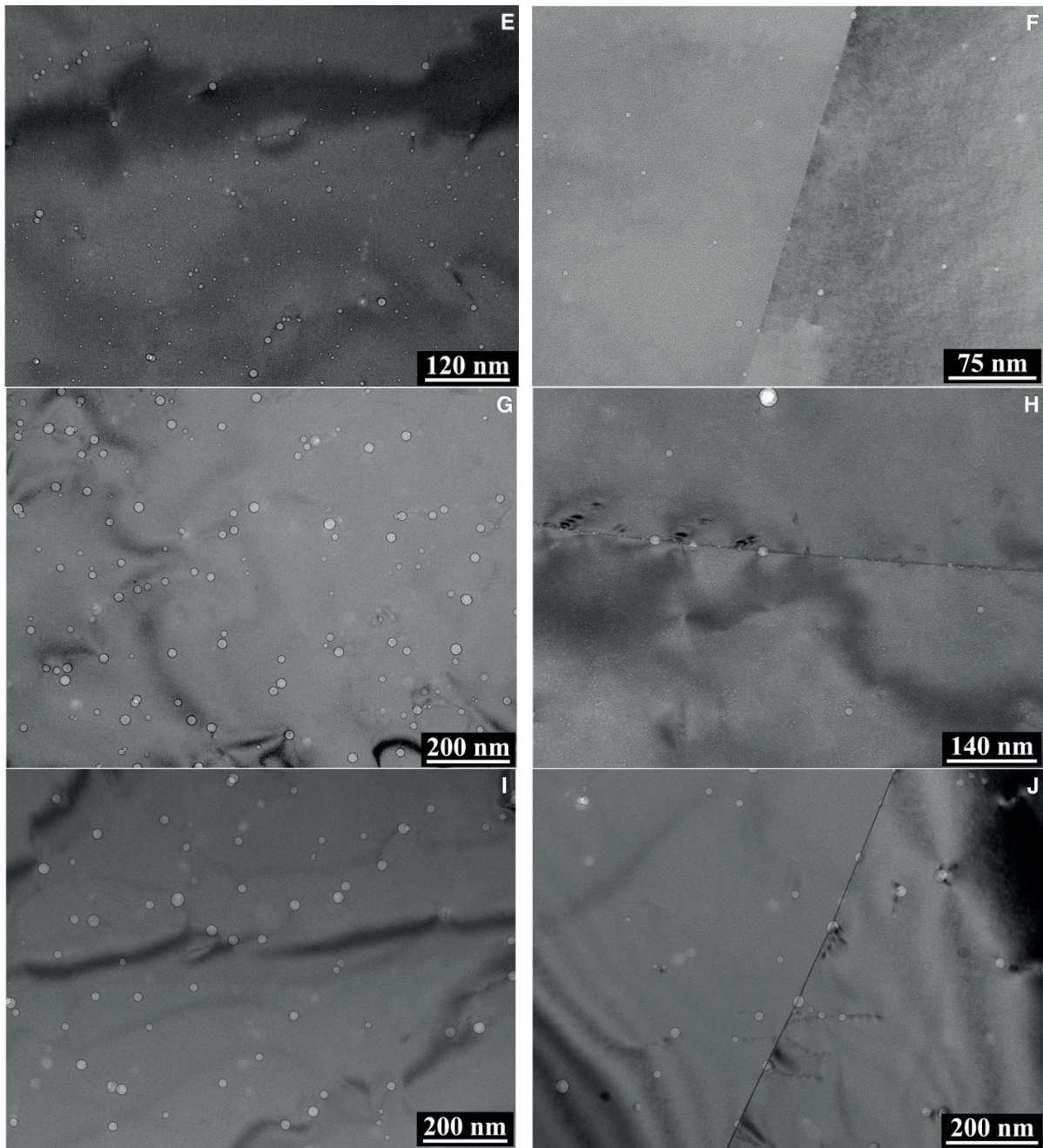
Figure 4.15. Bright field kinematical micrographs of the He-plates with 1000 appm: (A) as implanted GI (focal image), (B) annealed at 1000°C GI (under-focal image), (C) and (D) annealed at 650°C (under-focal image), (E) and (F) annealed at 750°C (under-focal image), (G) and (H) annealed at 850°C (under-focal image) and, (I) and (J) annealed at 900°C (under-focal image) GI and GB, respectively.

Figure 4.16 shows the bubble size distribution in GBs and in GIs obtained from the TEM micrographs after different annealing temperatures. GB and GI present similar bubble size distributions at all temperatures. At the lowest annealing temperatures (i.e. 750°C and 800°C), the number of bubbles counted below 1 nm for both, GB and GI, is expected to be slightly higher than the reported values since it was difficult to quantify the bubble size below 2 nm (objective aperture and pixel size limitations).

The increase of bubble size with increasing annealing temperature can be clearly observed in Figure 4.17. The distributions after PIA at 650 and 1000°C are not included in Figure 9. At 650°C, the distribution consisted in a single bar from 0 to 1 nm, whereas at 1000°C, the bubble size distribution was too large to be represented in the same figure. However, the distribution shape at 1000°C was similar to the one at 900°C. The best distribution fit in the GI after PIA below 850°C was obtained with the inverse Gaussian distribution, whereas above 850°C was a Gaussian distribution. The difference in the distribution at high and low PIA temperatures was due to the cut of the distribution below 1 nm bubble size; negative bubble sizes are not possible and below 1 nm the bubbles size distinction is limited. The distribution in the GB was less evident. The number of bubbles counted in the GBs was significantly smaller than in the GI and the distribution might not be fully representative. Singh et al. [221] reported that bubbles on the dislocation lines are larger than those in the matrix inducing a double peak and/or a longer tail behind the main distribution peak in the GI distributions. This study cannot confirm this observation because most of the bubbles counted were found to be in dislocation lines as will be shown hereinafter.
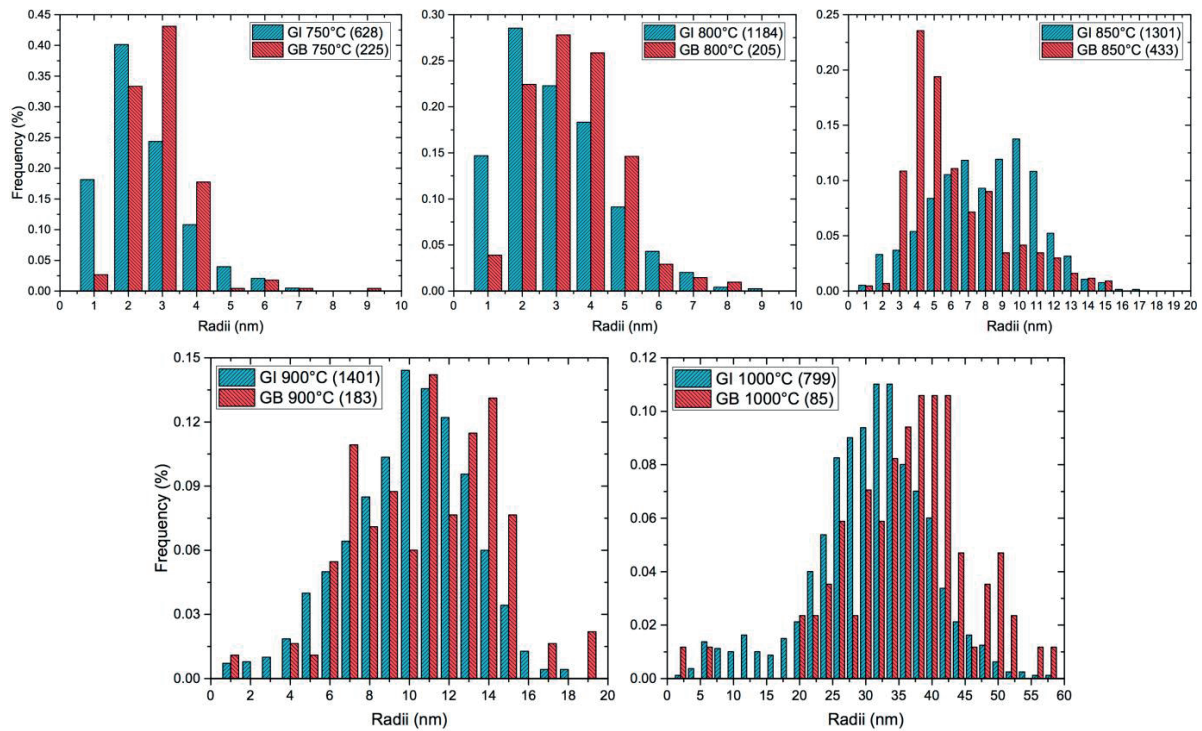
Figure 4.16. Comparison between the bubble size distribution of the He-plates with 1000 appm in the GI and on the GB for different heat treatments. In parentheses, the number of bubbles counted for each heat treatment. The bin size is 1 nm for all conditions except at 1000°C, which is 2 nm.
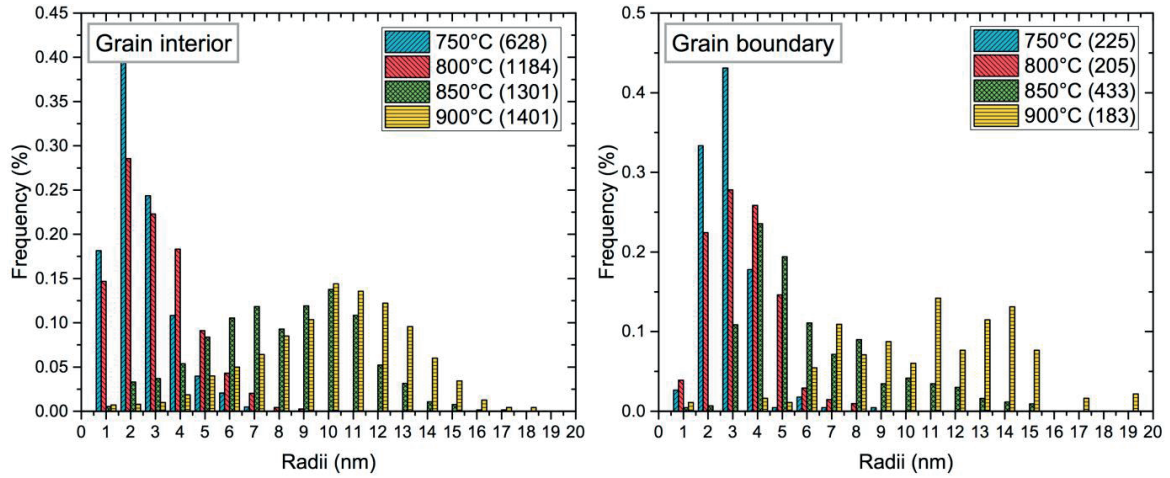
Figure 4.17. Bubble size distribution of the He-plates with 1000 appm in GI (left) and on GB (right) for different heat treatments. In parentheses, the number of bubbles counted for each heat treatment.

4.2.2 Helium bubbles and dislocations interaction

In order to study the location of the bubbles in the GI, the same micrograph region has been analysed in different orientations. This procedure allowed to image the dislocation in an area and to correlate it with the He bubbles. Figure 4.18 A-B (750°C) and C-D (850°C) clearly show that more than 95% of the bubbles are located on dislocations although some might still be invisible in this orientations. Moreover, it was generally perceived from the TEM micrographs that bubbles located on dislocation lines grow faster than the ones in the matrix. This indicates that dislocations lines are a source of vacancies, at least in the present case, when the concentration of vacancies in the material is above the thermal equilibrium concentration. Hence, the bubbles on dislocations relax their pressure faster than the ones in the matrix, where the vacancy capture radius is smaller.
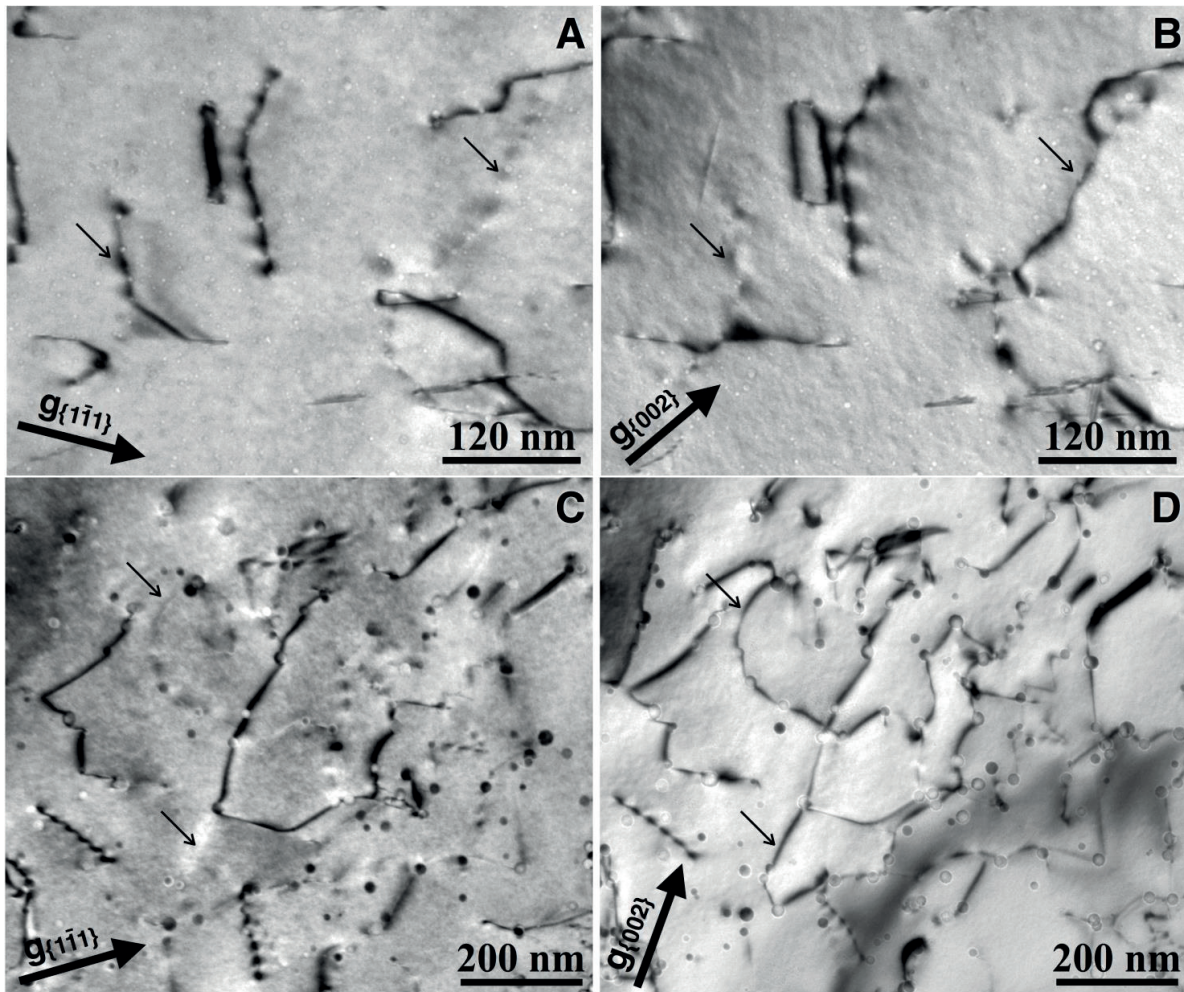
Figure 4.18. Bright field 2-beam dynamical micrographs of the plates implanted with 1000 appm and annealed at 750 (A-B) and 800°C (C-D). The arrows indicate dislocations that are invisible in one orientation and visible in the other.

The strain field produced by the dislocation lines distorts the atom lattice structure locally allowing their observation in the TEM micrographs. The distortion produced by the dislocation lines was observed to be minimized by the helium bubbles that sit on them; hence the He bubbles locally relaxed the strain field of the dislocation line. The Figure 4.18 shows this effect for different bubble sizes (Figure 4.18 A-B versus C-D). Usually, there was more than one bubble per dislocation which produced the contrast fade off on different locations of the dislocation line.

4.2.3   Bubble growing mechanism

The average radii and density of bubbles in GIs and in GBs are plotted in Figure 4.19. As shown earlier, higher annealing temperature increased the bubble size and reduced the density in the same way on GBs and in GIs. The bubble sizes in the GIs and on the GBs were very similar. At a given annealing temperature, the measured bubble size in this study is one order of magnitude higher than the bubble size reported in other studies where the helium implantation was carried out at room temperature [222]. However, annealing between 750 and 850°C gave similar bubble average radii and density than the observations in BFB and flux thimbles tubes extracted from nuclear internals [131, 132, 133, 134, 135, 136].

The bubble coarsening is governed by MC or by OR [175, 176]. These models describe the bubble growth as [223]:

$$\bar{r}_b \propto [C_{He} D_B t_a]^{1/n} \qquad \text{(MC, [175])} \qquad\qquad \text{Eq. 4.1}$$

$$\bar{r}_b \propto [\hat{c}_{He} D_i t_a]^{1/n} \qquad \text{(OR, [176, 177, 178, 179])} \qquad\qquad \text{Eq. 4.2}$$

Where D_B is the pressure dependent self-diffusion coefficient which depends on the atomic transport mechanism (surface diffusion or volume diffusion), t_a is the annealing time, $\hat{c}_{He}$ is the helium concentration dissolved in the matrix, C_{He} is the implanted helium concentration, D_i is the pressure dependent effective diffusivity of the He in the matrix (i=He, He gas dissociation controlled) or the volume self-diffusion coefficient (i=v, vacancy dissociation controlled) and n is the exponent value that depends on the active diffusion mechanism which varies from 4 to 5 for MC and from 3 to 4 for OR [171].

Introducing the first Fick's law of diffusion in Eq. 4.1 or Eq. 4.2, an Arrhenius equation can be deduced as follows:

$$D(T) = D_0 \exp\left(-\frac{Q}{kT}\right) \rightarrow \bar{r}_b \approx \left[r_0 \exp\left(-\frac{Q}{kT}\right)\right]^{\frac{1}{n}} \qquad\qquad \text{Eq. 4.3}$$

Where D_0 is the temperature-independent pre-exponential constant in m²/s, Q is the activation energy in eV, k is the Boltzmann constant in eV/K, T is the annealing temperature in K and r_0 is the temperature-independent pre-exponential constant in nm that is the product of all the constants in the equation Eq. 4.1 or Eq. 4.2. The exponent value (n) is inherent in the experimental data when the apparent activation (E_a=Q/n) energy is obtained from the Eq. 4.3. Hence, the average radii can be calculated using the following equation:

$$\bar{r}_b \approx r_0 \exp\left(-\frac{E_a}{kT}\right) \qquad\qquad \text{Eq. 4.4}$$
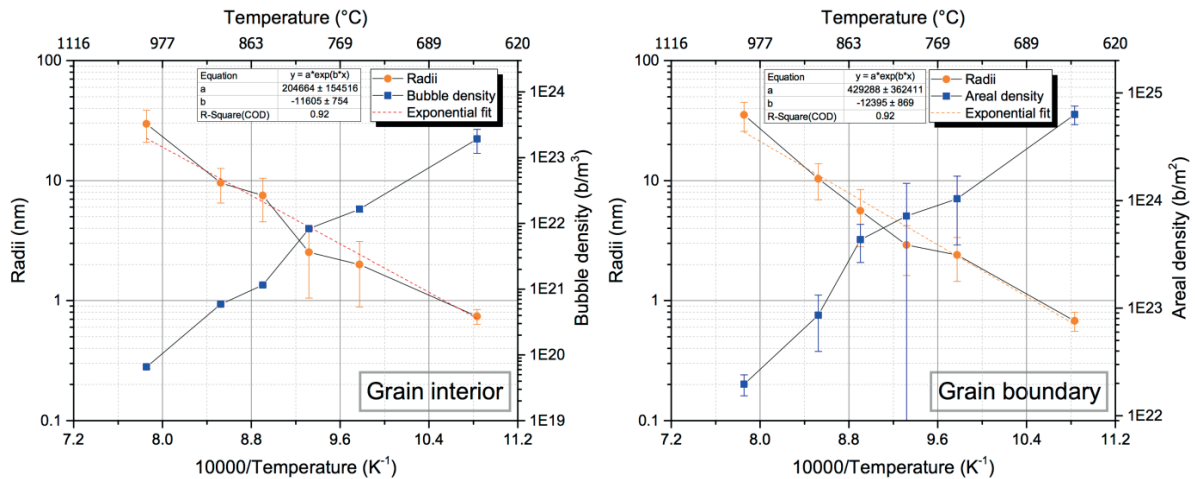
Figure 4.19. Bubble size and density evolution in GIs (left) and on GBs (right).

Figure 4.19 shows the average He bubble radii and density evolution in the GI (right) and in the GB (left) in function of the inverse of temperature. The average radius consistently increases with increasing annealing temperature, but it does not show a change of slope from low to high

temperatures, although this is observed in other publications [171, 172, 173, 174, 223]. However, the radii evolution with temperature follows an Arrhenius equation along the studied temperature range (i.e. Eq. 4.4). The active coarsening mechanism can be determined from the parameters of the Arrhenius equation included in Figure 4.19. The apparent activation (E_a) energy is 1 and 1.07 eV for GI and GB, respectively. Chernikov et al. [214] reported similar apparent activation energies for bubbles growing near the surface in helium-implanted nickel. These high energies suggest that OR mechanism is the prevailing growing mechanism and it would imply activation energies (Q) between 3 and 4 eV which are compatible with the He atom dissociation controlled OR energy in nickel (~3.5 eV [173]). To confirm the coarsening mechanism, the pre-exponent factor of the Arrhenius equation found in Figure 4.19 can be used. The pre-exponents are 2×10^{-4} and 4×10^{-4} m for GI and GB respectively. These values are 3-4 orders of magnitude smaller than for MC (1.4×10^{-8} m for nickel in [214]) and in the order of magnitude for OR mechanism (5.5×10^{-4} m for nickel in [214]).

4.2.4   Bubble's average spacing and GB coverage

Figure 4.20 shows the average spacing (L) and GB coverage (α) calculated with Eq. 3.19 and Eq. 3.20. A similar bubble average spacing in GI and on GB is observed. The GB coverage and the average spacing increased significantly with increasing the annealing temperature. Once the bubbles are big enough (r~1 nm), the bubble migration/diffusion towards the GB is unlikely since the bubble growing mechanism is by OR. The highest GB coverage was below 10% but care should be taken given that the scatter values are really big due to the standard deviation associated with the areal density.
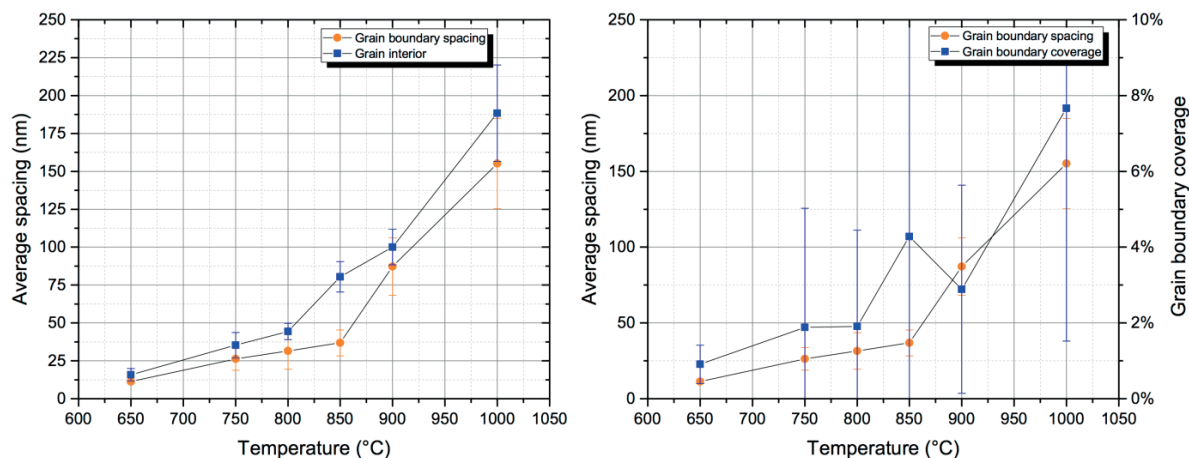
Figure 4.20. Change of bubble average spacing (left) and GB coverage (right) with increasing annealing temperature. The bubble average spacing and the GB coverage are calculated with Eq. 3.19 and Eq. 3.20, respectively.

4.2.5   Helium concentration

Specimen	GI radii (nm)	GB radii (nm)	Density (bubble/nm³)	GI spacing (L, nm)	GB spacing (L, nm)	GB coverage (α, %)	Cal. C_{He} (appm)

Plate 1000°C	29.7 ±8.9	35.2 ±9.6	6.57×10⁻⁸ ±4.2×10⁻⁹	188 ±32	155 ±30	8 ±6	814
Plate 900°C	9.6 ±3.1	10.3 ±3.4	5.9×10⁻⁷ ±1.8×10⁻⁸	100 ±12	87 ±19	3 ±3	721
Plate 850°C	7.5 ±3	5.6 ±2.8	1.2×10⁻⁶ ±2.9×10⁻⁸	80 ±10	37 ±9	4 ±7	966
Plate 800°C	2.5 ±1.34	2.9 ±1.3	8.3×10⁻⁶ ±4.1×10⁻⁷	44 ±5	32 ±12	2 ±3	815
Plate 750°C	2 ±1.1	2.4 ±1	1.7×10⁻⁵ ±1.7×10⁻⁶	35 ±8	26 ±7	2 ±3	895
Plate 650°C	0.7 ±0.1	0.7 ±0.1	1.9×10⁻⁴ ±7.7×10⁻⁵	16 ±4	11 ±1	0.9 ±0.5	548

The helium concentration was calculated with Eq. 3.28 for each He-plate impl using the average bubble size and density given in Table 4.3. The calculated He concentration is close to 1000 appm when the samples were annealed above 750°C. This indicates that the bubbles are in equilibrium and that most of the He atoms are in the bubbles. However, at 650°C, the calculated helium concentration is too low to consider the bubble in equilibrium, so most probably they are over-pressurized and/or a significant amount of the bubbles are still below the resolution limit of the TEM (<2 nm).

Table 4.3. Summary of the TEM study carried out in He-plates with 1000appm. The ± stands for the standard deviation of the distributions and measurements. The bubble average spacing, the grain boundary coverage and the He concentration are calculated with Eq. 3.19, Eq. 3.20 and Eq. 3.28, respectively.

The annealing temperature at which the bubble pressure reaches equilibrium with the surface energy is about 200-300°C lower than the reported by Chen et al. in 304L [173] where the He implantation was carried out at room temperature. Hence, the evolution of helium in nuclear internals and its effects depend significantly on the irradiation/implantation temperature. This result is in line with the observations from Zang et al. [174], where a change of bubble size and density was observed when a double temperature implantation, first low and then high temperature, was performed.

An increase of the bubble size due to a preferential absorption of vacancies without associated He would increase the calculated He concentration above the implantation concentration. The concentration results indicate that the annealing temperature did not increase the vacancies supply to the bubbles since the calculated He concentration is still below the implantation concentration.

4.3   Effect of He implantation on GB segregation

GB RIS is studied in order to predict the possible effects of the elemental enrichment/depletion on the GB strength and GB electrochemical activity/corrosivity during tensile tests in HTW. This study was performed at the FEI TALOS F200X in ETH Zurich. The point to point resolution of TALOS in STEM mode is about 0.16 nm, which provides more accurate results than most of the GB studies published so far. Moreover, TALOS can obtain elemental maps in minutes, thanks to the four detectors surrounding the sample and the high intensity of the electron beam.
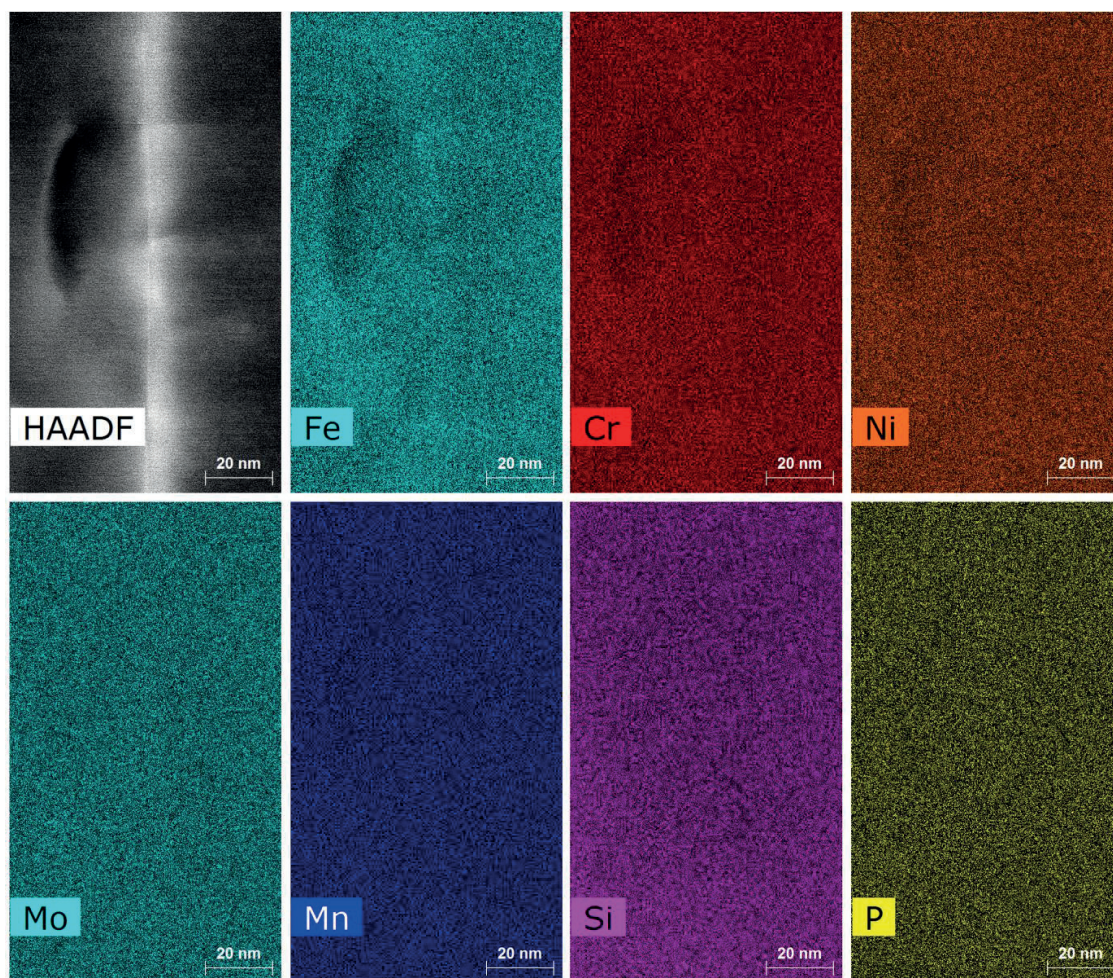
Figure 4.21. Non-quantitative distribution of the elemental composition on one GB region in the SA sample.

4.3.1 Elemental composition on SA GB

Prior to analysing the elemental composition of the as-implanted sample, the SA sample was studied in order to better assess the GB RIS after He-implantation. Three different GB regions were analysed. Figure 4.21 shows one of the analysed GB regions and the distribution of its elements. At a first glance, no GB segregation can be observed, neither enrichment nor depletion. The averaged elemental composition across the GB shown in Figure 4.22 confirms the homogeneity of the elements in the studied region. The three analysed GB showed the same results.
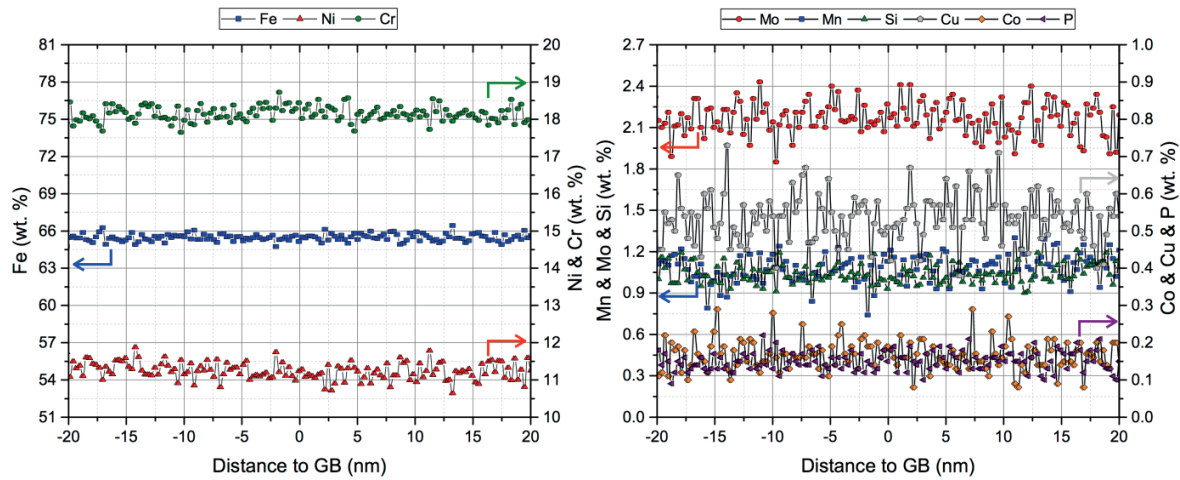
Figure 4.22. Averaged elemental composition profiles of the main alloying elements (left) and minor alloying elements (right) across the GB.

The elemental composition obtained agrees well with the chemical analysis performed in the original 316L block. The concentration of the main alloying elements is within $\pm 1\%$ of the chemical analysis shown in Table 3.1, being Ni below and Fe/Cr slightly above the expected values. The concentration of the minor alloying elements shows that the Si and Cu are twice the expected values (Figure 4.22). This is due to the production of characteristic X-rays coming from the sample holder (Cu) and the EDX detector (Si). The other elements are in agreement with the values in Table 3.1.

Although a homogeneous concentration in the GB region might be expected in SA 316L, previous studies showed enrichment of Cr and Mo on the GBs together with some Fe and Ni depletion [224, 225]. These studies performed the SA treatment cooling down the samples in air, whereas the samples studied here were quenched in water in order to avoid any type of GB segregation.

4.3.2   Elemental composition on as-implanted GB

Similarly to the SA sample, two GBs were analysed from the as-implanted sample with 1000 appm He. Figure 4.23 shows one of the analysed GB regions and the distribution of its elements. Again, the non-quantitative maps do not show clear RIS on the GB with the exception of Mo, where a lighter colour can be observed on the GB.

The averaged elemental composition across the GB of all the elements, except Mo, is shown in Figure 4.24. The GB concentrations are similar to the matrix concentrations. The concentration of Fe on the GB seems to be slightly below the matrix concentration, but the amount is too low to be clearly distinguished with this scale from the data scatter. Moreover, the concentration of Si, Co, Cu and P are slightly overestimated in detriment to the concentration of Ni. This is caused by the difficulties in removing the Bremsstrahlung contribution in the spectra. However, this overestimation does not affect the profile across the GB, since it is consistent in the entire region.
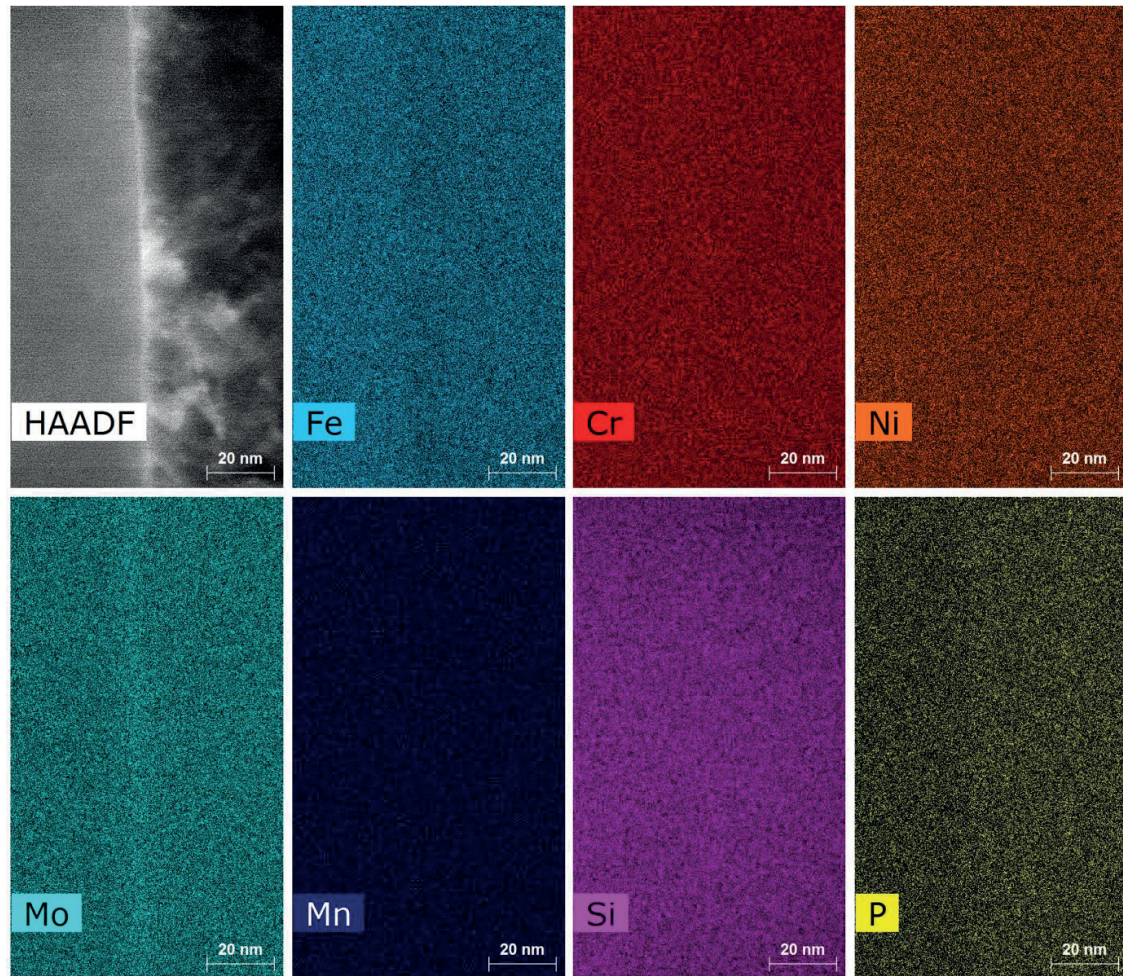
Figure 4.23. Non-quantitative distribution of the elemental composition on one GB region in the as-implanted sample with 1000 appm He.
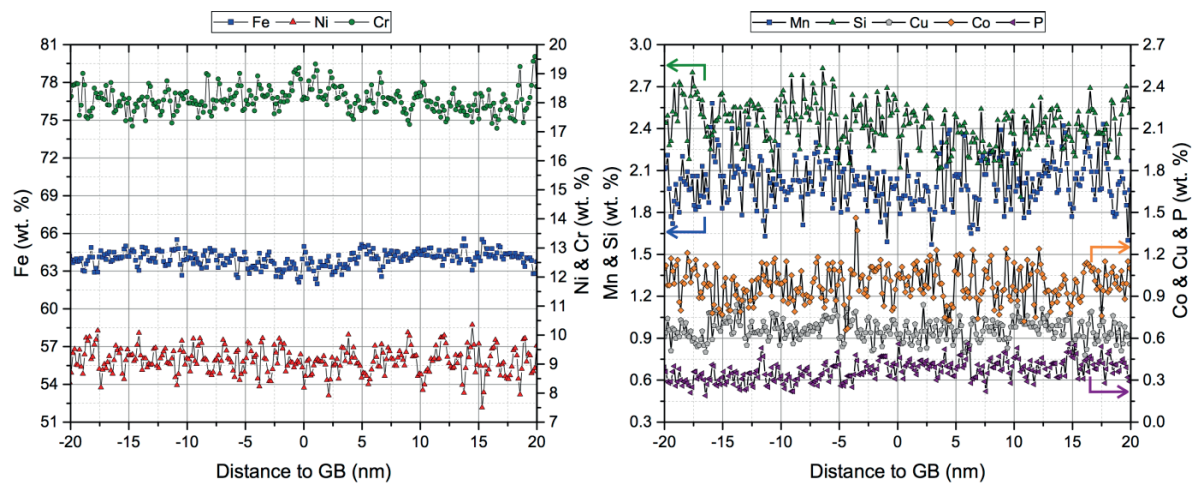
Figure 4.24. Averaged elemental composition profiles of the main alloying elements (left) and minor alloying elements (right) across the GB in the as-implanted sample with 1000 appm He.

Figure 4.25 shows the detailed concentration profiles of Mo, Fe and Cr on the two studied GBs. The calculated quantity of Mo in the matrix is similar to the SA condition, but the concentration on the GB

is almost 1% wt. (~3% wt.) higher than in the matrix (2.1 % wt.); which corresponds to about 50% higher concentration. The enrichment region is within the first 5 nm from the GB, and a slight depletion seems to occur at a distance of 10-15 nm from the GB. This result is expected since previous studies showed that radiation produces W-shape of Mo concentration on the GBs vicinity [49, 145]. On the other hand, Fe appears to be slightly depleted by ~0.5-1% wt. This amount corresponds to less than 1.5% of the matrix concentration so it is difficult to observe in the non-quantitative maps in Figure 4.23. The Fe depletion on GB is not unexpected as it has been already reported in previous studies [144]. Finally, Cr did not show any sign of depletion.
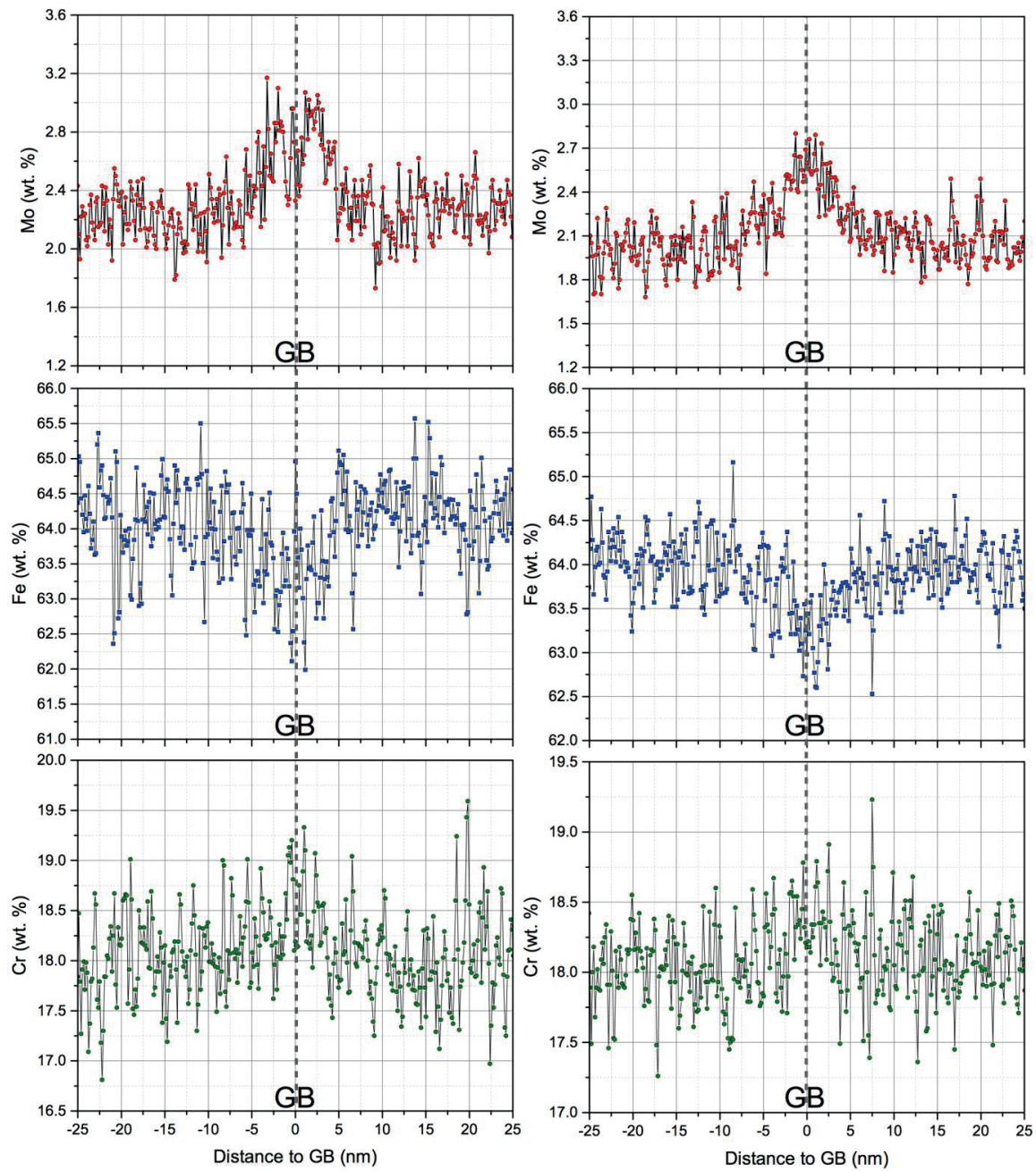
Figure 4.25. Averaged elemental composition profile of Mo, Fe and Cr across the GB.

In summary and as expected, no Cr depletion or Si enrichment occurred, which could significantly affect the SCC susceptibility, in contrast to the typical RIS developed after significant displacement damage (> 1 dpa).

4.4 He effects on IASCC

The tensile response (i.e. stress-strain curve), the fracture morphology and the deformation microstructure of the He-implanted and PIA samples were compared to the non-implanted SA and CW conditions. The effect of CW is also analysed here.

4.4.1 Tensile test results

The tensile properties of the samples tested in HTA and HTW were very similar for a given material condition. The results are discussed hereafter and summarized in Table 4.4.

4.4.1.1 Effect of CW

Figure 4.26 shows that the CW causes an increase of $Rp_{0.2\%}$ and UTS but a decrease of US in all conditions. The tensile properties at HTA and HTW are similar. Nevertheless, the results showed that a little difference on CW level can have a significant impact on the tensile properties. This effect is mainly produced by an inhomogeneous plastic deformation during the CW process by tensile testing a standard sample. The as-received sample (from manufacturing) had a diameter error (three times the standard deviation), along the gauge length, below 1%; whereas after the CW process this error increased up to 10%. Hence, the level of CW can vary up to 10% from the estimated value.

The true stress-strain curve of representative SA and CW samples tested in RTA show similar strain and stress levels after adding the CW level received by the CW sample prior to the test (Figure 4.27). This result is expected since the CW sample was manufactured from a previously deformed standard sample.
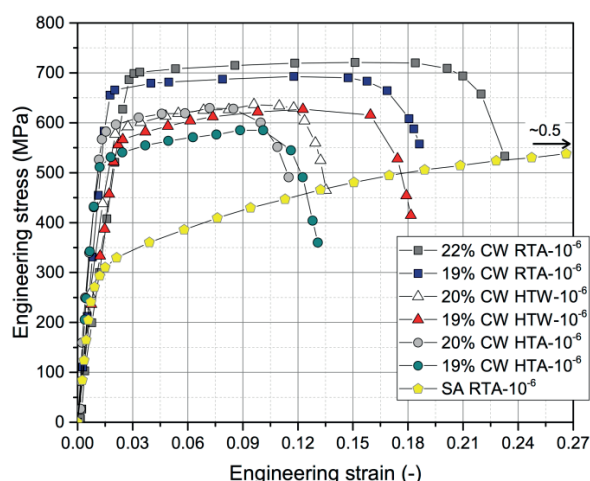
Figure 4.26. Engineering stress-strain curves in CW samples tested in RTA, HTA and HTW with slightly different CW. A representative SA sample tested in RTA is also included for comparison.
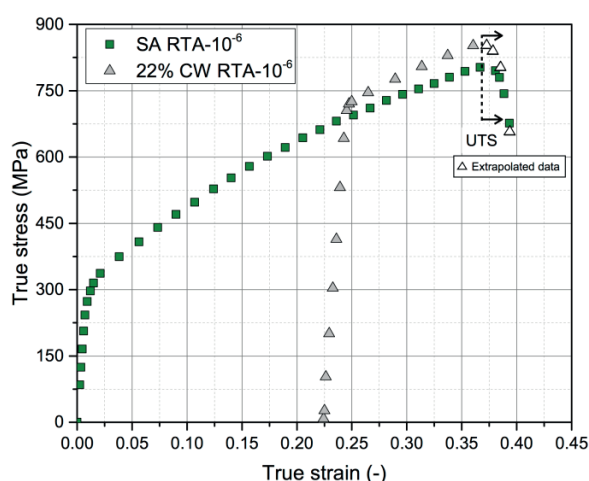
Figure 4.27. True stress-strain curves in a representative SA sample and in a 22% CW sample showing similar strain and stress levels after adding the level of CW performed.

In line with the results obtained in SA samples, the increase of temperature in air also caused a drop in $Rp_{0.2\%}$ of about 130 MPa (19%), in UTS of 100 MPa (14%), in US of 0.045 (39%) and in RA of 0.03

(3%) with respect to RTA values. The scatter of the results is significantly higher than in SA samples due to a slightly different CW levels for each specimen.

4.4.1.2   Effect of HTW Environment

The HTW effect in SA samples produced a remarkable softening with ~15 % decrease of $Rp_{0.2\%}$ as it was mentioned earlier in the subchapter 4.1. CW and He implanted samples, on the other hand, showed a moderate hardening and increase of $Rp_{0.2\%}$ and UTS in HTW of about ~5-10% with respect to the HTA properties. Note however that this observation is based on a single test only and might be rather related to the usual sample to sample scatter, due to small local variations in CW and/or displacement damage from He implantation (Figure 3.5).

4.4.1.3   Effect of He implantation and post-implantation annealing

He implantation resulted in a moderate but remarkable increase in $Rp_{0.2\%}$ and reduction in work hardening capacity (UTS - $Rp_{0.2\%}$) in as-implanted SA and CW samples at both, 300 appm (0.05 dpa) and 1000 appm (0.16 dpa) (Table 4.4). The hardening is comparable and consistent with other literature data of AuSS at the same level of displacement damage but without He. Thus, the hardening seems to be primarily due to the displacement damage and not to the He bubbles (Figure 4.28). According to the results of Odette and Lucas [226], the irradiation hardening resulting from a mixed spectrum can mainly be attributed to displacement damage. Odette and Lucas proposed a correlation to estimate the YS in terms of neutron dose (dpa) in 300-series SS irradiated and tested at about 300°C:

$$\Delta\sigma_y = 670\ (\pm 75)\left[1 - \exp\left(-\frac{dpa}{2}\right)\right]^{0.5} \qquad\qquad \text{Eq. 4.5}$$

The results of this work correlate fairly well with these data. The hardening after He-implantation at 1000 appm is higher than the values predicted by Odette and Lucas. This might be produced by the homogeneously distributed He nano-bubbles in the grains, which is estimated to be few tens of MPa and will be reported in the subchapter 4.5.
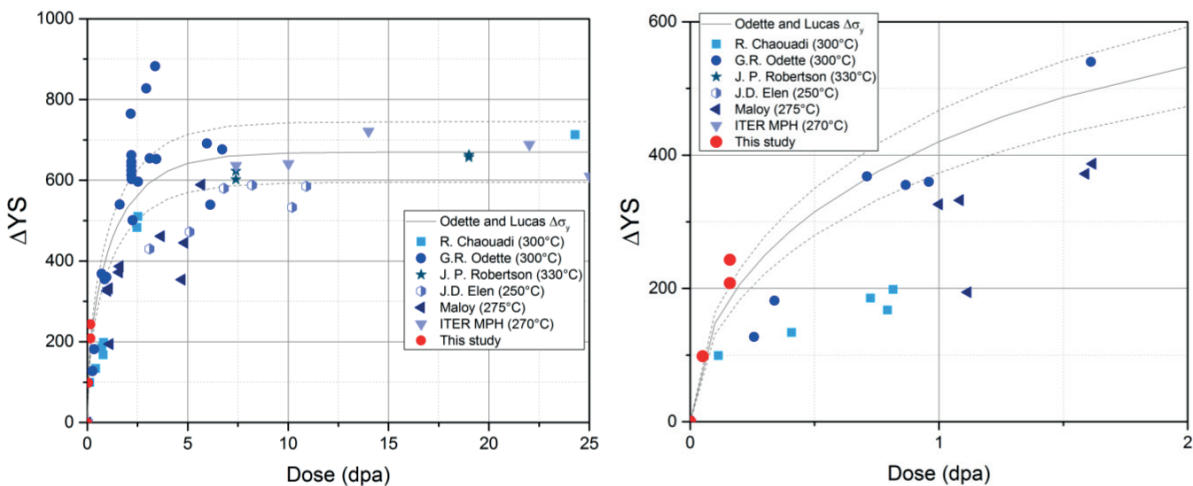
Figure 4.28. Comparison between the increase of YS with irradiation damage for tensile tests with He-implanted samples (300 and 1000 appm) in HTW and the Odette and Lucas equation w/o the error associated to the YS plateau (±75MPa) [226] (Left: Full does range. Right: Zoom of low dose range). References: R. Chaouadi - [227] , G.R. Odette - [226], J.P. Robertson - [47], J.D.Elen - [228], Maloy [216] and ITER MPH from Chaouadi [227].

In contrast to the $Rp_{0.2\%}$ and the UTS, the US was barely affected by He implantation in the SA materials (Figure 4.29-Figure 4.30). In CW materials, on the other hand, 1000 appm He implantation leads to drastic uniform elongation reduction, whereas the increase of $Rp_{0.2\%}$ and UTS was similar to the SA samples (Figure 4.31). The hardening induced by the CW and the implantation at 1000 appm He shifted the $Rp_{0.2\%}$ to above 750 MPa.
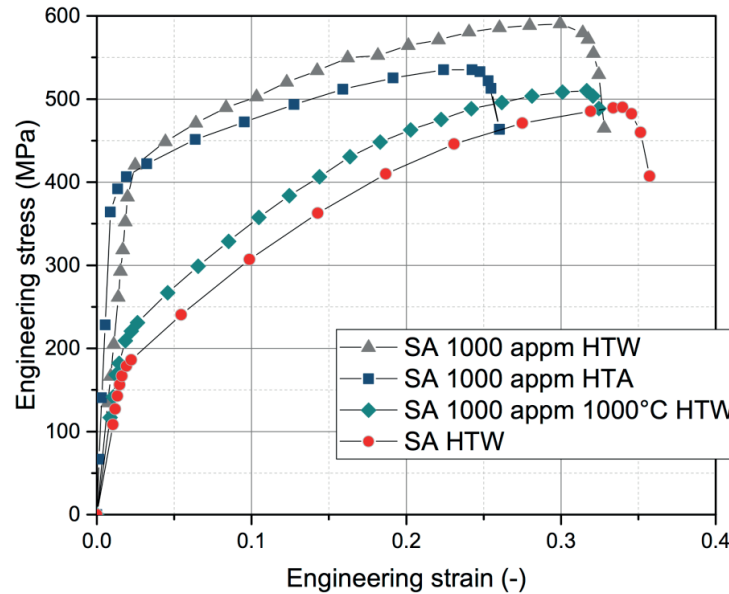
Figure 4.29. Engineering stress-strain curves in SA samples with/out 1000 appm He in HTW and in HTA. One implanted sample was annealed at 1000 °C for one hour (rhomboid symbol).
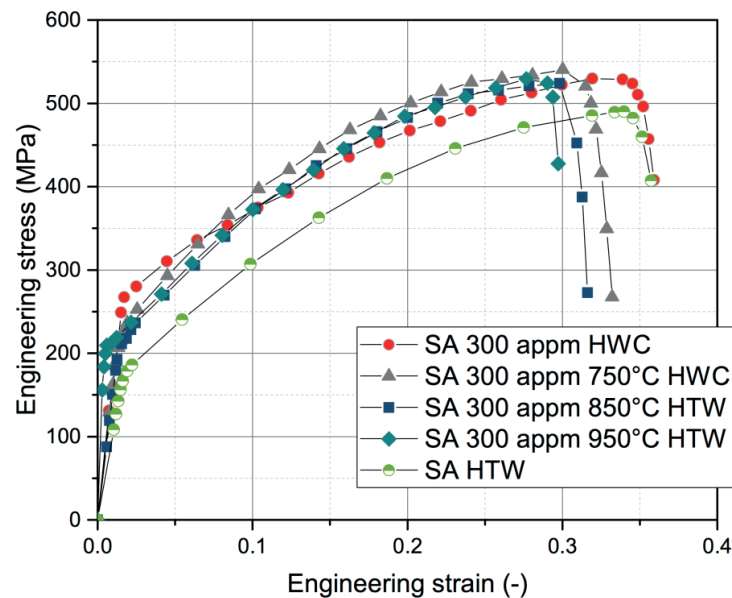
Figure 4.30. Engineering stress-strain curves in SA samples with/out 300 appm He in HTW. Three samples were annealed from 750 to 950 °C.

At this strength level, IG and TG SCC may have higher chance to be observed in AuSS in HTW in pre-cracked samples. However, it is difficult to be reproduced in accelerated SSRT with smooth samples. TG-C fracture was observed with full loss of macroscopic plastic deformation capacity in SSRT

performed with smooth samples in vacuum at 25 °C and 300 °C by Ullmaier and Chen [11], but both, displacement damage ($\geq$ 1 dpa) and He contents ($\geq$ 10'000 appm) where much higher than in this work.

Radiation-induced black dots damage, dislocation loops and strain hardening capacity (UTS - $Rp_{0.2\%}$) are fully recovered by PIA at temperatures above 750 °C (Figure 4.29 and Figure 4.30), but higher $Rp_{0.2\%}$ and UTS remain. No persistent irradiation hardening was observed following PIA from 550°C to 950°C with 100 appm, suggesting that the dpa level and the He concentration are not enough to substantially change $Rp_{0.2\%}$ (Table 4.4/Figure 4.32). However, UTS values were about 30 MPa above the SA tested in HTW. The He content alone cannot explain the UTS increase since $Rp_{0.2\%}$ should be also higher. Given that the UTS in HTA is the same for non-implanted samples and samples implanted with 100 appm, the combined effect of hydrogen and He might be the reason of the higher UTS in HTW.

Test conditions	He conc. (appm)	Heat treatment	$Rp_{0.2\%}$ (MPa)	UTS (MPa)	US	RA	Fracture mode
SA- HTA 10^{-6} s^{-1}	100	550°C-1h	205	547	0.25	0.76	100% TG-D
SA- HTW 10^{-6} s^{-1}	100	850°C-1h	179	523	0.25	0.58	91% TG-D 9% TG-C
SA- HTW 10^{-6} s^{-1}	100	950°C-1h	182	531	0.26	0.51	89% TG-D 11% TG-C
SA- HTW 10^{-6} s^{-1}	300	-	273	532	0.30	0.67	99.8% TG-D 0.2% TG-C
SA- HTW 10^{-6} s^{-1}	300	750°C-1h	220	541	0.26	0.52	83.6% TG-D 17.4% TG-C
SA- HTW 10^{-6} s^{-1}	300	850°C-1h	212	533	0.26	0.78	100% TG-D
SA- HTW 10^{-6} s^{-1}	300	950°C-1h	209	530	0.27	0.53	88.8% TG-D 12.2% TG-C
SA- HTW 10^{-6} s^{-1}	1000	-	418	594	0.26	0.67	99.3% TG-D 0.7% TG-C
SA- HTA 10^{-6} s^{-1}	1000	-	383	547	0.23	0.76	100% TG-D
SA- HTW 10^{-6} s^{-1}	1000	739°C-1h	298	n/a	n/a	n/a	n/a
SA- HTW 10^{-6} s^{-1}	1000	1000°C-1h	198	512	0.27	0.48	98% TG-D 2% TG-C
19% CW- RTA 10^{-6} s^{-1}	-	-	662	695	0.09	0.79	100% TG-D
22% CW- RTA 10^{-6} s^{-1}	-	-	692	723	0.14	0.73	100% TG-D
20% CW- HTA 10^{-6} s^{-1}	-	-	579	631	0.06	0.68	100% TG-D
19% CW- HTA 10^{-6} s^{-1}	-	-	515	590	0.08	0.79	100% TG-D
19% CW- HTW 10^{-6} s^{-1}	-	-	570	634	0.11	0.56	91% TG-D 9% TG-C
20% CW- HTW 10^{-6} s^{-1}	-	-	576	641	0.08	0.66	99.9% TG-D >0.1% TG-C
20% CW- HTW 10^{-6} s^{-1}	1000	-	734	740	0.013	0.61	100% TG-D
19% CW- HTW 10^{-7} s^{-1}	1000	-	787	790	0.001	0.54	97.5% TG-D 2.5% TG-C

Table 4.4. Summary of the engineering tensile test results.

The remaining higher $Rp_{0.2\%}$ and UTS after annealing at different temperatures are quite similar among the materials with the same He concentration (Figure 4.33). This effect mainly results from the He bubble hardening, which depends on the bubble size and density (e.g. DBH model [229, 230]), that in turn depend on the implantation conditions (dose, dose rate and temperature) and annealing temperature.

Indeed, dislocation loops and black dots formed during the He implantation are considered to be annealed after heat treatment above 750 °C for one hour (discussed later in 4.4.3 Deformation microstructure). This is in line with Tsay et al. [231], who showed that after a heat treatment above 650 °C no black dots remained and only 10% of the as-implanted loop population survived. Therefore, the remaining hardening observed in this work after annealing above 750 °C is certainly due to the He bubbles.
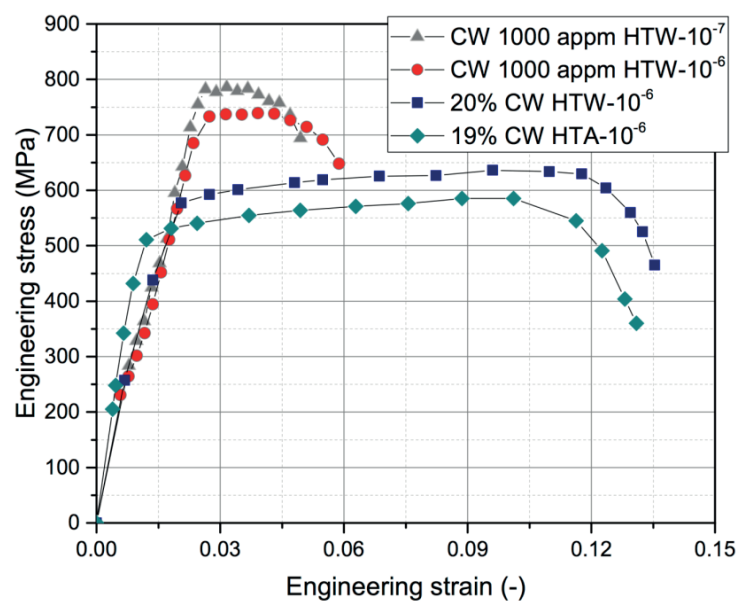
Figure 4.31. Engineering stress-strain curves of CW samples with/out 1000appm He implantation tested in HTW and in HTA.
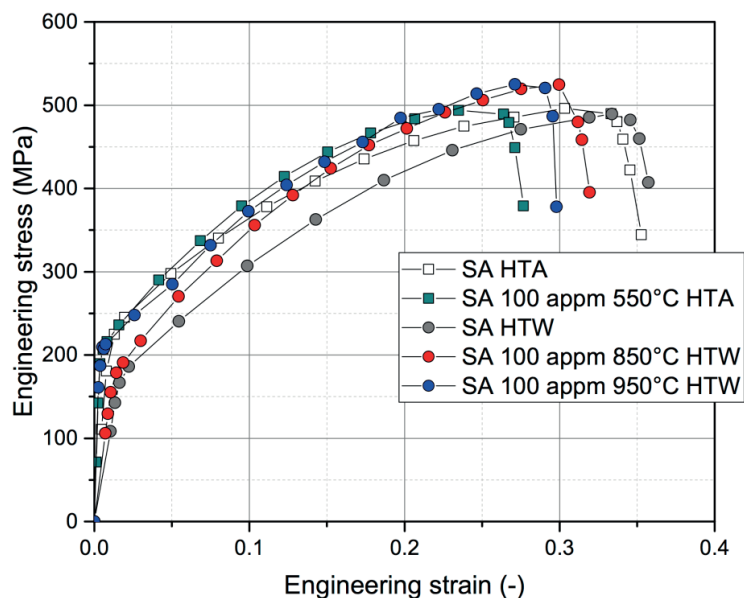
Figure 4.32. Engineering stress-strain curves of SA samples with/out 100appm He implantation tested in HTA (square symbols) and in HTW (circle symbols). All the implanted samples were PIA from 550 to 950°C for 1 hour.
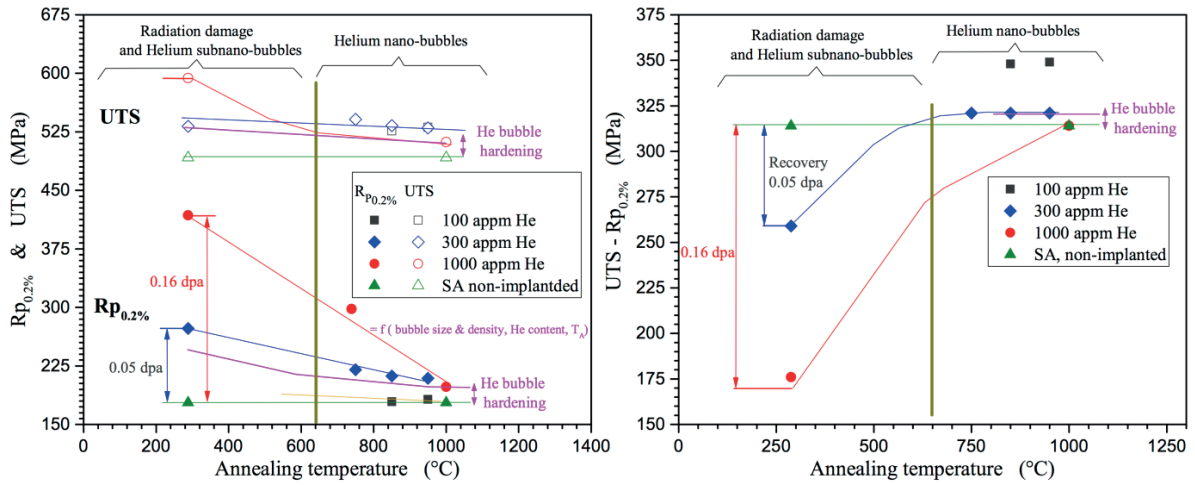
Figure 4.33. Rp$_{0.2\%}$ and UTS evolution (left) and strain hardening evolution (right) with increasing annealing temperature and varying He content. All samples tested in HTW.

4.4.2 Fracture mode

The dominant fracture mode of all material conditions in both, HTA and HTW, was TG-D fracture by microvoid formation, growth and coalescence (Figure 4.34-Figure 4.37). In HTW, minor and varying contributions of TG-C micro-cracks were detected starting at the water-wetted surface of the samples that ranged from 0 to 18% of the total fracture area (Table 4.4/Figure 4.8). No IG cracking was observed so far. Thus, neither CW, nor He implantation, nor PIA modified the failure process significantly. The absence of IG cracking is probably due to an insufficient He enrichment on the GBs as well as to the low probability of dislocation channelling occurrence in these samples. Indeed dislocation channelling comes into play for doses greater than about 0.1 dpa [150, 151].
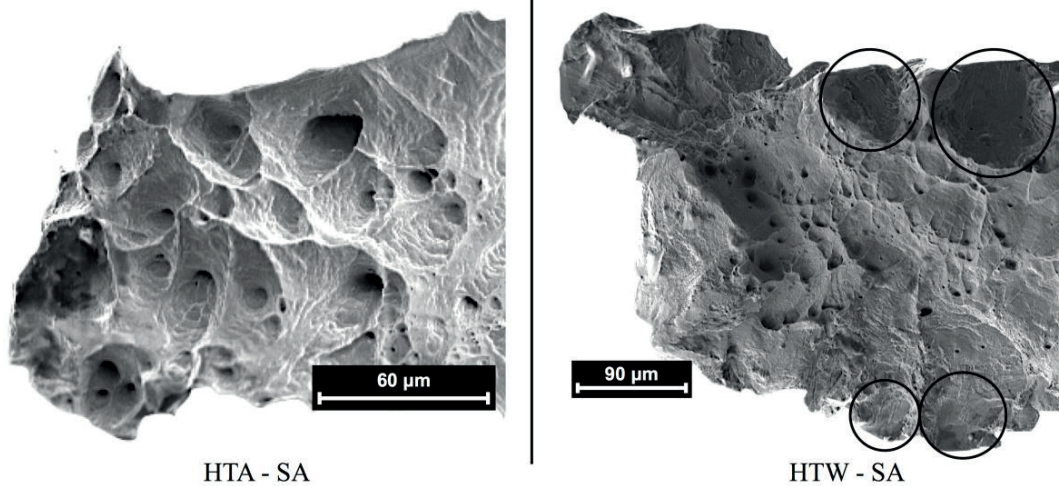
Figure 4.34. Excerpt of fracture surface of the SA samples tested in HTA and HTW. Both samples showed dominant TG-D fracture with minor contributions to TG-C in HTW (black circles).

The GB coverage after annealing is too low (<10%) to significantly reduce the GB strength with respect to the matrix and, at the same time, the matrix hardening is completely annealed above 750 °C, which again prevents any localized deformation. This result is consistent with the work of Jiao et al. [148], who showed that PIA reduced irradiation hardening and the degree of localized deformation. So

far, IG cracking of single GBs in micro-mechanical tests [10] and TG-C in polycrystalline materials [11] with He implantation were only observed at very high He contents with 20'000 and 10'000 appm He and higher irradiation damage (~1 dpa), respectively.
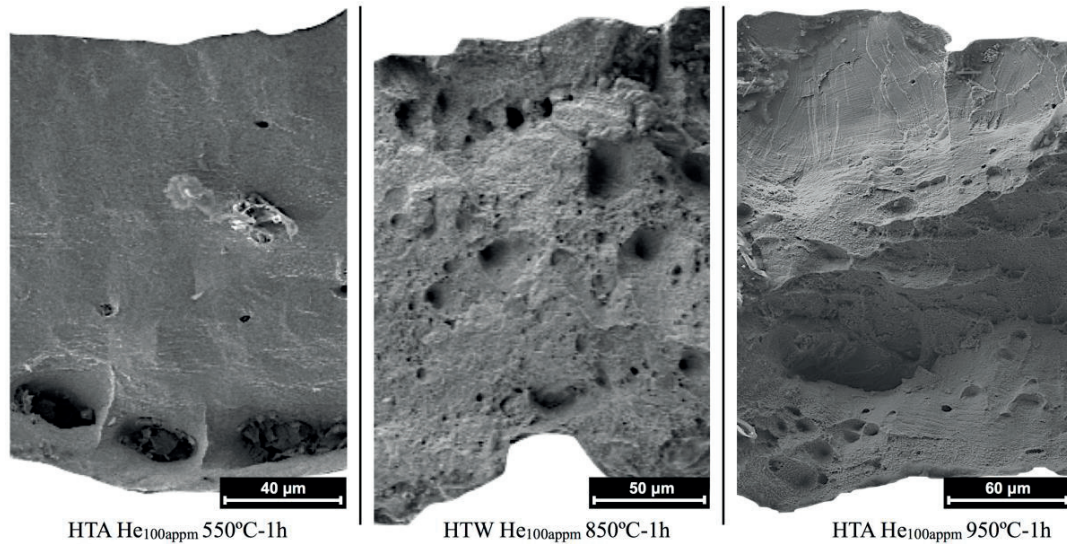
Figure 4.35. Excerpt of fracture surface of the samples tested with 100 appm in HTA and HTW. All the samples show dominant TG-D with minor contributions of TG-C in HTW.
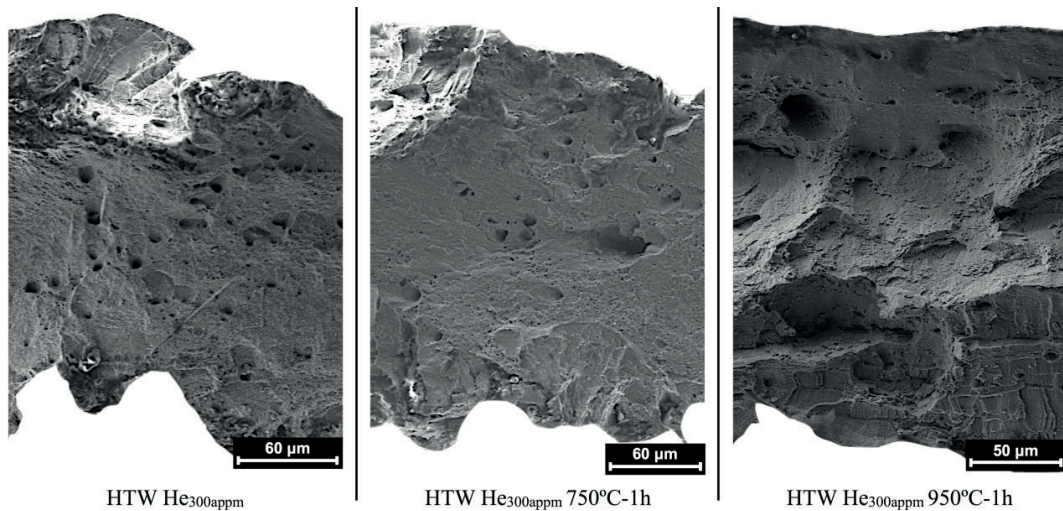
Figure 4.36. Excerpt of fracture surface of the samples tested with 300 appm. All the samples show dominant TG-D with minor contributions of TG-C in HTW.

As mentioned in the subchapter 4.1, the TG-C surface micro-cracks always formed at the water-touched sample surface along deformation bands and were only present in HTW conditions (Figure 4.8). He-implantation, PIA or CW did not significantly change the morphology of these surface cracks in HTW (Figure 4.38 and Figure 4.39). The TG-C cracks were observed along the whole gauge section, suggesting that they already initiated before the onset of necking. At a first glance, the number of cracks and their openings were smaller and the surface crack length and crack depth shorter in the He implanted samples, indicating that He bubbles could trap some of the hydrogen available from the environment and corrosion reactions, reducing the degree of hydrogen embrittlement by various mechanisms.

Generally, the ductile dimples on the fracture surface formed in the centre of the samples are smaller in HTW than in HTA, indicating that hydrogen could play a role in reducing the void size (Figure 4.34). This effect has been also reported by Matsuo et al. [93]. Apart from the TG-C surface cracks, He implantation did not contribute to any particular change on the fracture surface with 300 appm in as-implanted and annealed (up to 950°C) conditions (Figure 4.36). The as-implanted He samples with 1000 appm tested in HTA and HTW showed a fracture surface similar to the as-implanted 300 appm (Figure 4.37) [232]. Therefore, the ductile dimple size was similar to non-implanted materials for the same environment. This suggests that the nucleation sites for micro-void formation and the subsequent growth and coalescence processes are the same, and the He bubbles play a minor role in the ductile damage process. However, the PIA carried out at 1000°C changed significantly the appearance of the fracture surface (Figure 4.37). The rupture appearance is microscopically ductile with a minor contribution of TG-C fracture ($\sim$ 2%), but almost free of larger macroscopic dimples. The average He bubble diameter in this condition is about 60 nm, which is not far from the dimple diameters observed. Large He bubbles seem thus to affect the ductile damage process.
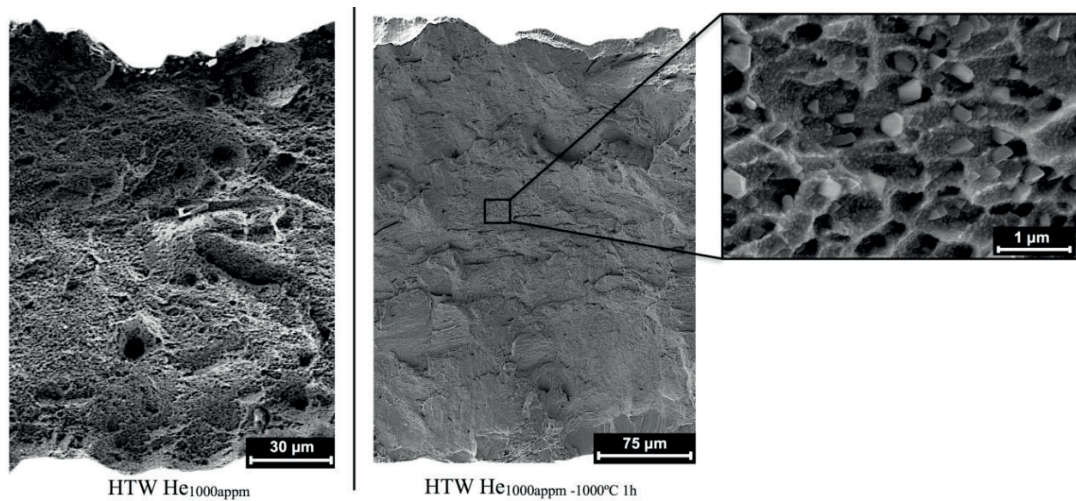
Figure 4.37. Excerpt of fracture surface of the samples tested with 1000 appm in HTW with/out PIA. A detail of the fracture surface is given for the heat-treated sample.
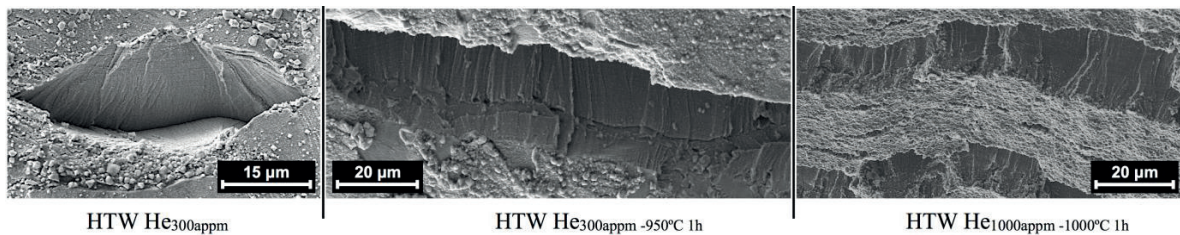
Figure 4.38. Typical TG-C cracks formed on the sample surface during SSRT in HTW with different sample conditions.

HTA SA HTA He$_{1000\ appm}$

HTW SA HTW He$_{300\ appm}$ HTW He$_{1000\ appm}$
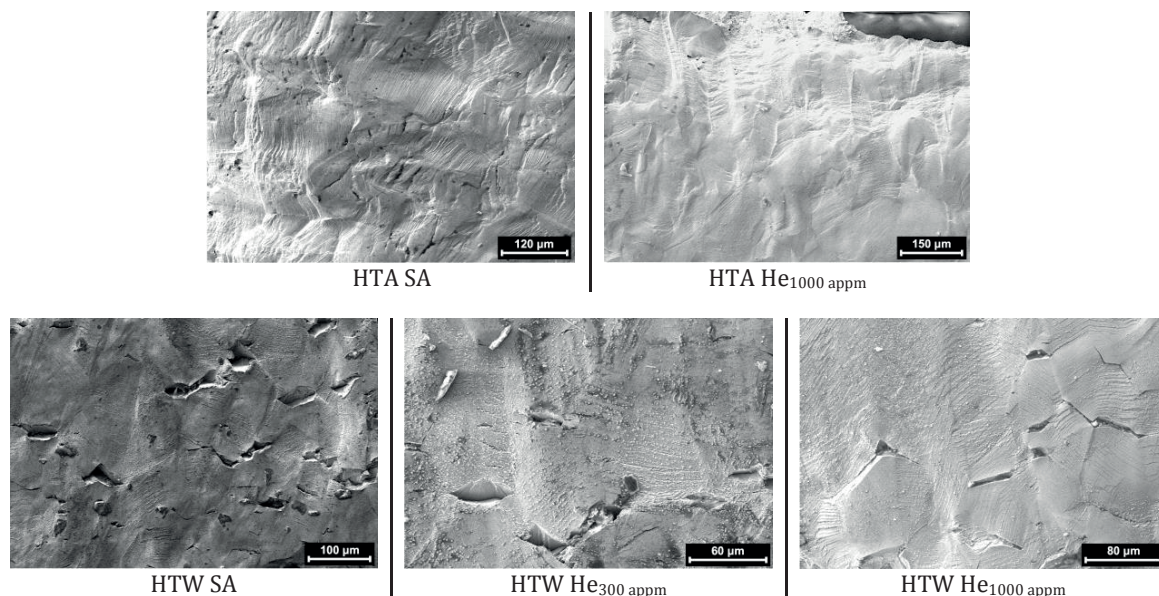
Figure 4.39. Sample surface detail of the samples tested in different environment and material conditions.

4.4.3 Deformation microstructure

TEM investigations revealed slightly different deformation microstructures between SA/CW and as-implanted He samples (Figure 4.40). All the TEM samples were taken from the gauge length outside the necking region and were thus plastically strained up to the US (e.g. ~ 30 % for SA non-implanted material). The sum of 20% CW and US for CW materials is similar to the SA ones. The CW materials with 1000 appm He had a highly deformed initial microstructure and hence, this made the differentiation of changes in deformation mechanism rather challenging.

SA and CW samples show a high dislocation density arranged in cell walls separated by relatively dislocation-free regions (Figure 4.40-A, -B and -G). Deformation bands, both twins and slip bands can be observed (Figure 4.41). As-implanted SA samples showed also a high density of dislocations, but well-developed dislocation arrangements were not identified (Figure 4.40-D,-F). Moreover, many black dots were observed in between the dislocation network, which could be irradiation defects (< 1 nm) that act as obstacles for dislocation motion. As-implanted CW samples, on the other hand, showed a microstructure that resembled that of SA samples, although the dislocation cells were generally less well defined (Figure 4.40-H). The similar structure is not surprising, since, on one hand, dislocation cells were already formed during CW and on the other hand, a part of the irradiation damage or He might be absorbed by the forest dislocation network during implantation.

The PIA samples also showed well-developed dislocation cell structures (Figure 4.40-C,-E). The implantation induced black dot damage and extended defects were completely recovered above ≥ 750 °C and the He bubbles were insufficient to produce a significant change in deformation structures (Figure 4.42). According to Holt [220], a requirement for 3D cell formation is high cross slip ability. A reduction of the dislocation cross slip ability, e.g. due to the black dots, can enhance the formation of localized planar deformation bands and prevent the formation of 3D dislocation cell structures. Thus, it is expected to have a more localized deformation in the He as-implanted samples. In fact, more deformation bands, mainly slip bands, were produced in such samples. This is consistent with the change of deformation microstructure which might be a precursor for IASCC. Jiao and Was in [154] have shown that IASCC susceptibility is more correlated to the degree of localized deformation than

other parameters like SFE, hardening or radiation-induced segregation. In the present study, the degree of localized deformation induced by the He bubbles and the He implantation damage is not enough to change substantially the deformation mode, hence higher radiation damage might be needed in order to produce IASCC.

SA - HTW

SA - HTA

SA - HTW He$_{1000\ appm}$ 1000°C-1h

SA - HTW He1000 appm

SA - HTW He$_{300\ appm}$ 750°C-1h

SA - HTW He300 appm

CW - HTW   CW- HTW He1000 appm
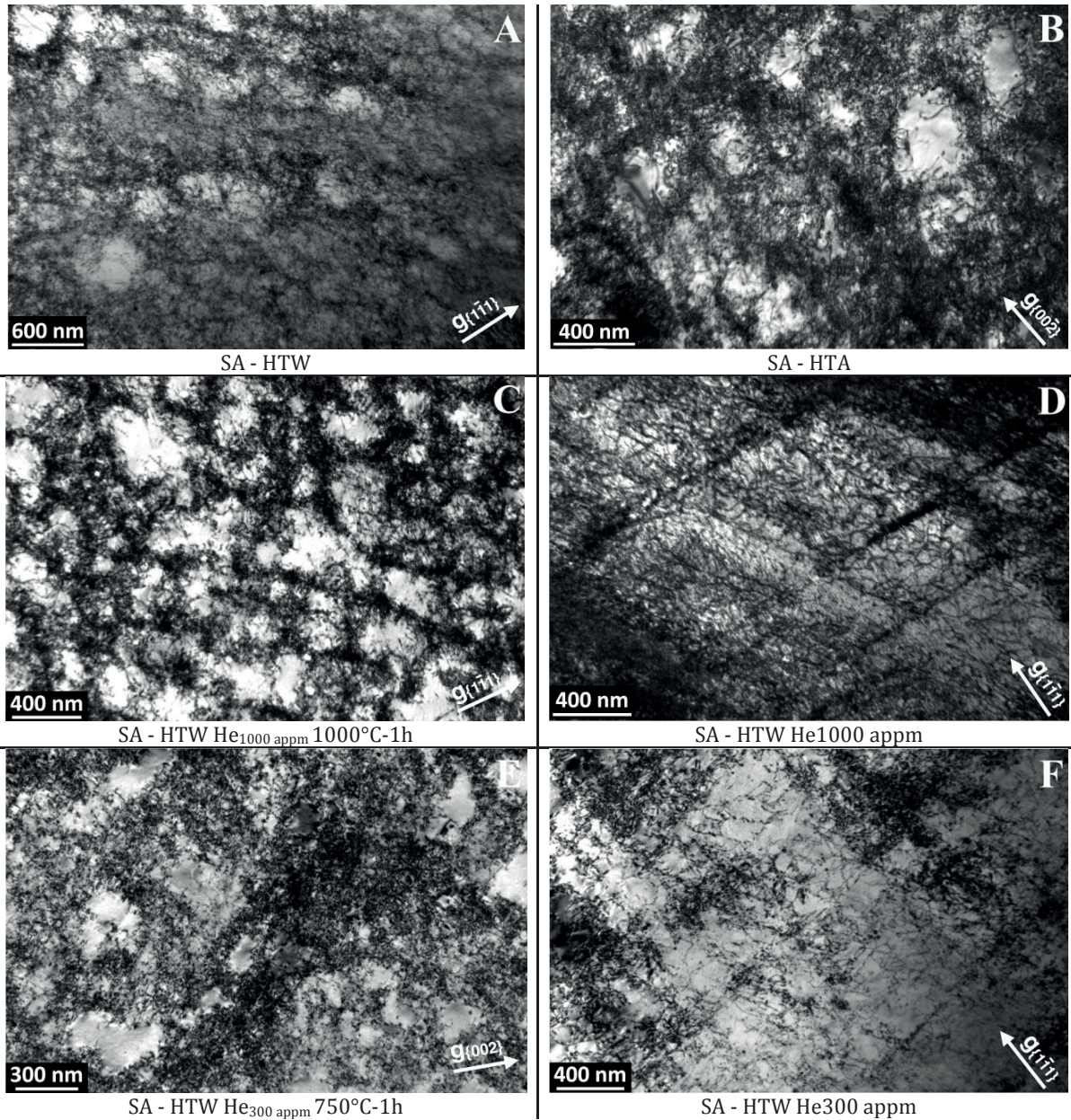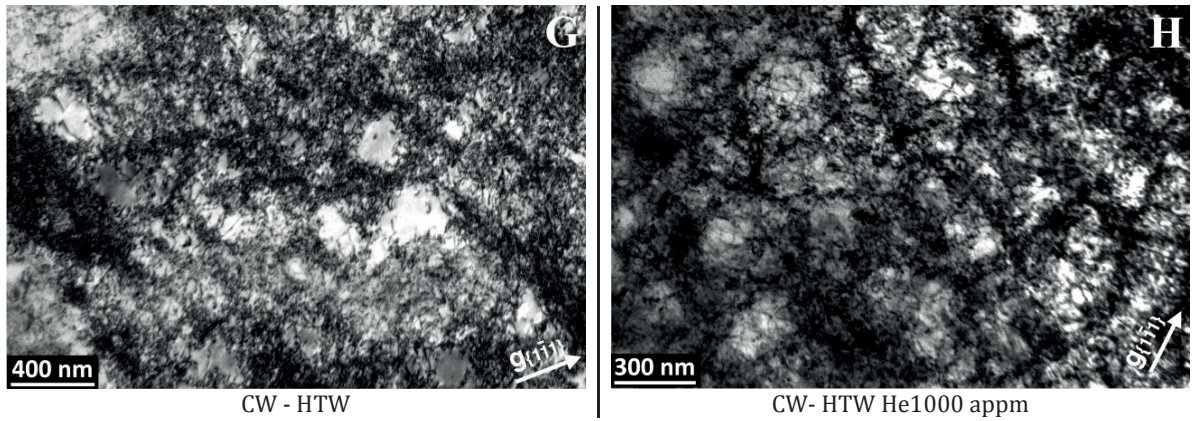
Figure 4.40. Bright field 2-beam dynamical micrographs of the TEM samples prepared from tested samples.

SA - HTA   SA - HTW He$_{1000\ appm}$
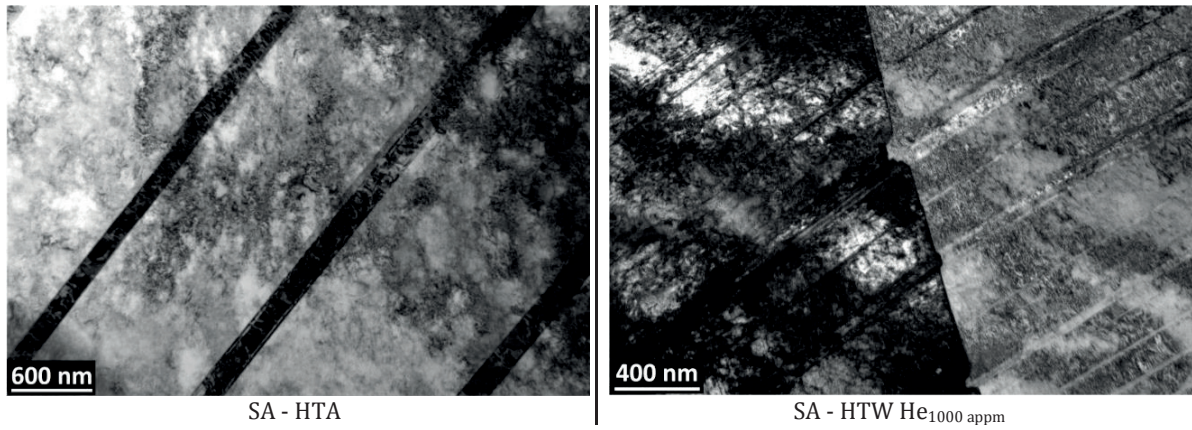
Figure 4.41. Bright field images of the deformation bands observed in the TEM samples.
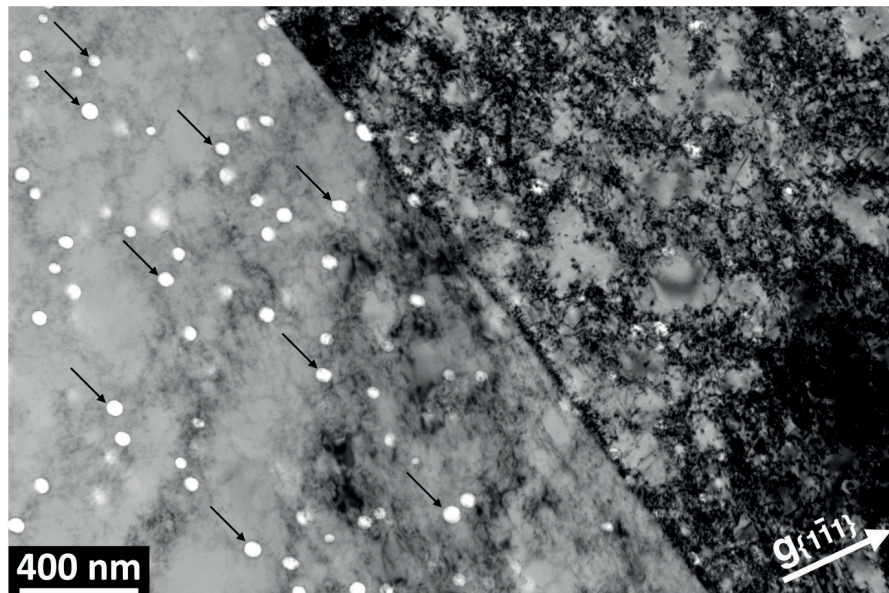
Figure 4.42. GB underfocus (~1 μm) bright field 2-beam dynamical micrograph (right) of the TEM sample prepared from the tested sample in HTW that contained 1000 appm and was heat-treated at 1000 °C. The black arrows point at some of the He bubbles (left) in a grain at kinematical conditions.

4.5 He hardening

He bubbles are considered to be weak obstacles for dislocation motion [39, 233]. The study of its effects on materials strength is rather challenging because the He implantation is always accompanied with the formation of black dots, dislocation loops, vacancy clusters and precipitates. Among all these defects, dislocation loops usually dominate the measured stress change below 450°C [49]. The results presented above showed that annealing above 750 °C for 1h results in a complete recovery of the irradiation damage, which is consistent with the reported results by Tsay et al [231]. Under this situation, the hardening contribution from obstacles other than He bubbles is negligible.

Table 4.5 contains the $\Delta Rp_{0.2\%}$ between the PIA samples and the non-implanted samples tested in HTW. The TEM samples prepared from the tensile samples were also used to study the He bubble average size, density and concentration. In this case, the He concentration calculated from the tested samples showed significantly higher values than the implantation concentration. This can be produced by the deformation of the bubbles along the tensile direction during the tensile test (up to 30% US), which produced an overestimation of the bubble pressure, due to the calculation of the radius with the bubble area instead of the bubble curvature (Figure 4.43).

Sample	PIA	He-conc. (appm)	$\Delta Rp_{0.2\%}$ (MPa)	Radii (nm)	Density (bubble/nm³)	GI spacing (L, nm)	Cal. He conc. (appm)
1	1000°C	1000	24	27.5 $\pm$7.4	1×10^{-7} $\pm7.3\times10^{-9}$	157 $\pm$38	1048
2	739°C	1000	123	1.8 $\pm$0.8	5.6×10^{-5} $\pm2.9\times10^{-6}$	22 $\pm$3	1943
3	950°C	300	29	17.6 $\pm$5.3	1×10^{-7} $\pm4.6\times10^{-9}$	179 $\pm$26	441
4	850°C	300	37	3.9 $\pm$2.1	1.6×10^{-6} $\pm7.9\times10^{-8}$	77 $\pm$9	404
5	750°C	300	45	1.4 $\pm$0.5	2.6×10^{-5} $\pm7\times10^{-7}$	30 $\pm$2	387

Table 4.5. Summary of the TEM study and the $\Delta Rp_{0.2\%}$ increase in the PIA samples tested in HTW. The $\pm$ stands for the standard deviation of the measurement (distribution & measurement).The bubble average spacing and the He concentration are calculated with Eq. 3.19 and Eq. 3.28, respectively.
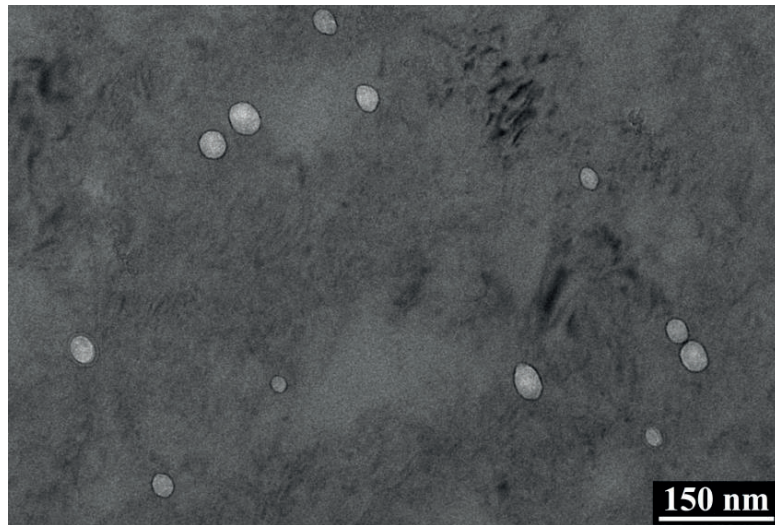
Figure 4.43. Bright field kinematical micrograph of the He implanted sample with 300 appm, annealed at 950°C and tested in HTW.

4.5.1 Hardening models

Combing the tensile results and the bubble information after PIA in Table 4.5, the He bubble hardening can be assessed using a hardening model. Different models have been proposed to calculate the stress required to move a dislocation through an array of small defects. The most used models to characterize the strength of small obstacles are the DBH, the Friedel Kroupa and Hirsh (FKH) and the Bacon, Kocks and Scattergood (BKS) models.

The DBH model (Eq. 4.6) has become the reference model for irradiation-induced defects [39, 49, 230, 233, 234]. This model assumes that a resolved shear stress produces a force perpendicular to the gliding dislocation, pushing the dislocation against a series of obstacles. The dislocation bows out between the obstacles until a critical shear stress is achieved and it overcomes the obstacle/s. The stress needed to overcome a given obstacle depends on the barrier strength or hardening coefficient (α). Lucas in [233] proposed a hardening coefficient for small bubbles of 1/5. In the BDH model, the length of the free dislocation segment is equal to the mean distance between the centres of the obstacles ($l = 1/\sqrt{Nd}$), and it is considered to be appropriate for α-values greater than about 1/4 [235].

The FKH model (Eq. 4.7) was developed using an infinitely long straight edge dislocation interacting with a distribution of prismatic loops or cavities [50, 230, 236]. In this model, the effective interparticle spacing is increased compared to the planar geometric spacing as described in the DBH model. As a result, there is less extensive dislocation bowing than in the DBH model so the dislocation breakaway occurs at lower stresses. This model is considered to be appropriate for α-values lower than about 1/4 [235]. Kroupa and Hirsch in [236] proposed a hardening coefficient for cavity clusters of 1/10.

The BKS model (Eq. 4.8) includes dislocation self-interaction and finite size of randomly spatially distributed and impenetrable spherical defects [50, 237]. The factor $\frac{1}{2\pi}[\ln(L/b)]^{-1/2}$ accounts for the interaction over one bowing loop and the factor $[\ln(D'/b) + 0.7]^{3/2}$ takes into account the mutual loop interaction and the randomness of the obstacle array.

The FKH model was shown to be adequate for weak obstacles ($\alpha<0.25$) and the DBH for strong obstacles ($\alpha>0.25$) [238]. However, both, the FKH and the DBH models, are based on geometrically distributed obstacles, whereas the BKS model is more realistic since it takes into account the randomness of the distribution. The selection of the model is not straightforward since the estimated barrier strength of the He bubbles for the FKH and DBH models is on the limit of both models ($0.1<\alpha<0.2$), and should be lower than impenetrable ($\alpha=1$) for the BKS model. Each model has its pros and cons, for this reason, all the models were considered in this study in order to clarify the best model and its parameters for assessing the He bubble hardening.

$$\Delta\sigma_y = \alpha_i\,M\mu b(N_i d_i)^{1/2} \qquad\qquad \text{Eq. 4.6}$$

$$\Delta\sigma_y = \alpha_i\,M\mu b r_i(N_i)^{2/3} \qquad\qquad \text{Eq. 4.7}$$

$$\Delta\sigma_y = \alpha_i M\mu b(N_i d_i)^{1/2}\frac{1}{2\pi}\left[\ln\left(\frac{l}{b}\right)\right]^{-1/2}\left[\ln\left(\frac{D'}{b}\right)+0.7\right]^{3/2} \qquad\qquad \text{Eq. 4.8}$$

where i is the type of defect (voids, bubbles, dislocation loop, etc.), M is the Taylor factor ($\sim$3.06), μ is the shear modulus ($\sim$76 GPa), b is the Burgers vector for fcc ($\sim$0.255 nm), N_i is the particle density of type i defects, d_i is the diameter of type i defects, l is the obstacle spacing ($l = 1/\sqrt{Nd}$) and D' is the effective obstacle diameter $\left(D' = \frac{d \cdot l}{d+l}\right)$.

4.5.2 Hardening models evaluation

The YS increase is directly proportional to the hardening coefficient in all the hardening models (Eq. 4.6-Eq. 4.8). Although some hardening coefficients have been found in the literature [233, 50, 236], the TEM observations and the results obtained from the SSRT in HTW summarized in Table 4.5 are used to estimate the hardening coefficients for each model.

Figure 4.44-Figure 4.46 show the α-values calculated for each data set and model according to Eq. 4.6-Eq. 4.8. The FKH and the DBH models showed an increase of the hardening coefficient with increasing bubble diameter, whereas the BKS model has a relatively constant hardening coefficient ($\alpha_{avg} \approx 0.3$). These results are consistent with the simulations from Sobie et al. [50], where they observed an increase of the hardening coefficient with the void size using the DBH model, but a constant coefficient using the BKS model. However, the experimental hardening coefficients found for helium bubbles in this study (316L) are two or even three times smaller than the ones reported by Sobie et al. [50] with voids in iron. The most plausible explanation is that the hardening coefficient depends on the temperature at which the simulations/tests are carried out, the material structure and the helium/void ratio [51]. On the other hand, Peng and Dai [239] found a hardening coefficient of about 0.1 for He bubbles of 1.5 nm using the DBH model. This result is close to the present observations. The temperature dependence and the size effect were also confirmed by the dislocation dynamic simulations reported by Monnet [240]; the stress saturated at a certain defect size and was significantly affected by temperatures from 0 K to room temperature. However, Monnet's simulations [240] with the BKS model showed an increase of hardening with the defect size, which differs from the experimental results presented here and the simulations from Sobie et al. [241].

113
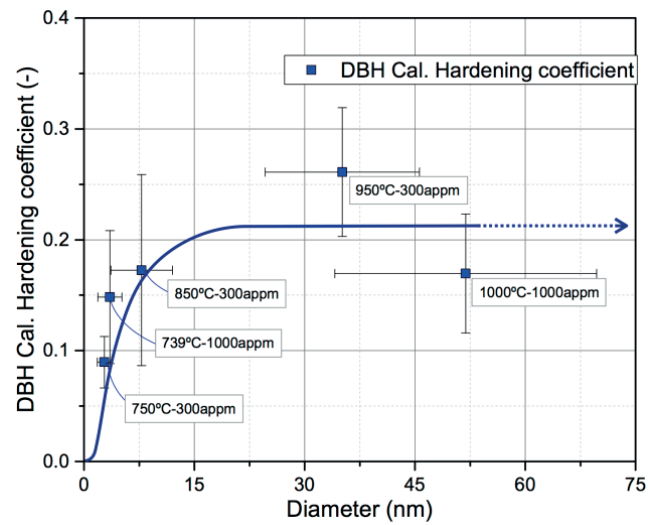
Figure 4.44. Calculated hardening coefficient to fit the experimental results with the DBH model versus the average bubble diameter.
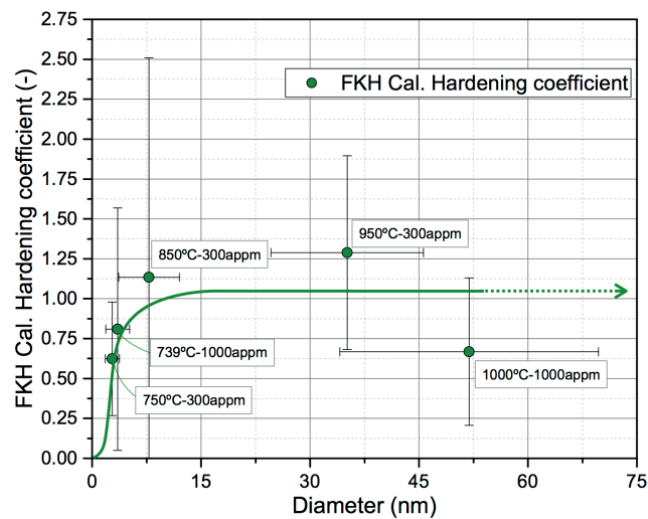
Figure 4.45. Calculated hardening coefficient to fit the experimental results with the FKH model versus the average bubble diameter.
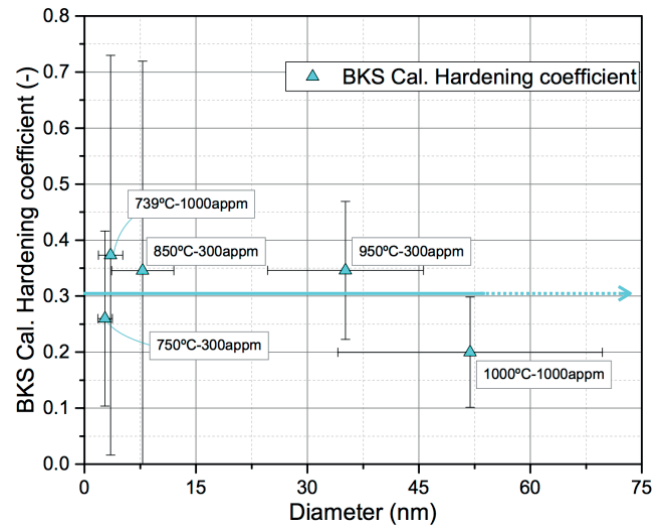
Figure 4.46. Calculated hardening coefficient to fit the experimental results with the BKS model versus the average bubble diameter.

None of the studies published so far used values of the He bubble hardening coefficient similar to the ones obtained here [49, 233, 236]. Usually, a constant hardening coefficient is used for a given type of defect, which leads to erroneous prediction of the YS increase when the FKH and the DBH models are used. It is evident that there is a significant difference between the α-values calculated with the FKH model and the DBH/BKS models. This difference is produced by the consideration of higher defect spacing in the FKH model as it is shown in Figure 4.47. The average obstacle spacing is about 5.6 times bigger in the FKH than in the DBH. In the FKH model, only the defects that are interacting with the gliding dislocations are considered in the calculation since it is assumed that the forces exerted on the gliding dislocations are concentrated very close to the defect (<2r, being r the defect radius) and hence can be regarded as point defects. On the other hand, the DBH model takes into account all the defects regardless of the ones interacting or not with dislocations so the hardening coefficient might be underestimated with this model.
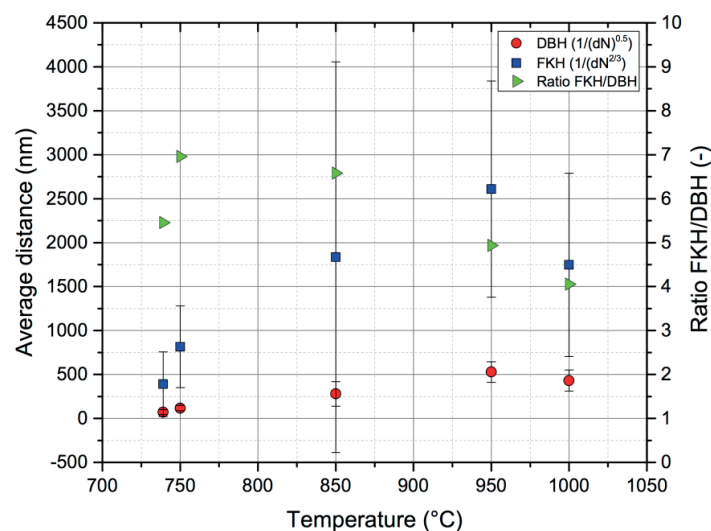
Figure 4.47. Average obstacle spacing calculated with the DBH and the FKH models and their ratio versus temperature.

The predicted hardening coefficients for the DBH and FKH models were extrapolated to a curve that depends on the bubble diameter (coloured curves in Figure 4.44 and Figure 4.45). The measured bubble diameters for each sample were distributed in incremental bars each one with a range of 0.25 nm. The $\Delta Rp_{0.2\%}$ was calculated for each bar taking into account the variation of the hardening coefficient. For short-range obstacles, Bement in [230] proposed a root-sum-square (RSS) and a linear sum for obstacles for similar barrier strength and, for many similar weak and few strong obstacles, respectively. In the present case, the He bubble hardening coefficient varies significantly with the diameter so the total $\Delta Rp_{0.2\%}$ was assumed to follow a superposition law [242]:

$$\Delta Rp_{0.2\%T} = \left(\sum \Delta Rp_{0.2\%}^{\xi} \right)^{\frac{1}{\xi}}$$

Eq. 4.9

Where $\Delta Rp_{0.2\%}$ is the increase of YS for a group of bubble sizes and $\Delta Rp_{0.2\%T}$ is the total increase of YS. The value of ξ can be determined minimizing the least square error between the sum of the different contributions and the tensile result:

$$Variance = \sigma^2 = \frac{1}{5} \sum_{i=1}^{5} \left(\Delta Rp_{i,0.2\%tensile} - \left(\sum \Delta Rp_{i,0.2\%}^{n} \right)^{1/\xi} \right)^2$$

Eq. 4.10

Where the subscript i denotes the test and the bubble information for each condition given in Table 4.5. Table 4.6 shows that the optimum ξ value is 1.7 and 2.5 for the FKH and DBH models, respectively. These results are quite close to Sobie et al. in [50], where they used the superposition law to study the simultaneous effect of voids and SIA loops on hardening.

The calculated $\Delta Rp_{0.2\%T}$ and the tensile results are summarized in Table 4.7. All the models describe the experimental results fairly well as it is shown in Figure 4.48. Forcing the slope of the plot between the tensile and the calculated $\Delta Rp_{0.2\%}$ to pass through the origin, one can obtain the fit of the linear regression. With the current scenario, the DBH model has the slope closest to one but the highest least square error (residual sum of squares divided by the number of data points). The BKS model gives a fair estimation of the tensile results (slope 0.88) and the lowest error. Besides, the hardening coefficient of the BKS model does not change with the particle size and hence, the sources of error are minimized. The error in the FKH model is in between the BKS and DBH models and the slope is very close to one, indicating that this model can successfully represent the hardness produced by He bubbles.

FKH model		DBH model	
ξ	σ^2	ξ	σ^2
1.35	2022	1.9	1307
1.5	536	2	850
1.6	242	2.3	304
1.65	190	2.4	256
1.7	176	2.45	244
1.75	188	2.5	239
1.8	219	2.55	239
1.9	312	2.7	262

Table 4.6. Iteration results to obtain the ξ value that minimizes the least square error for the FKH and DBH models.

Sample	Test $\Delta Rp_{0.2\%}$ (MPa)	FKH $\Delta Rp_{0.2\%}$ (MPa)	DBH $\Delta Rp_{0.2\%}$ (MPa)	BKS $\Delta Rp_{0.2\%}$ (MPa)
1000°C-1000 appm	24	25	18	37
739°C-1000 appm	123	121	116	101

950°C-300 appm	29	5	10	26
850°C-300 appm	37	26	30	32
750°C-300 appm	45	58	72	53
Regression (Figure 4.48)	Slope 1 R^2 - 1	Slope 0.96$\pm$0.10 R^2 - 0.96	Slope 0.97$\pm$0.12 R^2 - 0.94	Slope 0.88$\pm$0.08 R^2 - 0.97

Table 4.7. Experimental $\Delta Rp_{0.2\%}$ from tensile tests and calculated $\Delta Rp_{0.2\%}$ with different hardening coefficient models.

It is difficult to evaluate which model is more physically realistic, but it seems plausible that the hardening coefficient increase with the defect size, that the hardening coefficient has a tendency to unity and, that only the defects interacting with gliding dislocations are taken into account. The FKH model appears to be the model with these characteristics and perhaps the one with more physical meaning among the three models analysed.
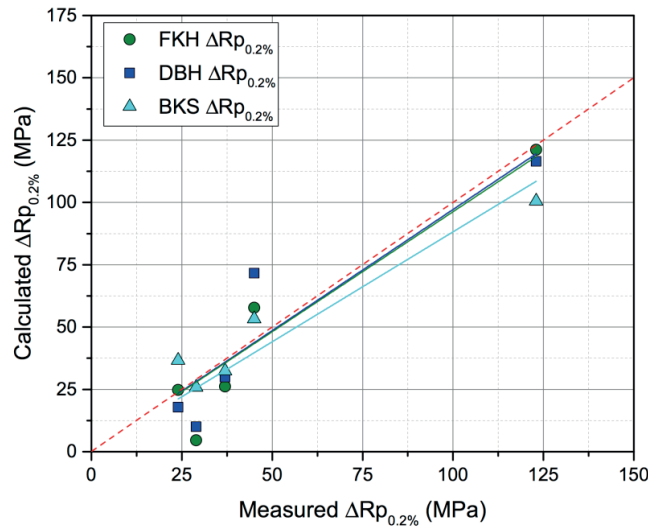
Figure 4.48. Comparison between the calculated $\Delta Rp_{0.2\%T}$ for the FKH, DBH and BKS models versus the measured tensile $\Delta Rp_{0.2\%}$.

Deo et al. mentioned in [243] that experimental observations from Maloy et al. in [244] suggested that He did not affect $Rp_{0.2\%}$. Those experiments were based on the He production in an accelerator at 50-164°C. The resulting He bubbles were small (< 1nm diameter) and the damage produced in the material was high. According to Figure 4.44-Figure 4.45, the helium hardening contribution below 5 nm is limited, but at this diameter size the bubble density is one or two orders of magnitude higher and this might compensate for the low hardening coefficient. Nevertheless, the hardening produced by the irradiation damage above 5-10 dpa saturates so it is not possible to assess the He contribution in those conditions using tensile tests. Instead, nanoindentation tests would better assess the He effect as observed by Hunn et al. [245] and Camus [246].

4.6 Nanoindentation

A spherical tip of radius 10 μm was used to perform nanoindentation tests in SA, CW, as-implanted SA and PIA plates. Figure 4.49 shows the matrix of indents performed in different GB for each condition. This approach allowed assessing the indentation yield stress at 0.2% strain ($Rp_{ind\ 0.2\%}$), the hardness and the strain hardening exponent (n) change with the specimen microstructure and grain-to-grain misorientation. The results were compared with the corresponding changes of the tensile

parameters (YS, strain-hardening, etc.). While a number of empirical calibrations between macro-indentation and tensile properties have already been proposed for Berkovich tips, these tests provide new information to test the validity of the existing calibrations and to propose more adequate ones. Figure 4.50 shows the indentation properties of the samples obtained from the ISS curves.
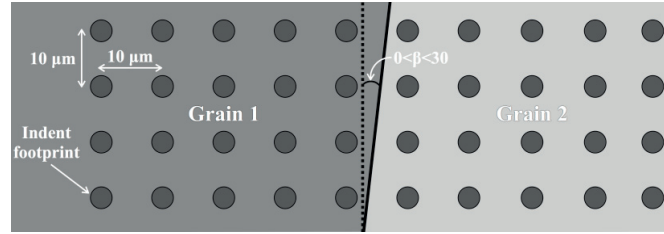
Figure 4.49. Schematic representation of the indentation test matrix carried out in GBs. The minimum indent to indent separation is 10 μm.
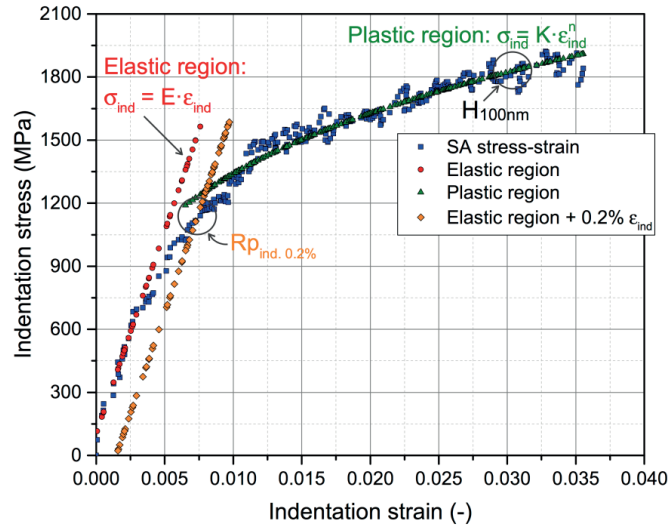
Figure 4.50. Stress-strain curve of a spherical indentation test in the SA sample showing the parameters studied: the indentation yield strength ($Rp_{ind\ 0.2\%}$), the hardness (H), the hardening coefficient (n) and the hardening constant (K).

4.6.1   Grain boundary effect

Different GBs have been studied for each sample condition in order to assess whether He weakens the GB in comparison to SA and CW samples. Figure 4.51 shows the $Rp_{ind\ 0.2\%}$ and the hardening change for two different GBs in the PIA at 650°C. In GB-1, a decrease of $Rp_{ind\ 0.2\%}$ and hardness can be observed once the GB is crossed whereas in GB-7, this change does not occur and the properties of both grains are similar. The hardness and the $Rp_{ind\ 0.2\%}$ decrease/increase occurred within a region of 5μm from the GB. The plasticity parameters (K and n) seem to be insensitive to the grain orientation (Figure 4.52). This result was also observed in all the other conditions (e.g. Figure 4.53 in the CW sample), but no clear GB weakening was found. This is in line with the tensile results in HTW where no IASCC was found.
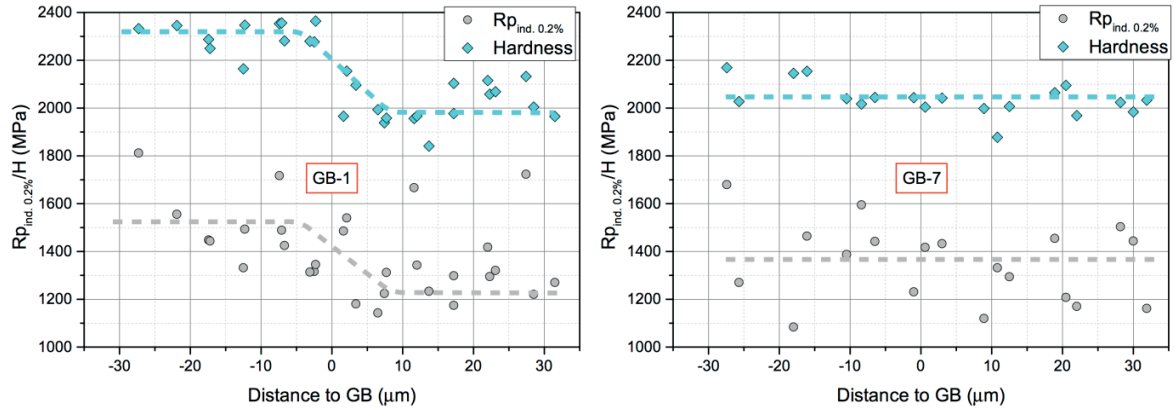
Figure 4.51. Rp$_{ind\ 0.2\%}$ and hardness trend as a function in distance from the GB, GB-1 (left) and GB-7 (right), for two different GBs from the PIA at 650°C sample.
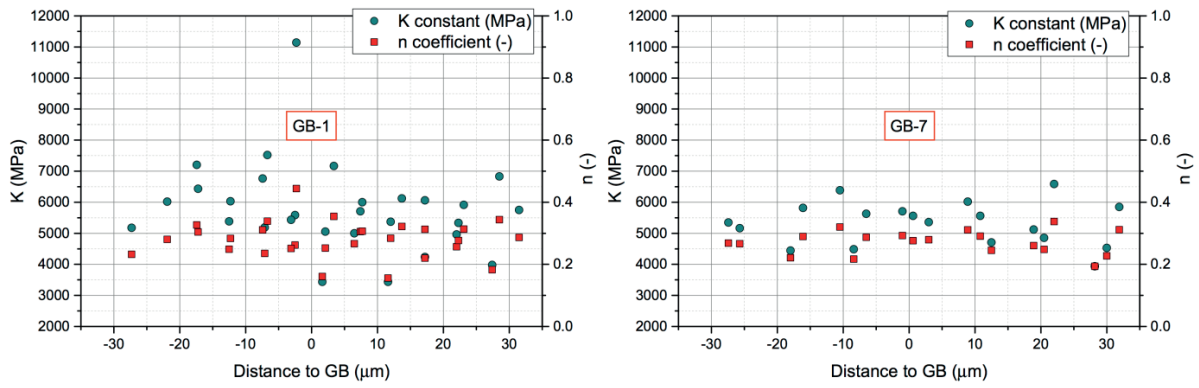
Figure 4.52. K and n trend as a function in distance from the GB for two different GBs, GB-1 (left) and GB-7 (right), from the PIA at 650°C sample.
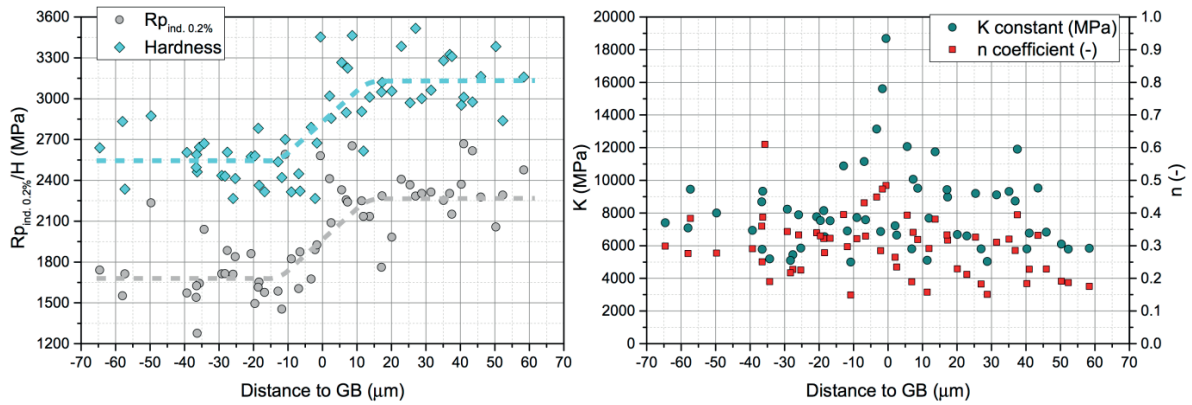
Figure 4.53. Trends in indentation properties as a function in distance from the GB-1 of the CW sample for Rp$_{ind\ 0.2\%}$ and hardness (left) and K and n (right).

4.6.2 Effect of grain orientation

It is difficult to assess the change in indentation properties in more than fifty GBs with more than one thousand indents, six different sample conditions and different grain orientations. Given that the nanoindentation technique and/or the He concentration in the GBs did not reveal noticeable GB effects, the average properties of each grain were studied. Figure 4.54 and Figure 4.55 show the

average indentation properties obtained in each grain with a distance above 5 um from the GB in order to neglect grain to grain effects.

The grain to grain misorientation had a limited effect on the $Rp_{ind\ 0.2\%}$ and hardness with average changes within 15% in SA, as-implanted and PIA samples (Figure 4.54). Usually, the average values on each side of the GB were within the standard deviation of the neighbouring grain. However, the CW samples showed clear grain to grain misorientation effect on the indentation properties between neighbouring grains with differences that in some cases exceeded 30% of the neighbouring average grain. This result is not unexpected. The CW level was obtained by tensile testing the samples to 20% strain. Doing so, the plastic deformation is heterogeneous and some grains contained many deformation bands and other less. Overall, the $Rp_{ind\ 0.2\%}$ and hardness were higher in all the grains in comparison to the other conditions. Generally, it can be observed that grains with higher $Rp_{ind\ 0.2\%}$ also have higher hardness.

The plastic properties of the material under spherical indentation (K and n) seem to increase with the CW level but, no significant difference can be observed between SA and PIA samples. The K and n of one grain are always within the standard deviation of the neighbouring grain. The indentation hardening coefficient has been reported to increase with radiation level due to the multi-axial stress-state underneath the indenter tip. This produces the activation of several slip systems, whereas in uniaxial stress state the easier slip system is the dominant one [247]. This is consistent with the increase of hardening coefficient observed in the CW samples. The little contribution of hardening coming from the He bubbles seems not to be enough to see significant effects in the hardening coefficient.
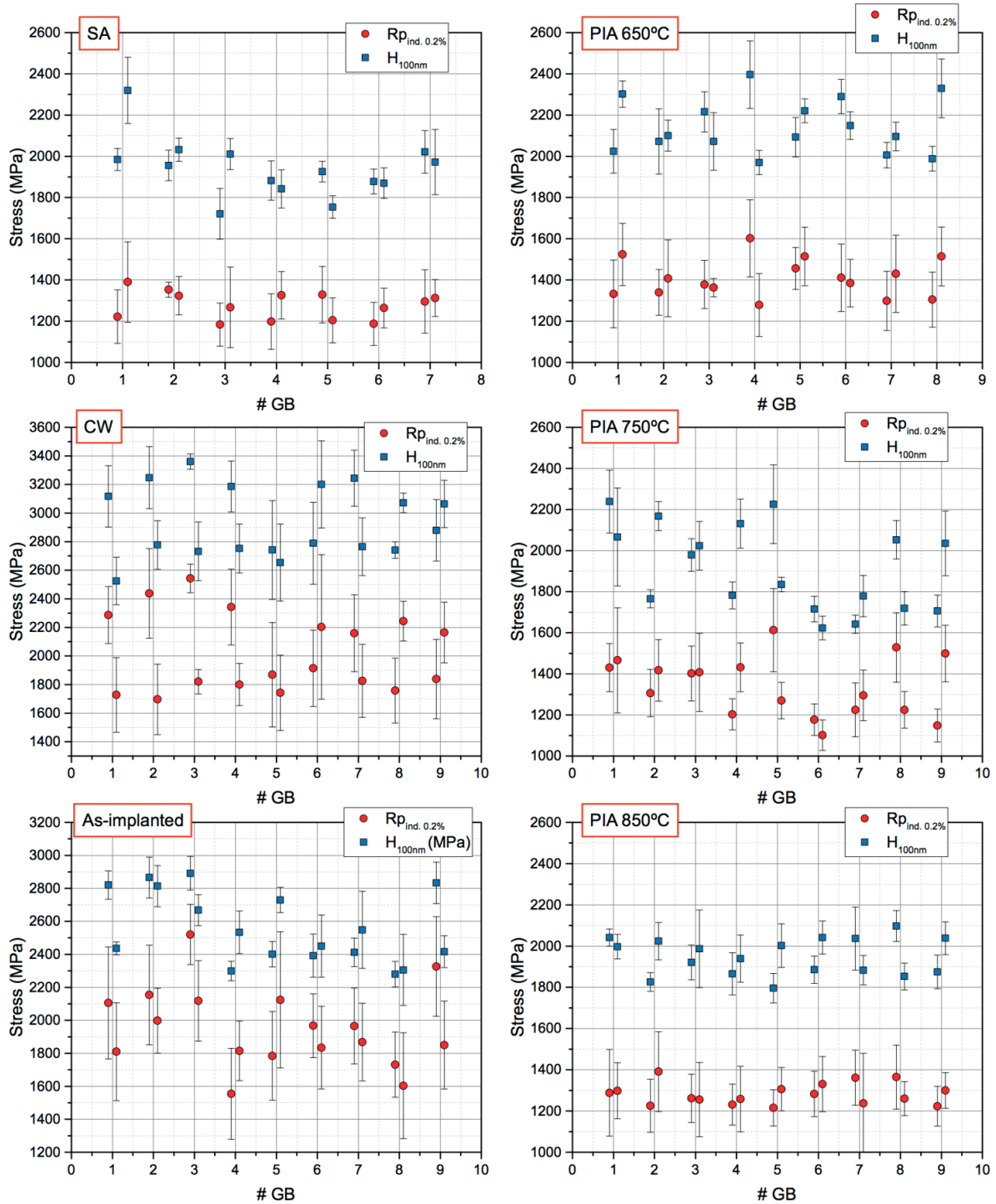
Figure 4.54. Average and standard deviation of $Rp_{ind\ 0.2\%}$ and hardness calculated in both sides of the studied GBs for all conditions. The average was obtained with the tests that had a distance above 5 μm from the GB in order to neglect grain to grain effects.
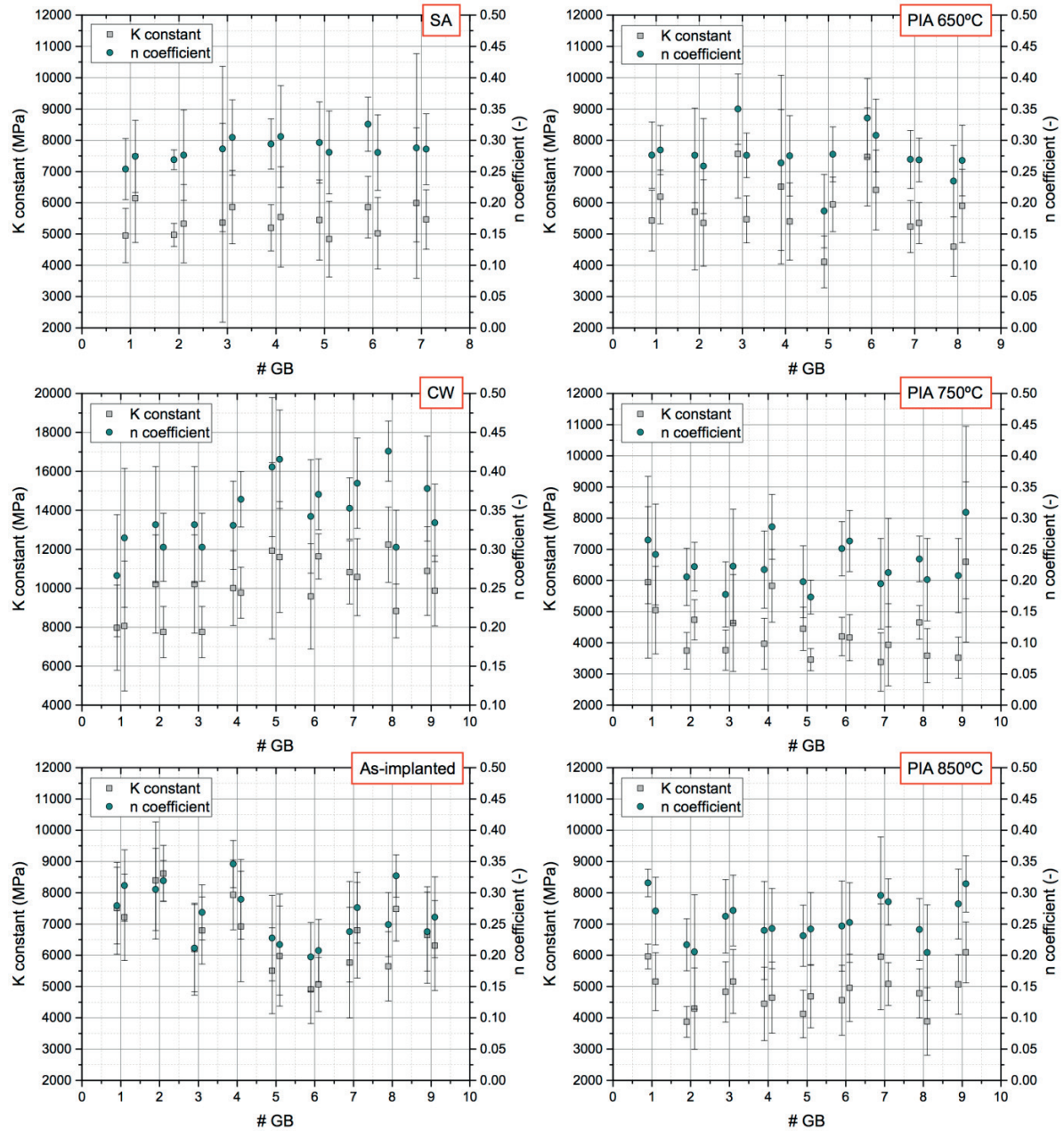
Figure 4.55. Average and standard deviation of K and n calculated in both sides of the studied GBs for all conditions. The average was obtained with the tests that had a distance above 5 μm from the GB in order to neglect grain to grain effects.

Table 4.8 summarizes and collects all the grain orientations studied for each sample condition, and the $Rp_{ind\ 0.2\%}$ and hardness are represented in the inverse pole figure in Figure 4.56 and Figure 4.57, respectively. Although there are some orientations missing in the inverse pole figure, it can be seen that the indenter properties might be quite homogeneous (although the different Schmid factors) for the different orientations in the SA and PIA samples, but not in the CW sample. The CW performed by tensile test preferably oriented the grains in the {0 0 1} and {1 1 1} planes, forming texture, which is consistent with the finding in ref. [248]. The grains in the {0 0 1} planes showed significantly higher indenter properties than the {1 1 1} planes, although the Schmid factor are higher in the {0 0 1} planes

(0.408$_{\{0\ 0\ 1\}}$ versus 0.272$_{\{1\ 1\ 1\}}$). The EBSD maps showed significantly higher deformation bands in the {1 1 1} planes than in the {0 0 1}. One hypothesis is that the existing deformation bands might facilitate the accommodation of the plastic deformation by enabling the dislocations to move through the existing deformation bands, hence decreasing the Rp$_{ind\ 0.2\%}$. On the other hand, {1 1 1} planes showed significantly higher indentation strain hardening which might be the result of dislocations saturation in the existing deformation bands. Pathak et al. [248] showed the opposite results in Fe-3%Si than here, i.e. higher indentation properties in the {1 1 1} than in the {0 0 1}. However, the CW was performed under compression test instead of tensile test; hence the resulting deformation microstructure might be different.

Condition (Plane)	Indents #	E_{ind} (MPa)		Rp$_{ind\ 0.2\%}$ (MPa)		H$_{100nm}$ (MPa)		n (-)		K (MPa)	
-	-	AVG	STD	AVG	STD	AVG	STD	AVG	STD	AVG	STD
SA (1 1 3)	7	207	12	1222	130	1984	53	0.25	0.05	4952	867
SA (1 4 5)	10	212	14	1390	195	2320	161	0.27	0.06	6143	1413
SA (2 3 10)	5	210	6	1353	37	1956	74	0.27	0.02	4972	367
SA (0 7 10)	12	180	21	1323	93	2032	57	0.28	0.07	5332	1252
SA (6 7 10)	11	190	23	1183	104	1721	123	0.29	3180	5362	3180
SA (0 3 8)	13	201	20	1267	195	2011	75	0.30	1173	5862	1173
SA (3 4 9)	7	187	21	1198	135	1882	95	0.29	739	5200	739
SA (2 2 5)	5	194	23	1326	115	1842	93	0.31	1603	5546	1603
SA (1 3 8)	6	194	26	1328	137	1926	50	0.30	1282	5450	1282
SA (7 9 10)	8	204	13	1204	109	1754	55	0.28	1209	4838	1209
SA (1 6 10)	5	190	17	1187	104	1878	60	0.33	985	5861	985
SA (1 5 9)	16	196	20	1264	96	1870	73	0.28	1143	5027	1143
SA (1 2 10)	13	201	22	1296	153	2021	103	0.29	2404	5990	2404
SA (2 3 5)	5	199	23	1312	90	1972	158	0.29	950	5463	950
CW (0 1 7)	37	214	7	2245	224	3159	209	0.29	0.07	8896	2016
CW (5 6 8)	26	206	14	1728	261	2525	167	0.31	0.09	8057	3336
CW (1 1 10)	11	213	9	2438	314	3247	217	0.33	0.07	10214	2519
CW (2 3 9)	5	212	9	1697	247	2777	170	0.30	0.04	7749	1316
CW (1 3 9)	3	208	12	2543	100	3360	54	0.36	0.05	11467	2233
CW (6 7 8)	5	211	11	1820	85	2732	205	0.41	0.04	11808	1435
CW (1 2 10)	27	213	10	2285	250	3146	174	0.33	0.05	9961	1881
CW (7 8 10)	58	207	16	1858	286	2760	276	0.38	0.07	10616	3170
CW (1 1 2)	26	203	14	1884	357	2822	281	0.40	0.06	11611	2455
CW (5 5 7)	5	198	18	1758	227	2741	58	0.43	0.04	12238	1933
CW (0 3 9)	4	212	4	2244	140	3072	69	0.30	0.05	8833	1377
CW (6 7 10)	19	213	9	1838	278	2880	215	0.38	0.07	10883	2276
PIA 650°C (5 5 6)	20	203	15	1322	153	2011	92	0.26	0.05	5122	965
PIA 650°C (N/A)	9	198	26	1524	151	2302	64	0.28	0.04	6189	860
PIA 650°C (4 4 9)	16	197	17	1339	111	2072	158	0.28	0.08	5714	1860
PIA 650°C (3 5 9)	19	206	21	1409	178	2170	78	0.29	0.07	6133	1454
PIA 650°C (1 5 9)	8	191	24	1378	116	2216	97	0.35	0.06	7560	1409
PIA 650°C (5 6 9)	10	201	17	1428	89	2086	111	0.21	0.05	4519	807
PIA 650°C (N/A)	7	211	13	1602	187	2397	164	0.26	0.14	6516	2467
PIA 650°C (5 9 10)	7	209	15	1278	152	1970	59	0.28	0.06	5401	1236
PIA 650°C (1 7 9)	15	203	16	1514	142	2220	58	0.28	0.04	5948	876
PIA 650°C (2 9 9)	13	207	15	1384	115	2149	67	0.31	0.06	6409	1276
PIA 650°C (3 9 10)	9	207	17	1298	143	2006	62	0.27	0.05	5239	833
PIA 650°C (0 9 10)	8	205	16	1430	187	2096	69	0.27	0.03	5351	656
PIA 650°C (N/A)	11	207	13	1514	143	2329	142	0.27	0.06	5899	1173
PIA 750°C (N/A)	6	218	6	1431	117	2239	153	0.26	0.10	5941	2429
PIA 750°C (2 7 8)	14	198	23	1372	210	1965	195	0.23	0.07	4662	1223
PIA 750°C (1 2 10)	4	189	22	1306	116	1765	44	0.21	0.05	3745	584
PIA 750°C (5 8 9)	12	206	17	1417	150	2168	70	0.22	0.04	4736	644

PIA 750°C (2 7 10)	10	210	8	1402	134	1979	79	0.18	0.05	3766	649
PIA 750°C (4 5 9)	11	207	14	1408	190	2023	119	0.22	0.09	4634	1554
PIA 750°C (0 1 8)	32	207	12	1385	130	1984	100	0.25	0.05	4776	857
PIA 750°C (2 7 9)	7	213	11	1613	203	2226	192	0.20	0.06	4449	694
PIA 750°C (4 9 10)	42	203	15	1270	112	1776	90	0.24	0.08	4462	1463
PIA 750°C (1 5 7)	28	203	16	1230	98	1737	82	0.22	0.07	3918	968
PIA 850°C (3 4 6)	11	201	22	1266	185	1963	43	0.28	0.03	5203	432
PIA 850°C (3 5 10)	16	193	15	1298	136	1997	60	0.27	0.05	5158	922
PIA 850°C (2 2 5)	14	201	14	1391	194	2024	91	0.21	0.09	4294	1299
PIA 850°C (3 5 5)	21	198	16	1261	117	1921	84	0.26	0.06	4829	966
PIA 850°C (2 7 8)	7	200	19	1256	180	1987	188	0.27	0.06	5162	1019
PIA 850°C (6 7 9)	35	192	16	1255	122	1869	89	0.24	0.08	4476	1160
PIA 850°C (4 4 9)	17	198	17	1238	139	1952	120	0.24	0.06	4648	1137
PIA 850°C (4 7 9)	11	188	16	1216	88	1796	72	0.23	0.05	4124	760
PIA 850°C (4 6 9)	18	197	14	1331	134	2042	80	0.25	0.06	4958	1076
PIA 850°C (3 6 9)	10	196	23	1362	134	2037	153	0.30	0.09	5951	1692
PIA 850°C (6 8 9)	12	194	20	1237	243	1883	71	0.29	0.04	5083	684
PIA 850°C (1 1 2)	20	198	18	1365	155	2097	75	0.24	0.05	4781	787
PIA 850°C (1 4 5)	15	194	14	1260	83	1853	64	0.20	0.08	3882	1077
PIA 850°C (0 1 2)	14	196	18	1223	97	1875	82	0.28	0.06	5069	953
PIA 850°C (5 6 9)	11	186	10	1300	87	2038	79	0.31	0.05	6093	971
As-impl. (1 2 7)	29	208	13	2348	259	2862	95	0.24	0.07	6737	1467
As-impl. (7 9 9)	4	200	11	1810	297	2436	38	0.31	0.06	7215	1380
As- impl. (1 6 10)	12	202	13	2154	302	2866	124	0.31	0.07	8395	1871
As- impl. (0 3 6)	8	213	5	1998	197	2814	125	0.32	0.03	8616	897
As- impl. (4 5 9)	4	204	19	2118	244	2668	94	0.27	0.04	6793	1075
As- impl. (3 5 6)	5	201	16	1555	276	2299	59	0.35	0.04	7931	1117
As- impl. (3 5 9)	11	215	11	1815	180	2533	129	0.29	0.06	6921	1766
As- impl. (1 2 3)	11	216	9	1784	269	2401	77	0.23	0.07	5504	1374
As- impl. (1 1 5)	7	215	13	2124	413	2729	76	0.22	0.08	5974	1599
As- impl. (1 7 15)	7	209	12	1967	194	2392	131	0.20	0.06	4904	1090
As- impl. (3 7 10)	14	215	5	1834	250	2450	188	0.21	0.05	5067	864
As- impl. (4 5 7)	11	200	13	1965	230	2412	87	0.24	0.08	5765	1768
As- impl. (5 7 7)	26	207	14	1810	220	2435	185	0.26	0.05	6313	1367
As- impl. (2 7 13)	8	201	15	1603	321	2305	216	0.33	0.03	7478	1023
As- impl. (1 1 8)	13	209	7	2326	302	2833	126	0.24	0.06	6645	1542
As- impl. (7 9 10)	8	210	9	1850	267	2416	97	0.26	0.06	6310	1437

Table 4.8. Average (AVG) and standard deviation (STD) of the indentation properties in function of the grain condition and orientation. The grain orientation is given in the standard triangle.
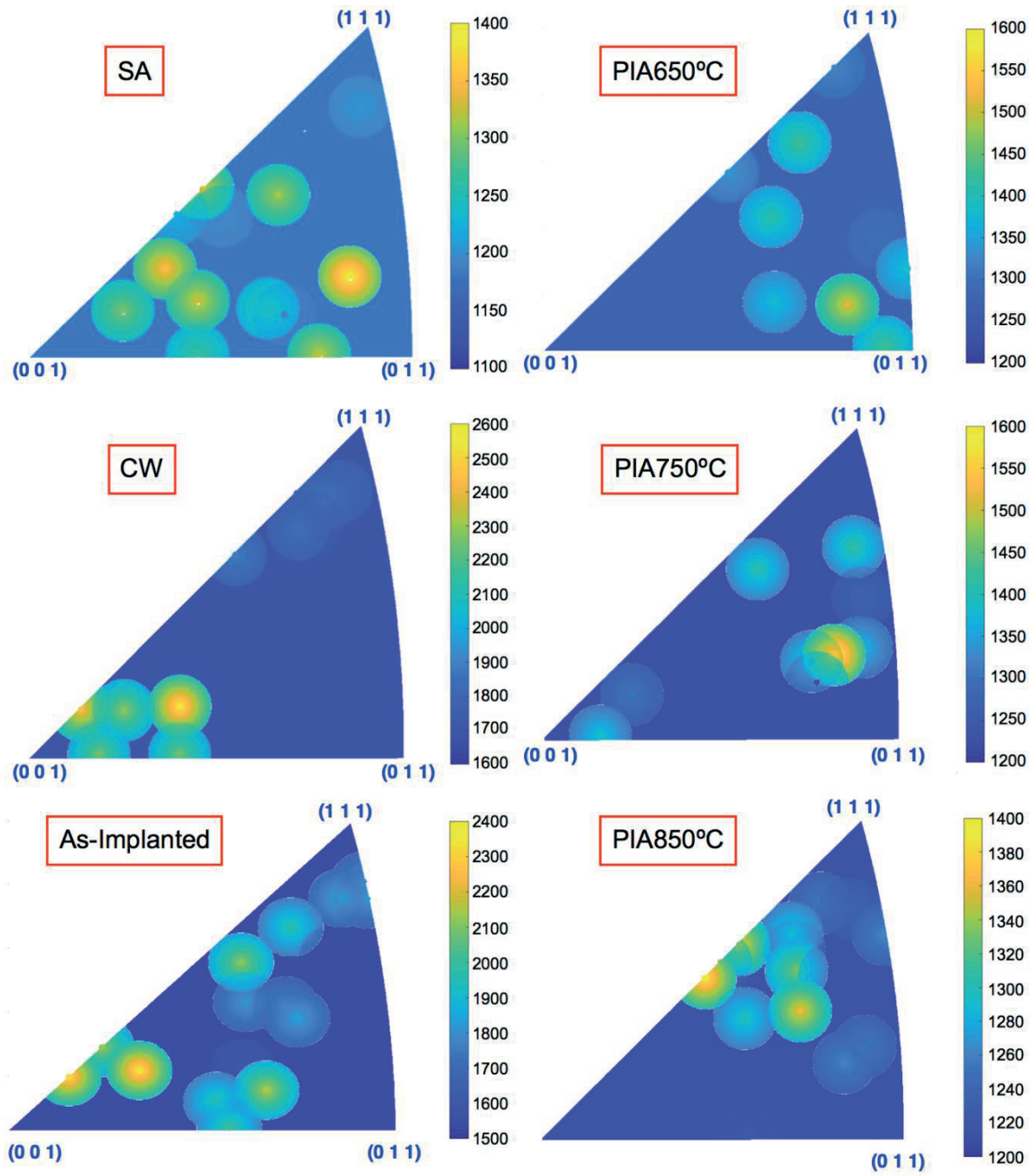
Figure 4.56. Inverse pole figure showing the Rp$_{ind\ 0.2\%}$ values for the different sample conditions and orientations.
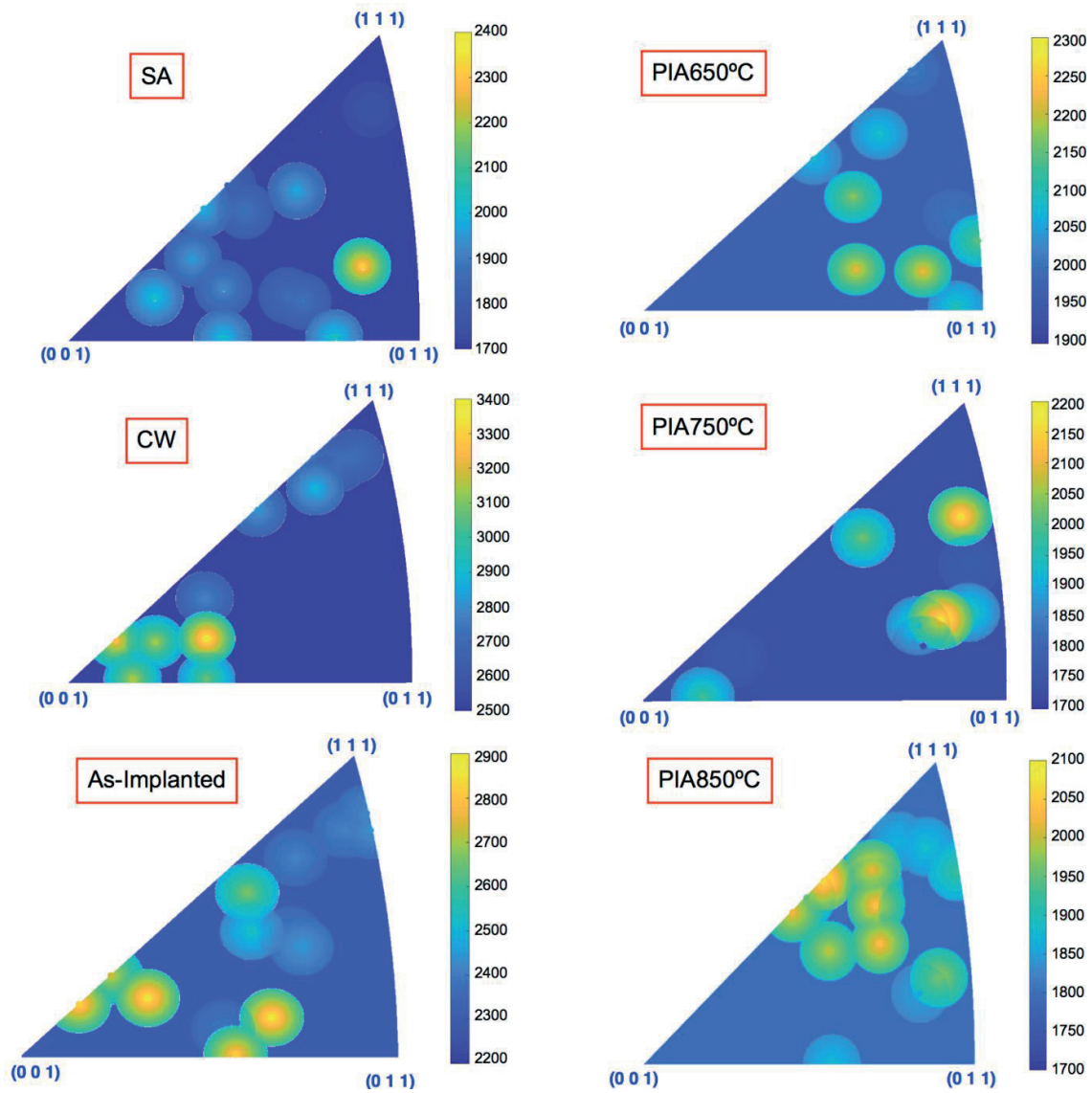
Figure 4.57. Inverse pole figure showing the hardness values for the different sample conditions and orientations.
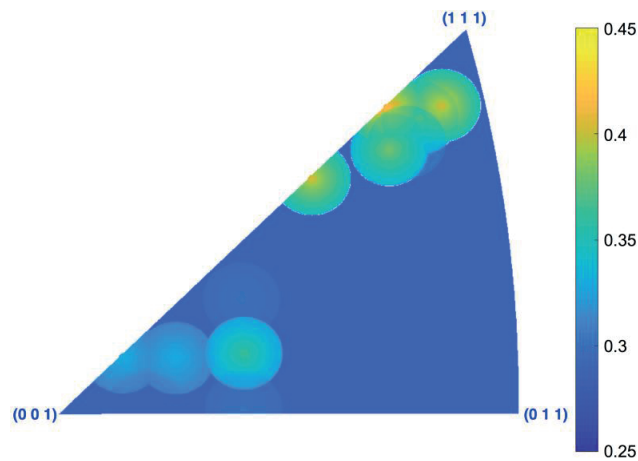
Figure 4.58. Inverse pole figure showing the indentation strain hardening coefficient in the CW sample.

The average results for each sample condition are summarized in Table 4.9. The representative load-displacement and stress-strain curves are shown in Figure 4.59. The CW sample shows the highest increase of load and YS, followed by the as-implanted sample, the PIA samples (from the lowest to the highest annealing temperature) and the SA sample, which is the softest one. Given the scatter of the data and the tests itself, it is not easy to distinguish these details from the representative stress-strain curves in Figure 4.59. However, the general trend, the average in Table 4.9, shows a consistent difference. In any case, the He effect in PIA above 750°C does not show a remarkable change in comparison to the SA sample. This indicates that an increase of ~40 MPa (see subchapter 4.5) cannot successfully be observed with this technique and the current statistical error. On the other hand, the results in the SA condition are in agreement with the results published by Weaver et al. [247], where they found a $Rp_{ind\ 0.2\%}$ of ~1360±140 MPa for 304 AuSS which is within the standard deviation of the presented results with 316L AuSS (1275±133 MPa).

Condition	# of indents	E_{ind} (MPa)		$Rp_{ind\ 0.2\%}$ (MPa)		H_{100nm} (MPa)		n (-)		K (MPa)	
		AVG	STD	AVG	STD	AVG	STD	AVG	STD	AVG	STD
SA	123	197	20	1275	133	1949	94	0.29	0.08	5452	1606
CW	234	209	12	2005	276	2908	225	0.35	0.07	9958	2578
PIA 650°C	152	203	18	1410	146	2146	203	0.28	0.06	5819	1293
PIA 750°C	166	205	15	1343	139	1918	112	0.23	0.07	4473	1193
PIA 850°C	242	195	17	1285	140	1953	91	0.25	0.06	4822	1036
As-implanted	178	208	12	1988	262	2588	133	0.26	0.06	6566	1422

Table 4.9. Average (AVG) and standard deviation (STD) of the indentation properties in function of sample condition.
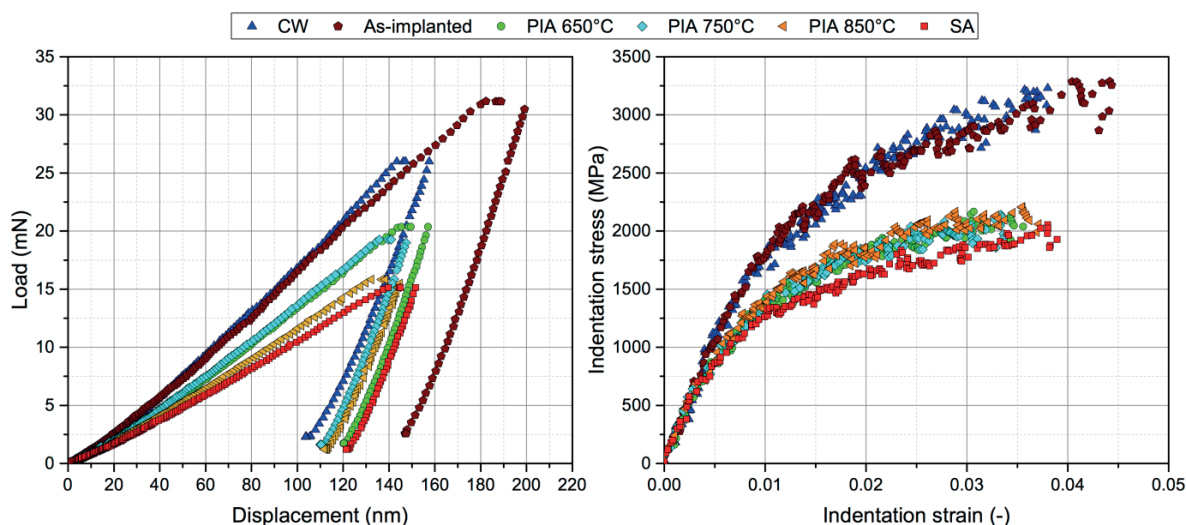
Figure 4.59. Representative load-displacement curves and stress-strain curves for SA, CW, As-implanted and PIA (650-750°C).

4.6.3 Comparison tensile and indentation properties

The indentation tests were carried out at room temperature so they can only be compared to tensile tests performed in the same conditions. This is the case for the SA and CW samples. A representative SA and CW tensile tests at RTA were used to compare the stress-strain curve to its indentation homolog. The tensile curves were transformed to true stress-strain as:

$$\varepsilon_t = \ln\left(1 + \varepsilon_{eng}\right)$$

<div align="right">Eq. 4.11</div>

$$\sigma_t = \sigma_{eng}\left(1 + \varepsilon_{eng}\right)$$

<div align="right">Eq. 4.12</div>

Where ε is the strain, σ is the stress and the subscripts eng and t stand for engineering and true, respectively. Then, the elastic part of the strain was subtracted in order to remove the effect of the machine stiffness as follows:

$$\varepsilon_p = \varepsilon_t - \frac{\sigma_t}{E_{test}}$$

<div align="right">Eq. 4.13</div>

Where ε_p is the true plastic strain and E_{test} is the apparent tensile modulus of the elastic region in the tensile test. Similarly, the elastic strain of the ISS curve was also removed using:

$$\varepsilon_{ind,p} = \varepsilon_{ind} - \frac{\sigma_{ind}}{E_{ind}}$$

<div align="right">Eq. 4.14</div>

Where $\varepsilon_{ind,p}$ is the true indentation plastic strain. The hardening parameters (K_p and n_p) were obtained using the plastic stress-strain curves with the following equation:

$$\sigma = \sigma_y + K_p\varepsilon^{n_p}$$

<div align="right">Eq. 4.15</div>

The plastic stress-strain curves are shown Figure 4.60; it is evident that the indentation curve in the CW sample has higher strain hardening than the SA sample, but the contrary for the tensile results. Given the relatively small penetration depth, the plastic strain is below 0.03 strain so the hardening parameters were obtained from the range of ~0.005 to ~0.025 strain. The plastic properties obtained with Eq. 4.15 from Figure 4.60 are summarized in Table 4.10, where δ is the ratio $Rp_{ind\ 0.2\%}$ to $Rp_{0.2\%}$.
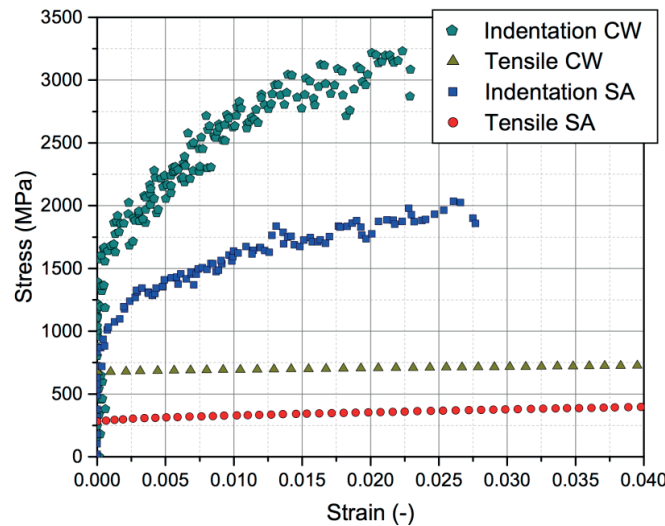
Figure 4.60. True stress-strain curves obtained with the instrumented indenter and the tensile machine after removing the elastic part of the curves.

The nanoindentation data reported here was carried out in single grains, whereas the tensile data accounts for the grain hardening effect, i.e. Hall-Petch effect [35, 36] described in Eq. 2.2; thus $Rp_{ind\ 0.2\%}$ and $Rp_{0.2\%}$ correspond to σ_i and σ_y, respectively. Therefore, the δ values in Table 4.10 cannot successfully correlate the indentation to the tensile data. On the other hand, the hardening exponent appears to be constant for all the tests and sample conditions, but the hardening constant is material

and test dependent. The latter hinders any possibility of plastic flow correlation. However, a correlation between K_p and CW could be obtained, if different CW levels are tested by SSRT and nanoindentation.

Parameters	Tensile SA	Tensile CW	Indent SA	Indent CW
Rp$_{0.2\%}$	281	673	1177	1859
K$_p$	1012	423	9142	19600
n$_p$	0.67	0.64	0.65	0.68
δ	-	-	4.5*	3*

*Calculated with the average from Table 4.9.

Table 4.10. YS and strain hardening parameters obtained from the tensile and indentation tests carried out at RTA.

If the contribution of the $k_{hp}/\sqrt{s}$ in Eq. 2.2 is constant, i.e. it does not significantly depend on the material condition then:

$$Rp_{0.2\%_{CW}} - Rp_{0.2\%_{SA}} = \sigma_{i_{CW}} + \frac{k_{hp}}{\sqrt{s}} - \left(\sigma_{i_{SA}} + \frac{k_{hp}}{\sqrt{s}} \right) = \sigma_{i_{CW}} - \sigma_{i_{SA}}$$

Eq. 4.16

This should then be proportional to $\Delta Rp_{ind\ 0.2\%}$ since the indentation size and structure effects should be compensated to each other too, so:

$$\frac{Rp_{ind\ 0.2\%_{CW}} - Rp_{ind\ 0.2\%_{SA}}}{Rp_{0.2\%_{CW}} - Rp_{0.2\%_{SA}}} = \delta$$

Eq. 4.17

The resulting δ value from Eq. 4.17 is ~1.75. Patel and Kalidindi [249] suggested a constant δ value of about 2.0 after comparing finite element modelling spherical indentation tests to uniaxial tests, whereas Donohue et al. [250] suggested a value about 1.3 with a similar approach. However, Weaver et al. [247] proposed an experimental value of 2.9 instead of 2.0. Both, Patel and Weaver, tried to compare spherical indentation with uniaxial testing by means of single crystal orientation. These δ values are slightly above the value estimated here. The possible reasons might be associated to the tests scatter, the limited reproducibility of the micro-tensile tests results, the indentation size effects, and that the Hall-Petch effect might be somehow different for different material conditions. However, the latter is not expected to influence the $Rp_{0.2\%_{CW}} - Rp_{0.2\%_{SA}}$ result in more than 4 MPa [251].

4.6.4   Indentation size and structure effects

Recently, Hou et al. [252] showed that the mean indentation pressure/hardness, or in this work the indentation stress (σ_{ind}), of a ball indenter measured on annealed polycrystalline copper follows a Hall-Petch type equation:

$$\sigma_{ind} = \sigma_{0,ind} + \frac{K_{HP}}{\sqrt{D}}$$

Eq. 4.18

Where $\sigma_{0,ind}$ is the fundamental friction stress in GPa, which is dislocation density independent whereas σ_i in Eq. 2.2 already contains the dislocation contribution [251]; K_{HP} is an averaged Hall-Petch constant in GPa·μm$^{0.5}$; and D is the combined length scale parameter in μm, which is the spatial frequency of all obstacles to dislocation motion. When several length scale parameters control the dislocation mean free path such as the projected contact radius (a), grain size (s), the average obstacle

distance for He bubbles (l_b), and the initial dislocation mean spacing (l_s), one can rewrite the Hall-Petch contribution as:

$$\frac{K_{HP}^2}{D} = \frac{k_1}{a} + \frac{k_2}{s} + \frac{k_3}{l_s} + \frac{k_4}{l_b} + \cdots$$

Eq. 4.19

Where k_1, k_2, k_3 and k_4 are the scaling parameters for each defect or structure type in $GPa^2 \cdot \mu m$. In the indentation carried out in this study, the grain size diameter and the initial dislocation density and size should be the same (or very similar) in the SA and the PIA samples (PIA $\geq 650°C$). Moreover, given the similar indentation modulus and $Rp_{ind\ 0.2\%}$ in these samples, the variation of the projected radius is negligible, and values around 475 nm are obtained for the SA and the PIA samples. Thus, Eq. 4.18 can be rewritten as follows:

$$\sigma_{ind} = \sigma_{0,ind} + \sqrt{B + k_4 l_b^{-1}}$$

Eq. 4.20

Where B is a constant that combines the contribution of the grain size, indenter tip size and initial dislocations present in the material prior to indentation. Eq. 4.20 is only valid for samples with similar initial dislocation density, so the CW indents cannot be mixed with SA and PIA indents. $\sigma_{0,ind}$ can be estimated from the averaged $Rp_{0.2\%_{SA}}$ at RTA (Table 4.2) removing the contribution of the grain size using Eq. 2.2 ($k_{hp} \approx 621.4 MPa\ \mu m^{0.5}$ [251] and s=52 μm), and multiplying by the δ value found above.

$$\sigma_{0,ind} \approx \delta \left(Rp_{0.2\%_{SA}} - \frac{k_{hp}}{\sqrt{s}} \right) = 330\ MPa$$

Eq. 4.21

Using the $Rp_{ind\ 0.2\%}$ obtained from the nanoindentation (Table 4.9), the obstacle distance calculated from the He bubble density and size given in Table 4.3, and the estimated $\sigma_{0,ind}$, the fitting parameters in Eq. 4.20 can be calculated with an overdetermined (two unknowns and four equations) system (Table 4.11).

B (GPa²)	k_4 (GPa²μm)
0.87	1.7×10^{-2}

Table 4.11. Fitting parameters for indentation data obtained using Eq. 4.20 and data from Table 4.9 and Table 4.3.

Figure 4.61 shows that the calculated $Rp_{ind\ 0.2\%}$ fits with a linear regression of the experimental $Rp_{ind\ 0.2\%}$, but also that the main increase of $Rp_{ind\ 0.2\%}$ can be directly attributed to the inverse obstacle distance, which is actually the only variable assumed to exist in the equation. According to Hou et al. [253], the fundamental friction stress (σ_0) should be very low, typically about $10^{-5} \cdot \mu$, being μ the material shear stress (76 GPa); the value estimated here is about $4 \times 10^{-3} \cdot \mu$, indicating that the fundamental friction stress plays a minor role in nanoindentation ($< \sim 25\%$). However, the B parameter is difficult to predict because it depends on the elemental composition of the material, the grain size and the tip radius; a value about 1 GPa^2 seems, however, to be reasonable with literature [254, 253]. Finally, the k_4 parameter should be smaller than the k_3 parameter for sessile dislocations since the hardening coefficient of bubbles is lower than the one for dislocation loops; the value found (0.017 $GPa^2\mu m$) is effectively smaller than the one for sessile dislocations in NiAl alloy (0.08 $GPa^2\mu m$) [253]. Hence, the grain size, the projected indent radius and the initial dislocation distance appear to have the same influence in all the samples considered.
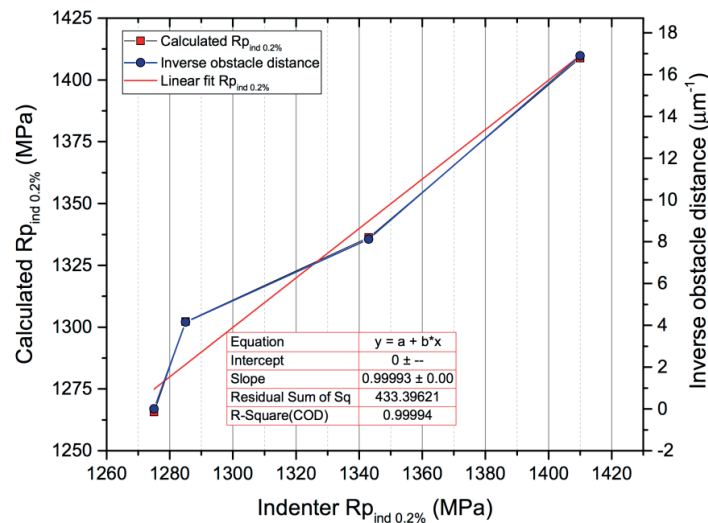
Figure 4.61. Calculated $Rp_{ind\ 0.2\%}$ using Eq. 4.20 with the fitting parameters given in Table 4.11 versus the experimental $Rp_{ind\ 0.2\%}$. The inverse obstacle distance (He bubbles) is also plotted versus the experimental $Rp_{ind\ 0.2\%}$. A linear correlation between the calculated and the experimental $Rp_{ind\ 0.2\%}$, and the experimental $Rp_{ind\ 0.2\%}$ and the inverse obstacle distance (He bubbles) can be observed.

4.7 General discussion

The following discussion is focused to the IASCC (initiation) susceptibility in hydrogenated high-temperature water at low ECP and to microstructural aspects only. Environmental and mechanical aspects like the effect of ECP, radiolysis or irradiation creep and residual stress relaxation, which also influence the IASCC behaviour in synergy with material aspects, are not covered. The IASCC behaviour at high ECP (BWR/NWC) is significantly different from that at low ECP (PWR, BWR/HWC) with low susceptibility. Furthermore, the following discussion is primarily based on the IASCC behaviour in post-irradiation tests. In-situ radiation effects like radiolysis and radiation enhanced diffusion are thus not considered. The accelerated short-term SSRT method is mechanical-dominated and may overlook certain more time-consuming corrosion- or diffusion-dominated initiation and precursor processes that may occur during long-term exposure. SSRT thus could erroneously feign a high IASCC resistance. SSRT tests usually involve IASCC initiation and subsequent crack growth and without adequate on-line monitoring, the separation of effects on initiation and growth is challenging. The parameter effects on initiation and growth are often similar, but can also be different. The localization of plastic deformation, e.g., usually has a strong effect on initiation at low ECP, whereas a more moderate effect on subsequent crack growth only. Furthermore, SCC and IASCC crack growth may be observed in pre-cracked specimens under conditions, where initiation from smooth surfaces in SSRT tests is extremely challenging (e.g., SCC in cold-worked AuSS at low ECP). A direct comparison of the SSRT results with actual in-service components is difficult, since loading conditions are very different. Furthermore, the irradiation-induced relaxation of weld residual stress, which is the main mechanical driving force for IASCC in most reactor internal components, and the main reason for the low IASCC susceptibility in PWRs in spite of the higher dpa accumulation, is an aspect that is not covered in the SSRT experiments. All these constraints and restrictions and the exact test conditions should be kept in mind, when one tries to generalize the observations to other system or reactor conditions or to crack growth.

IASCC, in particular at high ECP, is usually related to the conventional mechanisms like RIS and radiation hardening (Figure 2.39). The dpa threshold to produced IASCC appeared to be about 0.5 dpa

in high ECP (BWR/NMC) and about 2 to 3 dpa for low ECP (PWR, BWR/HWC) [1]. Recently, Busby et al. [145] showed that the individual effects of radiation hardening, total dislocation loop length and chromium, nickel, silicon and phosphor segregations are weakly correlated to IASCC after PIA in SSRT tests, but they suggested that the dense population of black dots can play a critical role in the cracking behaviour. Fukuya et al. [49] performed further PIA investigation and they concluded that IASCC could be attributed to the change of microstructures and hardening, but not to segregation. On the other hand, Fujimoto et al. [144] performed SSRT in simulated PWR conditions in reactor internals extracted from PWRs and FBRs. The IASCC susceptibility of AuSSs irradiated in a FBR showed significantly lower susceptibility than in PWR environment at the same high dose level, in spite of similar microstructures, hardening/YS levels and GB segregation. The main difference between both irradiations was the He content, which correlated fairly well to the IASCC susceptibility (Figure 2.40). The lab experiments from Chen et al. [12] also indicated that He might be the most plausible reason for the difference on IASCC susceptibility.

In this study, the helium implantation with 45 MeV up to 1000 appm produces at maximum 0.16 dpa according to the SRIM calculation. Hence, the He implantation to dpa ratio is about 6250 appm/dpa, whereas in the later stages of PWR reactors operation is about 10 appm/dpa [6]. Thus, the resulting microstructure and microchemistry are fundamentally different.

4.7.1 Displacement damage effect

Figure 4.62 shows the microstructural and microchemistry evolution of the PWR reactor internals with dpa and the equivalent (estimated) graph after the current He implantation. The total dislocation loop line, the cluster density and the chromium depletion are assumed to behave similarly under neutron or alpha particles irradiation. Although this might not be completely true, the expected difference is considered to be negligible for this discussion.
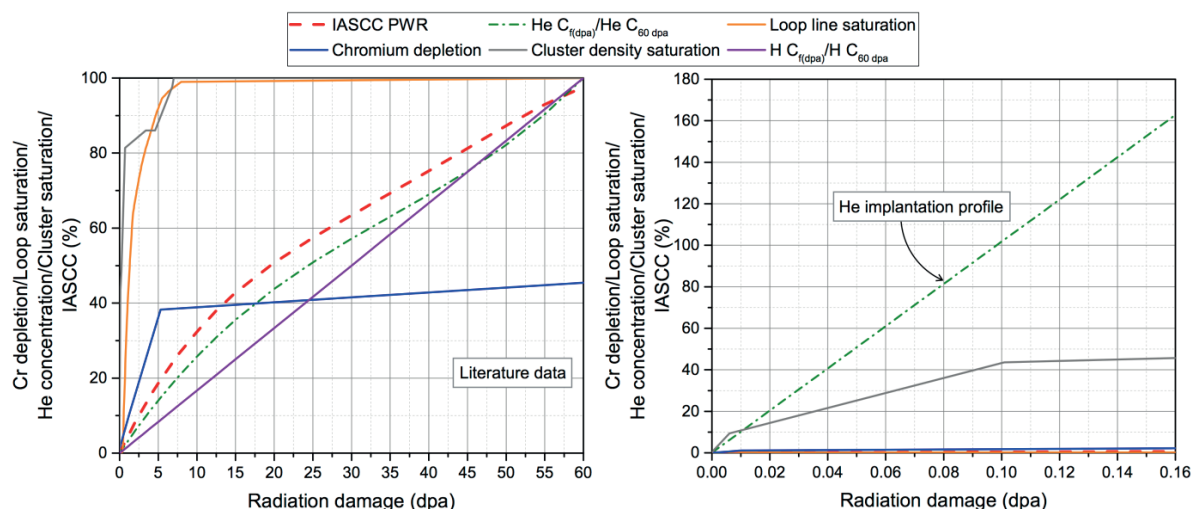
Figure 4.62. Microstructure and microchemistry evolution with dpa (left) and detail of the He implantation performed (right). Data adapted from different sources: relative chromium (Cr) depletion with respect to 60 dpa in % [42], relative total loop density saturation in % [46], relative He concentration accumulation with respect to 60 dpa in % [144], cluster density saturation in neutron irradiated nickel [255] and proton irradiated 304L [163], relative hydrogen (H) concentration accumulation with respect to 60 dpa in % [256] and, IASCC cracking found in form of % of the fracture surface showing IGSCC after SSRT in PWR/HWC [144].

In PWRs under neutron irradiation, the material undergoes significant microstructural and microchemistry changes. The IASCC susceptibility seems to be fairly well correlated to the He concentration up to ~650 appm, where the fracture surface shows 100% IG fracture. In the present study, although the He concentration was above the threshold for 100% IASCC (Figure 4.62), it was found that homogenised He concentration up to 1000 appm with a moderate radiation damage (<0.16 dpa) did not produce IASCC in accelerated SSRT in HTW. This indicates that He alone (with little black dots formation) is not responsible for IASCC. However, He remains a parameter that can play a key role in IASCC as will be discussed hereafter.

4.7.2 Post-implantation annealing effect

As mentioned earlier, PIA treatments were recently used to find the dominant factor for increasing the IASCC susceptibility after neutron and proton irradiation. Given that the annealing times and temperatures are different in the literature, the different microstructural and microchemistry changes with annealing have been plotted using the iron diffusion distance. The iron diffusion distance is calculated by $\sqrt{D \cdot t}$, where D is the iron self-diffusion coefficient and t the annealing time. The D depends on temperature by $D = D_0 \exp(-Q/kT)$, where T is the annealing temperature in K, k is the Boltzmann constant (8.62×10^{-5} eV/K) and Q is the activation energy of iron migration by interstitial mechanism in austenite. The values of D_0 and Q used are 4.9×10^{-5} m^2/s and 2.94 eV, respectively [257]. The % ratio of the as-implanted inverse average bubble distance and annealed inverse average bubble distance (indicated as "He") is included in the literature data collected in Figure 4.63. The as-implanted inverse average He bubble distance (i.e. 1/L) has been extrapolated from the exponential relation with the inverse of temperature given in Figure 4.64. This curve allowed having an idea of how the inverse He bubble distance might evolve with annealing as indicated in Figure 4.63. This curve might only be valid for irradiations/implantations at 300°C and PIA, since the He bubble coarsening also depends on the initial bubble size. The use of the inverse average He bubble distance simplified the mathematical value for 0 %, which is the inverse bubble distance of no bubbles in the material (1/∞); and 100%, which is the extrapolated inverse bubble distance at 300°C with 1000 appm He.

The Figure 4.63 shows a clear correlation between IASCC susceptibility, black dots annealing and a decrease of He bubble inverse distance. These three parameters evolve significantly faster than any of the conventional mechanisms studied so far. However, it is important to remark that this observation does not indicate that the black dot density and the He bubble distance (L) are the main parameters for IASCC susceptibility. The present study showed that He with about 40% of the black dot density (estimated from Figure 4.62) was not enough to produce IASCC, whereas from the PIA should be enough to produce more than 40% of IASCC. The most plausible explanation might be that the matrix is not yet saturated with other hardening sources, and hence the deformation microstructure might not be preferentially planar, i.e. to form deformation channels. Materials which are prone to planar deformation are more sensitive to SCC [156, 157]. Jiao and Was [154] recently reported that the localized deformation is the parameter that best correlates with IASCC.
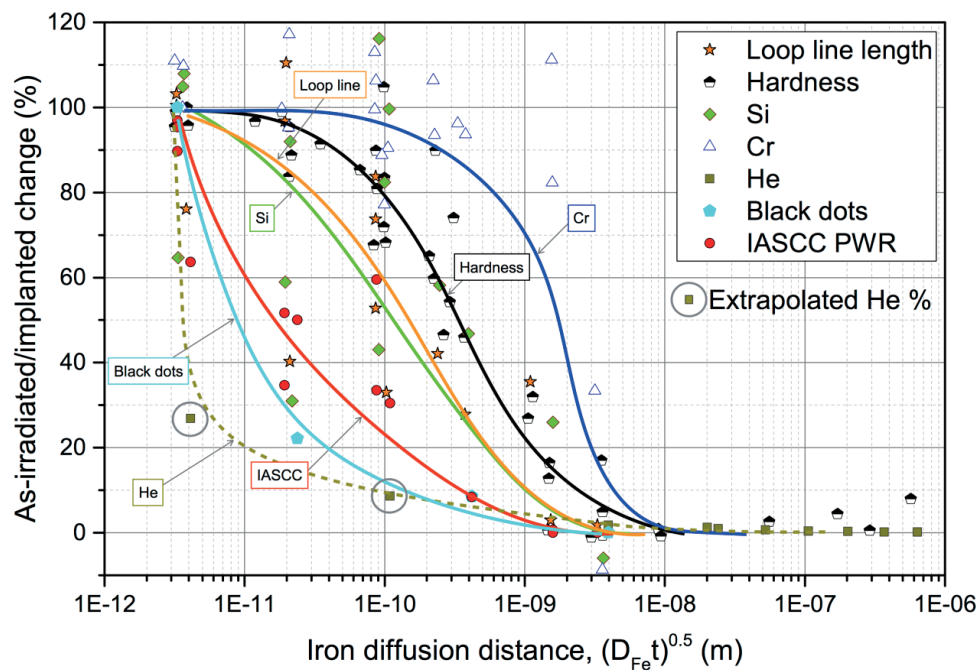
Figure 4.63.As-implanted/irradiated remaining changes in % for hardness measurement [49], total loop line length [49], silicon (Si) enrichment [49], chromium depletion (Cr) [49], helium inverse bubble distance (1/L), black dots [231], and IASCC cracking found in form of % of the fracture surface showing IGSCC after SSRT in PWR/HWC [145, 49].
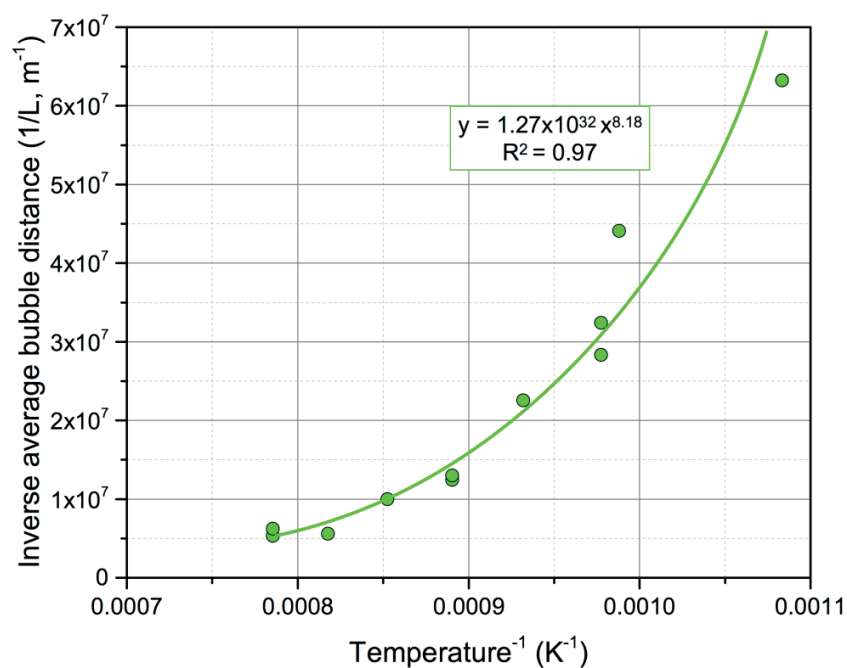
Figure 4.64. Average inverse bubble distance (1/L) versus the inverse of temperature calculated from the data in Table 4.3 and Table 4.5. The extrapolated curve is used to estimate the average bubble distance at 300°C and to foresee the as-implanted remaining bubble distance after annealing between 300 and 650°C.

4.7.3   Localized deformation effect

The SFE, the irradiation hardening and the precipitates/particles influence the deformation microstructure of the materials. The generation of new dislocations is more difficult at higher SFE but, their core size is smaller favouring the dislocation mobility. On the other hand, dislocations have more difficulties to cross-slip and climb in low SFE materials. This property is alloy dependent, but can have a relevant impact on localized deformation and IGSCC [153, 154, 156, 157, 158, 159].

The defects formed during irradiation (black dots, dislocation loops, voids, bubbles, precipitates) block the formation of new dislocations by Frank-Read sources or GB ledges [258], and act as obstacles for gliding dislocations (present in the material before application of the load). In this situation, the formation of dislocation cells is prevented and the formation of localized deformation is enhanced by dislocation channelling.

IGSCC is likely to be related to the impingement of intense, localized slip bands on GBs, which results in dislocation slip transfer to the neighbouring grain, cross-slip within the same grain, GB sliding and/or dislocations pile-up in the GB. Was et al. [158] found that the type of GB-dislocation interaction determines the susceptibility of IGSCC. At a certain stress, moving dislocations in a defect-free channel reach GBs where they are eventually absorbed. Further plastic deformation or dislocation absorption on the GBs results in dislocation glide within the GB. Hence, GB sliding is produced, which is confined close to the GB-dislocation channel intersection [259, 260]. This produces a concentration of strain in the GB which has been found to be experimentally correlated to IGSCC [261, 262, 263].

In the vicinity of a crack, a GB experiencing localized strain promotes the rupture of the passive oxide layer on the crack-tip and hence, accelerates "the film rupture anodic dissolution" mechanism, increasing the CGR. This effect appears to be more accentuated in oxygenated water as the threshold for IASCC in BWR is lower than in PWR. The penetration of oxygen along GBs can readily produce a thin oxide which weakens the GB capacity to deform and increases the probability to GB cracking by the selective oxidation model [264]. This effect is accentuated for materials with low SFE and/or highly irradiated material.

Hash et al. [265] have studied the IASCC susceptibility in BWR conditions for a combination of proton irradiated (0-1.67 dpa) and CW (0-35%) level with similar hardness values (~380 kg/mm^2). They have shown that the variant hardening sources may have a different effect on IASCC. The samples with doses above 0.6 dpa showed that the IASCC increased with the dose level but, below 0.6 dpa no IASCC was found despite the same hardness values and no detectable chromium depletion in the GB. This result is expected. During CW, the deformation forms dislocation cells microstructure with minor formation of slip bands (SFE dependent) due to the absence of defects, which would enhance the creation of dislocations channels. Further deformation in CW samples is not going to change the deformation mode of the material. However, the irradiation defects might influence the normal deformation mode of the material by enhancing localized deformation and IASCC. Thus, after He implantation, the susceptibility to IASCC for SA and CW should not be different. The formation of the dislocation cell structure in CW material act as sinks for irradiation-induced defects limiting the formation acumulation of extended irradiation-induced defects. Therefore, although unirradiated CW materials are more susceptible to SCC than SA materials in pre-cracked CT-specimens (Figure 2.25), it should not be surprising to see a decrease of the IASCC susceptibility in CW material after irradiation. Given the microstructure presented in Figure 4.40, the SA material might be more prone to IASCC than the CW due to the formation of a more planar mode of deformation.

4.7.4 Synergy of effects

The low susceptibility of IASCC below 10 dpa and the apparent saturation of RIS, dislocation loop size and density and black dots at about 5-10 dpa suggest that none of these mechanisms might play a dominant role on IASCC (accelerated SSRT in PWR/HWC). However, He and hydrogen concentrations build up seem to be closely related to IASCC. On the other hand, PIA annealing results correlated fairly well with the black dots recovery and the inverse average He bubble distance. Given these observations, He concentration or better, the inverse He bubble distance seems to be the most plausible cause of IASCC. However, the results presented in this thesis rule out that He alone (with very low displacement damage) can produce IASCC and reinforce the idea that IASCC might be exclusively enhanced by dislocation channelling, which is SFE and dpa dependent.

The dpa threshold for producing localized deformation decreases with decreasing the SFE, hence AuSSs with lower SFE are more prone to IASCC. The dpa threshold can be expressed in terms of RIS, black dot density, total dislocation loop size and inverse average He bubble distance, but not on hardening produced by CW or radiation hardening. It has been shown that the hardening source is important for producing IASCC initiation and that the CW level might increase the IASCC initiation time. In irradiated material, the YS increase is a function of black dots, total dislocation loop size and inverse average He bubble distance, so hardening does not express new information to this problem. Moreover, the effect of RIS depends on the environment, and the inverse average He bubble distance is difficult to be experimentally found.

The different IASCC susceptibility of PWRs and FBRs after neutron irradiation (Figure 2.40) and the results collected in this discussion (Figure 4.62 and Figure 4.63) indicate that He bubbles might be the main reason for increasing localized deformation and in turn for IASCC susceptibility. However, this can be a wrong statement if one does not consider the microstructure and the microchemistry of the material, because He alone (<1000 appm) and radiation damage without He (<48 dpa) cannot reproduce IASCC in PWR environment.

After saturation of the radiation damage, the helium builds up in the material might be an extra hardening source for blocking the dislocation motion and hence enhancing dislocation channelling. Although the obstacle strength of He bubbles depends on the He bubble size, the average bubble distance (or 1/L) seems to be a relevant parameter for producing IASCC in damage saturated material (> 5dpa). Moreover, although He bubbles might not preferentially grow in GB, the existing GB bubbles might help to stabilize voids/cracks in the GBs weakening the GB cohesion and facilitating GB cracking, sliding and/or rupture of the oxide passive film in the crack-tip.

Chapter 5 Conclusions and perspectives

5.1 Conclusions

Non-implanted miniaturized and standard 316L samples were tested in room temperature air (~25 °C), high-temperature air (~290 °C), oxygenated water conditions (~290 °C, 0.5 and 8 ppm O_2, BWR/NWC) and hydrogenated water conditions (~290 °C, 2.2 ppm H_2, PWR). All the tensile properties (UTS, $Rp_{0.2\%}$, US and RA) decreased with the increase of temperature in air and in water. The results indicated that both environment and sample geometry have a negligible effect on the tensile properties. Nevertheless, limited transgranular hydrogen-assisted SCC with a quasi-cleavage appearance was observed in hydrogenated high-temperature water with 2.2 ppm H_2. The main failure mechanism was still caused by microvoid coalescence and the quasi-cleavage facets covered between 1 and 14 % of the total fracture surface. Moreover, several transgranular cracks were formed in the gauge region, always initiating from the specimen surface. The RA was dominated by shear fracture in all high-temperature tests, both in air and in water. The tensile properties obtained and the fractography study carried out at room temperature in air (~25 °C), high-temperature air (~290 °C), oxygenated water conditions (~290 °C, 0.5 and 8 ppm O_2) and hydrogenated water conditions (~290 °C, 2.2 ppm H_2) clearly demonstrated that the miniaturized sample reveals the same results and behaviour than the standard sample under these conditions. Thus it is suitable to evaluate potential helium effects on IASCC susceptibility by miniaturized flat dog-bone samples.

Helium implantation at 300°C up to 1000 appm produces a limited amount of radiation-induced segregation. It was detected an enrichment of Mo (2.1→3 % wt.) and a slight depletion of Fe (64→63 % wt.) within the first 5 nm from the grain boundary. The concentration profile of Ni, Cr, Si and P did not change on the grain boundary, indicating that the corrosion resistance of the grain boundary should remain unchanged.

The helium evolution study performed in the TEM samples prepared from the PIA helium-plates revealed that the helium implantation temperature at 300°C leads to significantly different results than from room temperature implantation. First, no migration and coalescence mechanism was found at the tested temperatures (above 650°C); and second, the bubble internal pressure was in equilibrium with the surface energy at annealing temperatures above 750°C, which is ~300°C lower than for room temperature implantation. The PIA from 650 to 1000 °C showed that the bubble growing mechanism was Ostwald ripening in the grain interior and on the grain boundary. This suggests that the helium bubble coarsening mechanism might not only depend on the annealing temperature, but also on the initial bubble size (≥ 0.8 nm radii). The bubble size and the average bubble distance were similar in the grain interior and on the grain boundary, therefore the helium bubbles did not preferentially migrate to grain boundaries. Most of the helium bubbles in the grain interior were located on dislocations, where their nucleation and growth is favoured. The lack of clear depletion zone supports the conclusion that the migration and coalescence mechanism is not operating, and that the prevailing mechanism is Ostwald ripening.

Accelerated slow strain rate tests (10^{-6} - 10^{-7} s^{-1}) with smooth tensile samples in hydrogenated high temperature water with 2.2 ppm dissolved hydrogen at 290 °C did not induce IG(IA)SCC initiation in homogenized helium implantation at 300°C up to 1000 appm in SA, CW and PIA ($\leq$ 1000°C) conditions. However, the mechanically dominated short-term slow strain rate test may be too short to exclude SCC initiation and could overlook other more time-consuming (e.g. corrosion-dominated) precursor and initiation processes. The absence of IASCC might be related to the lack of a well-marked deformation mode change between the non-implanted and the implanted materials. The number of dislocation channels in the irradiated samples and the helium enrichment on the grain boundaries is insufficient to induce IASCC in these conditions. Furthermore, the grain boundary coverage with helium bubbles is probably too low ($\sim$10%) to significantly reduce the grain boundary strength with respect to the matrix strength. These results suggest that a helium concentration $\leq$ 1000 appm alone cannot induce IASCC, therefore there has to be some synergy between irradiation damage and helium concentration. The formation of irradiation-induced dislocation channels ($\geq$ 0.1 dpa) with high-stress concentration on grain boundaries, together with the current helium bubbles grain boundary coverage ($\sim$10%), could promote intergranular cracking.

The deformation microstructure of non-implanted SA/CW and as-implanted SA samples (> 0.05 dpa) changed from high dislocation density, arranged in cell walls separated by relatively dislocation-free regions, to more planar deformation, respectively. On the other hand, CW and PIA did not show a relevant implantation effects due to the previous formation of dislocation cells, and annealing of the black dots and extended defects (e.g. dislocation loops), respectively. Hence, the reduction of the dislocation cross slip ability was only observed in the as-implanted condition above 300 appm He. However, the degree of localized deformation induced by the helium bubbles and the helium implantation damage was not enough to change substantially the deformation mode, hence higher radiation damage might be needed in order to produce IASCC.

The $\Delta Rp_{0.2\%}$ and the microstructural changes between the PIA samples (> 750°C) and the non-implanted samples tested in hydrogenated high-temperature water were used to evaluate the hardening coefficient for the DBH, FKH and BKS models. The transmission electron microscope samples prepared from the tensile samples provided the helium bubble average size and density needed to apply the hardening models. The results showed that the hardening coefficient increased with increasing the bubble size in the DBH ($\sim$0 to 0.2) and FKH ($\sim$0 to 1) models, whereas remained constant in the BKS ($\sim$0.3) model. It is difficult to evaluate, which model is more physically realistic, but it seems plausible that the hardening coefficient increases with the defect size; that the hardening coefficient has a tendency to unity with increasing the defect size; and that only the defects interacting with gliding dislocations can contribute to hardening. The FKH model appears to possess these characteristics, so perhaps it is the model with more physical meaning among the three analysed models. However, the BKS model intrinsically considers the defect size effect; it does not depend on the sum of different defect size contributions; and it is the model with less accumulated errors, since there is no need to sum the contribution of different sizes as they can be treated together, provided that the defect type is the same.

The instrumented nano-indenter study on different grain to grain orientations did not show any grain boundary embrittlement at room temperature in as-implanted and PIA samples. This result agrees well with the accelerated SSRT results. Moreover, the grain orientation had a limited effect on the indentation properties with average changes within 15% in SA, as-implanted and PIA samples. The CW samples showed higher grain to grain deviation due to the preferential grain deformation during the CW process. The plastic properties (n and K) seemed to be little dependent on the grain orientation.

The ratio between the indentation-tensile $Rp_{0.2\%}$ is consistent with the literature results, once the indentation size and structure effects are removed. The increase of $Rp_{ind\ 0.2\%}$ from SA to PIA (>650°C) samples can be merely attributed to the bubbles hardening, which confirms the literature observations and the tensile results.

5.2 Perspectives

5.2.1 Follow-up projects

According to the results presented, there are many possibilities to continue studying the helium effects on IASCC. Literature data showed that IASCC at low electrochemical corrosion potential using slow strain rate tests might be correlated to the helium content, but this study indicated that a minimum amount of irradiation damage might be needed. Three possible research topics are proposed:

5.2.1.1 Pre-cracked specimens with helium

Miniaturized samples could be manufactured from compact test specimens, where a transgranular crack is already initiated by fatigue. Then, the miniaturized sample is implanted with helium, the transgranular crack is transitioned to an intergranular crack under the environmental testing conditions (e.g. PWR primary water), and the susceptibility to IASCC is monitored and compared to non-implanted samples in hydrogenated high-temperature water. This approach might help to understand whether helium can significantly increase the susceptibility to intergranular cracking in as-implanted and PIA samples.

5.2.1.2 Introduce stress during helium implantation

Helium implantation at 300°C (or higher) under tensile stress might decrease the capture efficiency of interstitials by the helium bubbles, so the bubble size might be bigger in the as-implanted condition. Meanwhile, the black dots and extended defects might be kept similar than without stress but with bigger bubble size, which might have higher contribution to hardening. Moreover, it is plausible that the implantation under stress enhances the migration/diffusion of helium bubbles/atoms to the grain boundaries, hence increase the grain boundary coverage.

5.2.1.3 Test specimens with higher radiation damage

The current results showed that helium alone (<0.16 dpa) is insufficient to produce IASCC in accelerated slow strain rate tests in hydrogenated high-temperature water with 2.2 ppm H_2. Therefore, future tests could include samples with higher irradiation damage (>1 dpa) and similar helium contents, which is a more realistic case. Three approaches can be used:

<u>Test specimens with simultaneous helium implantation and ion irradiation</u>

A solution to increase the damage induced in the miniaturized samples is simultaneous alpha and proton irradiation. The dual beam irradiation and the energy needed to penetrate half of the sample thickness can be already carried out in CEMHTI/CNRS cyclotron. However, the sample activity and the implantation time are significantly higher than in the present study. Hence, it would be reasonable to reduce the thickness of the sample in order to find the conditions at which IASCC occurs.

High content of helium and radiation damage

The SINQ target irradiation program (STIP) samples can reach up to 15 dpa/year and helium production rates of ~800 appm/year. The radiation damage and the helium production can be reduced depending on the location of the samples. However, the sample activity and contamination can be a problem for handling the samples. Thus, the samples should be irradiated many years before their use (e.g. 10 years).

Preparation of test specimens from reactor internal components

Miniaturised samples can be manufactured from structural components replaced from reactor pressure internals, such as baffle-former bolts. This would allow testing components irradiated at different dose, dose rate and temperature, so having a different microstructure (e.g. Figure 2.33).

References

[1] G. Was, Y. Ashida and P. Andresen, "Irradiation-assisted stress corrosion cracking," *Comprehensive Nuclear Materials,* vol. 5, pp. 177-205, 2012.

[2] K. Fukuya, "Current understanding of radiation-induced degradation in light water reactor structural materials.," *Journal of nuclear science and technology,* vol. 50, pp. 213-254, 2013.

[3] P. Andresen and G. Was, "Irradiation Assisted Stress Corrosion Cracking," in *Comprehensive Nuclear Materials*, vol. 2011, Elsevier, 2012, p. 177–205.

[4] F. Garner, "Radiation damage in austenitic steels," *Comprehensive Nuclear Materials,* vol. 4, pp. pp. 33-95, 2012.

[5] O. Chopra and A. Rao, "A review of irradiation effects on LWR core internal materials -IASCC susceptibility and crack growth rates of austenitic stainless steels.," *Journal of nuclear materials,* pp. 235-256, 2011.

[6] F. Garner, B. Oliver, L. Greenwood, D. Edwards, S. Bruemmer, M. Grossbeck and L. Martin, "Generation and retention of helium and hydrogen in austenitic steels irradiated in a variety of LWR and test reactor spectral environments," Fusion Materials Semiannual Progress Report for Period Ending, DOE-ER-0313/30, Jan. 2001.

[7] S. Belozerov, V. Neustroyev and V. Shamardin, "Studying helium accumulation in austenitic steels for evaluating radiation damage in internals of water-moderated water-cooled power reactors.," *The Physics of Metals and Metallography,* vol. 106, pp. 503-509, 2008.

[8] H. Schroeder and W. Liu, "Dependence of the tensile properties of 316L parent material and welds on implanted hydrogen and/or helium.," *Journal of nuclear materials,* Vols. 191-194, pp. 776-780, 1992.

[9] K. Takakura, K. Nakata, K. Fujimoto, K. Sakima and N. Kubo, "IASCC properties of cold worked 316 stainless steel in PWR primary water," in *14th International conference on environmental degradation of materials in nuclear power systems water reactors*.

[10] T. Miura, K. Fujii and K. Fukuya, "Micro-mechanical investigation for effects of helium on grain boundary fracture of austenitic stainless steel," *Journal of Nuclear Materials,* vol. 457, pp. 279-290, 2015.

[11] H. Ullmaier and J. Chen, "Low temperature tensile properties of steels containing high concentration of helium," *Journal of nuclear materials,* vol. 318, pp. 228-233, 2003.

[12] Y. Chen, A. Rao, B. Alexandreanu and K. Natesan, "Slow strain rate tensile tests on irradiated austenitic stainless steels in simulated light water reactor environments," *Nuclear engineering and design,* vol. 269, pp. 38-44, 2014.

[13] J. Chen, Y. Dai, F. Carsughi, W. Sommer, G. Bauer and H. Ullmaier, "Mechanical properties of 304L stainless

steel irradiated with 800 MeV protons," *Journal of nuclear materials,* vol. 275, pp. 115-118, 1999.

[14] "HyperPhysics," Georgia State University, 18 January 2014. [Online]. Available: http://hyperphysics.phy-astr.gsu.edu/hbase/nucene/nucbin.html. [Accessed 21 12 2015].

[15] "International Atomic Energy Agency (IAEA)," 12 16 2015. [Online]. Available: https://www.iaea.org/PRIS/WorldStatistics/OperationalByAge.aspx. [Accessed 17 16 2015].

[16] K. Fukuya, "Radiation effects," in *Conference QMN Approach to Predicting SCC of Fe-Cr-Ni Alloys*, 2010.

[17] I. A. E. Agency, "Optimization of Water Chemistry to Ensure Reliable Water Reactor Fuel Performance at High Burnup and in Ageing Plant (FUWAC)," IAEA, Vienna, 2011.

[18] "Nuclear reactors, water chemistry of light water reactors," Encyclopedia of Chemical Technology, 2005.

[19] L. Oliver, B. Helmersson, E. Fredriksson, G. Ledergerber, W. Kaufmann, G. Wikmark, B. Cheng and A. Kucuk, "Review of water chemistry and corrosion products in a NWC plant transitioned to hydrogen injection and OLNC," in *NPC 2010 conference proceedings*, Toronto, Ontario (Canada), 3-8 Oct 2010.

[20] International atomic energy agency, "Assessment and management of ageing of major nuclear power plant components important to safety: PWR vessel internals," IAEA, Vienna, 1999.

[21] L. Niewolak, E. Wessel, T. Hüttel, C. Asensio-Jimenez, L. Singheiser and W. Quadakkers, "Behavior of Interconnect Steels in Carbon Containing Simulated Anode Gas of Solid Oxide Fuel Cells," *Journal of The Electrochemical Society,* vol. 159, pp. F725-F732, 2012.

[22] B. Leffler, "Stainless steels and their properties," 2011.

[23] J. Davis, Stainless Steels. The Materials Information Society., ASM International, 1994.

[24] P. Cutler and G. Coates, "The Role of Nickel in Stainless Steels," Indian Institute of Metals, 2011.

[25] "The effects of alloying elements," Outokumpu, [Online]. Available: http://www.outokumpu.com/en/products-properties/more-stainless/the-effects-of-alloying-elements%E2%80%8B/Pages/default.aspx.

[26] J. Dyson, "Gowelding," May 2014. [Online]. Available: http://www.gowelding.com/met/Schaeffler.jpg.

[27] J. Davis, Metals Handbook, 2nd edition: Materials Park, Ohio, ASM International, 1998.

[28] C. Hsieh and W. Wu, "Overview of Intermetallic Sigma (σ) Phase Precipitation In Stainless Steels.," *ISRN Metallurgy,* vol. Article ID 732471, p. 16 pages, 2012.

[29] K. Lo, C. Shek and J. Lai, "Recent developments in stainless steels.," *Materials Science and Engineering,* vol. 65, pp. 39-104, 2009.

[30] J. Song, Q. Li, C. Xiao and Y. Han, "Effect of alloying elements on microstructure and mechanical properties of high temperature die material Dm02 alloy.," *Materials Science Forum Vols.,* Vols. 546-549, pp. 1257-1260, 2007.

[31] M. Lewis and B. Hattersley, "Precipitation of M23C6 in Austenitic stainless steels," *Acta Metall.,* vol. 13, pp.

1159-1168, 1965.

[32] Z. Jiang, Z. Zhang, H. Li and Q. Ma, "Microstructural evolution and mechanical properties of aging high nitrogen austenitic stainless steels," *International Journal of Minerals, Metallurgy and Materials,* vol. 17, p. 729, 2010.

[33] P. Scott, "A review of irradiation assisted stress corrosion cracking," *Journal of nuclear materials,* vol. 211, pp. 101-122, 1994.

[34] AK steel corporation, "Aksteel 316/316L product data sheet," 2007. [Online]. Available: http://www.aksteel.com/pdf/markets_products/stainless/austenitic/316_316l_data_sheet.pdf.

[35] E. Halle, "The Deformation and Ageing of Mild Steel," in *Proceeding of physical society*, 1951.

[36] N. Petch, "The cleavage strength of polycrystals," *Journal of iron and steel research,* pp. 174:25-8, 1953.

[37] H. Khatak and B. Raj, Corrosion of austenitic stainless steels, Woodhead publishing limited, 2002.

[38] H. Seifert and S. Ritter, "EAC and EAF of carbon and low-alloy steels in high temperature water," in *Nuclear Corrosion Summer School*, Slovenia, 2015.

[39] G. Was, Fundamentals of radiation. Material science, Springer, 2007.

[40] G. Was and S. Bruemmer, "Effects of irradiation on intergranular stress corrosion cracking," *Journal of Nuclear Materials,* vol. 216, pp. 326-347, 1994.

[41] S. Bruemmer, B. Arey and L. Charlot, "Influence of chromium depletion on intergranular stress corrosion cracking of 304 stainless steel," *Corrosion science,* vol. 48, no. 1, pp. 42-49, 1992.

[42] D. Edwards, E. Simonen and S. Bruemmer, "Radiation-induced segregation behavior in austenitic stainless steels: Fast reactor versus light water reactor irradiations," in *Proceedings 13th international conference on environmental degradation of materials in nuclear power systems - water reactors*, Toronto (Canada), 2007.

[43] S. Bruemmer, E. Simonen, P. Scott, P. Andresen, G. Was and J. Nelson, "Radiation-induced material changes and susceptibility to intergranular failure of light-water-reactor core internals," *Journal of Nuclear Materials,* vol. 274, pp. 299-314, 1999.

[44] O. Chopra, "Degradation of LWR core internal materials to neutron irradiation," U.S. Nuclear regulatory commission, 2010.

[45] R. Stoenescu, Effects of neutron irradiation on the microstructure and mechanical properties of the heat affected zone of stainless steels welds., Doctoral thesis, EPFL, 2005.

[46] S. Bruemmer, B. Arey, L. Charlot and D. Edwards, "Microstructural, microchemical and hardening evolution in LWR-irradiated austenitic stainless steels," in *Proceedings of the ninth international symposium environmental degradation of materials in nuclear environmental degradation of materials in nuclear power systems-Water reactor. Metallurgical society*, Warrendale, PA, 1999.

[47] J. Robertson, I. Ioda, A. Rowcliffe, M. Grossbeck and S. Jitsukawa, "Temperature dependence of the deformation behavior of type 316 stainless steel after low temperature neutron irradiation," in *Effects of*

Radiation on Materials: 18th International Symposium, ASTM STP 1325, 1999, pp. 671-688.

[48] A. Seeger, "On the theory of radiation damage and radiation hardening," *Proceedings of the second united nations international conference on the peaceful uses of atomic energy,* vol. 6, pp. 250-273, Geneva. September 1958.

[49] K. Fukuya, M. Nakano, K. Fujii, T. Torimaru and Y. Kitsunai, "Separation of microstructural and microchemical effects in irradiation assisted stress corrosion cracking using post-irradiation annealing," *Journal of nuclear science and technology,* vol. 41, no. 12, pp. 1218-1227, 2004.

[50] C. Sobie, N. Bertin and L. Capolungo, "Analysis of obstacle hardening models using dislocation dynamics: application to irradiation induced defects," *Metallurgical and materials transactions A,* vol. 46A, pp. 3761-3772, 2015.

[51] R. Schäublin and Y. Chiu, "Effect of helium on irradiation-induced hardening of iron: A simulation point of view," *Journal of nuclear materials,* vol. 362, pp. 152-160, 2007.

[52] R. Gérard and F. Somville, "Situation of the baffle-former bolt in Belgian units," in *INCONE17*, Brussels, Belgium, 2009.

[53] T. Griesbach, G. Licina, P. Riccardella and J. Rashid, "A probabilistic approach to baffle bolt IASCC predictions," Structural Integrity Associates, Inc., California, United States, 2012.

[54] U. Chatterjee, S. Bose and S. Roy, Environmental degradation of metals: Corrosion technology series/14, Marcel Dekker, Inc., 2001.

[55] G. Was and P. Andresen, "Stress corrosion cracking behavior of alloys in aggressive nuclear reactor core environments," *Corrosion,* vol. 63, no. 1, pp. 19-45, 2007.

[56] L. Greenwood and F. Garner, "Hydrogen generation arising from the 59Ni(n,p) reaction and its impact on fission-fusion correlations.," *Journal of Nuclear Materials,* Vols. 233-237, pp. 1530-1534, 1996.

[57] F. Garner, L. Greenwood, E. Gilbert and M. Griffths, *Proceedings of the 14th int. conf. on environmental degradation of materials in nuclear power system.,* p. p. 1344, 2009.

[58] C. Kumai and T. Devine, "Influence of oxygen concentration of 288°C water and alloy composition on the films formed on Fe-Ni-Cr alloys," *Corrosion,* vol. 63, pp. 1101-1113, 2007.

[59] Y. Soma, C. Kato and M. Yamamoto, "Growth behavior of surface oxide layer on SUS316L stainless steel at the early stage of exposure to 288°C water," *Material transactions,* vol. 53, no. 1, pp. 195-200, 2012.

[60] R. Staehle, "Quantitative Micro-Nano (QMN) approach to SCC mechanism and prediction-starting a third meeting," *15th International conference on environmental degradation of materials in nuclear power systems-water reactors,* vol. 2, pp. 1452-1542, 2011.

[61] P. Andresen and D. Duquette, "The effects of dissolved oxygen, chloride ion and applied potential on the SCC behavior of type 304 stainless steel in 290 C water," *Corrosion,* vol. 36, no. 8, pp. 409-415, 1980.

[62] "Chloride induced transgranular stress corrosion cracking (TGSCC) of stainless steel components in German nuclear power plants," in *International symposium on "contribution of materials investigations to improve the safety and performance of light-water reactors"*, Fontevraud, France, 18–22 September 2006.

[63] F. Michel, "Evaluation of operating experience with regard to passive mechanical components – approach and new insights," Eurosafe.

[64] P. Andresen, "Understanding and predicting stress corrosion cracking (SCC) in hot water," in *Stress corrosion cracking of nickel-based alloys in water-cooled nuclear reactors*, Woodhead Publishing, 2016, pp. 169-238.

[65] P. Andresen, "Stress corrosion cracking (SCC) of austenitic stainless steels in high temperature light water reactor (LWR) environments," in *Understanding and Mitigating Ageing in Nuclear Power Plants*, Woodhead Publishing, 2010, pp. 236-307.

[66] D. Landolt, Corrosion and surface chemistry of metals, Lausanne: EPFL press, 2007.

[67] D. Du, K. Chen, L. Yu, H. Lu, L. Zhang, X. Shi and X. Xu, "SCC crack growth rate of cold worked 316L stainless steel in PWR environment," *Journal of Nuclear Materials,* vol. 456, pp. 228-234, 2015.

[68] P. Aaltonen and H. Hanninen, "Water chemistry and behavior of materials in PWRs and BWRs," (IAEA-TECDOC--965), International Atomic Energy Agency (IAEA), 1997.

[69] S. Gosselin, F. Simonen, S. Pilli and B. Lydell, "Probabilities of failure and uncertainty estimate information for passive components - A literature review," U.S. Nuclear regulatory commission, Washington, DC, 2007.

[70] J. Hakala, H. Hänninen and P. Aaltonen, "Stress corrosion and thermal fatigue - experiences and countermeasures in austenitic SS pipings of finish BWR-plants," *Nuclear engineering and design,* vol. 119, pp. 389-398, 1990.

[71] B. Gordon, "The effect of chloride and oxygen on the stress corrosion cracking of stainless steel: Review of literature," *Materials performance,* vol. 19, no. 4, pp. 29-38, 1980.

[72] J. Congleton, W. Zheng and H. Hua, "Stress corrosion cracking of annealed Type 316 stainless steel in high-temperature water," *Cossorion,* vol. 46, no. 8, pp. 641-627, 1990.

[73] Z. Szklarska-Smialowska, "Review of literature on pitting corrosion published since 1960," *Corrosion,* vol. 27, no. 6, pp. 223-233, 1971.

[74] J. Oldfield and W. Sutton, "Crevice Corrosion of Stainless Steels: I. A mathematical model," *British corrosion journal,* vol. 13, no. 1, pp. 13-22, 1978.

[75] K. Arioka, T. Yamada, T. Terachi and T. Miyamoto, "Dependence of stress corrosion cracking for cold-worked stainless steel on temperature and potential, and role of diffusion of vacancies at crack tips," *Corrosion,* vol. 64, no. 9, pp. 691-706, 2008.

[76] "BWRVIP-130: BWR vessel and internals project BWR water chemistry guidelines 2004 revision," EPRI technical report, Oct. 2004.

[77] K. Arioka, T. Yamada, T. Terachi and G. Chiba, "Cold Work and Temperature Dependence of Stress Corrosion Crack Growth of Austenitic Stainless Steels in Hydrogenated and Oxygenated High-Temperature Water," *Corrosion,* vol. 63, no. 12, pp. 1114-1123, 2007.

[78] P. Andresen, "Effects of Temperature on Crack Growth Rate in Sensitized Type 304 Stainless Steel and Alloy 600," *Corrosion,* vol. 49, no. 9, pp. 714-725, 1993.

[79] T. Terachi, T. Yamada, T. Miyamoto and K. Arioka, "SCC growth behaviors of austenitic stainless steels in simulated PWR primary water," *Journal of Nuclear Materials,* vol. 426, no. 1, pp. 59-70, 2012.

[80] Z. Lu, Y. Takeda and T. Shoji, "Some fundamental aspects of thermally activated processes involved in stress corrosion cracking in high temperature aqueous environments," *Journal of nuclear materials,* vol. 383, pp. 92-96, 2008.

[81] P. Maiya and N. Schack, "Stress corrosion cracking susceptibility of AISI 316 NG and 316 stainless steel in an impurity environment," *Corrosion,* vol. 41, no. 11, pp. 630-634, 1985.

[82] F. Scenini and A. Sherry, "Stress corrosion cracking of sensitized type 304 stainless steel in high-temperature water with anionic impurities contamination," *Corrosion,* vol. 68, no. 12, pp. 1094-1107, 2012.

[83] P. Andresen and D. Duquette, "The effect of chloride ion concentration and applied potential on the SCC behavior of type 304 stainless steel in deaerated high temperature water," *Corrosion,* vol. 36, no. 2, pp. 85-93, 1980.

[84] M. Hishida and H. Nakada, "Constant strain rate testing of type 304 stainless steel in high temperature water—Part II: An investigation of the chloride effect on stress corrosion cracking," *Corrosion,* vol. 33, no. 11, pp. 403-407, 1977.

[85] P. Andresen, "Emerging issues and fundamental processes in environmental cracking in hot water," *Corrosion,* vol. 64, no. 5, pp. 439-464, 2008.

[86] T. Anderson, Fracture mechanics: fundamental and applications, CRC Press Taylor & Francis Group, 2005.

[87] S. Hettiarachchi, R. Law, T. Diaz, W. Miller, R. Cowan, W. Keith, L. Kriege and R. Pathania, "Application of noble metal chemical addition technology to an operating BWR to mitigate IGSCC of reactor internals," in *NACE International p. 15, Paper 142*, San Diego, CA (United States), 22-27 Mar 1998.

[88] P. Andresen and F. F.P., "Life prediction by mechanistic modeling and system monitoring of environmental cracking of iron and nickel alloys in aqueous systems," *Materials science and engineering,* vol. 103, pp. 167-184, 1988.

[89] P. Scott and D. Tice, "Stress corrosion cracking in low alloy steels," *Nuclear engineering and design,* vol. 119, pp. 399-413, 1990.

[90] P. Andresen and L. Young, "Crack tip microsampling and growth rate measurements in low-alloy steel in high-temperature water," *Corrosion,* vol. 51, no. 3, pp. 223-233, 1995.

[91] F. Ford, "Environmentally assisted cracking of low-alloy steels," EPRI NP-7473-L, Palo Alto, CA (USA), January 1992.

[92] F. Ford and P. Combrade, "Electrochemical reaction rates on bare surfaces and their use in a crack prediction model for the low-alloy steel/water system," in *Proceedings 2nd international IAEA specialsist's meeting on sub-critical crack Growth, NUREG/CP-0067. Vol. 2, pp. 231 – 268*, Sendai, Japan, 15 – 17 Mai 1985.

[93] T. Matsuo, J. Yamabe and S. Matsuoka, "Effects of hydrogen on tensile properties and fracture surface morphologies of type 316L stainless steels," *International journal of hydrogen energy,* vol. 39, pp. 3542-

3551, 2014.

[94] T. Hryniewicz, P. Konarski, K. Rokosz and R. Rokicki, "SIMS analysis of hydrogen content in near surface layers of AISI 316L SS after electrolytic polishing under different conditions," *Surface & Coatings Technology,* vol. 205, pp. 4228-4236, 2011.

[95] S. Brauser and T. Kannengiesser, "Hydrogen absorption and diffusion in different welded duplex steels," *Welding in the world,* vol. 55, no. 5, pp. 26-36, 2011.

[96] Y. Kim, Y. Kim, D. Kim, S. Kim, W. Nam and H. Choe, "Effects of hydrogen diffusion on the mechanical properties of austenite 316L at ambient temperature," *material transaction,* vol. 52, no. 3, pp. 502-513, 2011.

[97] D. Edwards, F. Garner, B. Oliver and S. Bruemmer, "Microstructural evaluation of a cold-worked 316SS baffle bolt irradiated in a commercial PWR," in *Proceedings of tenth international conference on environmental degradation of materials in nuclear power systems water reactors*, Houston, TX (USA), 5 –9 Aug. 2001.

[98] S. Roychowdhury, H. Seifert, P. Spätig, Z. Que and S. Ritter, "Effect of high-temperature water and hydrogen on the fracture behaviour of a low-alloy reactor pressure vessel steel," in *17th International conference on environmental degradation of materials in nuclear power systems – water reactors*, Ontario, Canada., 2015.

[99] C. San Marchi and B. Somerday, "Technical reference for hydrogen compatibility of materials," Sandia report - SAND2012-7321, Livermore, CA (USA), Sep. 2012.

[100] F. Garner and L. Greenwood, "Neutron irradiation effects in fusion or spallation structural materials: Some recent insights related to neutron spectra," *Radiation effects and defects in solids,* vol. 144, no. 1-4, pp. 251-286, 2006.

[101] H. Seifert, S. Ritter, P. Spätig, S. Roychowdhury and J. Bai, "Final report on the SAFE project," *PSI internal report,* 2015.

[102] H. Birnbaum, "Hydrogen effects on deformation — Relation between dislocation behavior and the macroscopic stress-strain behavior," *Scripta metallurgica et materialia,* vol. 31, no. 2, pp. 149-153, 1994.

[103] I. Robertson, "The effect of hydrogen on dislocation dynamics," *Engineering fracture mechanics,* vol. 68, no. 6, pp. 671-692, 2001.

[104] S. Lynch, "Hydrogen embrittlement phenomena and mechanisms," *Corrosion Revision,* vol. 30, no. DOI 10.1515/corrrev-2012-0502, pp. 105-123, 2012.

[105] D. Bromley, "Hydrogen embrittlement of austenitic stainless steels SUS 316 and 316L," University of British Columbia, Vancouver (CAN), 2005.

[106] S. Gahr, M. Grossbeck and H. Birnbaum, "Hydrogen embrittlement of Nb I – macroscopic behavior at low temperatures," *Acta metallurgica,* vol. 25, pp. 125-134, 1977.

[107] C. Beachem, "A new model for hydrogen-assisted cracking (hydrogen embrittlement)," *Metallurgical transactions,* vol. 3, pp. 441-455, 1972.

[108] H. Birnbaum and P. Sofronis, "Hydrogen-enhanced localized plasticity a mechanism for hydrogen-related fracture," *Materials science and engineering,* vol. 176, no. 1-2, pp. 191-202, 1994.

[109] A. Tetelman and W. Robertson, "The mechanism of hydrogen embrittlement observed in iron-silicon single crystals," Technical report: Defence technical information center (US department of defense), Sep. 1961.

[110] C. Zapffe and C. Sims, "Hydrogen embrittlement, internal stress and defects in steels," *Transactions, American institute of mining and metallurgical engineers,* vol. 145, pp. 225-259, 1941.

[111] M. Nagumo, "Hydrogen related failure of steels–a new aspect," *Materials science and technology,* vol. 20, no. 8, pp. 940-950, 2004.

[112] S. Lynch, "Environmentally assisted cracking: Overview of evidence for an adsorption-induced localised-slip process," *Acta metallurgica,* vol. 36, pp. 2639-2661, 1988.

[113] S. Lynch, "Metallographic contributions to understanding mechanisms," *Metallography,* vol. 23, no. 2, pp. 147-171, 1989.

[114] A. Troiano, "The role of hydrogen and other interstitials in the mechanical behavior of metals," *Metallography microstructure and analysis,* vol. 52, pp. 54-80, 1960.

[115] R. Oriani and P. Josephic, "Equilibrium aspects of hydrogen-induced cracking of steels," *Acta metallurgica,* vol. 22, pp. 1065-1074, 1974.

[116] H. Birnbaum, "Mechanisms of hydrogen related fracture of metals," in *Hydrogen effects on materials behavior. Eds: Moody N.R., Thompson A.W.*, TMS, 1990, pp. 639-658.

[117] M. Nagumo, H. Yoshida, Y. Shimomura and T. Kadokura, "Ductile crack growth resistance in hydrogen-charged steels," *Materials transactions,* vol. 42, pp. 132-137, 2001.

[118] P. Andresen and L. Young, "Characterization of the role of electrochemistry, convection and crack chemistry in stress corrosion cracking," in *Proceedings 7th international symposium on environmental degradation of materials in nuclear power systems - water reactors*, Breckenridge, CO (USA), 6-10 Aug 1995.

[119] L. Young and P. Andresen, "Crack tip microsampling and growth rate measurements in a 0.021%S low alloy steel in high temperature water," in *7th International symposium on environmental degradation of materials in nuclear power plants: water reactors*, Breckenridge, CO (USA), 6-10 Aug 1995.

[120] F. Ford, "Overview of collaborative research into mechanisms of environmentally controlled cracking in the low-alloy pressure vessel steel/water system," in *Proceedings 2nd International IAEA specialist's meeting on sub-critical crack growth. Vol. 2, pp. 3 – 71.*, Sendai (Japan), 1985.

[121] Y. Lee, T. Shoji and K. Raja, "Evaluation of crack-tip solution chemistry of low-alloy steels in oxygenated high-temperature water," in *9th International symposium on environmental degradation of materials in nuclear power systems - water reactors. Eds: S. Bruemmer, P. Ford, G. Was*, Newport Beach (USA), August 1999.

[122] G. Gabetta, "Measure of chemical and electrochemical parameters inside an environmentally-assisted growing crack," in *Proceedings 3rd international IAEA specialist's meeting on sub-critical crack growth. Ed. W. Cullen*, Moscow (Rusia), 1990.

[123] G. Gabetta, "A method to measure electrochemical potential at the tip of a growing crack during an environmental fatigue test," *Fatigue and fracture of engineering materials and structures,* vol. 5, no. 3, pp. 215-220, 1982.

[124] P. Andresen, "Conceptual similarities and common predictive approaches for SCC in high temperature water systems," in *National association of corrosion engineers (NACE) conference*, Denver, CO (USA), 24-29 Mar 1996.

[125] K. Fukuya, S. Shima, H. Kazano and M. Narui, "Stress corrosion cracking and intergranular corrosion of neutron irradiated austenitic stainless steels," *Journal of nuclear materials,* Vols. 191-194, pp. 1007-1011, 1992.

[126] A. Jenssen and L. Ljungberg, "Irradiation Assisted Stress Corrosion Cracking of Stainless Alloys in BWR Normal Water Chemistry and Hydrogen Water Chemistry," 1993.

[127] G. Gordon and K. Brown, "Dependence of creviced BWR component IGSCC behavior on coolant chemistry," in *Proceedings 4th international conference on environmental degradation of materials in nuclear power systems - water reactors*, Houston, TX (USA), 1990.

[128] F. Garner and M. Toloczko, "Irradiation creep and void swelling of austenitic stainless steels at low displacement rates in light water energy systems," *Journal of nuclear materials,* vol. 251, pp. 252-261, 1997.

[129] N. Sakaguchi, S. Watanabe, H. Takahashi and R. Faulkner, "A multi-scale approach to radiation-induced segregation," *Journal of nuclear materials,* Vols. 329-333, pp. 1166-1169, 2004.

[130] G. Was and P. Andresen, "The nature of SCC in irradiated stainless steels and Nickel-base alloys in LWRs," *17th international corrosion congress,* vol. 5, pp. 2791-2811, 2008.

[131] P. Panait, E. Fargeas, M. Tommy-Martin, S. Miloudi, P. Moulart, N. Monteil and C. Pokor, "Metallurgical investigations of a baffle to former bolt located on a high level of the internal structures," in *Fontevraud 8 - Contribution of Materials investigations and operating experience to LWRs' safety, performance and reliability*, 2014.

[132] C. Pokor, Y. Thebault, J.-P. Massoud, M. Delnondedieu, D. Loisnard, P. Dubuisson, J. Kocik, E. Keilova, E. Lemaire and N. Ligneau, "Microstructural evolution of neutron irradiated stainless steels: comparison between irradiations in experimental reactors and in pressurized water reactors," in *Fontevraud 5 international symposium "contribution of materials investigations to improve the safety and performance of LWRs*, 2006.

[133] R. Pathania, "Characterization of Neutron-Irradiated 300-Series Stainless Steels to Assess Mechanisms of Irradiation-Assisted Stress Irradiation-Assisted Stress," EPRI, California, 2006.

[134] D. Edwards, E. Simonen, F. Garner, L. Greenwood, B. Oliver and S. Bruemmer, "Influence of irradiation temperature and dose gradients on the microstructural evolution in neutron-irradiated 316SS," *Journal of nuclear materials,* vol. 317, pp. 32-45, 2003.

[135] D. Edwards, F. Garner, S. Bruemmer and P. Efsing, "Nano-cavities observed in a 316SS PWR flux thimble tube irradiated to 33 and 70 dpa," *Journal of nuclear materials.*

[136] J. Michalicka, A. Hojna, E. Keilova and J. Kocik, "TEM radiation damage investigation of neutron irradiated

baffle-to-former bolt extracted from the decommissioned VVER-440 reactor vessel internals," in *16th International conference on environmental degradation of materials in nuclear power systems-water reactors 2013*, Asheville, North Carolina (US), 11-15 August 2013.

[137] J. Foster, D. Porter, D. Harrod, T. Mager and M. Burke, "316 stainless steel cavity swelling in a PWR," *Journal of Nuclear Materials,* pp. 207-215, 1995.

[138] W. Burns and P. Moore, "Water radiolysis and its effect upon in-reactor zircaloy corrosion," *Radiation effects and defects in solids,* vol. 30, no. 4, pp. 233-242, 1976.

[139] P. Andresen, F. Ford and J. Higgins, "Life prediction of boiling water reactor internals," in *Proceedings international conference on nuclear engineering (ICONE-4)*, New Orleans, LA (USA), 10-13 Mar 1996.

[140] S. Bruemmer and E. Simonen, "Radiation hardening and radiation-induced chromium depletion effects on intergranular stress corrosion cracking in austenitic stainless steels," *Corrosion,* vol. 50, no. 12, pp. 940-946, 1994.

[141] M. Kodama, Y. Ishiyama, S. Namatame, S. Suzuki, K. Fukuya, H. Sakamoto, K. Nakata and T. Kato, "Effect of pre-irradiation grain boundary chemistry on IASCC," in *Ninth international symposium on environmental degradation of materials in nuclear power systems - water reactors*, Newport Beach, CA (USA), 1-5 Aug 1999.

[142] N. Kodama, R. Katsura, J. Morisawa, S. Nishimura, S. Suzuki, K. Asano, K. Fukuya and K. Nakata, "IASCC susceptibility of austenitic stainless steels irradiated to high neutron fluence," in *Proceedings of the sixth international symposium on environmental degradation of materials in nuclear power systems - water reactors*, San Diego, CA (USA), 1-5 Aug 1993.

[143] G. Was, "Recent developments in understanding IASCC," in *Proceedings 11th international symposium on environmental degradation of materials in nuclear power systems - Water reactors*, Stevenson, WA (USA), 10-14 Aug 2003.

[144] K. Fujimoto, T. Yonezawa, E. Wachi, Y. Yamaguchi, M. Nakano, R. Shogan, J. Massoud and T. Mager, "Effect of the accelerated irradiation and hydrogen/helium gas on IASCC characteristics for highly irradiated austenitic stainless steels," in *Proceedings of the 12th International Conference on Environmental Degradation of Materials in Nuclear Power Systems*, 2005.

[145] J. Busby, G. Was and E. Kenik, "Isolating the effect of radiation-induced segregation in irradiation-assisted stress corrosion cracking of austenitic steels," *Journal of nuclear materials,* vol. 302, no. 1, pp. 20-40, 2002.

[146] A. Jacobs and S. Dumbill, "Effects on low temperature annealing on the microstructure and grain boundary chemistry of irradiated 304 SS and correlations with IASCC," in *Proceedings 7th international symposium on environmental degradation of materials in nuclear power systems - Water reactors*, Houston, TX (USA), 7-10 Aug 1995.

[147] K. Asano, K. Fukuya, K. Nakata and M. Kodoma, "Changes in grain boundary composition induced by neutron irradiation on austenitic stainless steels," in *Proceedings fifth international symposium on environmental degradation of materials in nuclear power systems - Water reactors*, Monterey, CA (USA), 25-29 Aug 1992.

[148] Z. Jiao, J. Hesterberg and G. Was, "Effect of post-irradiation annealing on hardening, localized deformation and IASCC of a proton-irradiated 304 stainless steel," in *17th International conference on environmental*

degradation of materials in nuclear power systems - water reactors, Ottawa, Ontario (US), 9-13 Aug 2015.

[149] R. Tucker, M. Wechsler and S. Ohr, "Dislocation channeling in neutron-irradiated niobium," *Journal of applied physics,* vol. 40, no. 1, pp. 400-408, 1969.

[150] N. Hashimoto and T. Byun , "Deformation-induced martensite formation and dislocation channeling in neutron-irradiated 316 stainless steel," *Journal of Nuclear Materials,* Vols. 367-370, no. B, pp. 960-965, 2007.

[151] M. Sauzay, K. Bavard and W. Karlsen , "TEM observations and finite element modelling of channel deformation in pre-irradiated austenitic stainless steels – Interactions with free surfaces and grain boundaries," *Journal of Nuclear Materials,* vol. 406, no. 1, pp. 152-165, 2010.

[152] T. Byun, N. Hashimoto and K. Farrell, "Deformation mode map of irradiated 316 stainless steel in true stress–dose space," *Journal of nuclear materials,* vol. 351, no. 1-3, pp. 303-315, 2006.

[153] Z. Jiao, J. Busby, G. Obata and G. Was, "Influence of localized deformation on irradiation-assisted stress corrosion cracking of proton-irradiated austenitic alloys," in *12th International conference on environmental degradation of materials in nuclear power systems-water reactors*, Salt Lake City, UT (US), 14 Aug 2005.

[154] Z. Jiao and G. Was, "Impact of localized deformation on IASCC in austenitic stainless steels," *Journal of nuclear materials,* vol. 408, pp. 246-256, 2011.

[155] H. Nishioka, K. Fukuya, K. Fujii and Y. Kitsunai, "Deformation structure in highly irradiated stainless steels," *Journal of nuclear science and technology,* vol. 45, no. 4, pp. 274-287, 2008.

[156] P. Swann, "Dislocation substructure vs transgranular stress corrosion susceptibility of single phase alloys," *Corrosion,* vol. 19, pp. 102-112, 1963.

[157] A. Thompson and M. Bernstein, "Ed. Fontana, G. and Staehle, R.W. The role of metallurgical variables in hydrogen-assisted environmental fracture," in *Advances in corrosion science and technology*, Boston, MA, Springer US, 1980, pp. 53-175.

[158] G. Was, B. Alexandreanu and J. Busby, "Localized deformation induced IGSCC and IASCC of austenitic alloys in high temperature water," *Key engineering materials,* Vols. 261-263, pp. 885-902, 2004.

[159] "Deformation microstructure of proton-irradiated stainless steels," *Journal of nuclear materials,* vol. 361, pp. 218-227, 2007.

[160] L. Fournier, M. Savoie and D. Delafosse, "Influence of localized deformation on A-286 austenitic stainless steel stress corrosion cracking in PWR primary water," *Journal of nuclear materials,* vol. 366, pp. 187-197, 2007.

[161] E. Esquivel and L. Murr, "Grain boundary contributions to deformation and solid-state flow in severe plastic deformation," *Materials science and engineering A,* vol. 409, pp. 13-23, 2005.

[162] D. Edwards, B. Singh and J. Bilde-Sørensen, "Initiation and propagation of cleared channels in neutron-irradiated pure copper and a precipitation hardened CuCrZr alloy," *Journal of nuclear materials,* vol. 342, pp. 164-178, 2005.

[163] Y. Dai, X. Jia, J. Chen, W. Sommer, M. Victoria and G. Bauer, "Microstructure of both as-irradiated and deformed 304L stainless steel irradiated with 800 MeV protons," *Journal of nuclear materials,* vol. 296, pp. 174-182, 2001.

[164] N. Yamamoto, T. Chuto, Y. Murase and J. Nagakawa, "Correlation between embrittlement and bubble microstructure in helium-implanted materials," *Journal of nuclear materials,* Vols. 329-333, pp. 993-997, 2004.

[165] S. Li, M. Grossbeck, Z. Zhang, W. Shen and B. Chin, "The effect of helium on welding irradiated materials," *Welding journal,* vol. 90, pp. 19-26, 2011.

[166] H. Trinkaus and B. Singh, "Helium accumulation in metals during irradiation - where do we stand?," *Journal of nuclear materials,* vol. 323, pp. 229-242, 2003.

[167] H. Schroeder, W. Kesternich and H. Ullmaier, "Helium effects on the creep and fatigue resistance of austenitic stainless steels at high temperatures," *Nuclear engineering and design/Fusion,* vol. 2, pp. 65-95, 1985.

[168] D. Reed, "A review of recent theoretical developments in the understanding of the migration of helium in metals and its interaction with lattice defects," *Radiation effects,* vol. 31, no. 3, pp. 129-147, 1976.

[169] H. Ullmaier, "The influence of helium on the bulk properties of fusion reactor structural materials," *Nuclear fusion,* vol. 24, no. 8, pp. 1039-1083, 1984.

[170] G. Amarendra, B. Viswanathan, R. Rajaraman and K. Gopinathan, "Positron lifetime studies of helium bubble kinetics in alpha-irradiated copper," in *Effects of radiation on materials: 15th international symposium. Ed. R.E. Stoller, A.S. Kumar, D.S. Gelles*, Philadelphia, PA (USA), 1992.

[171] V. Chernikov, H. Trinkaus and H. Ullmaier, "Helium bubbles in nickel annealed at T>0.7 Tm," *Journal of nuclear materials,* vol. 250, pp. 103-110, 1997.

[172] B. Singh and H. Trinkaus, "An analysis of the bubble formation behaviour under different experimental conditions," *Journal of nuclear materials,* vol. 186, pp. 153-165, 1992.

[173] J. Chen, S. Romanzetti, W. Sommer and H. Ullmaier, "Helium bubble formation in 800 MeV proton-irradiated 304L stainless steel and alloy 718 during post-irradiation annealing," *Journal of nuclear materials,* vol. 304, pp. 1-7, 2002.

[174] C. Zhang, K. Chen, Y. Wang, J. Sun and D. Shen, "Formation of bubbles in helium implanted 316L stainless steel at temperatures between 25 and 550°C," *Journal of nuclear materials,* vol. 245, pp. 210-216, 1997.

[175] P. Goodhew and S. Tyler, "Helium bubble behaviour in bcc metals below 0.65Tm," *Proceedings of the royal society of London,* vol. A 377, pp. 151-184, 1981.

[176] H. Trinkaus, "The effect of internal pressure on the coarsening of inert gas bubbles in metals," *Scripta metallurgica,* vol. 23, pp. 1773-1778, 1989.

[177] A. Markworth, "On the coarsening of gas-filled pores in solids," *Metallurgical transactions,* vol. 4, pp. 2651-2656, 1973.

[178] I. Lifshitz and V. Slyozov, "The kinetics of precipitation from supersaturated solid solutions," *Journal of*

physics and chemistry in solids, vol. 19, pp. 35-50, 1961.

[179] C. Wagner, "Theorie der Alterung von Niederschlägen durch Umlösen (Ostwald-Reifung)," *Zeitschrift für Elektrochemie, Berichte der Bunsengesellschaft für physikalische Chemie,* vol. 65, pp. 581-591, 1961.

[180] S. Khera, C. Schwaiger and H. Ullmaier, "The influence of stress on the early stages of void formation in a model stainless steel," *Journal of nuclear materials,* vol. 92, pp. 299-305, 1980.

[181] P. Jung, "Stress and stress transient effects on irradiation creep of 20% cold worked stainless steels and nickel alloys," *Journal of nuclear materials,* vol. 113, pp. 133-141, 1983.

[182] H. Schroeder and P. Batfalsky, "The dependence of the high temperature mechanical properties of austenitic stainless steels on implanted helium," *Journal of nuclear materials,* vol. 117, pp. 287-294, 1983.

[183] I. Batra, K. Sonnenberg and H. Ullmaier, "The influence of helium on high temperature fatigue of Type 316 stainless steel," in *Proceedings of the conference organized by the British nuclear energy society: Dimensional stability and mechanical behaviour of irradiated metals and alloys*, Brighton (UK), 11-13 Apr 1983.

[184] P. Jung, A. Schwarz and H. Sahu, "An apparatus for applying tensile, compressive and cyclic stresses on foil specimens during light ion irradiation," *Nuclear instruments and methods in physics research,* vol. A 234, pp. 331-334, 1985.

[185] "Cooling and temperature-stabilizing of thin specimens for mechanical measurements under light ion bombardment," *Nuclear instruments and methods,* vol. 154, pp. 207-212, 1978.

[186] J. Ziegler, M. Ziegler and J. Biersack, "The stopping and range of ions in matter," *Nuclear Instruments and Methods in Physics Research,* vol. B 268, pp. 1818-1823, 2010.

[187] R. Stoller, M. Toloczko, G. Was, A. Certain, S. Dwaraknath and F. Garner, "On the use of SRIM for computing radiation damage exposure," *Nuclear Instruments and Methods in Physics Research B,* vol. 310, pp. 75-80, 2013.

[188] M. Nastasi and J. Mayer, "Thermodynamics and kinetics of phase transformations induced by ion irradiation," *Materials Science Reports,* vol. 6, no. 1, pp. 1-51, 1991.

[189] A. Kohyama, K. Hamada and H. Matsui, "Specimen size effects on tensile properties of neutron irradiated steels.," *Journal of Nuclear Materials,* Vols. 179-181, pp. 417-420, 1991.

[190] W.C.Oliver and G. Pharr, "Measurement of hardness and elastic modulus by instrumented indentation: Advances in understanding and refinements to methodology," *Journal of Materials Research,* vol. 19, pp. 869-872, 2003.

[191] P. Spätig and N. Ilchuk, "On determination of the constitutive behavior of tempered martensitic steels from micro-indentations: application to eurofer97 steel.," *Journal of Nuclear Materials,* vol. 442, pp. 869-872, 2013.

[192] O. Takakuwa, Y. Kawaragi and H. Soyama, "Estimation of the yield stress of stainless steel from the Vickers hardness taking account of the residual stress.," *Journal of Surface Engineered Materials and Advanced Technology,* vol. 3, pp. 262-268, 2013.

[193] X. Li and B. Bhushan, "A review of nanoindentation continuous stiffness measurement technique and its applications," *Materials characterization,* vol. 48, pp. 11-36, 2002.

[194] W. D. Nix and H. Gao, "Indentation size effects in crystalline materials: a law for strain gradient plasticity," *Journal of the mechanics and physics of solids,* vol. 46, no. 3, pp. 411-425, 1998.

[195] Y. Huang, F. Zhang, K. Hwang, W. Nix, G. Pharr and G. Feng, "A model of size effects in nano-indentation," *Journal of the mechanics and physics of solids,* vol. 54, pp. 1668-1686, 2006.

[196] S. Kalidindi and S. Pathak, "Determination of the effective zero-point and the extraction of spherical nanoindentation stress-strain curves," *Acta materialia,* vol. 56, pp. 3523-3532, 2008.

[197] J. Deuschle, S. Enders and E. Arzt, "Surface detection in nanoindentation of soft polymers," *Journal of material research,* vol. 22, no. 11, pp. 3107-3119, 2007.

[198] G. Pharr, J. Strader and W. Oliver, "Critical issues in making small-depth mechanical property measurements by nanoindentation with continuous stiffness measurement," *Journal of materials research and technology,* vol. 24, pp. 653-666, 2009.

[199] S. Vachhani, R. Doherty and S. Kalidindi, "Effect of continuous stiffness measurement on the mechanical properties extracted using spherical nanoindentation," *Acta materialia,* vol. 61, pp. 3744-3751, 2013.

[200] M. Jenkins, "Characterization of radiation-damage microstructure by TEM," *Journal of Nuclear Materials,* vol. 216, pp. 124-156, 1994.

[201] O. Scherzer, "The theoretical resolution limit of the electron microscope," *Journal of Applied Physics,* pp. 20-29, 1949.

[202] M. Rühle and M. Wilkens, "Defocusing contrast of cavities -1. Theory," *Cryst. Lattice Defects,* vol. 6, p. 129, 1975.

[203] R. Schäublin, "Nanometric crystal defects in transmission electron microscopy," *Microscopy reserach and technique,* vol. 69, pp. 305-316, 2006.

[204] S. Jublot-Leclerc, M.-L. Lescoat, F. Fortuna, L. Legras, X. Li and A. Gentils, "TEM study of the nucleation of bubbles induced by He implantation in 316L industrial austenitic stainless steel," *Journal of nuclear materials,* vol. 466, pp. 646-652, 2015.

[205] A. De Backer, G. Adjanor, C. Domain, M. Lescoat, S. Jublot-Leclerc, F. Fortuna, A. Gentils, C. Ortiz, A. Souidi and C. Becquart, "Modeling of helium bubble nucleation and growth in austenitic stainless steels using an Object Kinetic Monte Carlo method," *Nuclear instruments and methods in physics research B,* vol. 352, pp. 107-114, 2015.

[206] F. Krumeich, "Properties of electrons, their interactions with matter and applications in electron microscopy," ETHzürich, Zürich, 2016.

[207] C. Hérbert, "CCMX Advanced course: Introduction to analytical electron microscopy," Laboratoire de spectrométrie et microscopie electronique, EPFL, Lausanne, 2014.

[208] R. Egerton, "Physics of Electron Scattering," in *Electron energy-loss spectroscopy in the electron microscope*, Springer, 2011, pp. 170-172.

[209] T. Malis, S. Cheng and R. Egerton, "EELS log-ratio technique for specimen-thickness measurement in the TEM," *Journal of electron microscopy technique,* vol. 8, pp. 193-200, 1988.

[210] R. Egerton and S. Cheng, "Measurement of Local Thickness by Electron Energy-Loss Spectroscopy," *Ultramicroscopy,* vol. 21, no. 3, p. 231–244, 1987.

[211] S. Kojima and S. Zinkle, "Radiation hardening in neutron-irradiated polycrystalline copper: barrier strength of defect clusters," *Journal of nuclear materials,* Vols. 179-181, pp. 982-985, 1991.

[212] H. Trinkaus, "Energetics and formation kinetics of helium bubbles in metals," *Radiation Effects,* vol. 78, no. 1-4, pp. 189-211, 1983.

[213] W. Jäger, R. Manzke, H. Trinkaus, G. Crecelius and R. Zeller, "Density and pressure of helium in small bubbles in metals," *Journal of nuclear materials,* Vols. 111-112, pp. 674-681, 1982.

[214] V. Chernikov, H. Trinkaus, P. Jung and H. Ullmaier, "The formation of helium bubbles near the surface and in the bulk in nickel during post-implantation annealing," *Journal of nuclear materials,* vol. 170, pp. 31-38, 1990.

[215] L. Murr, G. Wong and R. Horylev, "Measurement of interfacial free energies and associated temperature coefficient in 304 stainless steel," *Acta metallurgica,* vol. 21, pp. 595-604, 1973.

[216] S. Maloy, M. James and M. Toloczko, "The high temperature tensile properties on ferritic-martensitic and austenitic steels after irradiation in an 800 MeV proton beam," in *Conference proceedings seventh information exchange on actinide and fission product partitioning and transmutation*, Jeju, Republic of Korea, NEA, pp 669-678., 2003.

[217] A. Brozova and S. Lynch, "Transgranular stress-corrosion cracking in austenitic stainless steels at high temperatures," in *Corrosion in light water reactors: stress corrosion cracking*, Woodhead Publishing, 2007, pp. 149-161.

[218] B. Szost and P. Rivera-Diaz-del-Castillo, "Unveiling the nature of hydrogen embrittlement in bearing steels," *Scripta materialia,* vol. 68, no. 7, pp. 467-470, 2013.

[219] J. Herms, J. Olive and M. Puiggali, "Hydrogen embrittlement of 316L type stainless steel," *Materials Science and Engineering,* vol. A272, pp. 279-283, 1999.

[220] D. Holt, "Dislocation cell formation in metals," *Applied physics,* vol. 41, no. 8, pp. 3197-3201, 1970.

[221] B. Singh, T. Leffers, W. Green and M. Victoria, "Nucleation of helium bubbles on dislocations, dislocation networks and dislocations in grain boundaries during 600 MeV proton irradiation of aluminium," *Journal of nuclear materials,* vol. 125, pp. 287-297, 1984.

[222] J. Chen, S. Romanzetti, W. Sommer and H. Ullmaier, "Helium bubble formation in 800 MeV proton-irradiated 304L stainless steel and alloy 718 during post-irradiation annealing," *Journal of nuclear materials,* vol. 304, pp. 1-7, 2002.

[223] H. Schroeder and F. Fichtner, "On the coarsening mechanisms of helium bubbles - Ostwald ripening versus migration and coalescence," *Journal of nuclear materials,* Vols. 179-181, pp. 1007-1010, 1991.

[224] K. Nakata, O. Okada, Y. Ueki and T. Kamino, "Effects of foil thickness on measurement of grain boundary

segregation with FEG-TEM/EDS in austenitic stainless steels," *Journal of Electron Microscopy,* vol. 47, no. 3, pp. 193-200, 1998.

[225] E. Simonen and S. Bruemmer, "Thermally induced grain boundary composition and effects on radiation-induced segregation," in *Proceedings of 8th international symposium on environmental degradation of materials in nuclear power systems-water reactors*, Amelia Island, Florida (USA), 10-14 Aug 1997.

[226] G. Odette and G. Lucas, "The effects of intermediate temperature irradiation on the mechanical behavior of 300-series austenitic stainless steels," *Journal of nuclear materials,* Vols. 179-181, pp. 572-576, 1991.

[227] R. Chaouadi, E. Stergar and S. Gavrilov, "Effects of irradiation on the tensile properties and fracture properties of 316L stainless steel," in *International light water reactors material reliability conference*, Chicago (US), 1-4 August 2016.

[228] J. Elen and P. Fenici, "Fast Neutron Irradiation Hardening of Austenitic Stainless Steel at 250°C," *Journal of Nuclear Materials,* vol. 194, pp. 766-770, 1992.

[229] F. Bergner, C. Pareige, M. Hernández-Mayoral, L. Malerba and C. Heintze , "Application of a three-feature dispersed-barrier hardening model to neutron-irradiated Fe–Cr model alloys," *Journal of Nuclear Materials,* vol. 448, no. 1-3, pp. 96-102, 2014.

[230] A. Bement, "Fundamental materials problems in nuclear reactors," in *Second international conference on the strength of metals and alloys*, Pacific Grove (CA). p. 96-102, 30 Aug - 4 Sep 1970 .

[231] K. Tsay , O. Maksimkin , L. Turubarova , O. Rofman and F. Garner , "Microstructural defect evolution in neutron – Irradiated 12Cr18Ni9Ti stainless steel during subsequent isochronous annealing," *Journal of Nuclear Materials,* vol. 439, no. 1-3, pp. 148-158, 2013.

[232] I. Villacampa, J. Chen, P. Spätig, H. Seifert and F. Duval, "Helium effects on 316L austenitic stainless steel fracture mechanism," *Key Engineering Materials,* vol. 713, pp. 228-231, 2016.

[233] G. Lucas, "The evolution of mechanical property change in irradiated austenitic stainless steels," *Journal of nuclear materials,* vol. 206, no. 2-3, pp. 287-305, 1993.

[234] A. Seeger, "Radiation damage in solids," in *International atomic energy agency symposium Vol.1 101-127*, Vienna (AT), 1962.

[235] S. Zinkle and Y. Matsukawa, "Observation and analysis of defect cluster production and interactions with dislocations," *Journal of nuclear materials,* Vols. 329-333, pp. 88-96, 2004.

[236] F. Kroupa and P. Hirsch, "Elastic interaction between prismatic dislocation loops and straight dislocations," *Discussions of the Faraday Society,* vol. 38, pp. 49-55, 1964.

[237] D. Bacon, U. Kocks and R. Scattergood, "The effect of dislocation self-interaction on the Orowan stress," *Philosophical magazine,* vol. 28, no. 6, pp. 1241-1263, 1973.

[238] U. Kocks, "The theory of an obstacle-controlled yield strength - report after an international workshop," *Materials science and engineering,* vol. 27, pp. 291-298, 1977.

[239] L. Peng and Y. Dai, "Helium/induced hardening effect in ferritic/martensitic steels F82H and Optimax-A irradiated in a mixed spectrum of high energy protons and spallation neutrons.," *Journal of nuclear*

materials, vol. 417, pp. 996-1000, 2011.

[240] G. Monnet, "Multiscale modeling of precipitation hardening: Application to the Fe-Cr alloys," *Acta materialia,* vol. 95, pp. 302-311, 2015.

[241] C. Sobie, N. Bertin and L. Capolungo, "Analysis of obstacle hardening models using dislocation dynamics: application to irradiation induced defects," *Metallurgical and materials transactions A,* vol. 46A, pp. 3761-3772, 2015.

[242] U. Lagerpusch, V. Mohles, D. Baither, B. Anczykowski and E. Nembach, "Double strengthening of copper by dissolved gold-atoms and by incoherent SiO2-particles: how do the two strengthening contributions superimpose?," *Acta materalia,* vol. 48, pp. 3647-3656, 2000.

[243] C. Deo, C. Tomé, R. Lebensohn and S. Maloy, "Modeling and simulation of irradiation hardening in structural ferritic steels for advanced nuclear reactors," *Journal of nuclear materials,* vol. 377, pp. 136-140, 2008.

[244] S. Maloy, M. James, G. Willcutt, W. Sommer, M. Sokolov, L. Snead, M. Hamilton and F. Garner, "The mechanical properties of 316L/304L stainless steels, Alloy 718 and Mod 9Cr-1Mo after irradiation in a spallation environment," *Journal of nuclear materials,* vol. 296, pp. 119-128, 2001.

[245] J. Hunn, E. Lee, T. Byun and L. Mansur, "Helium and hydrogen induced hardening in 316LN stainless steel," *Journal of nuclear materials,* vol. 282, pp. 131-136, 2000.

[246] E. Camus, "Microstructure and hardening of steels containing high helium concentrations," in *Proceedings of the second international workshop on spallation materials technology. pp. 445-452*, Ancona (IT), 19-22 Sep 1997.

[247] J. Weaver, S. Pathak, A. Reichardt, H. Vo, S. Maloy, P. Hosemann and N. Mara, "Spherical nanoindentation of proton irradiated test techniques for measuring irradiation hardening," *Journal of nuclear materials,* vol. 493, pp. 368-379, 2017.

[248] S. Pathak, D. Stojakovic and S. Kalidindi, "Measurement of the local mechanical properties in polycrystalline samples using spherical nanoindentation and orientation imaging microscopy," *Acta materialia,* vol. 57, pp. 3020-3028, 2009.

[249] D. Patel and S. Kalidindi, "Correlation of spherical nanoindentation stress-strain curves to simple compression stress-strain curves for elastic-plastic isotropic materials using finite element models," *Acta Materialia,* vol. 112, pp. 295-302, 2016.

[250] B. Donohue, A. Ambrus and S. Kalidindi, "Critical evaluation of the indentation data analysis methods for extraction of isotropic uniaxial mechanical properties using finite element models," *Acta materialia,* vol. 60, pp. 3943-3952, 2012.

[251] K. Singh, S. Sangal and G. Murty, "Hall-Petch behaviour of 316L austenitic stainless steel at room temperature," *Materials science and technology,* vol. 18, no. 2, pp. 165-172, 2013.

[252] X. Hou, A. Bushby and N. Jennett, "Study of the interaction between the indentation size effect and Hall-Petch effect with spherical indenters on annealed polycrystalline copper," *Journal of physics D: Applied physics,* vol. 41, p. 7pp, 2008.

[253] X. Hou, N. Jennett and M. Parlinska-Wojtan, "Exploiting interactions between structure size and indentation size effects to determine the characteristic dimension of nano-structured materials by indentation," *Journal of physics D: Applied physics,* vol. 46, p. 7pp, 2013.

[254] X. Hou and N. Jennett, "Application of a modified slip-resistance theory to the indentation of single-crystal and polycrystalline copper to model the interactions between indentation size and structure size effects," *Acta materialia,* vol. 60, pp. 4128-4135, 2012.

[255] S. Zinkle, L. Snead, B. Singh and D. Edwards, "Comparison of defect cluster accumulation and pattern formation in irradiated copper and nickel," US Department of energy, office of fusion energy Semiannual progress report for period ending (DOE/ER-0313/17). Web. doi: 10.2172/114927., 01 Apr 1995.

[256] F. Garner, L. Greenwood and B. Oliver, "A reevaluation of helium/dpa and hydrogen/dpa ratios for fast reactor and thermal reactor data used in fission-fusion correlations," in *Effects of radiation on materials: 18th international symposium, STP13904S, R. Nanstad, M. Hamilton, F. Garner, and A. Kumar, Ed., ASTM international*, West Conshohocken, PA (USA), 1999.

[257] W. Gale and T. Totemeier, "Diffusion in metals," in *Smithells Metals Reference Book (Eighth Edition)*, Idaho Falls, ID (USA), 2004.

[258] B. Singh, A. Foreman and H. Trinkaus, "Radiation hardening revisited: role of intracascade clustering," *Journal of nuclear materials,* vol. 249, pp. 103-115, 1997.

[259] Z. Jiao and G. Was, "Localized deformation and IASCC initiation in austenitic stainless steels," *Journal of nuclear materials,* vol. 382, pp. 203-209, 2008.

[260] G. Kegg, C. Horton and J. Silcock, "Grain boundary dislocations in aluminium bicrystals after high-temperature deformation," *Philosophical magazine,* vol. 27, pp. 1041-1055, 1973.

[261] Y. Garud and T. Gerber, "An engineering model for predicting stress corrosion," in *Advances in life prediction methods. Eds.: D.A. Woodford and J.R. Whitehead*, New York, ASME, 1983, pp. 75-83.

[262] J. Boursier, D. Desjardins and F. Vaillant, "The influence of the strain-rate on the stress corrosion cracking of alloy 600 in high temperature primary water," *Corrosion science,* vol. 37, no. 3, pp. 493-508, 1995.

[263] J. Begley, "Strain rate damage model for alloy 600 in primary water," Westinghouse Electric Corporation, EPRI NP-7008, Project S303-8, October 1990.

[264] P. Scott and M. Le Calver, "Some possible mechanisms of intergranular stress corrosion cracking of Alloy 600 in PWR primary water," in *Proceedings of the sixth international symposium on environmental degradation of materials in nuclear power systems - water reactors*, 1993.

[265] M. Hash, J. Busby and G. Was, "The effect of hardening source in proton irradiation-assisted stress corrosion cracking of cold worked type 304 stainless steel," in *Effects of radiation on materials: 21st international symposium, ASTM STP 1447, Eds.: M. L. Grossbeck, T. R. Alien, R. G. Lott and A. S. Kurnar*, West Conshohocken, PA (USA), 2004.

IGNASI **VILLACAMPA ROSÉS**

31 years old
23 Dorfstrasse, Würenlingen 5305
Aargau, Switzerland
+34673343459
ignasi.villacampa@gmail.com

PROFILE

Specialised in **material science**, **mechanical** and **materials engineering**. More than 3 years experience in experimental testing and materials research.

EXPERIENCE

01/2014 – 12/2017 **PhD. Paul Scherrer Institut** - Villigen, Switzerland.

Thesis title: "*Helium Effects on Irradiated Assisted Stress Corrosion Cracking susceptibility of 316L Austenitic Stainless Steel.*"

The role of helium on the mechanical properties and IASCC behaviour was studied by slow strain rate tests with helium implanted solution-annealed and cold-worked 316L stainless steel miniaturised specimens. The PhD was carried out organising the work among three different groups and team members. Besides, the results where shared with international collaborators (SOTERIA founding) and swissnuclear.

03/2013 - 09/2013 **Master thesis. Commissariat à l'énergie atomique et aux énergies alternatives** -St. Paul les Durance, France.

Master thesis title: "*Thermo-mechanical behaviour of LWR fuel rod under power transient conditions using a multi-physics code.*"

Computation of three fission gas models and comparison with experimental data, validation of CARACAS fission gas model (in development), development of the cladding creep rate law and uncertainty and sensitivity analysis using a multi-physics code. Extension to BWR and PWR fuel rods. Ref: christine.struzik@cea.fr

06/2008 - 09/2008 **Construction manager. INFESA** - Barcelona, Spain.

Adaptation to the regulations and improving accessibility and remodelling of the station of Sarrià FGC. Arranging access to the street Cardinal Sentmenat (Barcelona, Spain). Property: GISA-FGC. Budged: 1,372,906.88 €.

EDUCATION

09/2007 - 06/2011 **Mechanical engineer. Universitat de Girona (UdG)** - Girona, Spain.

09/2011 - 09/2013 **European Master in Innovation in Nuclear Energy (EMINE). Universitat Politècnica de Catalunya / Institute Polytechnique de Grenoble (INP Grenoble)** - Barcelona, Spain / Grenoble, France. http://www.kic-innoenergy.com/education/master-school/msc-emine-european-master-in-nuclear-energy/

LANGUAGES

English: Advanced C2	**French:** Equivalent to B1+
Spanish: Mother-tongue	**Italian:** Equivalent to A2+
Catalan: Mother-tongue	**German:** Equivalent to B1

PUBLICATIONS

I. Villacampa, J. C. Chen, P. Spätig, H. P. Seifert, F. Duval, **"Helium Effects on 316L Austenitic Stainless Steel Fracture Mechanism"**, Key Engineering Materials, Vol. 713, pp. 228-231, 2016.

I. Villacampa, J. C. Chen, P. Spätig, H. P. Seifert, F. Duval, **"Helium Effects on IASCC Susceptibility in As-Implanted Solution Annealed, Cold-Worked and Post-Implantation annealed 316L Steel"**, Corrosion Engineering Science and Technology, Vol. 51 (8), pp. 567-577.

CONFERENCES

- Oral presentation: nuclear materials conference (**NuMat**), Montpellier, France.   7-10 Oct 2016.
- Oral presentation: International Conference on Fracture and Damage Mechanics (**FDM**), Alicante, Spain. 14-16 Sep 2016.
- Oral presentation: European Corrosion Congress (**EUROCORR**), Montpellier, France. 11-15 Sep 2016.
- Oral presentation: European Corrosion Congress (**EUROCORR**), Graz, Austria.   6-10 Sep 2015.
- Poster presentation: International cooperative group on environmentally assisted cracking (**ICG-EAC**), Prague, Czech Republic. 6-11 Apr 2014.

COMPUTER SKILLS

Matlab, inventor, AutoCAD, word, excel, powerpoint, vision, ALCYONE, scanning electron microscope (SEM), transmission electron microscope (TEM), focused ion beam (FIB), microshield, RELAP, Parcs.

OTHER COURSES

"Combining Structural & analytical Investigations of Matter at the Micro-, Nano- and Atomic Scales": Lausanne, École polytechnique fédérale de Lausanne (EPFL)

"Radiation protection for handling sealed and unsealed radiation sources": Villigen, Paul Scherrer Institut.

"Nuclear Corrosion Summer School": Bled, Slovenia.

"Certificate of professional development with Instrumented Indention": Lausanne, École polytechnique fédérale de Lausanne (EPFL).

ADDITIONAL INFORMATION

Former professional tennis player: 708th ATP, 51st Spanish and 8th Swiss.